

SQT

**NASA CONTRACTOR  
REPORT**

**NASA CR-152130**

**NASA CR-152130**

(NASA-CR-152130) STUDY OF AERODYNAMIC  
TECHNOLOGY FOR VSTOL FIGHTER/ATTACK  
AIRCRAFT: HORIZONTAL ATTITUDE CONCEPT  
Final Report (Northrop Corp.) 242 p  
HC A11/MF A01

N79-10024

Unclas  
CSCI 01A G3/02 37145

**STUDY OF AERODYNAMIC TECHNOLOGY  
FOR VSTOL FIGHTER/ATTACK AIRCRAFT –  
HORIZONTAL ATTITUDE CONCEPT**

*S. H. Brown*



*Prepared by*

*NORTHROP CORPORATION, AIRCRAFT GROUP*

*Hawthorne, Ca.*

*for Ames Research Center*

PRECEDING PAGE BLANK NOT REPRODUCED

### SUMMARY

An analysis was made of a horizontal attitude VSTOL (HAVSTOL) supersonic, fighter-attack aircraft concept. The concept features a close coupled canard in conjunction with a clipped delta wing. In addition, the General Electric RALS turbofan propulsion concept is used where the fan air from the twin turbofan engines is ducted forward and augmented for VSTOL operations. This split propulsion system allowed a lower supersonic drag to be achieved. The canard and RALS provide a match between the center of gravity and the resultant thrust vector for vertical flight while keeping the main engine, vectorable ADEN nozzles at the wing trailing edge. The latter generally provided favorable propulsive lift interference. The canard and trailing edge flaps are scheduled as a function of angle of attack and Mach number to minimize the drag-due-to-lift. Reaction control for subaerodynamic flight is obtained in pitch and yaw from the RALS and in roll from wing-tip jets powered by bleed air from the RALS duct.

Emphasis during the study was placed on development of aerodynamic characteristics, aerodynamic-propulsion interactions and the identification of aerodynamic uncertainties together with the development of a wind-tunnel program to resolve some of the uncertainties. Mass properties and performance were also estimated. The structural design and flight controls concept were only studied in sufficient depth to assure the credibility of the design.

The aerodynamic design of the vehicle includes flight at near neutral longitudinal stability at supersonic speeds, and 15 percent unstable at subsonic speeds. Also, active controls are used to stabilize the aircraft on the lateral directional axes. Fixed camber of the wing body was developed using the NASA-Ames program, as also was the optimum variable camber and canard deflection as a function of angle of attack and Mach number.

Aerodynamic data developed include static aerodynamic characteristics about all axes, control effectiveness, drag, propulsion induced effects and reaction control blending. One of the more important conclusions was that a combination of trim with canard and trailing edge flaps at subsonic speeds was not as effective as deleting the canard, retaining the stability margin, and trimming with trailing edge flaps alone.

Performance estimates show that the goals of 6.2 g sustained load factor at M 0.6 and a specific excess power of 274 m/sec (900 fps) at M 0.9 both at 3,048 m (10,000 ft) are exceeded.

Finally, aerodynamic uncertainties have been identified based on the program studies. The uncertainties are concerned with supersonic wave drag, canard effects on stability about all axes, optimum trim distribution between the canard and trailing edge flap, twin afterfairing drag, the value of vectored thrust for maneuver and propulsion induced effects in hover and transition. A wind tunnel test plan is developed to help resolve the uncertainties. In addition, a preliminary wind-tunnel model analysis has been made to fit with the test plan.

## SYMBOLS

a. c.	Aerodynamic Center
$a_l$	Aircraft Longitudinal Acceleration
$a_n$	Aircraft Normal Acceleration
AR	Aspect Ratio
$a_x$	Aircraft Longitudinal Acceleration
$a_y$	Aircraft Lateral Acceleration
$a_z$	Aircraft Vertical Acceleration
c	Mean Aerodynamic Chord
$C_D$	Drag Coefficient
$C_{DF}$	Flat Plate Skin Friction Drag Coefficient
$C_{DL}$	Drag-Due-to-Lift Coefficient
$C_{D_{MIN}}$	Minimum Drag Coefficient
$C_{D0}$	Drag Coefficient at Zero Lift
$C_{D_{VISC}}$	Viscous Drag Coefficient
$\Delta C_{DRN}$	Incremental Drag Coefficient Due to Reynolds Number Variation
$C_f$	Flat Plate, Skin Friction Coefficient
c.g., C. G.	Center Of Gravity
$C_L$	Lift Coefficient
$C_{L0}$	Lift Coefficient at Zero Angle-of-Attack
$C_{L_{BO}}$	Lift Coefficient for Buffet Onset
$C_{L_{MAX}}$	Maximum Lift Coefficient
$C_m$	Pitching Moment Coefficient

SYMBOLS (Continued)

$C_l$	Rolling Moment Coefficient
$C_{m_0}$	Pitching Moment at Zero Lift
$C_n$	Yawing Moment Coefficient
$C_Y$	Side Force Coefficient
D	Drag
e	Oswald Spanload Efficiency Factor
$^{\circ}\text{F}$	Degrees Fahrenheit
$F_N$	Net Thrust
$F_1$	Main Engine Thrust
$F_2$	Forward Nozzle Thrust
G, g	Acceleration Due to Gravity
$I_{XX}$	Roll Moment of Inertia
$I_{YY}$	Pitch Moment of Inertia
$I_{ZZ}$	Yaw Moment of Inertia
$^{\circ}\text{K}$	Degrees Kelvin
L	Lift
L/D	Lift to Drag Ratio
l	Length
M	Mach Number
m. a. c.	Mean Aerodynamic Center
$N_z$	Normal Load Factor
O. P. R.	Overall Pressure Ratio
$P_s$	Specific Excess Power
p, q, r	Angular Rates About Aircraft's y, x, and z Axes
"q"	Dynamic Pressure

### SYMBOLS (Continued)

$\Delta P$	Pilot's Pedal Displacement
$R_N$	Reynold's Number
$R_L, R_R$	Force at Left and Right Wingtip Reaction Jets
$S$	Area
$S_{cex}$	Canard Exposed Area
$SM$	Static Margin
$\Delta S_p, \Delta S_R$	Pilot's Fore-Aft and Lateral Stick Displacement
$S_W, S_{REF}$	Wing Reference Area
$S_{WET}$	Component Wetted Area
$T$	Thrust
$T_{LC}, T_{RC}$	Comanded Thrust from Left and Right Engines
$\Delta TL, \Delta TR$	Pilot's Throttle Levers -- Left and Right Engines
$T_F$	Thrust from Forward Nozzle
$T_{RL}, T_{RR}$	Thrust from Rear Left and Right Nozzles
$T/W$	Thrust to Weight Ratio
$U, V, W$	Aircraft Velocity Components Along X, Y, and Z Axes
$W/S$	Wing Loading
$\Delta U_C$	Pilot's Vertical Speed Command Switch
$X, Y, Z$	Aircraft Position with Respect to an Earth Reference
$V_S$	Stall Speed
$V_A$	Approach Speed
$z$	Vertical Height above Wing Chord Plane

SYMBOLS (Continued)

$\alpha$	Angle-of-Attack
$\beta$	Angle-of-Sideslip
$\gamma$	Ratio of Specific Heats
$\Delta$	Incremental Value
$\delta_C$	Canard Deflection
$\delta_f$	Trailing Edge Flap Deflection
$\delta_n$	Leading Edge Flap Deflection
$\delta_E, \delta_A, \delta_R$	Elevator*, Aileron* and Rudder Angles
$\delta_{EC}, \delta_{AC}, \delta_{RC}$	Commanded Elevator*, Aileron* and Rudder Angles
$\delta_1$	Rear Nozzle Vector Angle from Horizontal Reference
$\delta_2$	Forward Nozzle Vector Angle from Vertical Reference
$\ddot{\theta}$	Pitch Acceleration (rad/sec <sup>2</sup> )
$\theta$	Aircraft Pitch Attitude
$\lambda_F$	Fore-Aft Deflection Angle of Forward Nozzle
$\lambda_R$	Deflection Angle of Rear Nozzles
$\lambda_Y$	Lateral Deflection Angle of Forward Nozzle
$\lambda_{FC}$	Commanded Forward Nozzle Angle
$\lambda_{RC}$	Commanded Rear Nozzle Angle
$\phi$	Aircraft Roll Attitude
$\ddot{\phi}$	Roll Acceleration (rad/sec <sup>2</sup> )
$\psi$	Aircraft Heading
$\Lambda_{LE}$	Leading Edge Sweep

\*Note that Flaperons are termed elevators or ailerons in section 5.2 to distinguish their respective control functions.

## CONTENTS

<u>SECTION</u>		<u>PAGE</u>
	SUMMARY . . . . .	iii
	SYMBOLS . . . . .	v
1	INTRODUCTION . . . . .	1-1
2	AIRCRAFT DESCRIPTION . . . . .	2-1
	2.1 Design Philosophy . . . . .	2-1
	2.2 Design Guidelines . . . . .	2-2
	2.3 Aircraft Arrangement Description . . . . .	2-3
3	AERODYNAMIC CHARACTERISTICS . . . . .	3-1
	3.1 Wing Planform Selection . . . . .	3-1
	3.2 Longitudinal Axis Analysis . . . . .	3-4
	3.2.1 Minimum Drag . . . . .	3-4
	3.2.2 Basic Lift, Drag, and Pitching Moment . . . . .	3-5
	3.2.3 Longitudinal Stability Analysis . . . . .	3-6
	3.2.4 Trim Analysis . . . . .	3-9
	3.2.5 Maximum Lift and Buffet Onset . . . . .	3-10
	3.2.6 Longitudinal Aerodynamics Control Effectiveness . . . . .	3-11
	3.2.7 Wing Body Camber Design . . . . .	3-11
	3.3 Lateral-Directional Analysis . . . . .	3-68
	3.3.1 Lateral-Directional Stability . . . . .	3-68
	3.3.2 Lateral-Directional Control Effectiveness . . . . .	3-69
	3.4 Propulsion-Induced Effects . . . . .	3-91
	3.4.1 Cruise/Combat Flight Regime . . . . .	3-92
	3.4.2 Transition Flight Regime . . . . .	3-93
	3.5 Controls Blending . . . . .	3-113
4	PROPULSION CHARACTERISTICS . . . . .	4-1
	4.1 Engine Description . . . . .	4-1
	4.2 Propulsion Trades (Bypass Ratio Study) . . . . .	4-3
	4.3 Air Induction System Design Approach and Sizing . . . . .	4-5
	4.4 Exhaust Nozzle/Aft End Design Approach . . . . .	4-6
	4.5 Engine Installation Loss Assessment . . . . .	4-7
	4.6 Installed Engine Performance . . . . .	4-11
	4.7 Roll Reaction Control . . . . .	4-11

CONTENTS (Continued)

<u>SECTION</u>		<u>PAGE</u>
5	AIRCRAFT DESIGN .....	5-1
	5.1 Structural Design and Analysis .....	5-1
	5.1.1 Design Criteria .....	5-1
	5.1.2 Structural Materials .....	5-2
	5.1.3 Structural Description .....	5-2
	5.1.4 Structural Analysis .....	5-4
	5.2 Flight Control System .....	5-9
	5.2.1 Hover and Transition Regimes - Normal Operation .....	5-9
	5.2.2 Engine Failures in Hover or Transition .....	5-13
	5.2.3 Conventional Flight Regime .....	5-14
	5.3 Mass Properties .....	5-22
	5.3.1 Weight Estimates .....	5-22
	5.3.2 Balance .....	5-22
	5.3.3 Moments of Inertia .....	5-24
	5.4 Crew Station .....	5-25
	5.5 Subsystems .....	5-28
6	AIRCRAFT PERFORMANCE .....	6-1
	6.1 Flight Performance .....	6-1
	6.1.1 Baseline Aircraft Combat Performance .....	6-1
	6.1.2 Thrust Loading and Wing Loading Trades/ Aircraft Sizing .....	6-2
	6.1.3 Sensitivity Studies .....	6-3
	6.2 Takeoff and Landing Performance .....	6-20
	6.2.1 Vertical Takeoff .....	6-20
	6.2.2 Takeoff Transition .....	6-21
	6.2.3 Landing .....	6-21
	6.2.4 Short Takeoff and Landing .....	6-22
7	AERODYNAMIC UNCERTAINTIES .....	7-1
	7.1 Wave Drag at High Mach Number .....	7-1
	7.2 Canard Contribution to Stability .....	7-1
	7.3 Optimum-Canard-Flap Deflections at Subsonic Speeds .....	7-1
	7.4 Canard Effects on Directional Characteristics .....	7-2
	7.5 Twin Afterfairing Drag .....	7-2
	7.6 Vectored Thrust for Maneuver Enhancement .....	7-2
	7.7 Propulsion-Induced Effects in Hover and Transition .....	7-2

CONTENTS (Continued)

<u>SECTION</u>		<u>PAGE</u>
8	PROPOSED RESEARCH PROGRAM .....	8-1
	8.1 Research Objectives .....	8-1
	8.2 Wind Tunnel Test Plan .....	8-1
	8.3 Wind Tunnel Model Design .....	8-5
	8.3.1 General Consideration .....	8-5
	8.3.2 Aerodynamic Force Model .....	8-7
	8.3.3 Jet Effects Model .....	8-7
9	CONCLUSIONS .....	9-1
10	REFERENCES .....	10-1

TABLES

<u>TABLE</u>		<u>PAGE</u>
1-1	Supersonic VSTOL Problem Area and Conceptual Solution . . . . .	1-2
3-1	Minimum Drag Buildup by Component . . . . .	3-14
3-2	Viscous Drag Buildup by Component . . . . .	3-15
3-3	Drag Due to Lift with No Camber, M 1.2 . . . . .	3-16
3-4	Geometry Design Modes . . . . .	3-16
3-5	Drag Due to Lift with Design Camber, M 1.2 . . . . .	3-17
4-1	Fighter Escort Sizing Mission . . . . .	4-4
4-2	Aircraft Propulsion Loss Assessment . . . . .	4-10
5-1	Group Weight Statement . . . . .	5-23
5-2	Moments of Inertia . . . . .	5-24
5-3	Baseline Avionics Suite . . . . .	5-31
6-1	Typical Fighter Escort Mission . . . . .	6-5
8-1	Test Plan . . . . .	8-4
8-2	Comparison Model Size to Tunnel Size . . . . .	8-8

## ILLUSTRATIONS

<u>FIGURE</u>		<u>PAGE</u>
2-1	General Arrangement . . . . .	2-7
2-2	Cross-Sectional Area and Wetted Area Distributions . . . . .	2-9
2-3	Duct Area Distribution . . . . .	2-11
2-4	Inboard Profile . . . . .	2-13
2-5	Conformal Stores Matrix . . . . .	2-15
3-1	Wing Planform Selection . . . . .	3-3
3-2	Minimum Drag vs. Mach Number . . . . .	3-18
3-3	Altitude Effects on Minimum Drag. . . . .	3-19
3-4	Wave Drag Adjustments vs. Mach Number . . . . .	3-20
3-5	Wave Drag Planar Surface Adjustment . . . . .	3-21
3-6	Flight Test/Analytical Adjustment to Minimum Drag . . . . .	3-22
3-7	Lift vs. Angle of Attack at $M \leq 0.6$ , $\delta_n = 0$ , $\delta_c = 0$ . . . . .	3-23
3-8	Lift vs. Angle of Attack at $M \leq 0.6$ , $\delta_n = 24$ , $\delta_c = 0$ . . . . .	3-24
3-9	Trailing-Edge Flap Effectiveness at $M \leq 0.6$ , $\delta_n = 0$ , $\delta_c = 0$ . . . . .	3-25
3-10	Trailing-Edge Flap Effectiveness at $M \leq 0.6$ , $\delta_n = 24$ , $\delta_c = 0$ . . . . .	3-26
3-11	Drag Due to Lift at $M \leq 0.6$ , $\delta_n = 0$ , $\delta_c = 0$ . . . . .	3-27
3-12	Drag Due to Lift at $M \leq 0.6$ , $\delta_n = 24$ , $\delta_c = 0$ . . . . .	3-28
3-13	Lift-Drag Ratio at $M \leq 0.3$ , $\delta_n = 0$ , $\delta_c = 0$ . . . . .	3-29
3-14	Lift-Drag Ratio at $M \leq 0.6$ , $\delta_n = 24$ , $\delta_c = 0$ . . . . .	3-30
3-15	Lift vs. Angle of Attack at $M 0.3$ , $\delta_n = 0$ , $\delta_c = 0$ . . . . .	3-31
3-16	Lift vs. Angle of Attack at $M 0.9$ , $\delta_n = 24$ , $\delta_c = 0$ . . . . .	3-32
3-17	Trailing Edge Flap Effectiveness at $M 0.9$ , $\delta_n = 0$ , $\delta_c = 0$ . . . . .	3-33
3-18	Trailing Edge Flap Effectiveness at $M 0.9$ , $\delta_n = 24$ , $\delta_c = 0$ . . . . .	3-34
3-19	Drag Due to Lift at $M 0.9$ , $\delta_n = 0$ , $\delta_c = 0$ . . . . .	3-35
3-20	Drag Due to Lift at $M 0.9$ , $\delta_n = 24$ , $\delta_c = 0$ . . . . .	3-36
3-21	Lift-Drag Ratio at $M 0.9$ , $\delta_n = 0$ , $\delta_c = 0$ . . . . .	3-37

ILLUSTRATIONS (Continued)

<u>FIGURE</u>		<u>PAGE</u>
3-22	Lift-Drag Ratio at M 0.9, $\delta_n = 24$ , $\delta_c = 0$ . . . . .	3-38
3-23	Lift vs Angle of Attack at M 1.2, $\delta_n = 0$ , $\delta_c = 0$ . . . . .	3-39
3-24	Trailing Edge Effectiveness at M 1.2, $\delta_n = 0$ , $\delta_c = 0$ . . . . .	3-40
3-25	Drag Due to Lift at M 1.2, $\delta_n = 0$ , $\delta_c = 0$ . . . . .	3-41
3-26	Lift-Drag Ratio at M 1.2, $\delta_n = 0$ , $\delta_c = 9$ . . . . .	3-42
3-27	Lift vs Angle of Attack at M 1.6, $\delta_n = 0$ , $\delta_c = 0$ . . . . .	3-43
3-28	Trailing Edge Flap Effectiveness at M 1.6, $\delta_n = 0$ , $\delta_c = 0$ . . . . .	3-44
3-29	Drag Due to Lift at M 1.6, $\delta_n = 0$ , $\delta_c = 0$ . . . . .	3-45
3-30	Lift/Drag Ratio M 1.6, $\delta_n = 0$ , $\delta_c = 0$ . . . . .	3-46
3-31	Drag Due to Lift . . . . .	3-47
3-32	Spanload Efficiency vs. Static Margin . . . . .	3-48
3-33	Aerodynamic Center Error vs. Nose Area Moment Coefficient . . . . .	3-49
3-34	Canard Effects on Lift at M $\leq 0.6$ . . . . .	3-50
3-35	Canard Effects on Lift at M 1.2 . . . . .	3-51
3-36	Canard Effects on Static Stability at M $\leq 0.6$ . . . . .	3-52
3-37	Canard Effects on Static Stability at M 1.2 . . . . .	3-53
3-38	Aerodynamic Center Location . . . . .	3-54
3-39	Leading Edge Flap Schedule, CG = 0.26 $\bar{c}$ . . . . .	3-55
3-40	Canard Deflection Schedule, CG = 0.26 c . . . . .	3-56
3-41	Optimum Trailing Edge Flap Deflection for Trim . . . . .	3-57
3-42	Optimum Subsonic Trim Polars . . . . .	3-58
3-43	Optimum Supersonic Polars . . . . .	3-59
3-44	Trim Lift-Drag Ratio . . . . .	3-60
3-45	Maximum Usable Lift . . . . .	3-61
3-46	Lift Coefficient for Buffet Onset . . . . .	3-62
3-47	Canard Effectiveness at M 0.9, $\delta_n = 24$ , $\delta_f = 0$ . . . . .	3-63
3-48	Canard Effectiveness at M 1.2, $\delta_n = 0$ , $\delta_f = 0$ . . . . .	3-64
3-49	Canard Control Effectiveness . . . . .	3-65
3-50	Trailing Edge Flap Control Effectiveness . . . . .	3-66
3-51	Geometry Model for Aerodynamic Analysis . . . . .	3-67

ILLUSTRATIONS (Continued)

<u>FIGURE</u>		<u>PAGE</u>
3-52	Side Force at M 0.6 . . . . .	3-71
3-53	Side Force at M 0.9 . . . . .	3-72
3-54	Side Force at M 1.2 . . . . .	3-73
3-55	Side Force at M 1.6 . . . . .	3-74
3-56	Yawing Moment at M 0.6 . . . . .	3-75
3-57	Yawing Moment at M 0.9 . . . . .	3-76
3-58	Yawing Moment at M 1.2 . . . . .	3-77
3-59	Yawing Moment at M 1.6 . . . . .	3-78
3-60	Rolling Moment at M 0.6 . . . . .	3-79
3-61	Rolling Moment at M 0.9 . . . . .	3-80
3-62	Rolling Moment at M 1.2 . . . . .	3-81
3-63	Rolling Moment at M 1.6 . . . . .	3-82
3-64	Vertical Tail Control Effectiveness at M 0.6 . . . . .	3-83
3-65	Vertical Tail Control Effectiveness at M 0.9 . . . . .	3-84
3-66	Vertical Tail Control Effectiveness at M 1.2 . . . . .	3-85
3-67	Vertical Tail Control Effectiveness at M 1.6 . . . . .	3-86
3-68	Elevon Roll Control Effectiveness at M 0.6 . . . . .	3-87
3-69	Elevon Roll Control Effectiveness at M 0.9 . . . . .	3-88
3-70	Elevon Roll Control Effectiveness at M 1.2 . . . . .	3-89
3-71	Elevon Roll Control Effectiveness at M 1.6 . . . . .	3-90
3-72	Effect of Deflected Thrust on Lift . . . . .	3-95
3-73	Induced Lift Due to Thrust Vectoring . . . . .	3-97
3-74	Induced Pitching Moment Due to Thrust Vectoring . . . . .	3-98
3-75	Propulsion-Induced Lift in Transition . . . . .	3-99
3-76	Propulsion-Induced Pitching Moment in Transition . . . . .	3-104
3-77	Propulsion-Induced Rolling Moment in Transition . . . . .	3-109
3-78	RAIS Wake Contribution to Propulsion - Induced Lift in Transition . . . . .	3-111
3-79	RAIS Wake Contribution to Propulsion - Induced Pitching Moment . . . . .	3-111
3-80	RAIS Wake Contribution to Propulsion - Induced Rolling Moment . . . . .	3-112
3-81	Roll Moment Blending . . . . .	3-115

ILLUSTRATIONS (Continued)

<u>FIGURE</u>		<u>PAGE</u>
4-1	Remote Augmented Lift System (RALS) . . . . .	4-2
4-2	Air Induction System Configuration . . . . .	4-5
4-3	Engine Compressor Bleed Rates . . . . .	4-8
4-4	Matched Inlet Recovery . . . . .	4-9
5-1	Structural Diagram . . . . .	5-7
5-2	Airframe - Flight Control System Configuration . . . . .	5-16
5-3	Attitude Augmentation . . . . .	5-17
5-4	Speed Augmentation . . . . .	5-18
5-5	Transition-Landing Sequence . . . . .	5-19
5-6	Crossfeed Matrix Details . . . . .	5-20
5-7	Rolling Moments After Engine Loss . . . . .	5-21
5-8	Fixed Seat - General Arrangement . . . . .	5-27
6-1	Effect of Load Factor and Mach Number on Specific Excess Power at 3048 M (10,000 ft) . . . . .	6-6
6-2	Effect of Load Factor and Mach Number on Specific Excess Power at 6096 M (20,000 ft) . . . . .	6-7
6-3	Effect of Load Factor and Mach Number on Specific Excess Power at 9144 M (30,000 ft) . . . . .	6-8
6-4	Specific Excess Power Contour at 1g . . . . .	6-9
6-5	Sustained Maneuver Capability . . . . .	6-10
6-6	Aircraft Sizing Matrix . . . . .	6-11
6-7	Variation of Specific Excess Power with T/W and W/S for Aircraft Sizing Matrix . . . . .	6-12
6-8	Variation of Sustained Load Factor with T/W and W/S for Aircraft Sizing Matrix . . . . .	6-13
6-9	Performance Goals Relationship to Aircraft Sizing Matrix . . . . .	6-14
6-10	Specific Excess Power Levels on Aircraft Sizing Matrix . . . . .	6-15
6-11	Sustained Load Factor Levels on Aircraft Sizing Matrix . . . . .	6-16
6-12	Effect of Thrust, Specific Fuel Consumption, Drag and Empty Weight . . . . .	6-17
6-13	Effect of Thrust, Specific Fuel Consumption, Drag and Empty Weight . . . . .	6-18

ILLUSTRATIONS (Continued)

<u>FIGURE</u>		<u>PAGE</u>
6-14	Thrust Vectors for Rotation . . . . .	6-24
6-15	Thrust Vectors to Hold 20° Pitch on Deck . . . . .	6-25
6-16	Takeoff Transition Trajectory . . . . .	6-26
6-17	Primary Nozzle Thrust Vector Command . . . . .	6-27
6-18	Short Takeoff Performance . . . . .	6-28
6-19	Single Engine Landing Performance . . . . .	6-29
8-1	Wind Tunnel Model Wing . . . . .	8-9
8-2	Model Scale Requirements for Propulsion Simulator Size . . . . .	8-10
8-3	Engine Simulator Performance . . . . .	8-11
8-4	Pipe Mach No. — Simulator Drive and Bleed Lines . . . . .	8-12
8-5	Ames 9 x 7 Wind Tunnel Envelope . . . . .	8-14
8-6	Wind Tunnel Model Support Concepts . . . . .	8-15
8-7	Wind Tunnel Dynamic Pressure and Reynolds Number Characteristics . . . . .	8-16
8-8	Balance Envelope . . . . .	8-17
8-9	Model Sketch . . . . .	8-18

SECTION 1  
INTRODUCTION

The study of aerodynamic technology of VSTOL fighter/attack class aircraft is being pursued by the NASA Ames Research Center and the David Taylor Naval Ship Research and Development Center. This document reports the work covered under the joint sponsorship of these organizations in Phase I of Contract NAS 2-9771, "Study of Aerodynamic Technology for VSTOL Fighter/Attack Aircraft." This phase covered the period from 1 November 1977 to 31 May 1978. Phase I objectives were:

1. To identify and analyze two high performance VSTOL concepts having potential utility to fulfill the Navy fighter/attack role.
2. To estimate the aerodynamic, propulsion, and performance characteristics of these concepts and to assess technical uncertainties requiring additional research.
3. To outline a wind tunnel program in which these aerodynamic uncertainties would be investigated and which would provide a data base for future use.

The VSTOL fighter/attack concepts studied both employ the lift/cruise propulsive lift concept; one is a vertical attitude configuration termed VATOL, and the other is a horizontal attitude configuration and is termed HAVSTOL. This report deals with the HAVSTOL concept. Results of the study of the VATOL concept are presented in NASA CR 152131.

Satisfying the combined requirements of supersonic flight and vertical takeoff provides a significant design challenge. The severity of this challenge is increased by the need to deal with the fighter-related issues of agility and combat persistence while minimizing the problems associated with the presence of engine exhaust flow in proximity to the aircraft and ground surface.

A listing of the major problem areas and the conceptual solutions offered by horizontal and vertical attitude configurations is presented in Table 1-1. This table shows that, compared with the VATOL, the HAVSTOL is a more complex approach to

**TABLE 1-1. SUPERSONIC VSTOL PROBLEM AREA AND CONCEPTUAL SOLUTION**

SUPERSONIC VSTOL PROBLEM AREA	COMPARISON OF SOLUTIONS	
	HORIZONTAL ATTITUDE VSTOL: L/C CONCEPT; TWIN, VARIABLE CYCLE, TURBOFANS	VERTICAL ATTITUDE BSTOL: L/C CONCEPT, TWIN VARIABLE TURBINE, DRY TURBOJETS
ACHIEVEMENT OF SMOOTH, LOW CROSS- SECTIONAL AREA	PROPULSIVE LIFT SEPARATION, WIDE-SPACED AFTERFAIRINGS	THRUST ALWAYS THROUGH C.G. C.G. CONVENTIONAL REAR ENGINE CONFIGURATION SHAPING
SUCKDOWN	MINIMIZE BY CONFIGURATION SHAPING, HIGH ATTITUDE LIFTOFF AND TOUCHDOWN	INHERENTLY MINIMUM BASE AREA
FOUNTAIN	AVOID BY JET LOCATION AND DIRECTION, HIGH ATTITUDE LIFTOFF AND TOUCHDOWN	CLOSELY SPACED NOZZLES; NO FOUNTAIN
EXHAUST INGESTION	AVOID FOUNTAINS, INLET LOCATION, HIGH ATTITUDE LIFTOFF AND TOUCHDOWN	LAUNCH AND RECOVERY OUT- SIDE DECK EDGE TO AVOID WALL JET INFORMATION
SHIP INTERFACE	NORMAL VTOL OPERATIONS, EXCEPTIONAL STO PERFORMANCE VERY LOW CONVENTIONAL APPROACH/LANDING SPEEDS	VERTICAL OPERATIONS RESTRICTED TO SPECIALIZED GANTRY, PILOT ATTITUDE MAINTAINED BY ROTATING COCKPIT ENCLOSURE, STO BY LIMITED SINK OFF BOW (OR SKI- JUMP), CONVENTIONAL ATTITUDE APPROACH/LANDING SPEED REQUIRES ARRESTING HOOK

achieving supersonic performance and a minimum level of propulsion-induced interferences, but that its short takeoff performance and shipboard interface are superior.

During this study, emphasis was placed on the aerodynamic and propulsion areas. Supporting work in structures, flight control, avionic, and component areas was completed only to the extent needed to assure that the concept was credible. Correspondingly, the cruise-combat regime was emphasized and the hover-transition regimes studied to the extent necessary to assure configuration credibility.

Because of the emphasis placed on the aerodynamics and propulsion technological areas, the identification of aerodynamic uncertainties and a test program to resolve them, the baseline aircraft concept was not sized for any particular mission. Rather, a typical possible VTO gross weight of 13608 kg (30,000 lb) was selected together with a STO overload gross weight of 18144 kg (40,000 lb). However, performance characteristics for a typical fighter escort mission were developed for both the baseline aircraft and an aircraft sized to a 925 km (500 nm) radius. The sized aircraft had a VTO gross weight of 14400 kg (31,800 lb). All of the data developed herein except for a minor amount of performance data are for the baseline aircraft concept.

A number of individuals have made major contributions to this study and are identified below. The work was performed under the general direction of Dr. P. T. Wooler.

H. A. Gerhardt	Aerodynamics
W. S. Chen	Aerodynamics
J. C. Carlson	Aerodynamics
H. Ziegler	Propulsion - Induced effects
R. Hoenig	Propulsion
T. J. Weir	Configuration Integration
R. English	Flight Performance
W. Darby	Takeoff Performance
R. Kostanty	Flight Controls

PRECEDING PAGE BLANK NOT FILLED

## SECTION 2

### AIRCRAFT DESCRIPTION

This section presents some of the design philosophy and guidelines used to develop the aircraft concept and then the concept is described. The description includes general arrangement and inboard profile drawings and cross-section and wetted area distributions.

#### 2.1 DESIGN PHILOSOPHY

The design philosophy of the horizontal attitude VSTOL (HAVSTOL) is to apply the techniques of supersonic aircraft design to a VSTOL aircraft concept. Subsonic VSTOL configurations have tended to exhibit large volume concentrations at the center of gravity due to common wing, engine and nozzle locations. Past design solutions for supersonic VSTOL aircraft generally have provided division of the propulsive lift system by a combination of lift engines, used only during terminal flight, and vectorable cruise engines. The lift plus lift/cruise approach generally permits configuration arrangements with satisfactory cross-sectional area distributions and realistic tolerances to center of gravity movement but requires maximum afterburning on the cruise engines for adequate combat performance in addition to development and maintenance of multiple engine types.

The configuration under study has a lift/cruise propulsion system which divides the engine airflow into separate exhausts forward and aft of the center of gravity. The General Electric "Remote Augmented Lift System (RAALS)" variable cycle turbofan engine concept provides most of the advantages of lift engines without separate rotating hardware and separate inlets. The twin-engine design, feeding a single remote augmentor, has additional safety over lift plus lift/cruise configurations for engine-out during VTO flight. This safety results from the ability to maintain aircraft attitude with the remaining engine thrust, thus giving the pilot time and proper attitude to execute a safe ejection.

The configuration also reflects consideration of propulsive-lift interference, supersonic wave drag, high-angle-of-attack aerodynamics, and IR signature. The

twin engine design uses closely-spaced primary nozzles and a common forward nozzle so that in the propulsive lift mode each acts as a single jet and eliminates fountain tendencies at the exhaust locations. The location of the primary engine nozzles is favorable with respect to nozzle/wing integration. Propulsive-aerodynamic interactions associated with the forward nozzle will be reduced primarily by operating concept rather than configuration shaping. A lift off concept is utilized that has initial rotation to a high attitude prior to application of full liftoff thrust. Forward nozzle suckdown and the mid-body fountain are reduced or eliminated, both by raising the forward jet away from the ground and by fore and aft jet orientation. The concept is directly application to STO operations by allowing full use of wing/canard lift at high angle of attack in addition to propulsive lift.

Separated, twin afterfairings are used to reduce nozzle/aft end interference potential in both the vertical and horizontal flight modes. The geometry is shaped to avoid high speed exhaust scrubbing and to create ejector slots between the afterfairings and nozzles in the vertical mode for positive lift interference and lower average exhaust temperature. The twin afterfairings increase effective fineness ratio and create a favorable compression interaction on the lower surface of the wing.

The configuration features close-coupled canard surfaces to enhance high-angle-of-attack characteristics. The multiple lifting surface arrangement permits smoother blending of components and reduced frontal area for minimum wave drag.

The horizontal attitude concept provides the operating flexibility and STO performance desired but incurs associated complexity in aircraft configuration integration. This arrangement has an inherent operational commonality with anticipated "Type A" VSTOL aircraft configurations.

## 2.2 DESIGN GUIDELINES

The initial design guidelines for the VSTOL aircraft configuration were: a vertical takeoff (VTO) weight of 13,608 kg (30,000 lb) and a STO weight of 18,144 kg (40,000 lb). The performance requirements of a 6.2g sustained turn capability at M 0.6 at 3048 m (10,000 ft) and a specific excess power capability  $P_g$  of 274.3 m/sec (900 ft/sec) at M 0.9 at 3048 m (10,000 ft). Installed engine thrust was not less than the VTO weight times 1.20 to ensure sufficient tropical-day thrust for vertical takeoff. The wing sweep should be enough to allow the leading edge to remain subsonic for maneuver at M 1.2.

### 2.3 AIRCRAFT ARRANGEMENT DESCRIPTION

The HAVSTOL concept is shown in the general arrangement drawing of Figure 2-1. This high performance fighter/attack aircraft is designed for a VTO weight of 13,608 kg (30,000 lb) with a wing loading of  $293 \text{ kg/m}^2$  (60 psf), an installed thrust-to-weight ratio of 1.2 on a tropical day and a fuel fraction of 0.34.

Distinguishing features of the concept are:

- 1) Close-coupled canard surfaces mounted on 2-D side inlets.
- 2) "Remote Augmented Lift System" (RALS) variable cycle turbofan engine.
- 3) Twin-engine design feeding a single remote augmentor.
- 4) Vectorable Aden nozzles.
- 5) Twin afterfairings that create ejector slots in the VTO mode.
- 6 Clipped delta wing with maneuvering flaps.
- 7) Provision for high-attitude liftoff.

Integration of the aircraft was achieved by paying close attention to the overall area distribution and the maximum cross section area as shown in Figure 2-2. It is desired that the aircraft total area distribution closely match an ideal area distribution and that the maximum cross-section area be a minimum to minimize the supersonic wave drag. The maximum area usually tends to peak at the aircraft center of gravity; incorporation of the RALS propulsion system allows the engines to be located aft of the maximum area and the remote augmentor forward of the maximum area. This arrangement permits the fuselage fuel and disposable stores to be located at the aircraft center of gravity without the usual associated buildup of the maximum area although the duct forward to the remote augmentor does add to the cross-sectional area.

Careful location of different aircraft components is required to match the target area distribution. As shown in the general arrangement, the engine inlet is located behind the cockpit with the canard just aft of the inlets and the wing directly behind the canard resulting in a gradual area buildup on the forward side of the area distribution while placing the wing and canard areas on either side of the maximum area. The aft side of the area distribution is smoothed by the addition of twin afterfairings located on the wing and extending aft of the engine nozzles. These fairings reduce the slopes on the area distribution plot and provide ideal locations for twin vertical

tails and main landing gear. Also shown in Figure 2-2 are wetted area distribution, body fuel distribution, and in Figure 2-3 the engine duct area distribution.

The leading and trailing edge flap system and the canard are scheduled together as a function of Mach number and angle of attack for minimum drag at lift. In addition the trailing edge flaperon provides pitch and roll control. The canard may also be used to assist in trim at very high attitudes and, potentially, for maneuvering with thrust vectoring.

Reaction control jets are located in each wing tip to provide roll control in the vertical takeoff and landing flight regime. Yaw, and pitch control are achieved through scheduling of the remote augmentor thrust and nozzle deflection. Longitudinal translation is provided by collective deflection of the primary nozzles.

In balancing the aircraft, three critical modes must be considered: static weight balance, thrust balance and fuel balance. Static weight balancing is facilitated by locating the engines as far aft in the fuselage as the thrust balance will permit. The afterbodies allow the landing gear and some equipment bays to be placed at a relatively aft location. These items, plus the weight of the wing, balance the forward weights of the cockpit, radar, avionics, and canards. To locate the resultant thrust vector at the center-of-gravity location, the remote augmentor can be located to balance the engine thrust moment in the vertical takeoff and landing regime. Fuel is then balanced about the c.g. by locating the fuselage fuel slightly forward of the c.g., to balance the wing and afterfairing fuel located aft of the c.g.

Subsystems integration is achieved by the consideration of functional location, maintainability and survivability. The functional location of systems is of primary importance in the reduction of weight and volume. As shown on the inboard profile, Figure 2-4, the location of the radar, avionics and cockpit close together is functional in that all require air-conditioning, and close proximity to each other and the ECS minimizes the ducting and temperature losses.

Fighter/attack aircraft have long been designed to meet a high level of performance, while configured with little or no weapons. When, in the real operational world, these aircraft are loaded with external bombs and tanks, their performance is degraded such that they become vulnerable to attack from lower-performance aircraft. It has been recognized that better aircraft/weapon integration is necessary to improve aircraft performance and weapon delivery.

A total of six weapon configurations have been shown on the Conformal Stores Matrix, Figure 2-5. The first five are representative of advanced air-to-ground weapons concepts. The sixth represents state-of-the-art guided weapon, with large span fixed main lifting surfaces in combination with a cruciform configuration. This type of weapon is carried on the fuselage corners either semi-submerged or tangent-mounted. Air-to-air missiles are carried internally in the fuselage and launched externally from tubes. Minimum aircraft performance degradation and low detection signature are primary factors that influenced the weapon configuration and carriage.

ORIGINAL PAGE IS  
OF POOR QUALITY

LEUDDUJ. ERAM

PRECEDING PAGE BLANK NOT RELATED

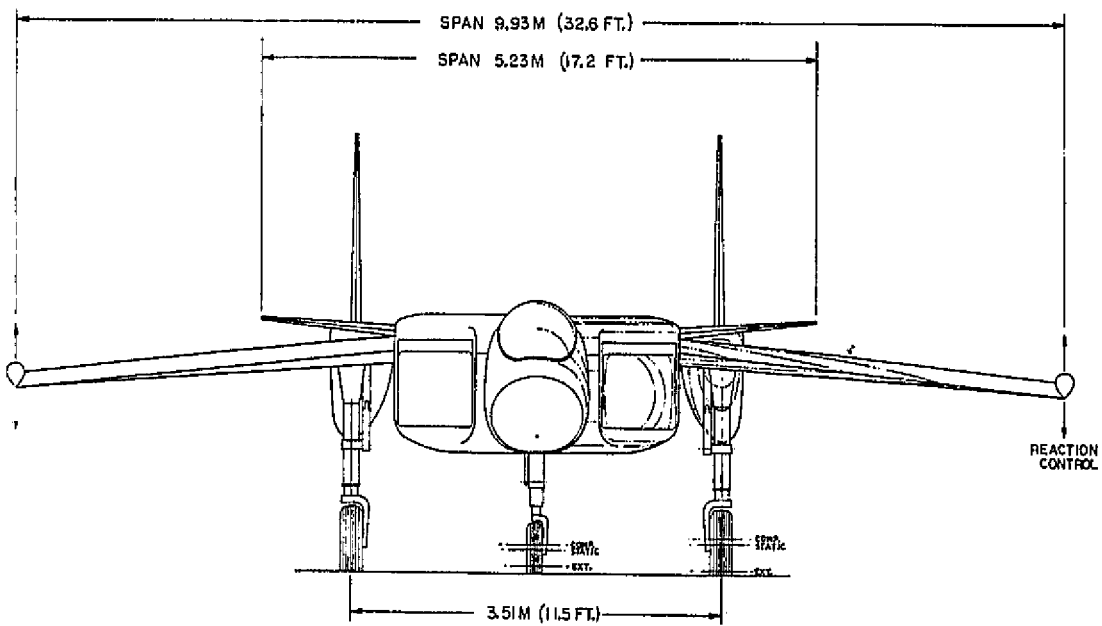
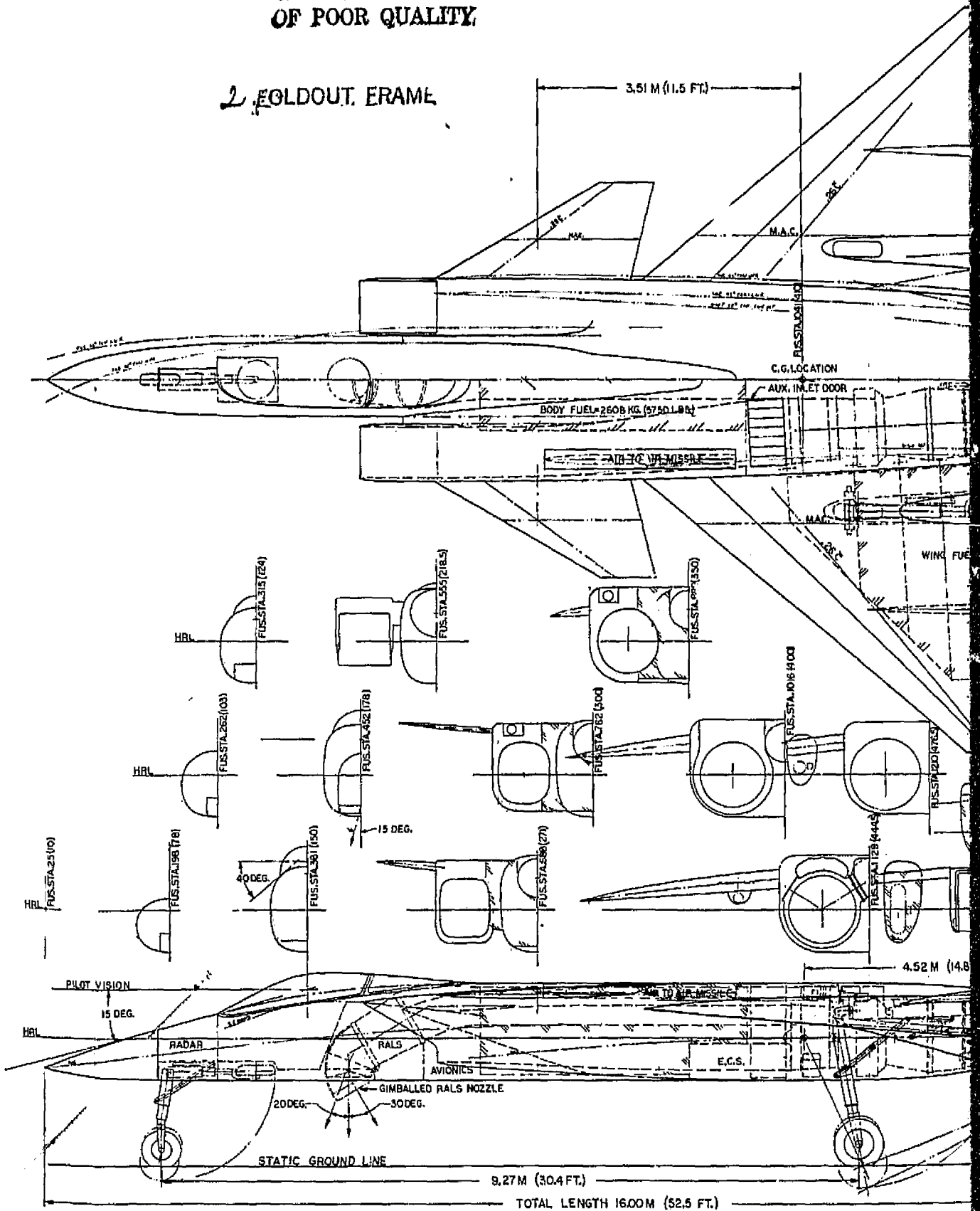


FIGURE 2-1. GENERAL ARRANGEMENT

ORIGINAL PAGE IS  
OF POOR QUALITY

2. FOLDOUT. ERAME



ORIGINAL PAGE IS  
OF POOR QUALITY

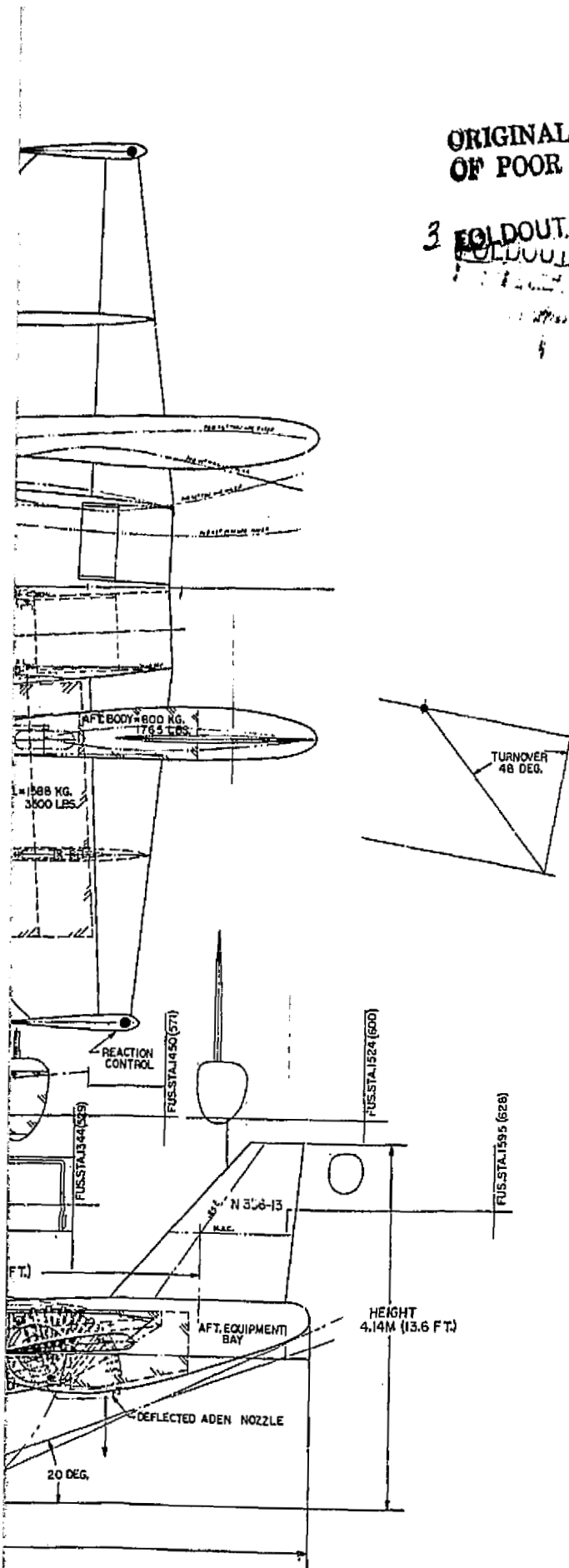
3 FOLDOUT, ERAME  
FOLDOUT, ERAME

BASIC DIMENSIONAL DATA				
BASIC SURFACES	UNITS	WING	HORIZ. TAIL	VERT. TAIL
REFERENCE AREA	M <sup>2</sup> (FT <sup>2</sup> )	45.43 (500)	4.23 (45)	4.83 (52)
ASPECT RATIO	AR	2.12	1.53	1.31
TAPER RATIO	A	0.18	0.272	0.310
THICKNESS RATIO	t/c	0.04	0.04	0.04
L.E. SWEEP ANGLE	DEG	50	60	42.5
C/A SWEEP ANGLE	DEG	40.8	53.6	33.3
DIHEDRAL/CANT ANGLE	DEG	-5	5	0
INCIDENCE ANGLE	DEG	—	—	—
TWIST ANGLE	DEG	—	0	0
AIRFOIL		65A004		
PROJECTED SPAN	M (FT)	8.93 (97)	5.23 (56)	1.70 (18)
ROOT CHORD	M (FT)	7.83 (84)	2.61 (28)	2.81 (30)
TIP CHORD	M (FT)	1.63 (17)	1.70 (18)	1.70 (18)
MEAN AERO CHORD	M (FT)	2.14 (23)	1.70 (18)	1.70 (18)
TAIL ARM 0.26 C <sub>r</sub> TO 0.25 C <sub>r</sub>	M (FT)	2.14 (23)	1.70 (18)	1.70 (18)
TAIL VOLUME COEFFICIENT	V	—	.059	.047
CONTROL SURFACES				
TOTAL AREA	M <sup>2</sup> (FT <sup>2</sup> )	4.23	4.23	4.83
PERCENT SPAN	%	74		ALL
PERCENT CHORD	%	12.52		MOVING
DEFLECTION	DEG	15	15	15

	KG	LBS.	WETTED AREA	M <sup>2</sup> (FT <sup>2</sup> )
STRUCTURE	3,603	7,940	NET BODY	74.8 (805)
POWER PLANT	3,180	7,011	WING	54.3 (584)
FIXED EQUIPMENT	1,634	3,604	HORIZ. TAIL	8.5 (91)
EMPTY WT.	8,417	18,555	VERT. TAIL	9.7 (104)
USEFUL LOAD	186	408	NACELLE	
OPER. WT. EMPTY	8,603	18,963	AFTERBODIES	19.0 (204)
PAYLOAD	163	360		
FUEL	4,843	10,677		
TAKEOFF GROSS WT.	13,609	30,000	TOTAL	166.3 (1788)

NOTES:

- POWERPLANT: (2) G.E. 1E/VVCE-6 RALS ENGINES  
THRUST: 18,000 LB/ENGINE S.L. STATIC  
T.I.T.: 3200° F B.P.R.: 0.7
- NET DENSITY:  $\rho = \frac{GW}{VOL} = \frac{13,609}{249.6} = 54.5 \text{ KG/M}^3 \text{ (34 LB/FT}^3\text{)}$



OLDOUT FRAME

ORIGINAL PAGE IS  
OF POOR QUALITY

PRECEDING PAGE BLANK NOT RELEASED

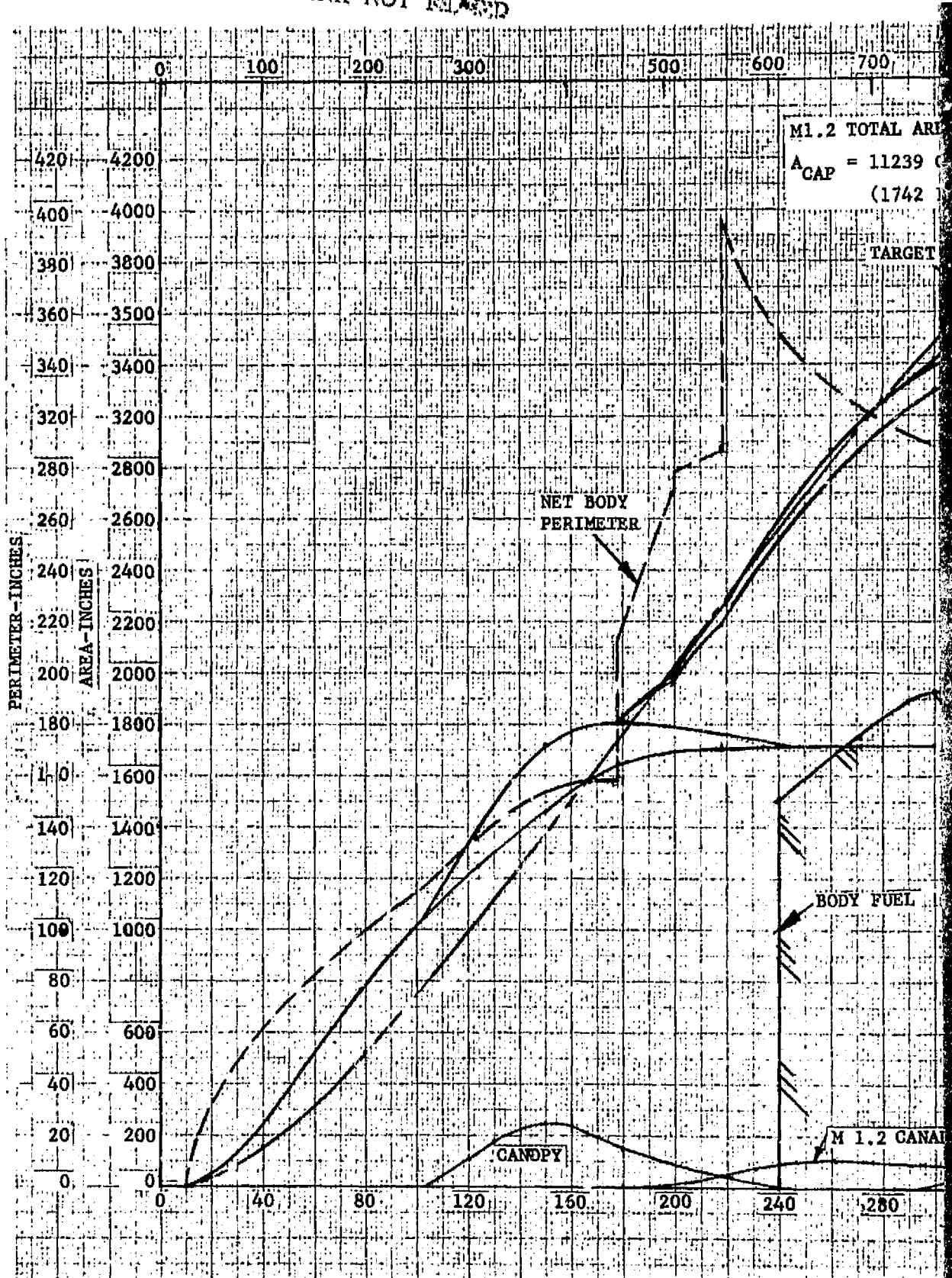
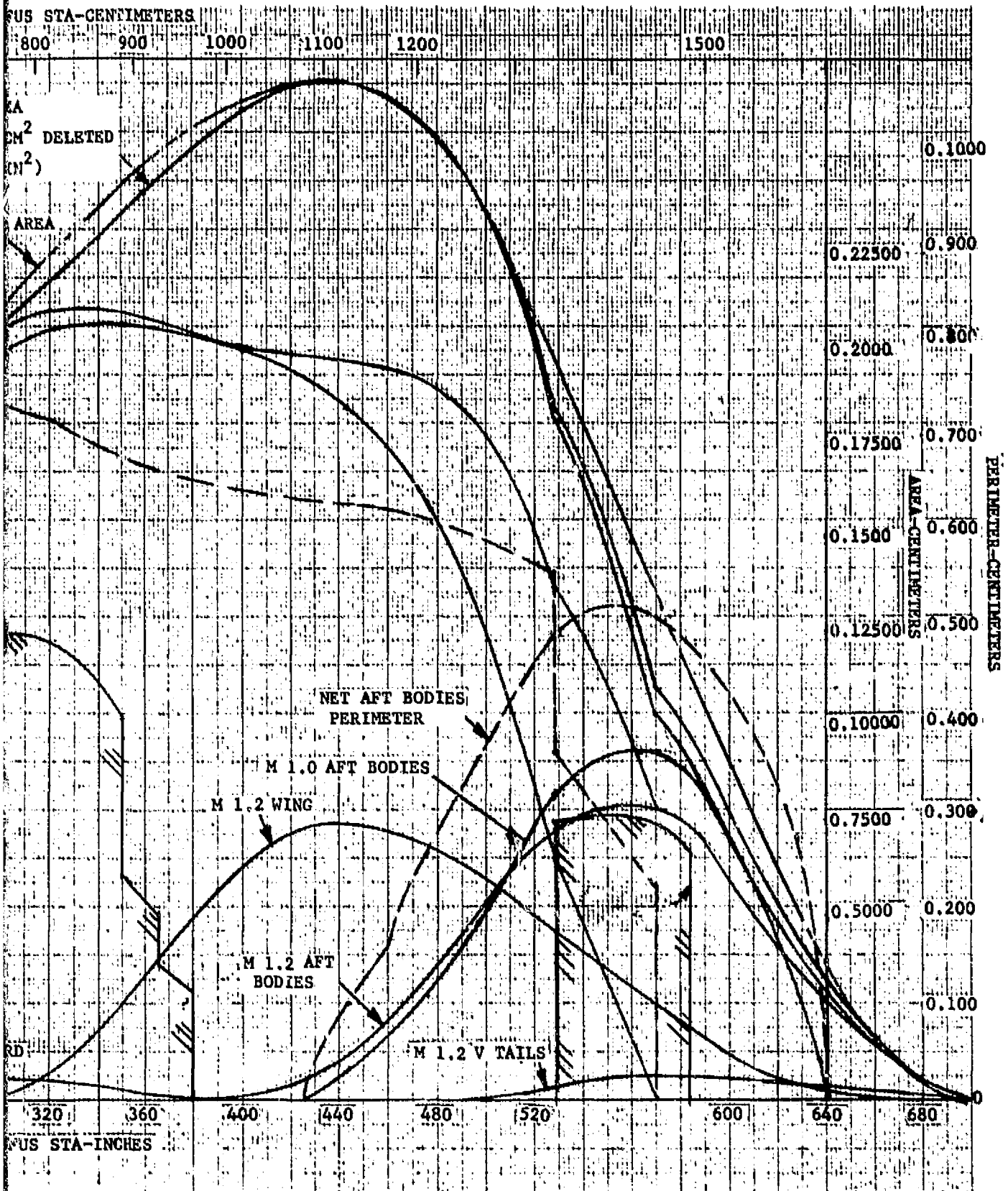


FIGURE 2-2. CROSS-SECTIONAL AREA AND WETTED AREA DISTRIBUTIONS

2  
ORIGINAL PAGE IS  
OF POOR QUALITY



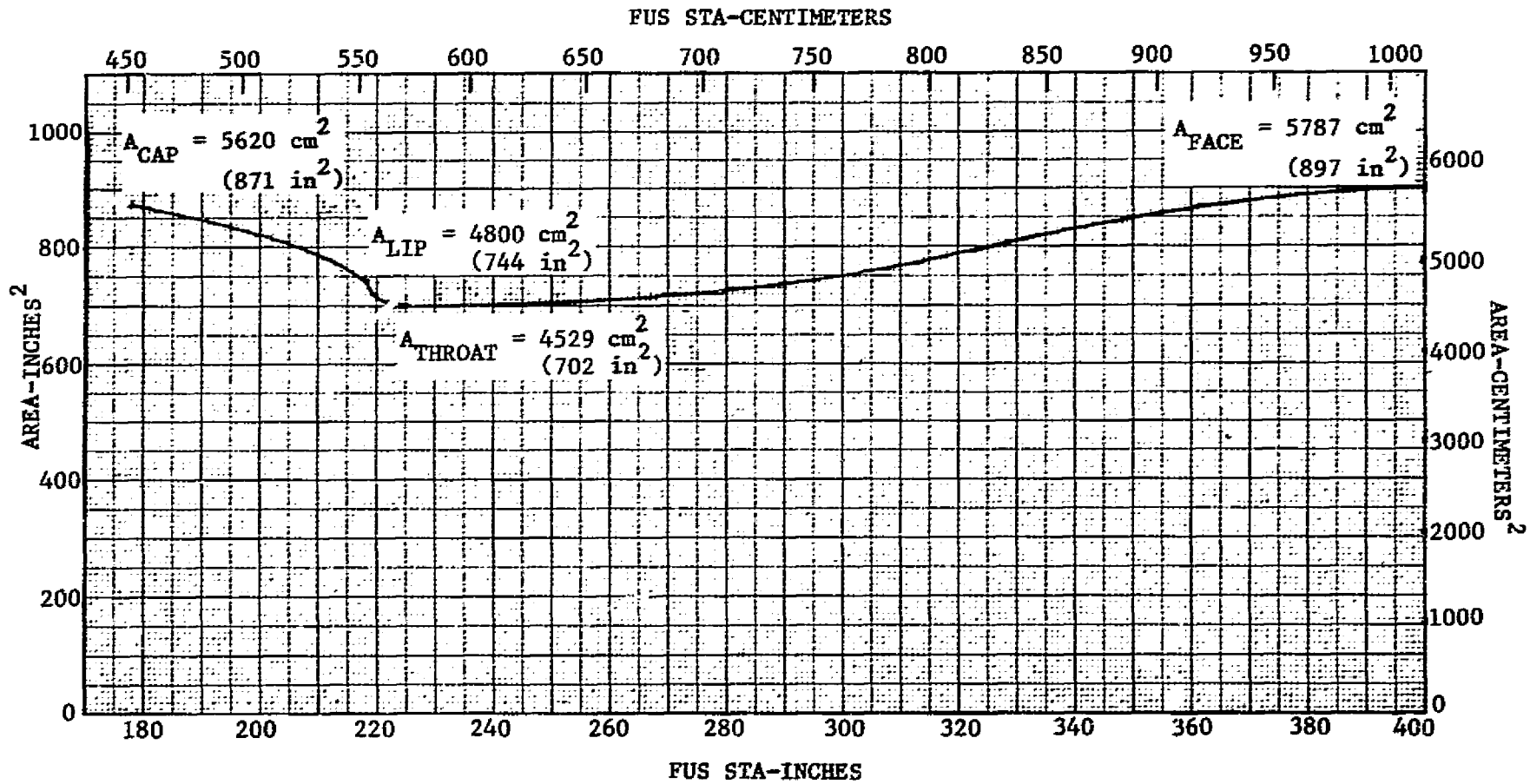


FIGURE 2-3. DUCT AREA DISTRIBUTION

PRECEDING PAGE BLANK NOT FILMED

PRECEDING PAGE BLANK NOT RELEASED  
REGLDOUT. ER

ORIGINAL PAGE IS  
OF POOR QUALITY

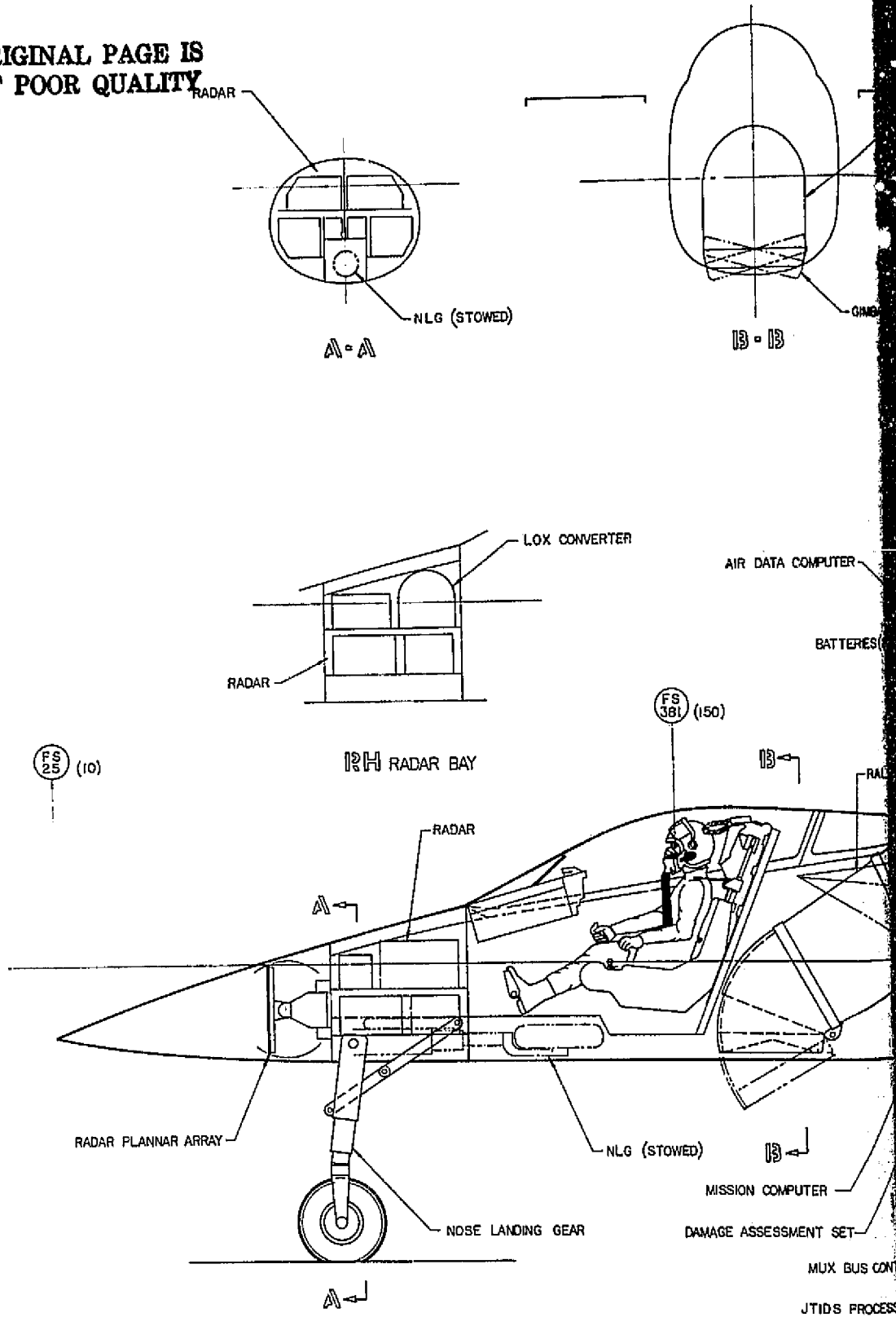
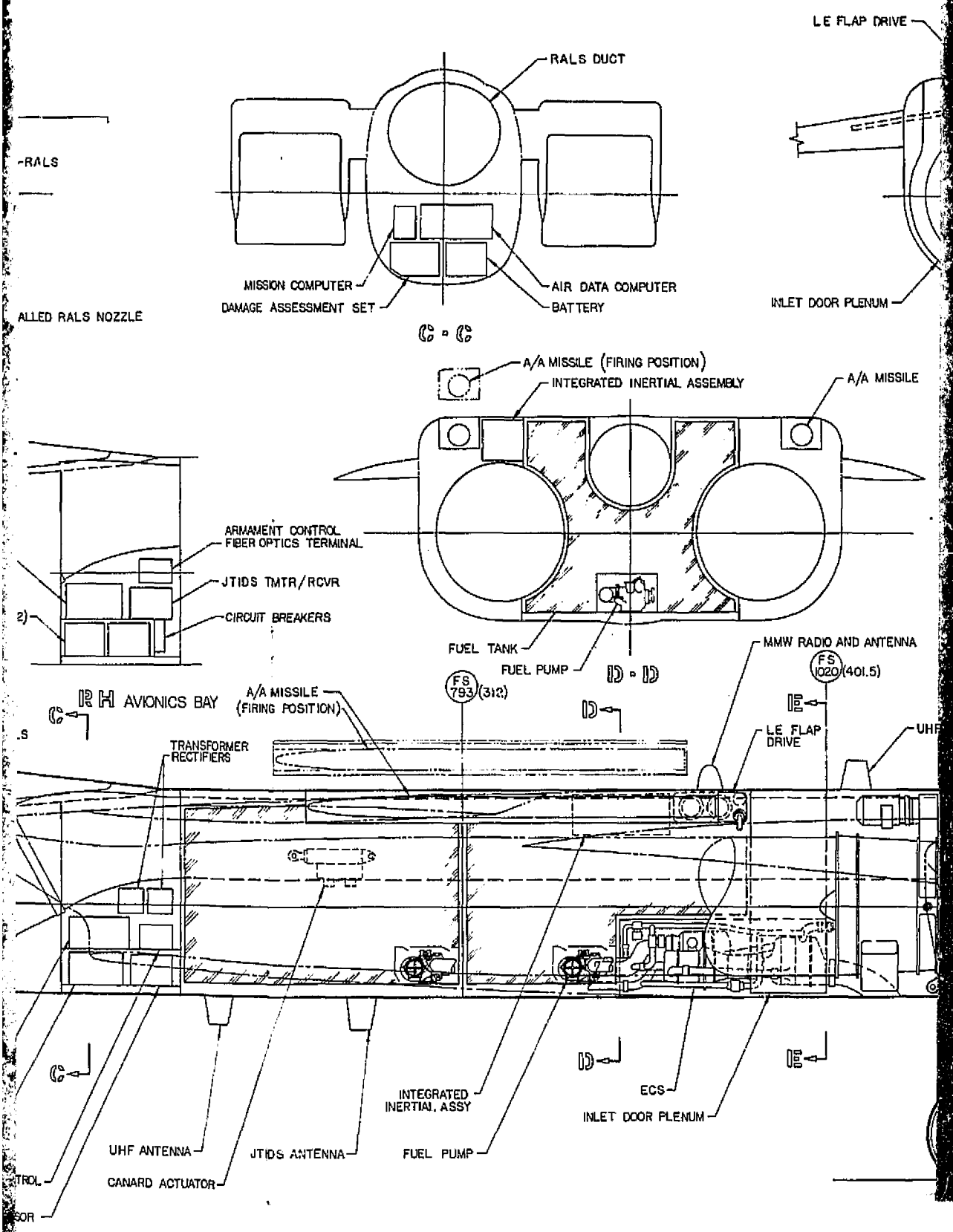
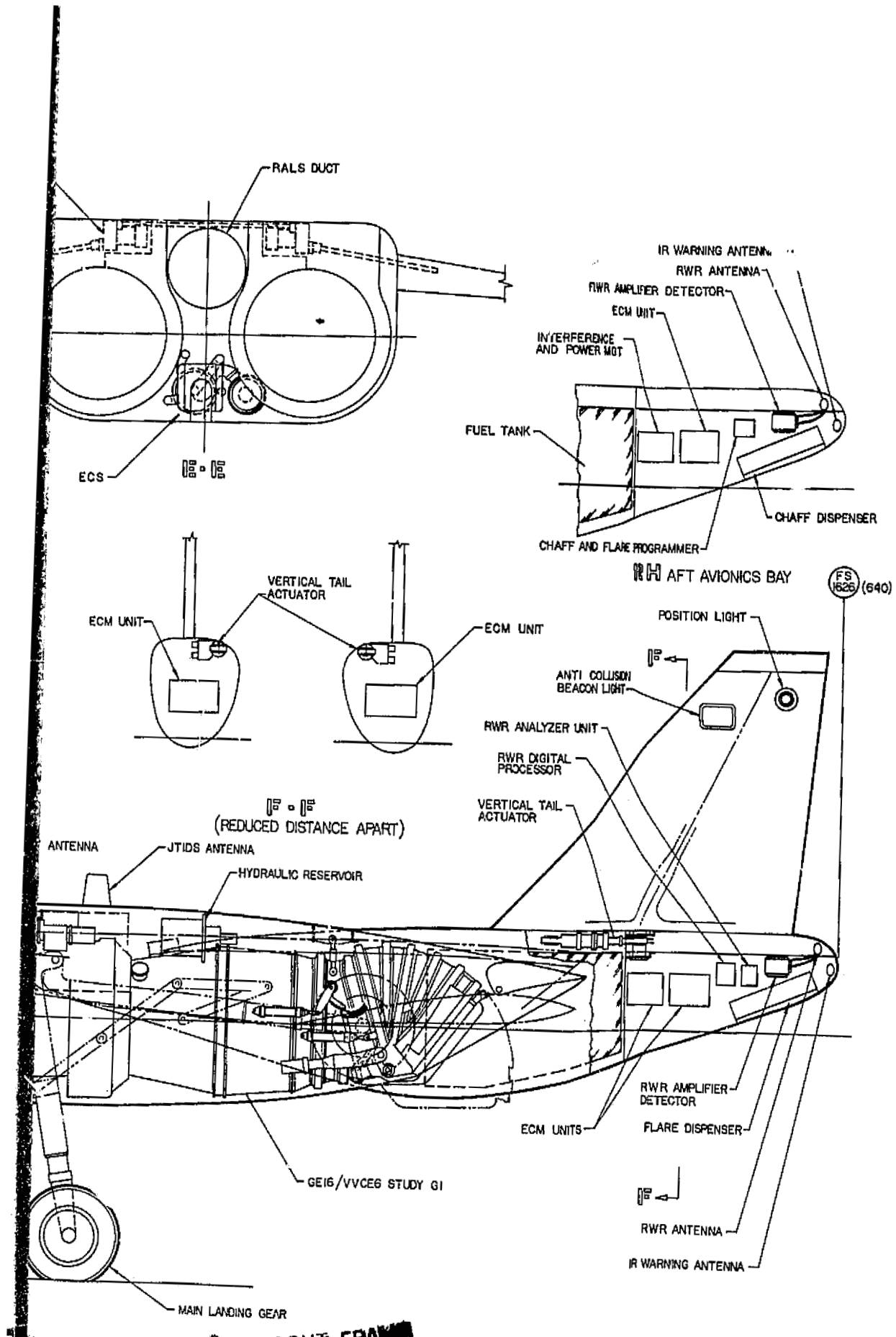


FIGURE 2-4. INBOARD PROFILE

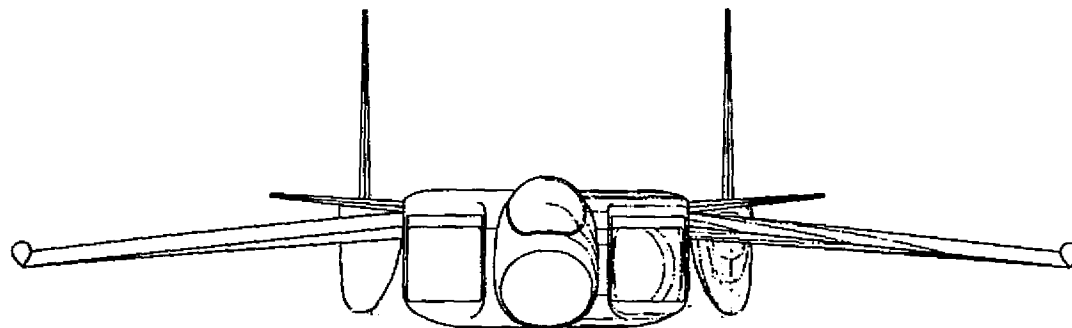
2. HOLDOUT FRAME ORIGINAL PAGE IS  
 OF POOR QUALITY



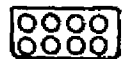


**3 BOLDOUT FRAME**

**ORIGINAL PAGE IS OF POOR QUALITY**



BOOSTERED MINI-MISSILE POD



OFF-BORESIGHT MISSILE POD



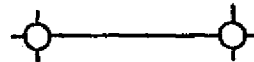
1250-LB CLASS GLIDE WEAPON



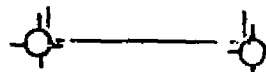
2500-LB CLASS GLIDE WEAPON



2500-LB CLASS POWERED WEAPON RAMJET



BODY CORNER SEMI-SUBMERGED FINNED WEAPON



BODY CORNER TANGENT FINNED WEAPON

PRECEDING PAGE BLANK NOT REPROD

FIGURE 2-5. CONFORMAL STORES MATRIX

PRECEDING PAGE BLANK NOT FILLED

### SECTION 3

#### AERODYNAMIC CHARACTERISTICS

The emphasis on aerodynamic and propulsion integration in current high-thrust-to-weight ratio aircraft is increased for a VSTOL design by the additional complications of propulsive lift generation and transition interactions. Supersonic VSTOL concepts must also reflect a consideration of the overall volume distribution, as well as the detailed inlet and exhaust interfaces. Achieving a good volume distribution is made difficult due to the necessity for having the propulsive lift vector coincident with the gravity vector. On the other hand, concurrent integration of an active control system facilitates optimization of the vehicle shape. It is projected that control systems which will be available in the 1990+ time period will permit usage of a 15% negative static margin at subsonic speeds. The aircraft then will be balanced such that the canard and trailing-edge flap deflections for trim, at a given lift, approach those for minimum drag due to lift. Thus, the aircraft is trimmed for high L/D over a wide range of lift coefficients. At supersonic speeds, the aft shift in aerodynamic center results in near-neutral static margin so that the trim drag is small.

The wing planform reflects a consideration of the trimming properties of aircraft with negative stability discussed above, and the achievement of low subsonic wave drag. The wing camber and twist are determined for an improved drag polar at low supersonic speeds, but without having to pay appreciable camber-drag penalties at low lift coefficient. The leading- and trailing-edge flaps provide good subsonic polars, and the canard may be used for high angle-of-attack flow control in order to trim thrust-vectoring pitching moments and to provide control at high angle of attack.

#### 3.1 WING PLANFORM SELECTION

The wing design was developed during an ongoing fighter technology IR&D program. The wing selection study examined a range of wing planforms to investigate the impact on aircraft turn performance, acceleration capability, maximum speed and overall weight. The wings were configured with trailing edge flaps acting as pitch

trim controls (applicable to both tailless or zero trimload tailed designs) and automatic leading-edge flaps.

The use of negative static margin at subsonic speeds permits the aircraft to be balanced such that the trailing edge flap deflection for trim, at a given lift, matches the setting for minimum drag due to lift; so that, the aircraft is trimmed for best L/D over a wide range of lift coefficients. At supersonic speeds, the shift in aerodynamic center results in near-neutral static margin, again allowing the least drag due to lift and trim. The synergism in this approach was found applicable over the full range of wings evaluated.

Three baseline configurations using a common, fixed engine were developed, including detailed area ruling and weight evaluation. Perturbations in aspect ratio, sweep, thickness, and wing camber were made to refine and optimize each baseline. Throughout, a fuel sizing mission, incorporating specific cruise, subsonic turn, supersonic turn and acceleration segments was used to establish the minimum weight/maximum performance geometry. Figure 3-1 summarizes some of the results of the study in the form of parameter ratios relative to the wing of this investigation. For the comparison shown, wing loadings were chosen to provide equal sustained turn rate at M 0.9 and 30,000 feet altitude. This resulted in the wings having approximately the same span. The advantages evidenced by the baseline wing reflect a cross-sectional area distribution closer to ideal and a higher structural efficiency.

ORIGINAL PAGE IS  
OF POOR QUALITY

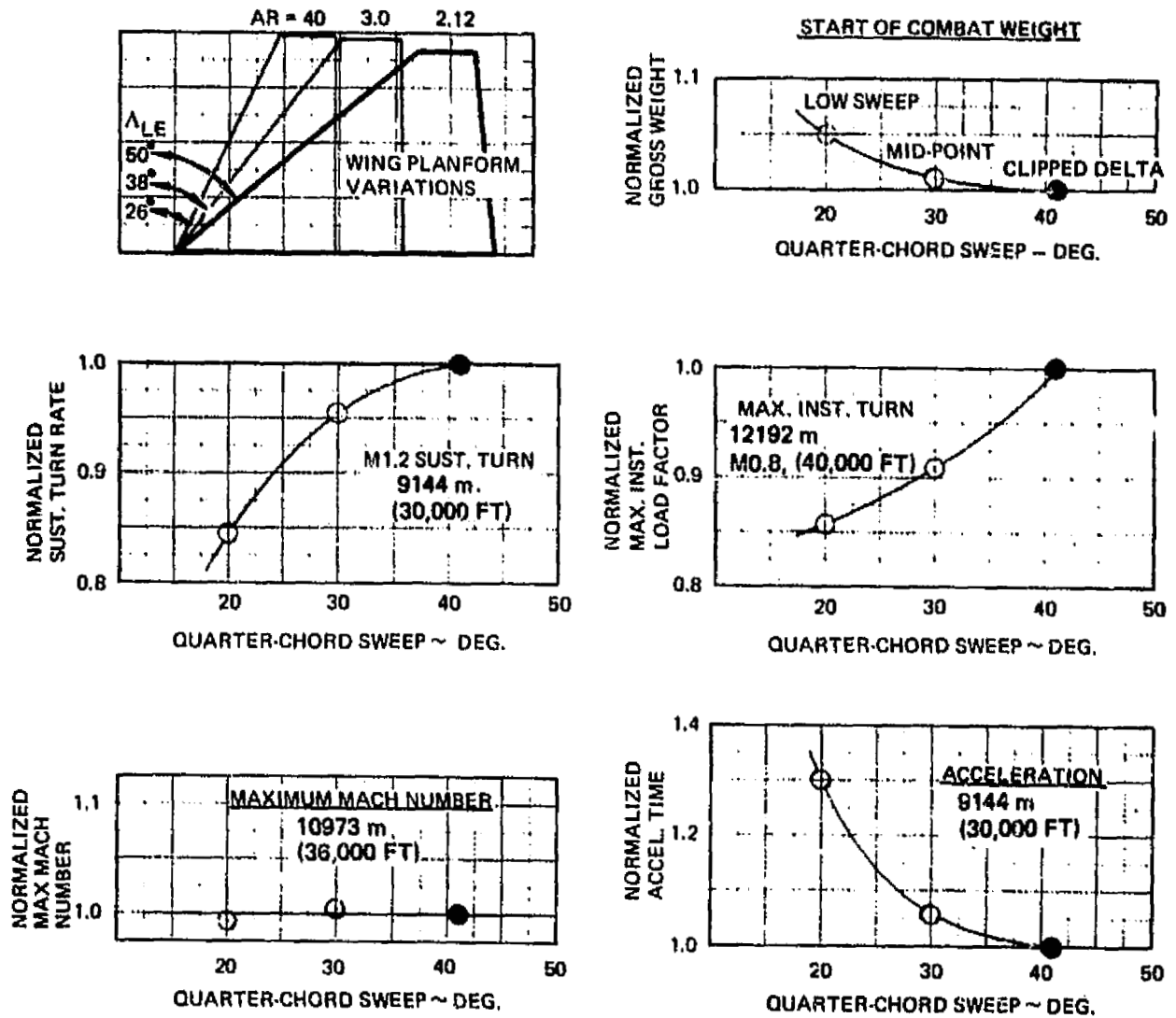


FIGURE 3-1. WING PLANFORM SELECTION

## 3.2 LONGITUDINAL AXIS ANALYSIS

The aerodynamic analyses presented in Section 3 are for the clean configuration and do not include the effects of conformal, external stores.

### 3.2.1 Minimum Drag

The minimum drag includes all drag components that are independent of lift and engine throttle position. The reference conditions for thrust-drag bookkeeping purposes are as follows: 1) maximum open nozzle position with nozzle static pressure ratio ( $P_9/P_{am}$ ) equal to unity; 2) inlets operating at the supercritical mass flow point at each Mach number (spillage drag for this condition is included in the aircraft drag); 3) altitude of 9144 m (30,000 ft). Inlet bleed, ventilation, ram cooling drag increments and other components are included in the installed thrust data as shown in Table 4-2.

The minimum drag estimate is presented in Figure 3-2 as a function of Mach number at the reference altitude. Variation in minimum drag level with altitude is shown in Figure 3-3. The detailed drag buildup for the design is included as Table 3-1. This table presents the individual drag components for several Mach numbers at the reference altitude condition. The viscous drag component is further broken into its components in Table 3-2 for the reference altitude and M 0.5.

Skin friction coefficients were obtained using charts contained in Reference 1. An equivalent roughness of 0.00127 cm (0.0005 in) was utilized to determine cut-off Reynold's number effects. Form factors were obtained from Reference 2 and an interference factor of 1.05 was applied to all planar surface components.

Wave drag was calculated using the Langley Wave Drag Program outlined in Reference 3. Two adjustments were made to the drag levels obtained from the program. The first adjustment, shown in Figure 3-4, adjusts the wave drag as a function of Mach number for the input option selected in this study. To facilitate input and area ruling studies, the equivalent circular area input option was selected. Analysis of the YF-17, using both the equivalent circular area and the actual cross-section geometry inputs, agreed with previous NASA tests showing an increasingly optimistic drag level with Mach number when using the circular input option. The adjustment in Figure 3-4 is based on differences obtained in the YF-17 study. The second adjustment is a correction factor developed at Northrop, based on wind tunnel data and applied to the wave drag of all wing and empennage surfaces. The adjustment is due

to the fact that substituting three-dimensional bodies for wing surfaces generally results in underestimating the wing wave drag, especially for wings of low sweep having supersonic leading edges. The adjustment is a function of Mach number, sweep angle, and thickness ratio, and is shown in Figure 3-5. This adjustment is on the order of  $\pm 3\%$  of the total wave drag estimate.

Subsonic canopy pressure drag was determined using data available in Reference 4 as a function of canopy frontal area. The supersonic drag increment is accounted for in the wave drag area. The reference spillage drag is included in the minimum drag. Subsonic afterbody-nozzle drag is based on scaled YF-17 afterbody wind tunnel test data. The supersonic afterbody-nozzle drag is included in the wave drag. The drag increment for boundary layer diverters was estimated using the data from Reference 5 as a function of frontal area and included wedge angle. The transonic drag levels between M 0.8 and M 1.2 were based on the drag rise characteristics of existing aircraft. The remaining miscellaneous drag items include wing actuator fairings, wing tip pods protruberance, gaps, vents, doors, etc., and are based on YF-17 analyses and data from References 4 and 6.

A final correction was applied to the minimum drag buildup. It is based on the difference obtained when comparing the YF-17 flight test drag to an analytical drag buildup. The subsonic and supersonic adjustments are shown in Figure 3-6. These data have been scaled from the YF-17 by wetted area and then ratioed to the proper reference area.

### 3.2.2 Basic Lift, Drag, and Pitching Moment

Basic subsonic aerodynamic data for the concept have been generated for two leading edge flap deflections and a range of trailing-edge flap deflections. The results for  $M \leq 0.6$  are presented in Figures 3-7 through 3-14; those for M 0.9 are presented in Figures 3-15 through 3-22. The components of lift and pitching moment were obtained using the program developed by Carmichael and Woodward, which accounts for the incremental effects of leading-edge and trailing-edge flaps on the wing, as well as twist and camber effects on  $C_{L_0}$ ,  $C_{m_0}$ , and the aerodynamic center location. The program is based on a method which assumes zero leading-edge suction. This assumption does not have any significant effect on the lift and pitching moment results. However, at subsonic Mach numbers it leads to an over-prediction of drag. The amount of leading edge suction which will actually be present depends primarily upon

the wing leading-edge geometry and sweep. Since there is currently no accepted method for determining the suction level, a semi-empirical method was used to determine the polars. First, the effect of canards on drag-due-to-lift was obtained and then these effects were incremented on the wing-body polars derived from wind tunnel test data for a similar configuration with the same wing planform (see References 7 through 10). The incremental effects were obtained by running the configuration with and without canards on the Woodward program. As described in Section 3.2.3, Stability Analysis, it was found that the presence of canards results in a constant decrement in the spanload efficiency factor over a wide range of lift coefficients. The polars determined in this way are by necessity based not only on wing-body test data, but also on the canard increment from the Woodward program. The results, as shown in Figures 3-11, 3-12, 3-19 and 3-20, are believed to give a more accurate estimate of the aerodynamic characteristics than those obtainable from the computer program alone.

Supersonic data were estimated entirely from Woodward program calculations. For supersonic Mach numbers, the assumption of zero leading edge suction is less critical. One reason is that suction is a lower percentage of total drag. Another reason is that at low supersonic Mach numbers the reliance on leading edge suction to achieve a good polar is reduced due to designing the wing camber and twist at  $M 1.2$  and  $C_L = 0.2$  (see Section 3.2.7). At the higher Mach numbers where the leading edge is approaching a supersonic condition, suction has only a minor effect on drag. Results for  $M 1.2$  and  $M 1.6$  are presented in Figures 3-23 through 3-30. Adjustments were made only to the trim line for a c. g. location of  $0.26 \bar{c}$  to conform with the aerodynamic center position determined in Section 3.2.3.

### 3.2.3 Longitudinal Stability Analysis

The effect of static margin on the subsonic aerodynamics was determined with the use of the Carmichael-Woodward program (Reference 11). Incremental effects for canard, leading-edge and trailing-edge flaps, wing camber and angle of attack were computed and control deflections determined for minimum drag-due-to-lift as a function of lift coefficient and moment center.

The drag polars at  $M 0.6$  for various camber distributions are shown in Figure 3-31. Comparison of the polars for the flat wing and the design-camber wing (see Section 3.2.7 for details), with no canard or flap deflections, shows that there is a

slight reduction in drag at a given lift due to wing camber. The polar which is obtained by deflecting the canard, leading- and trailing-edge flaps to achieve least drag at a given lift without a pitching moment constraint (untrimmed) shows a large reduction in drag over the flat and design-camber wings. Also shown in Figure 3-31 are the surface deflections. As expected, large deflections of the flaps occur at the higher lift coefficients. However, the deflection of the canard is negative, trailing edge up, which shows a tendency for the canard to unload. This is caused by the fact that the wing with leading- and trailing-edge flaps is a more efficient lift-producer than the canard. If a trim pitching moment constraint is imposed, the polar is degraded. This is because the canard still shows a tendency to unload so that the effective stability of the configuration is increased, and the trailing-edge flap deflection is reduced considerably from its optimum, untrimmed value.

The effect of static stability on polar shape has been further studied and comparisons made with the VATOL configuration (Reference 9) which is a tailless configuration. The Oswald efficiency parameter "e" is shown plotted against static margin in Figure 3-32. For each of the configurations, as the static stability is reduced, "e" increases and then levels off with the knee of the curve being at about  $-0.15 \bar{c}$  for the VATOL configuration, and a somewhat larger negative number for the HAVSTOL configuration. The asymptotic levels for both configurations are very nearly the same. However, the configuration without a canard has a better "e" for the static margins of interest.

Also shown on Figure 3-32 are test data for the VATOL configuration and for a configuration featuring a canard. The test data have a somewhat higher value of "e" due to theoretical method assumption of zero leading edge suction.

On an unstable airplane, the degree of negative longitudinal stability must be carefully chosen to achieve the associated performance benefits without creating conditions in which the capabilities of the control system are exceeded. As the center-of-gravity position also has to be fixed rather precisely because of thrust balancing conditions, the aerodynamic center position has to be carefully determined. Therefore, a considerable effort was undertaken to determine the a. c. position. The effort was concentrated on determining the aerodynamic center at M 1.2 which will be the nominal c. g. position, as neutral stability at that flight condition is the design goal.

The basic tool for the a. c. calculations was the NASA Ames (Woodward-Carmichael) wing-body computer program used in conjunction with NASA and Northrop

test data of similar configurations for a more accurate modeling of forebody effects. Previous experience with the wing-body program showed that the body contribution to stability is underestimated when compared to test results. The error in computed a. c. is less when the body is represented as a lifting surface rather than a body of revolution. For either representation it is necessary to establish a certain forebody geometry characteristic as a correlation parameter which most closely matches the test data incremental a. c. due to forebody.

For the case of bodies of revolution, the characteristic parameter appears to be the product of the maximum cross-sectional area forward of the wing panel and the distance from the theoretical center of pressure (on an isolated forebody from NACA TR 1307) to the intersection of the body and the leading edge of the exposed root chord of the forward wing panel.

The nose volume coefficient is not a good correlation parameter when the body is simulated by a low aspect ratio wing surface. A better parameter in this case is the product of the projected body planform area forward of the exposed forward wing panel and the distance to the nose center of pressure. As Figure 3-33 shows, in the range of interest in particular, good agreement of theory and test is indicated.

In particular, for the wing-body configurations, the computed a. c. is estimated to be only 0.15 $\bar{c}$  different from the test a. c. M 1.2. Similar correlation results at subsonic speeds (M0.6) show the computed a. c. to be 0.02 $\bar{c}$  difference from the test a. c.

Based on an evaluation of NASA test results (Reference 12), the Carmichael-Woodward program overestimates by a substantial amount the forward a. c. shift due to adding the canards. The expected canard effect on lift and pitching moment, based on test data is shown in Figure 3-34 to 3-37. The test data indicate a constant forward shift in a. c. of 0.11 $\bar{c}$  at both M0.6 and M1.2 for the canard (exposed canard surface area to wing reference area equals 0.09). This increment, together with the correction for forebody geometry, was applied to the estimates for the wingbody configuration, obtained using the Carmichael-Woodward program, to generate the a. c. variation with Mach number for the complete configuration as shown in Figure 3-38.

The aerodynamic center is located at 0.11 $\bar{c}$  and 0.28 $\bar{c}$  at M0.6 and M1.2, respectively. The c. g. position is set at 0.26 $\bar{c}$ , dictated by control system requirements that limit the maximum longitudinal instability to no more than -15 percent of  $\bar{c}$ . This means a positive static margin of 2 percent will exist at M 1.2, which will result in a slight trim drag penalty.

#### 3.2.4 Trim Analysis

As described in Section 3.2.3, a program was developed which uses the incremental effects as computed with the NASA Ames wing-body program for canard, leading-edge, and trailing-edge flaps, wing camber and angle-of-attack. The program optimizes the control deflections for minimum drag-due-to-lift as a function of trimmed lift coefficient at a given center of gravity. The method is believed to give good predictions for the optimum control deflections.

The leading-edge flap and canard deflection schedules are shown in Figures 3-39 and 3-40, respectively. The corresponding trailing-edge flap deflections for trim are shown in Figure 3-41. Note that the canard deflection increases negatively (leading edge down) with angle of attack, an indication that this control surface is being unloaded as angle of attack is increased.

At the higher angles of attack, the canard deflection will be determined by flow control requirements. The original plan was to use the NASA Langley Research Center Asymmetric Vortex-Lattice Program (Computer Program No. 4737) to estimate the subsonic high angle of attack, lift, drag and pitching moment. The results would have been used to determine the optimum canard deflections at high attitude. The version which was available during the investigation was only applicable to flat wings, and so could not be used. Thus, canard deflections required at high attitudes are not known at this time.

The canard deflection decreases toward the positive direction with Mach number, becoming only nominally negative as M1.6 is reached. The curve for M1.6 is defined for the case of undeflected leading-edge flaps.

The leading-edge flaps (Figure 3-39) are limited to a maximum deflection of 30 degrees, which is reached at about  $\alpha = 20$  degrees at subsonic speeds. Small negative deflections occur at low angles-of-attack to counterbalance the wing nose droop camber effect. Benefits are seen to accrue even at M1.6, where the optimum leading-edge goes from negative to positive deflections as  $\alpha$  is increased. Some doubt exists, however, as to whether this finding is real, especially at M1.6, where the wing has already gone supersonic. For this and other practical reasons, the leading-edge flaps are limited to positive deflections only.

Relatively small trailing-edge flap deflections are needed for trim (Figure 3-41) as compared to either canard or leading-edge flaps. At Mach 1.2 and 1.6, negative

deflections (trailing edge up) are required to trim out the 2 to 5 percent positive static margin for the c. g. location of 0.26 $\bar{c}$ .

The foregoing trim schedules resulted in the optimum trim polars shown in Figures 3-42 and 3-43. The maximum spanload efficiency factor is 0.91 at  $M \approx 0.6$ , and 0.748 and  $M 0.9$ . The supersonic polars show a trim drag penalty of 18 to 19 counts at zero lift due to camber effects which were built into the selected wing design. The polar at  $M 2.0$  is estimated using methods presented in DATCOM. Optimum lift-drag ratios for the range of Mach numbers are presented in Figure 3-44.

### 3.2.5 Maximum Lift and Buffet Onset

The estimate of maximum lift,  $C_{L_{max}}$ , as a function of Mach number is presented in Figure 3-45. Subsonic  $C_{L_{max}}$  values were determined from test data of a similar configuration. At supersonic speeds,  $C_{L_{max}}$  values may be estimated using the methods derived in NACA RM L8F23. The method used is based on a limiting pressure coefficient compared to a vacuum ( $P_{limit} = Y/2 P_{vacuum}$ ). The following assumptions are made:

1. The angle of attack is high and the shock is normal in front of the wing.
2. All pressures on the wing upper surface are at the limiting value
3. Average normal force on the wing lower surface is proportional to the projected surface normal to free stream.
4. The airfoil is thin.

The values of  $C_{L_{max}}$  thus derived are about 0.9 of the  $C_{L_{max}}$  with a vacuum on the upper surface of the airfoil.

Buffet onset lift coefficients were estimated using wind tunnel test data from Reference 7. As previously noted, the wing which was tested had the same planform as the study aircraft. The balance roll strain gauge dynamic output was recorded as the angle of attack of the model was increased. The angle of attack at which the root mean square of the rolling moment showed a significant increase was used to determine buffet onset. These data have been adjusted upward by about 0.1 lift coefficient to account for the difference in angle of attack for a given lift coefficient between the study aircraft and the test configuration. These results are shown in Figure 3-46 for various Mach numbers and leading and trailing edge flap deflections. Leading and trailing edge flaps, individually and in combination are seen to increase the buffet .

onset boundary. The buffet onset variation with Mach number is similar in shape and lower than  $C_{Lmax}$  at subsonic Mach numbers as expected. At supersonic Mach numbers no buffet is expected up to  $C_{Lmax}$ .

### 3.2.6 Longitudinal Aerodynamic Control Effectiveness

Longitudinal control is obtained through deflection of the canard and trailing edge flaps. Since the canard acts ahead of, and the trailing-edge flaps act behind the c.g. position, a fine balance must be maintained between the two to achieve the desired results in control, trim and performance. Based on the stability analysis presented in Section 3.2.3, the control for optimum aerodynamic performance, i. e., minimum drag at a given lift, was found to be obtained when the canard is deflected negatively (leading edge down) in combination with the trailing-edge flap deflection. The trailing-edge flaps may be deflected either positively or negatively, depending on whether the aircraft is in stable or unstable flight. Note that the leading-edge flaps act only to improve the wing span loading, and have little or no influence on the control effectiveness.

Canard effectiveness at M0.9 and M1.2 is shown in Figures 3-47 and 3-48. The corresponding control parameters in lift and pitching moment as a function of Mach number are presented in Figure 3-49. Good pitch control is seen over the range of Mach numbers. The effect of canard deflection on lift is small.

Trailing-edge flap effectiveness is presented in Figures 3-9, 3-10, 3-17, and 3-18. The corresponding flap control derivatives as a function of Mach number are shown in Figure 3-50. Strong effectiveness in both lift control and pitch control is obtained.

### 3.2.7 Wing-Body Camber Design

The conventional approach to wing-body camber design has been to first determine the wing camber which minimizes drag for a specified lift or pitching moment coefficient at a given Mach number. The body area is then wrapped around the wing such that the body area growth is the same above and below the projected wing camber surface within the body. This approach is deficient in two important areas. First, the body is essentially uncambered in the spanwise direction so that the wing camber in this region is greatly modified by the presence of the body. Second, the optimum camber for the wing in the presence of the body is expected to be quite different from

the wing-alone camber. Additionally, the use of pressure loadings in the optimization procedure precludes the imposition of geometric constraints such as a straight line for a control hinge.

An alternate approach, which was used in this study, utilizes a selection of component distributions of camber and twist. Each of the component shapes embodies desired geometric constraints (such as flap hinge lines) so that any combination of the shapes will also satisfy the same constraints. The bodies are modeled as thin cambered surfaces. Based on previous comparisons with wind tunnel test data the model configuration was divided into ten equal width chordwise strips (Figure 3-51). Appropriate element distributions were selected along each strip (not shown in Figure 3-51) such that a total of 134 elements were used.

The NASA/Ames Wing-Body Aerodynamics computer program was used for the calculations. Each configuration was first analyzed as a flat planform with various combinations of control surface deflections at M 1.2. The results of these calculations are summarized in Table 3-3.

An optimum distribution of wing camber with limited twist was also calculated for the design conditions of M 1.2, a lift coefficient of 0.2 and zero pitching moment coefficient. Geometry, rather than pressure control modes were selected for these calculations with constraints of straight flap hinge lines and single curvature body camber. Geometry modes also facilitate the optimization of control surface deflections at off-design conditions. The selected modes are listed in Table 3-4. The "root" designation means that the particular mode varies from a nominal value at the wing root to zero at the tip. For the "tip" designation, the variation is from a nominal value at the wing tip to zero at the root. The root is defined as the airplane center line, but the wing camber is only effective outboard of the body which is defined separately.

The NASA/Ames program was used to calculate the aerodynamic load distribution for each mode. The interference drag terms between modes were then calculated. The optimum combination of modes was calculated to minimize the wave drag due to lift at the design conditions cited above. The configuration was designed with and without canard camber and twist. The difference was only about two drag counts (0.0002) at the design conditions. The "design" is, therefore, defined with body camber, wing camber and twist, and a flat canard at an optimum deflection.

The configuration was initially optimized with zero leading and trailing edge flap deflections at the design point. The resulting surfaces have unacceptably high values of twist so that a limit was placed on the twist. Flap deflection modes were then introduced to reoptimize. The calculations included various combinations of canard, leading edge and trailing edge flap deflections. Again, the criterion was trim and minimum drag over the appropriate angle of attack range. These results are summarized in Table 3-5.

The design mean lines along the center line of each chordwise strip are shown twice scale in Figure 3-51.

TABLE 3-1. MINIMUM DRAG BUILDUP BY COMPONENT

h = 9144 m (30,000 ft)

$S_{REF} = 46.5 \text{ m}^2 (500 \text{ ft}^2)$

COMPONENT	M 0.3	M 0.6	M 0.9	M 1.2	M 1.6
VISCOUS	.0108	.0097	.0088	.0080	.0072
WAVE/DRAG RISE	.0000	.0000	.0013	.0168	.0207
SUBSONIC CANOPY	.0002	.0002	.0002	(IN WAVE DRAG)	
SUBSONIC AFTERBODY NOZZLE	.0009	.0009	.0009	(IN WAVE DRAG)	
SPILLAGE	.0000	.0000	.0001	.0012	.0001
BOUNDARY LAYER DIVERTER	.0000	.0000	.0002	.0007	.0013
MISCELLANEOUS	.0008	.0008	.0011	.0025	.0025
FLIGHT TEST ADJUSTMENT	.0016	.0016	.0016	-.0011	.0017
TOTAL	.0143	.0132	.0142	.0281	.0335

TABLE 3-2. VISCOUS DRAG BUILDUP BY COMPONENT

M 0.50

h = 9144 m (30,000 ft)

$S_{REF} = 46.5 \text{ m}^2 (500 \text{ ft}^2)$

COMPONENT	$l-C_m$	$S_{WET}/S_{REF}$	$R_N/10^7$	$C_f$	$\Delta C_{D_F}$	FORM FACTOR	INTERF. FACTOR	$\Delta C_{D_{VISC.}}$
FUSELAGE	1427	1.620	6.680	.00216	.00350	1.112	1.00	.00389
WING	437	1.158	2.038	.00258	.00299	1.048	1.05	.00329
WING PODS	561	0.402	2.626	.00249	.00100	1.047	1.50	.00157
VERTICAL	149	0.208	0.697	.00309	.00064	1.048	1.05	.00070
CANARDS	185	0.182	0.864	.00297	.00054	1.048	1.05	.00059
TOTAL		3.570			.00867			.01004

TABLE 3-3. DRAG DUE TO LIFT WITH NO CAMBER, M 1.2

Lift Coefficient	0	0.2	0.4
<u>Untrimmed</u>			
(Canard 0°)	0	0.0116	0.0463
<u>Trimmed With:</u>			
T.E. Flaps (Canard 0°)	0	0.0113	0.0452
Opt L.E. and T.E. Flaps (Canard 0°)	0	0.0107	0.0428
Canard, Flaps 0°	0	0.0109	0.0436
Opt L.E. and T.E. Flaps, Canard - 1.6°	0.0005	0.0102	0.0413
Opt L.E. and T.E. Flaps, Opt Canard	0	0.0102	0.0408

TABLE 3-4. GEOMETRY DESIGN MODES

Mode Number	Mode
1	Flat Angle of Attack
2	Liner Twist
3	Root L.E. Droop
4	Tip L.E. Droop
5	Root Camber
6	Tip Camber
7	Root Reflex
8	Body Bend (Flat Nose Droop)
9	Body Camber (Curved Nose Droop)
10	Canard Deflection
11	Canard Linear Twist
12	Canard Camber (Uniform)
13	L.E. Flap Deflection
14	T.E. Flap Deflection

TABLE 3-5. DRAG DUE TO LIFT WITH DESIGN CAMBER, M 1.2

Lift Coefficient	0	0.2	0.4
<b>Untrimmed:</b>			
Uncambered (Ref. Table 3-3)	0	0.0116	0.0463
Design Camber (Canard $0^\circ$ )	0.0020	0.0098	0.0407
Design Camber (Canard - $2.8^\circ$ )	0.0025	0.0086	0.0378
<b>Trimmed</b>			
T.E. Flaps (Canard $0^\circ$ )	0.0024	0.0101	0.0403
Opt L.E. and T.E. Flaps (Canard $0^\circ$ )	0.0019	0.0101	0.0336
Canard (Flaps $0^\circ$ )	0.0020	0.0086	0.0369
T.E. Flaps (Canard - $2.8^\circ$ )	0.0024	0.0086	0.0373
Opt L.E. and T.E. Flaps (Canard - $2.8^\circ$ )	0.0021	0.0086	0.0364
Opt L.E. and T.E. Flaps, Opt Canard	0.0016	0.0086	0.0359

$S_{REF} = 46.5 \text{ m}^2 (500 \text{ FT}^2)$

$h = 9144 \text{ m (30,000 FT)}$

ROUGHNESS = .00127 CM (.0005 IN)

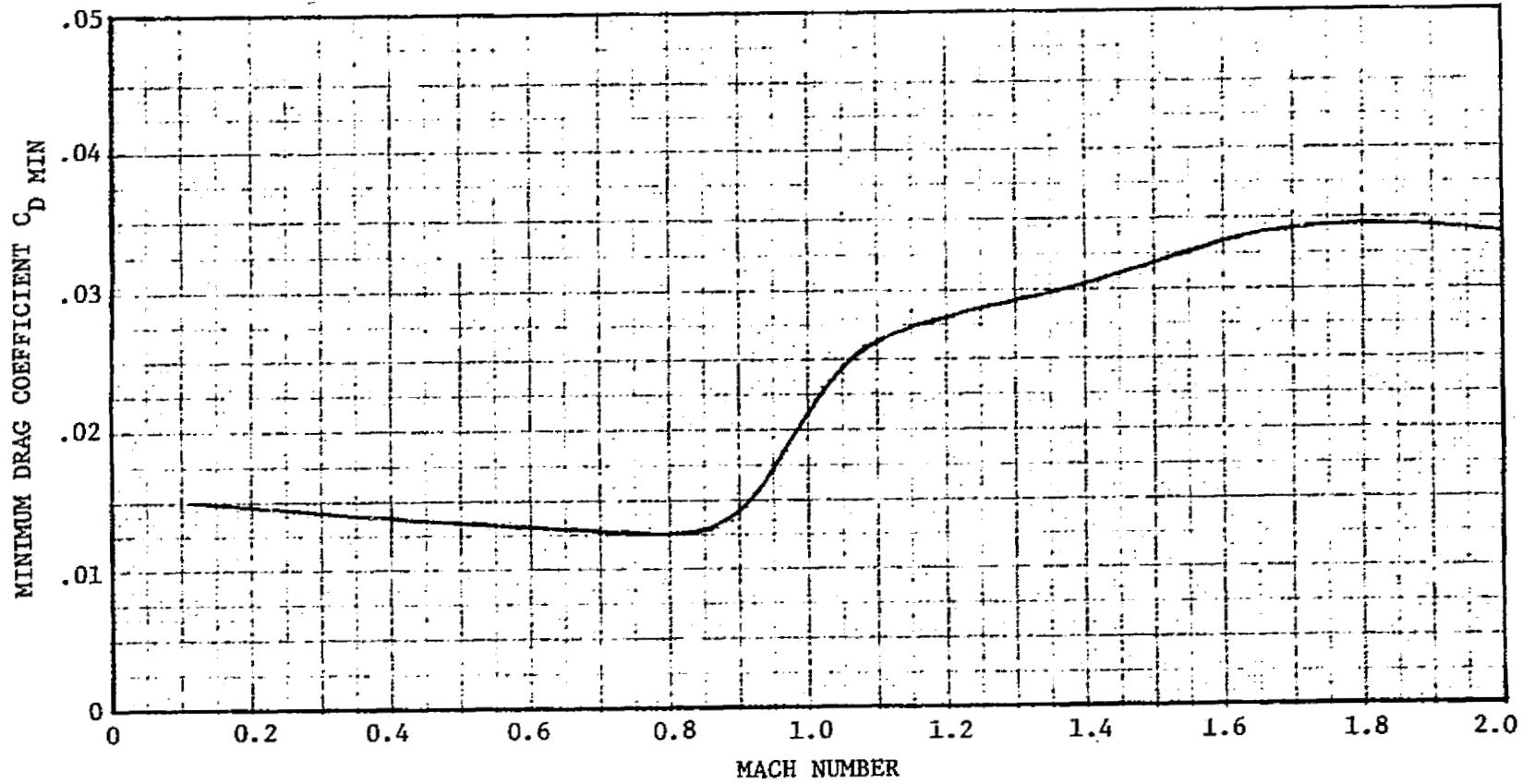
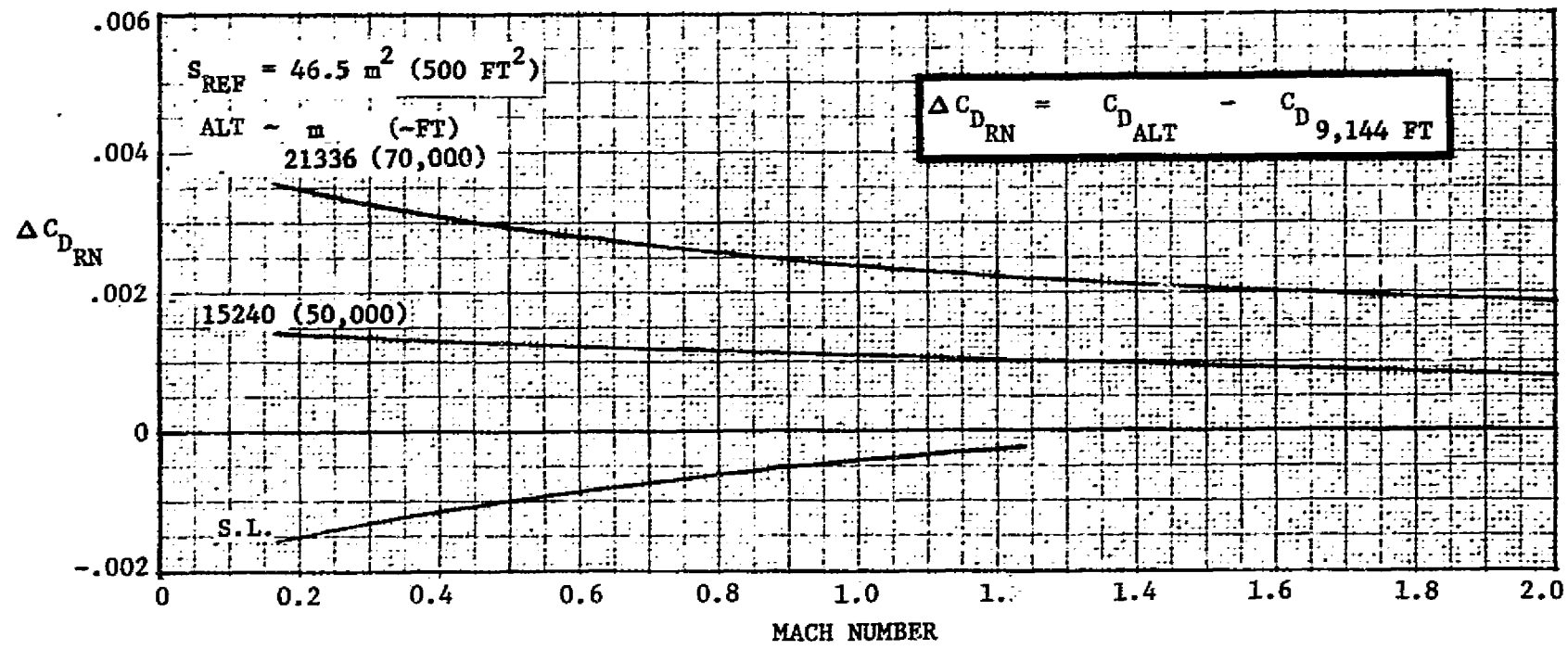


FIGURE 3-2. MINIMUM DRAG VS MACH NUMBER

ORIGINAL PAGE IS  
OF POOR QUALITY



3-19

FIGURE 3-3. ALTITUDE EFFECTS ON MINIMUM DRAG

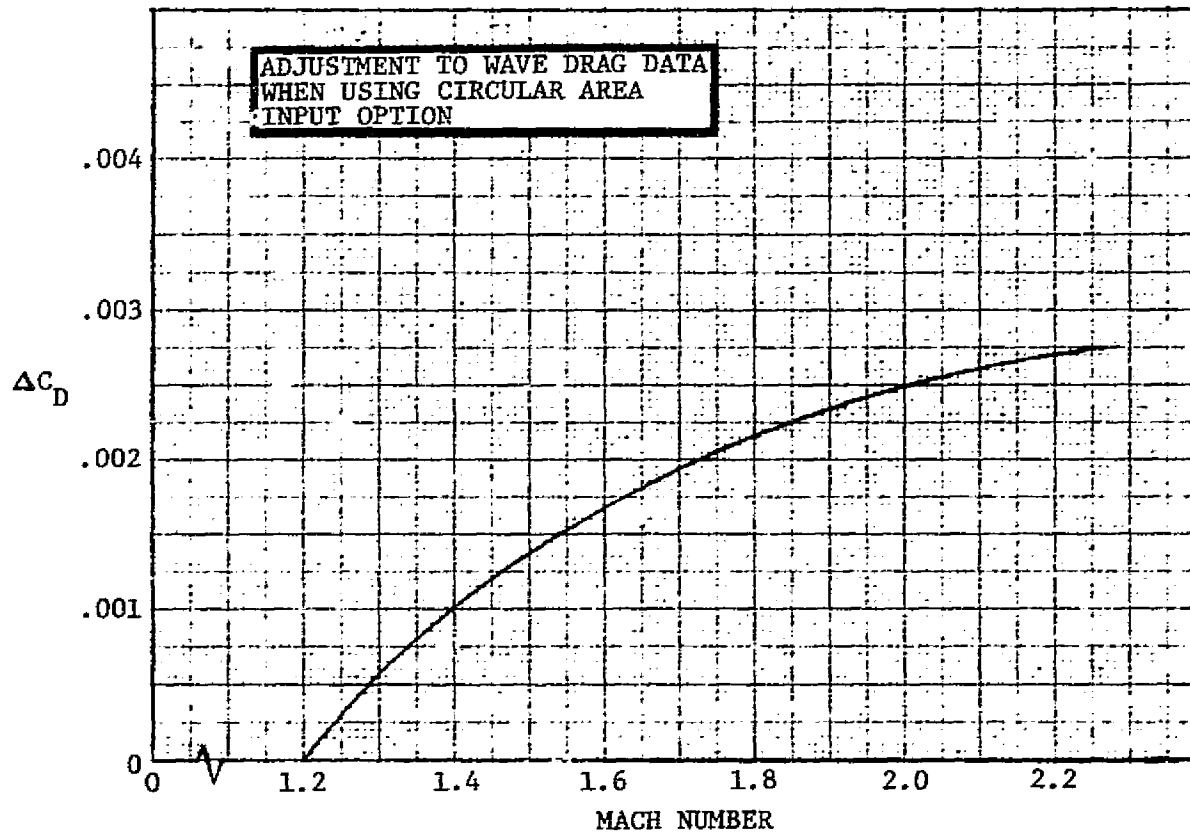
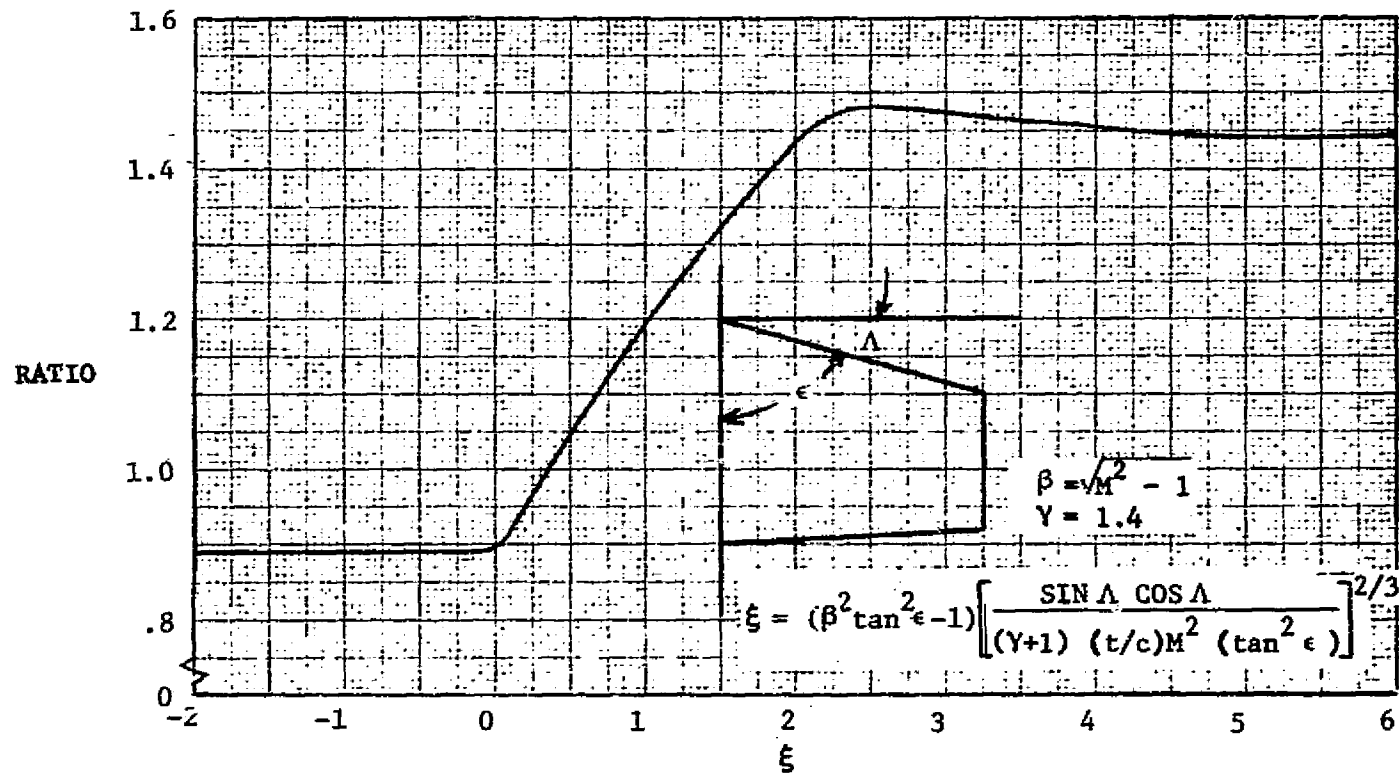


FIGURE 3-4. WAVE DRAG ADJUSTMENT VS MACH NUMBER



ORIGINAL PAGE IS  
OF POOR QUALITY

FIGURE 3-5. WAVE DRAG PLANAR SURFACE ADJUSTMENT

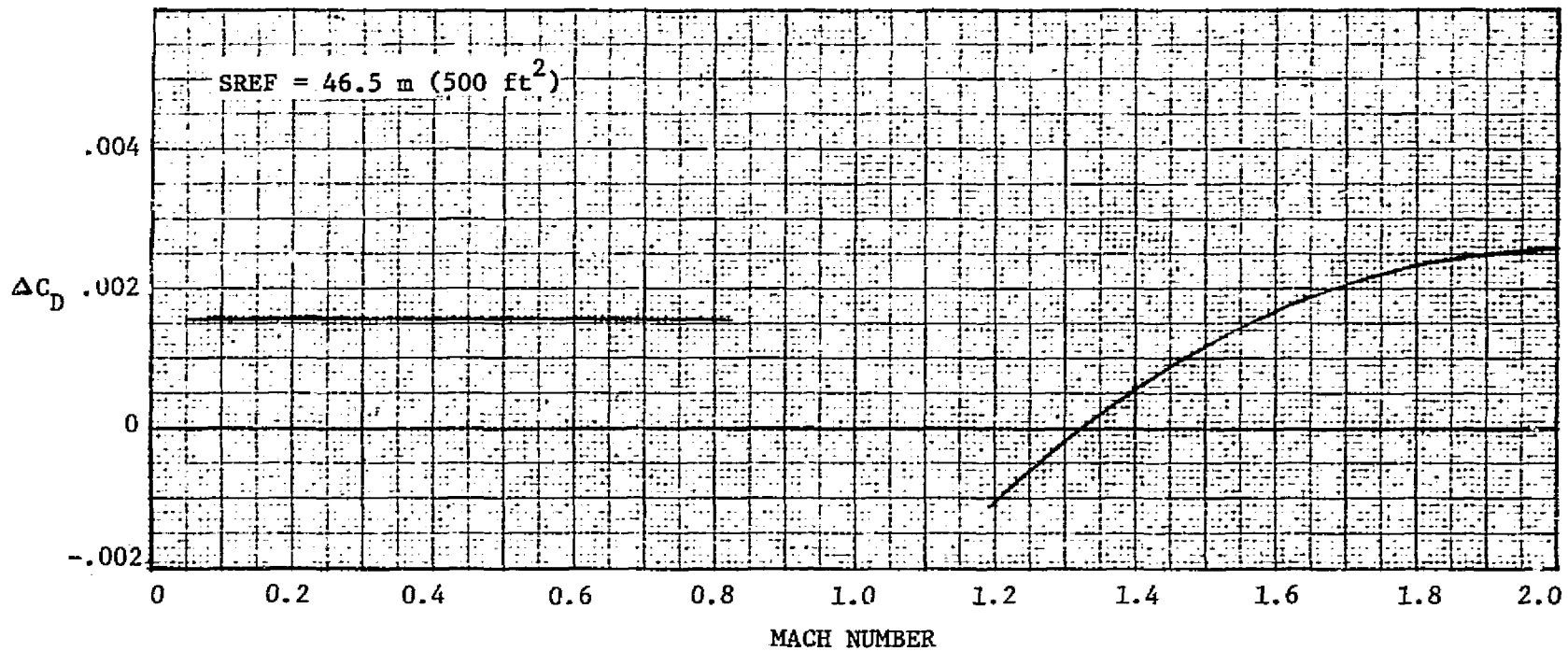


FIGURE 3-6. FLIGHT TEST/ANALYTICAL ADJUSTMENT TO MINIMUM DRAG

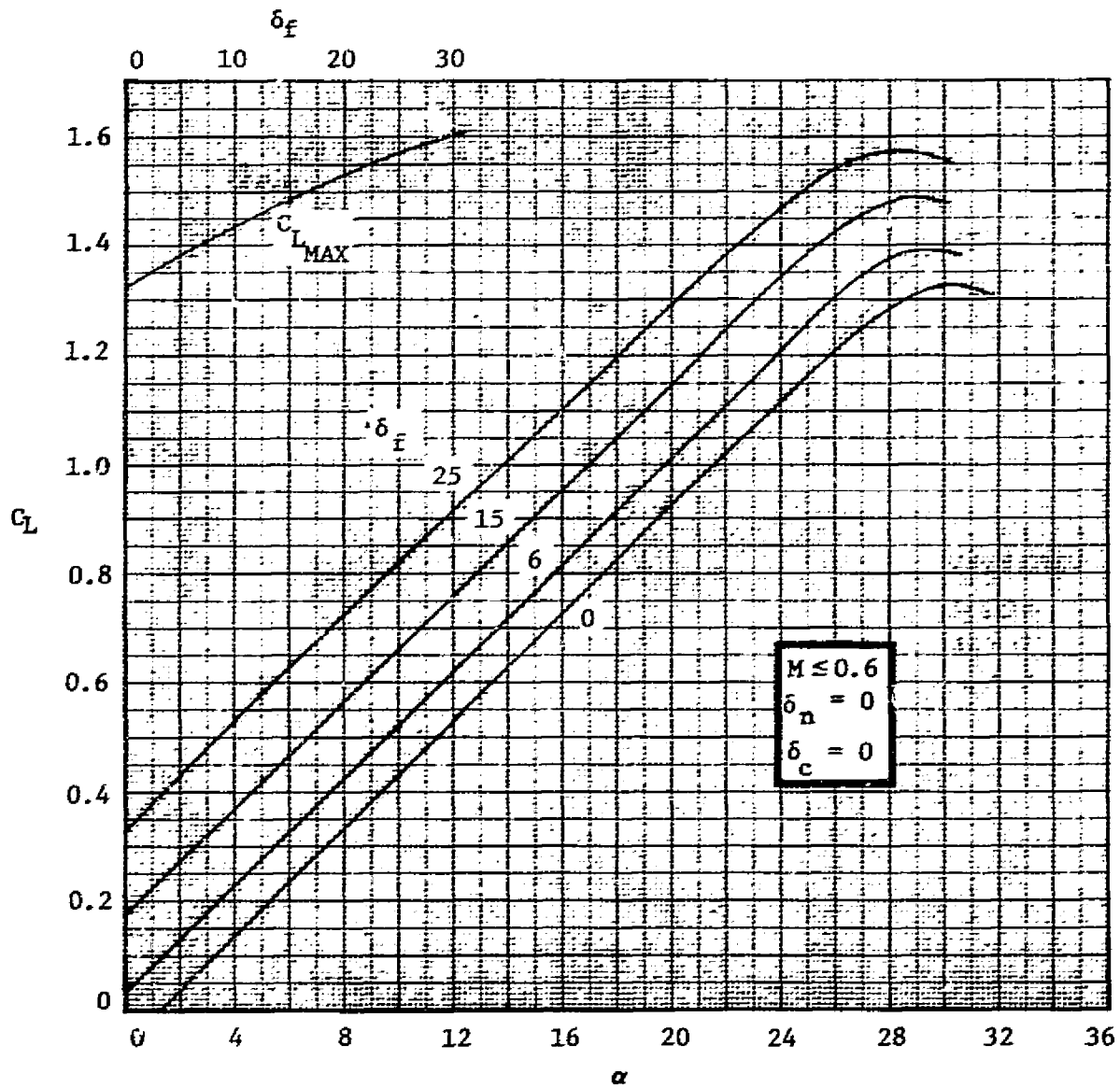


FIGURE 3-7. LIFT VS ANGLE OF ATTACK AT  $M \leq 0.6$ ,  $\delta_n = 0$ ,  $\delta_c = 0$

ORIGINAL PAGE IS  
OF POOR QUALITY

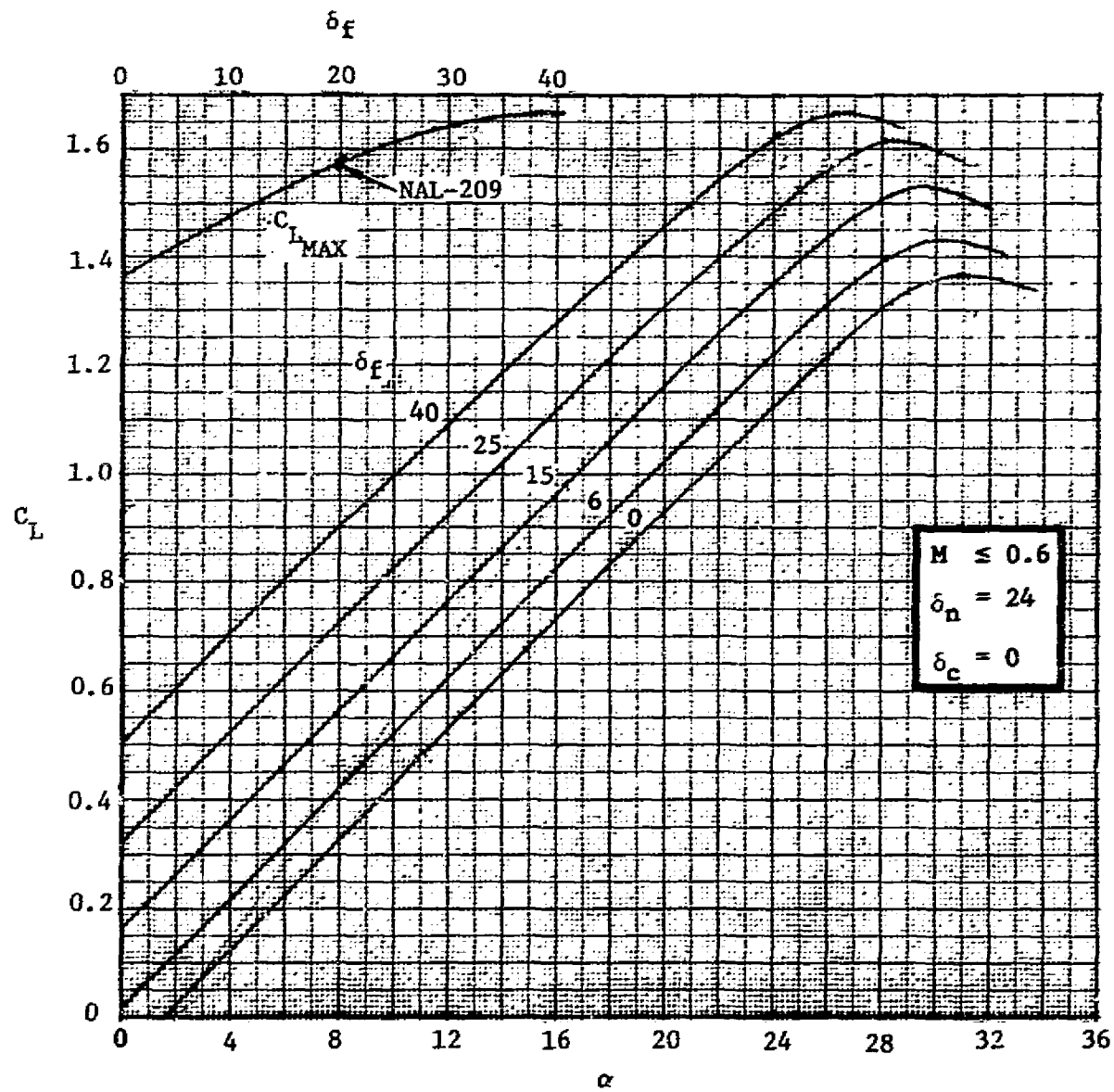


FIGURE 3-8. LIFT VS ANGLE OF ATTACK AT  $M \leq 0.6$ ,  $\delta_n = 24$ ,  $\delta_c = 0$

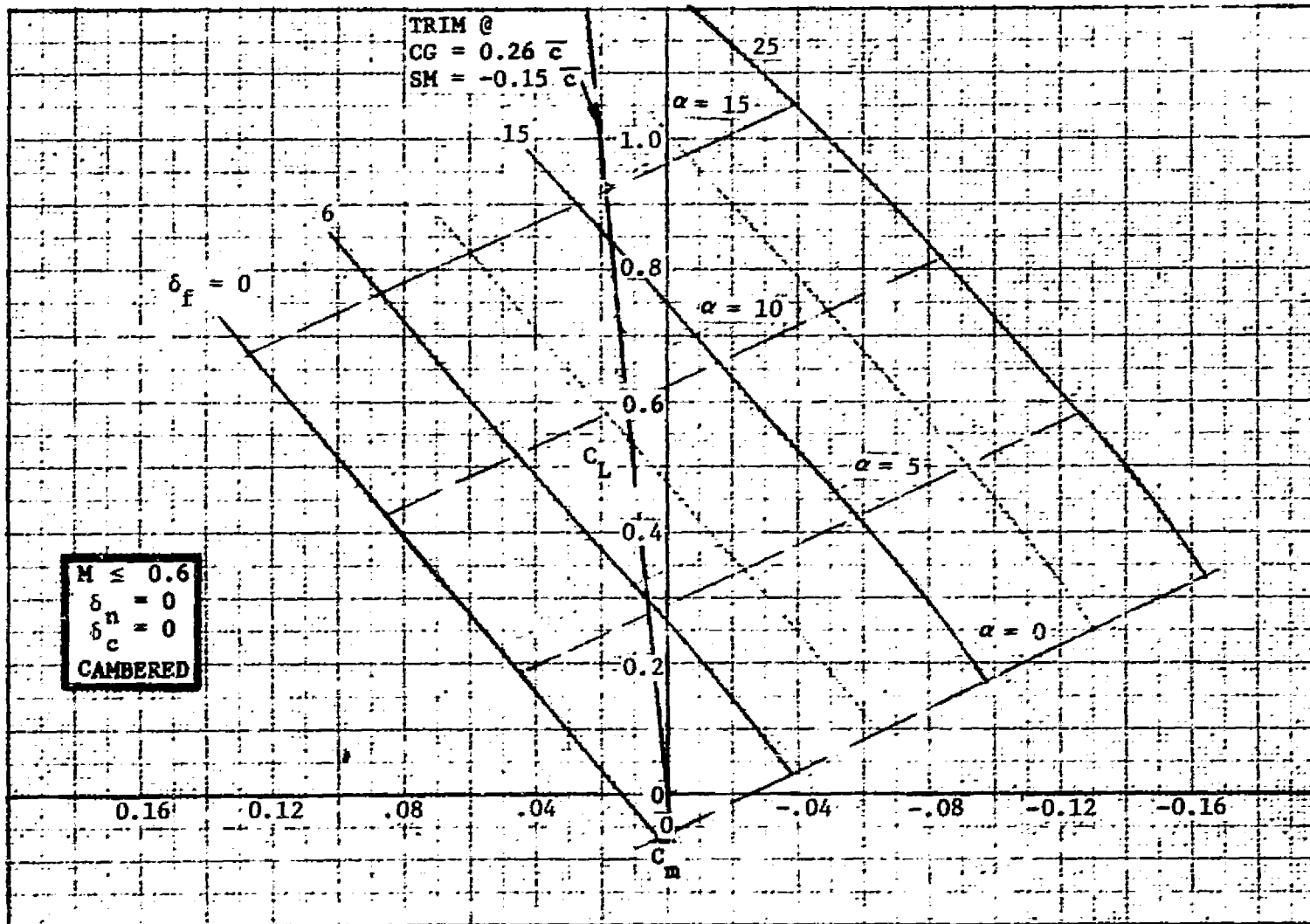


FIGURE 3-9. TRAILING-EDGE FLAP EFFECTIVENESS AT  $M \leq 0.6$ ,  $\delta_n = 0$ ,  $\delta_c = 0$

ORIGINAL PAGE IS  
 OF POOR QUALITY

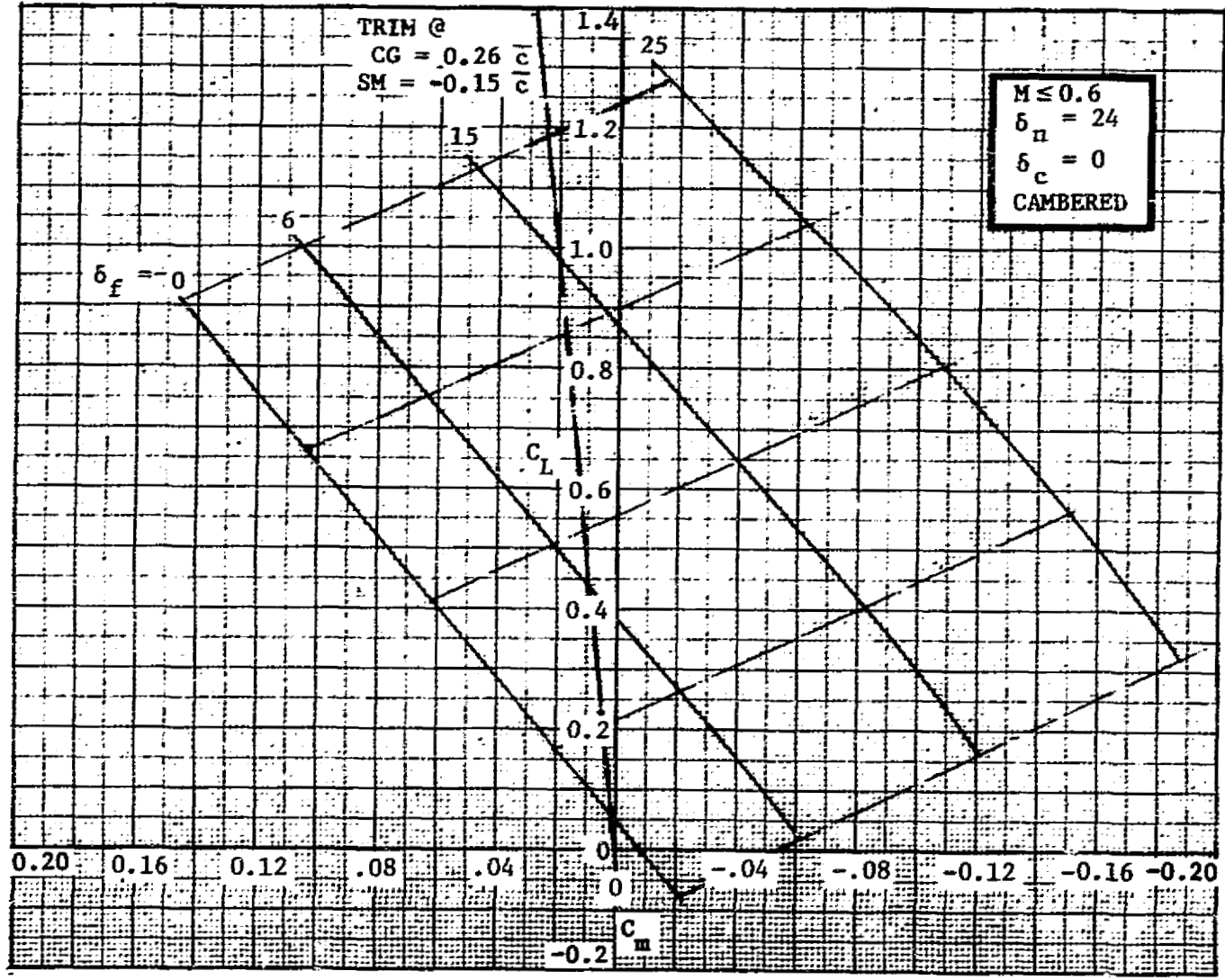


FIGURE 3-10. TRAILING-EDGE FLAP EFFECTIVENESS AT  $M \leq 0.6$ ,  $\delta_n = 24$ ,  $\delta_c = 0$

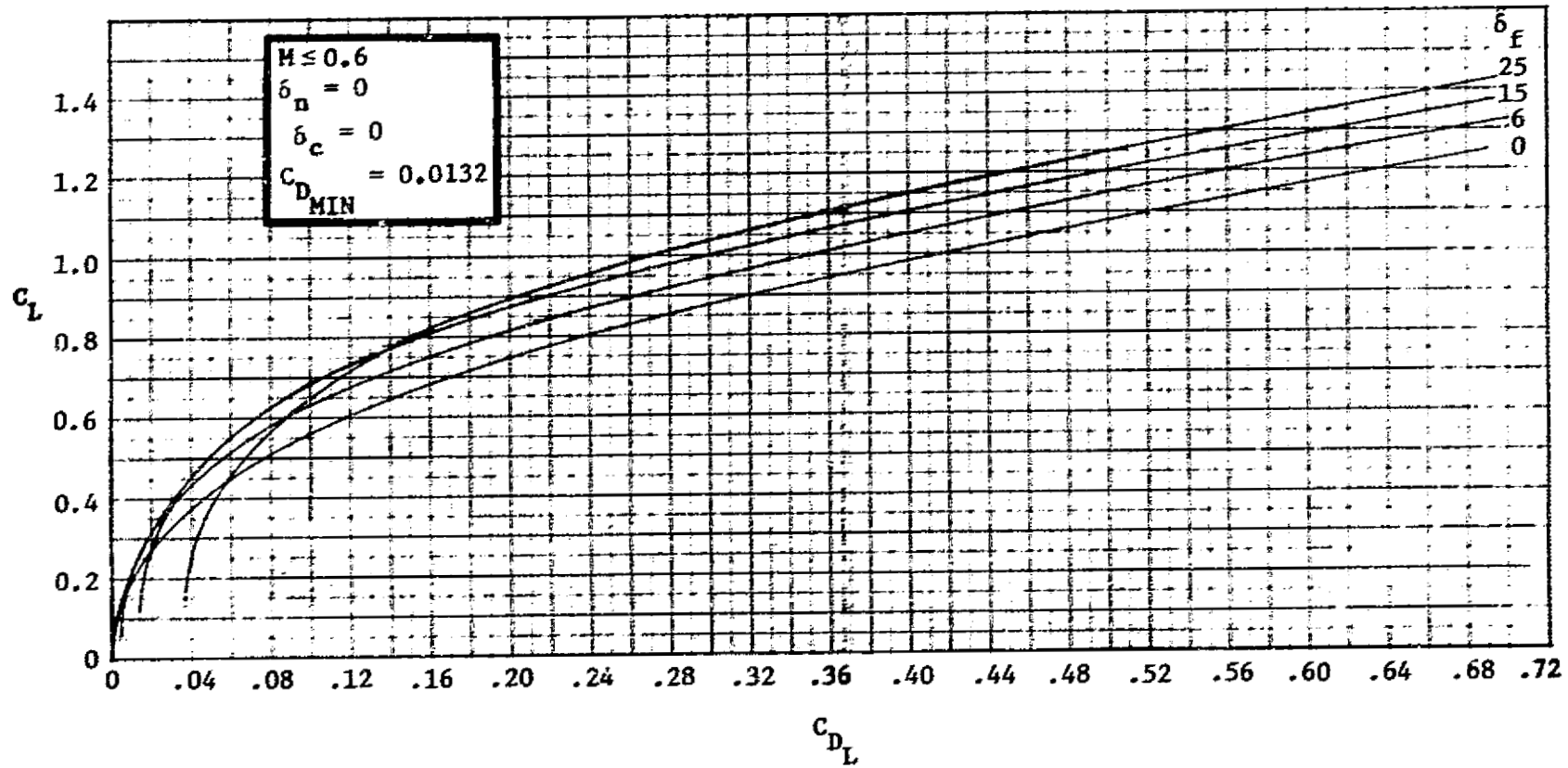
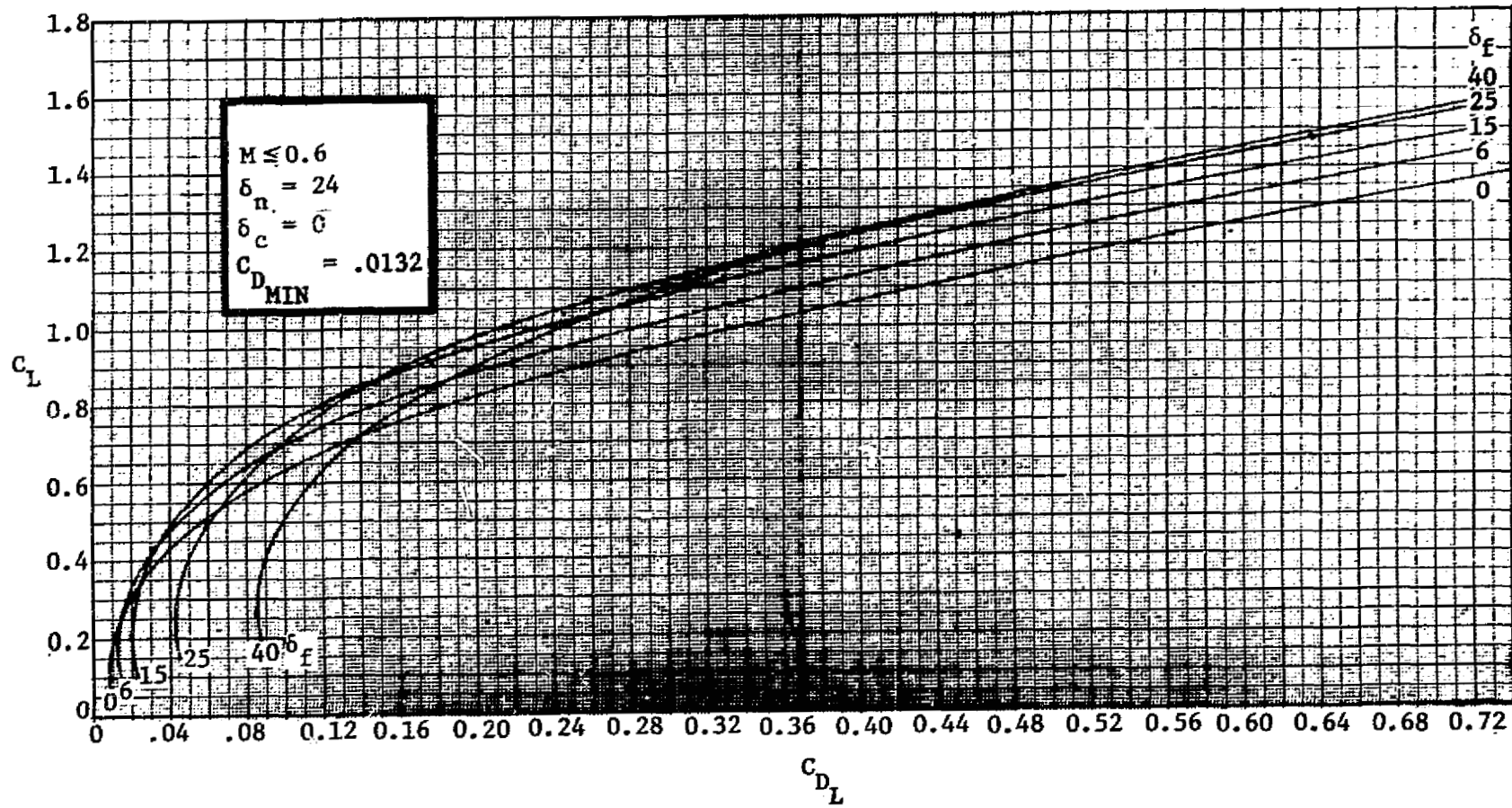


FIGURE 3-11. DRAG DUE TO LIFT AT  $M \leq 0.6$ ,  $\delta_n = 0$ ,  $\delta_c = 0$


 FIGURE 3-12. DRAG DUE TO LIFT AT  $M \leq 0.6$ ,  $\delta_n = 24$ ,  $\delta_c = 0$

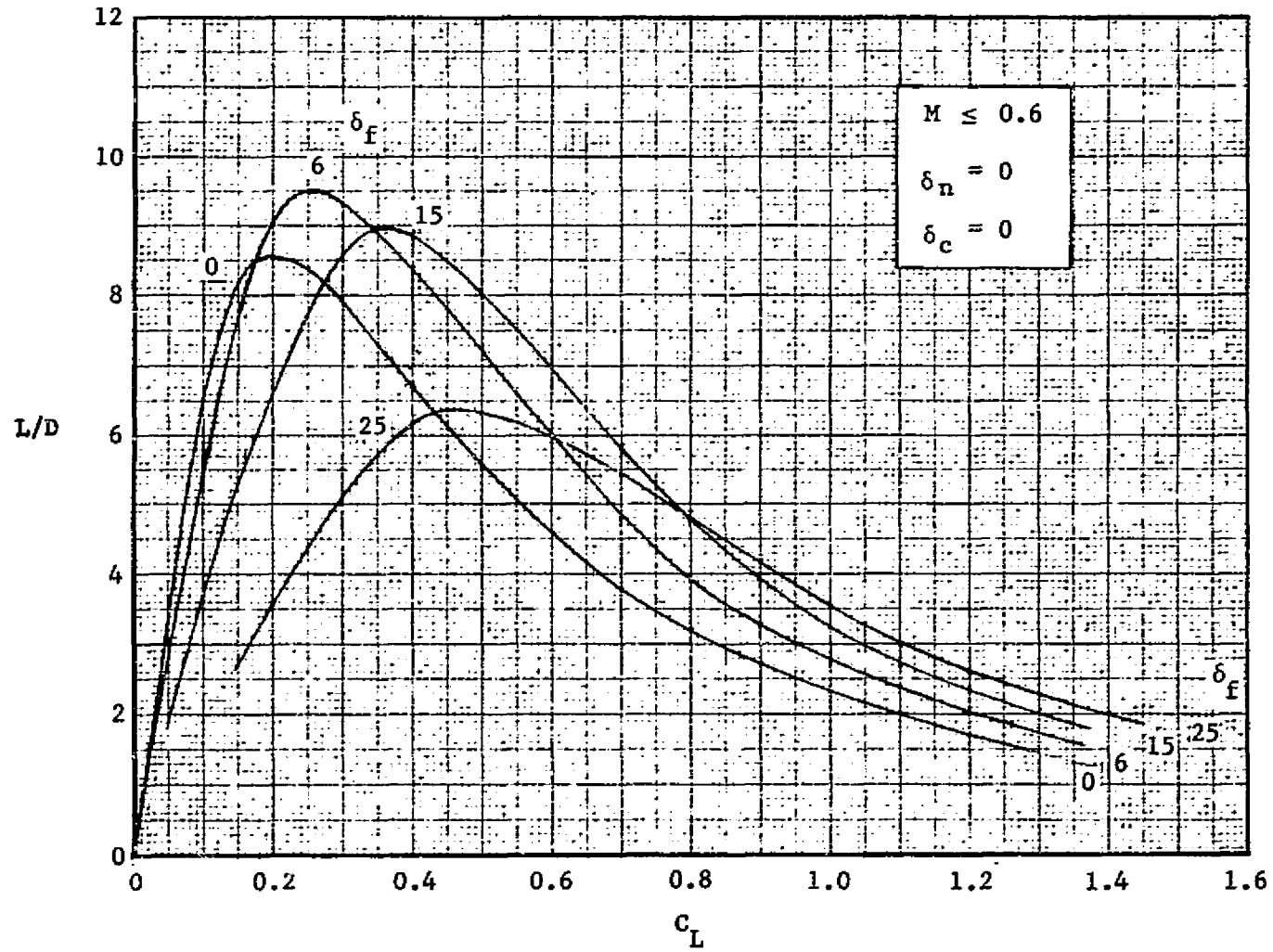


FIGURE 3-13. LIFT-DRAGE RATIO AT  $M \leq 0.6$ ,  $\delta_n = 0$ ,  $\delta_c = 0$

ORIGINAL PAGE IS  
OF POOR QUALITY

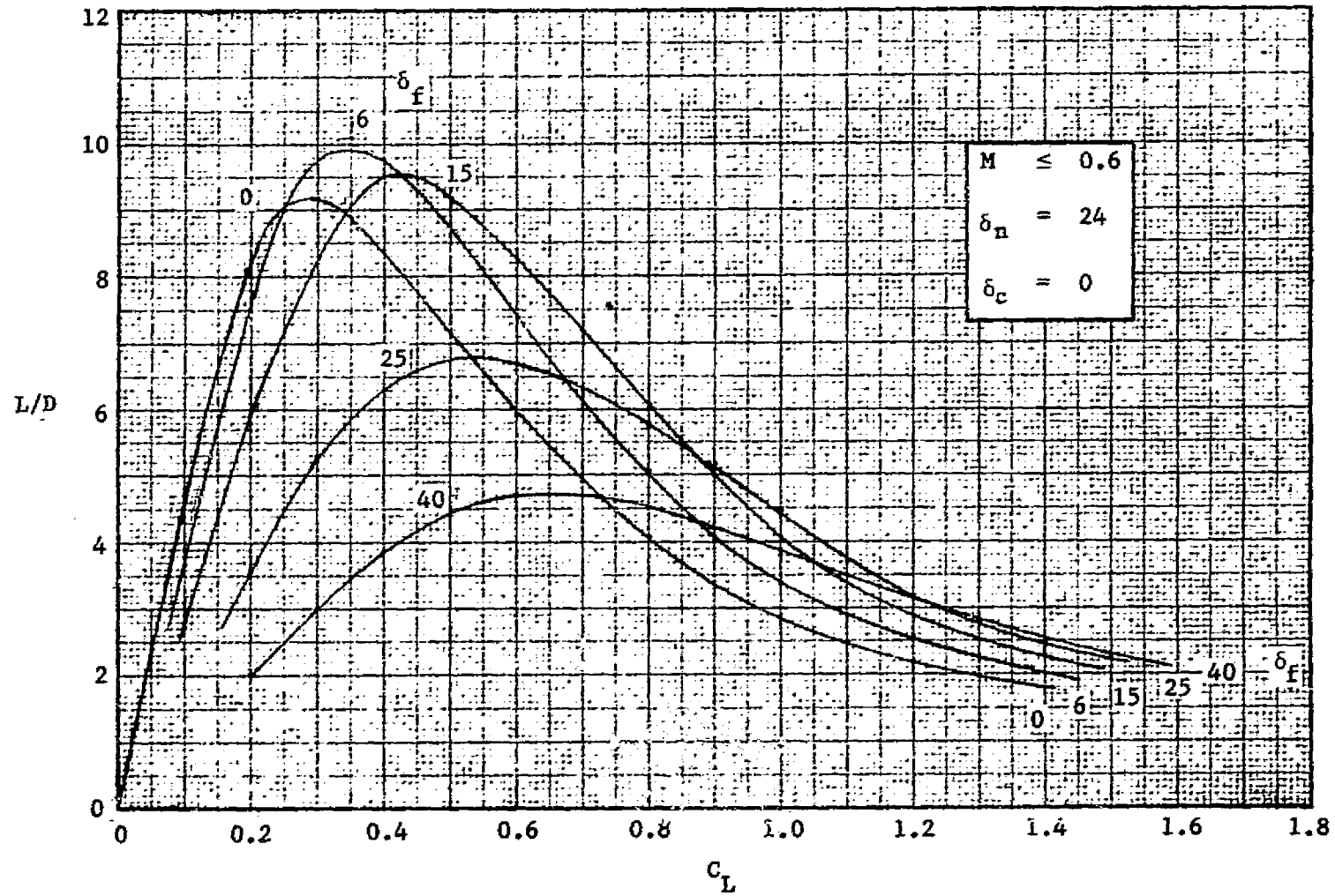


FIGURE 3-14. LIFT-DRAGE RATIO AT  $M \leq 0.6$ ,  $\delta_n = 24$ ,  $\delta_c = 0$

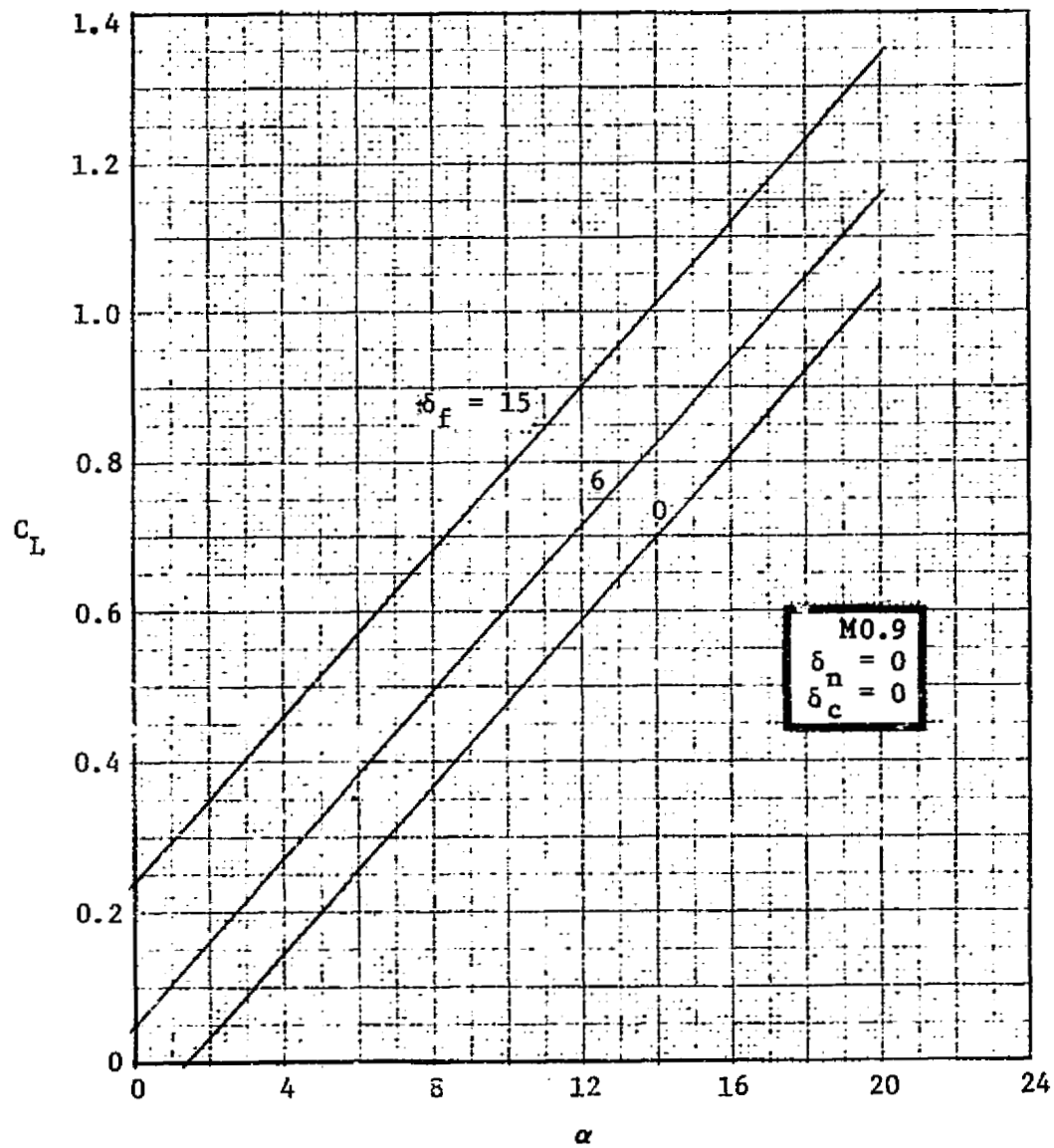


FIGURE 3-15. LIFT VS ANGLE OF ATTACK AT M0.9,  $\delta_n=0$ ,  $\delta_c=0$

ORIGINAL PAGE IS  
OF POOR QUALITY

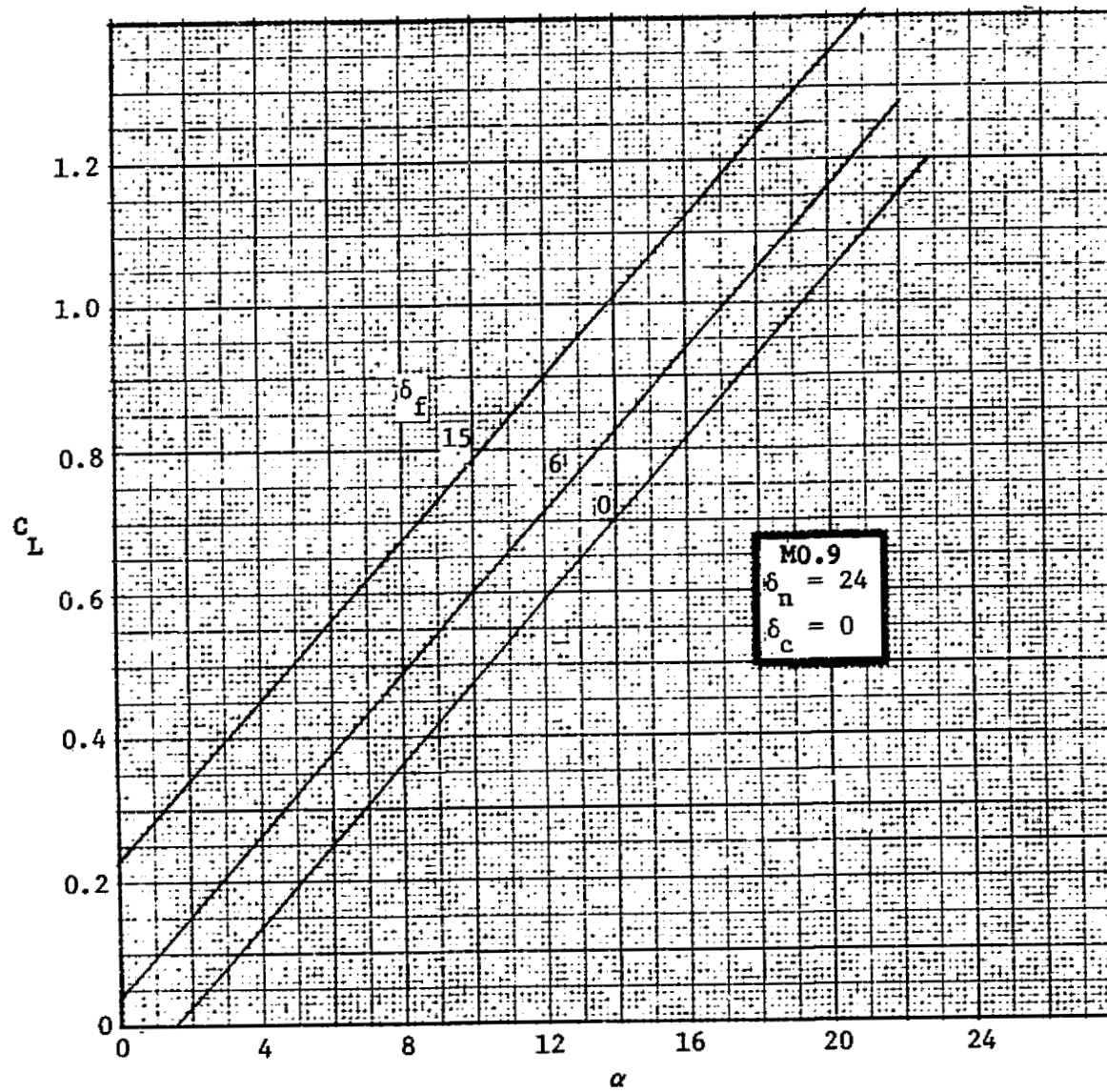


FIGURE 3-16. LIFT VS ANGLE OF ATTACK AT MO.9,  $\delta_n = 24$ ,  $\delta_c = 0$

ORIGINAL PAGE IS  
OF POOR QUALITY

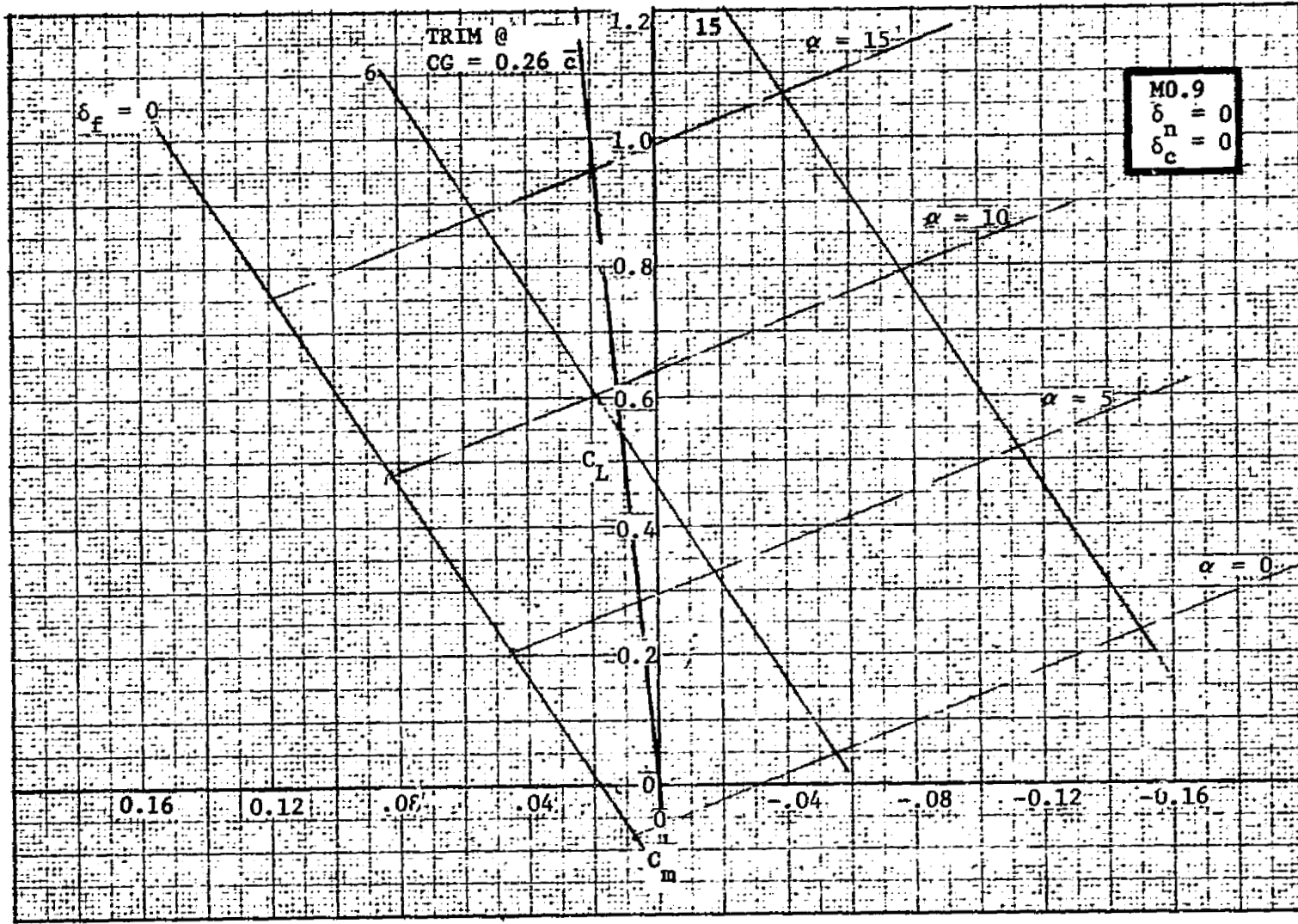


FIGURE 3-17. TRAILING EDGE FLAP EFFECTIVENESS AT  $M_0 = 0.9$ ,  $\delta_n = 0$ ,  $\delta_c = 0$

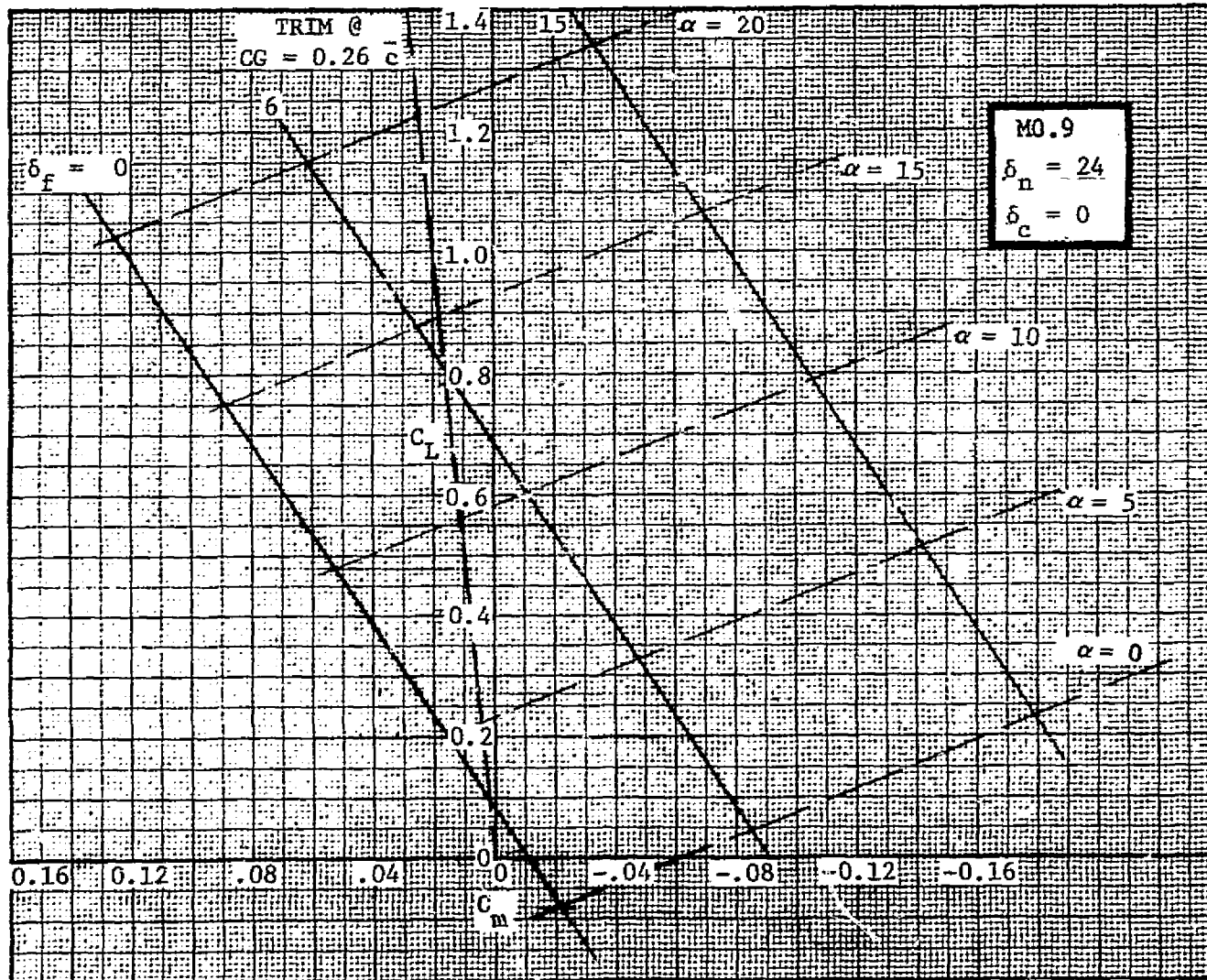
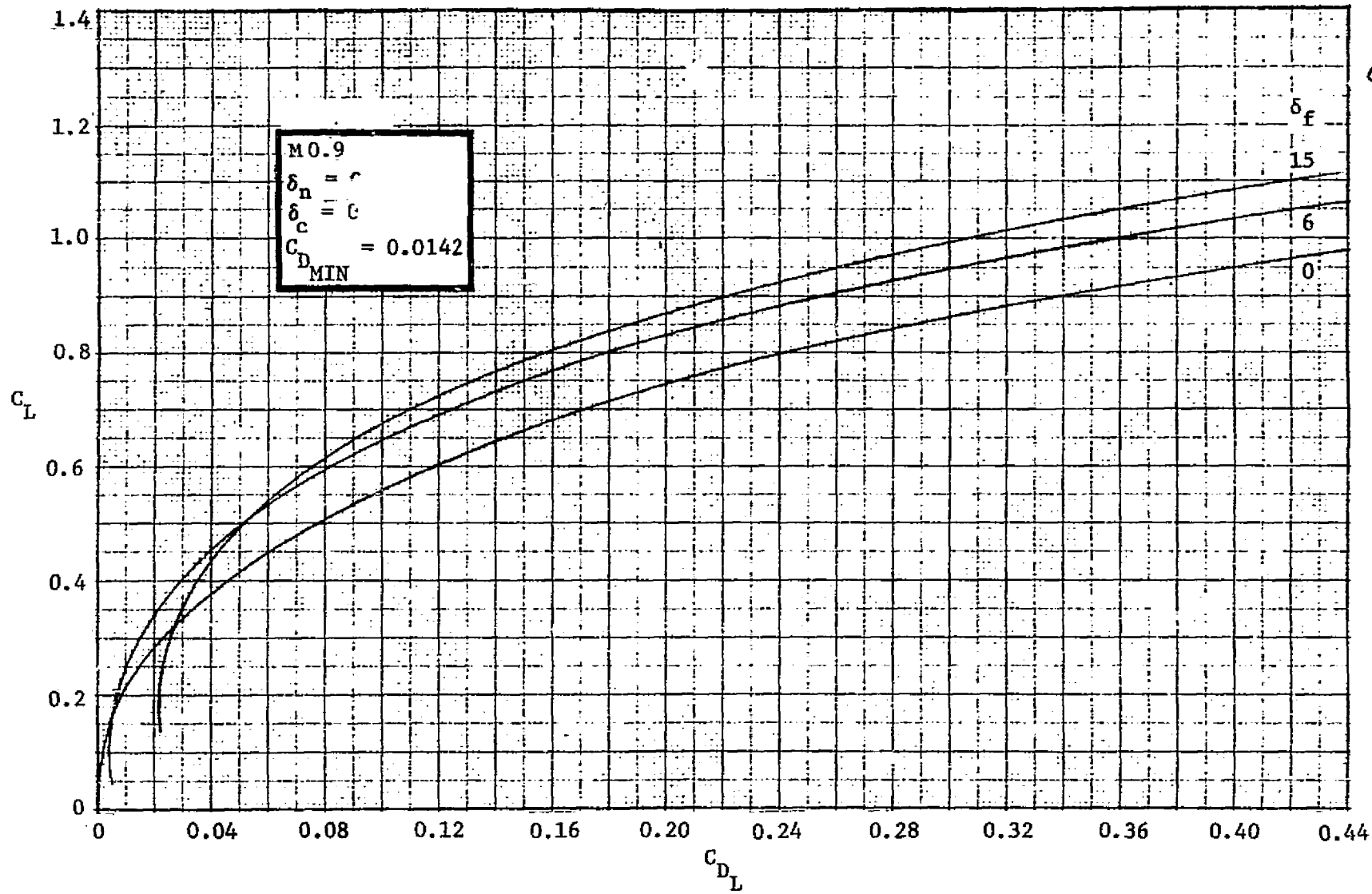


FIGURE 3-18. TRAILING EDGE FLAP EFFECTIVENESS AT M0.9,  $\delta_n = 24$ ,  $\delta_c = 0$



ORIGINAL PAGE IS  
OF POOR QUALITY

FIGURE 3-19. DRAG DUE TO LIFT AT  $M 0.9$ ,  $\delta_n = 0$ ,  $\delta_c = 0$

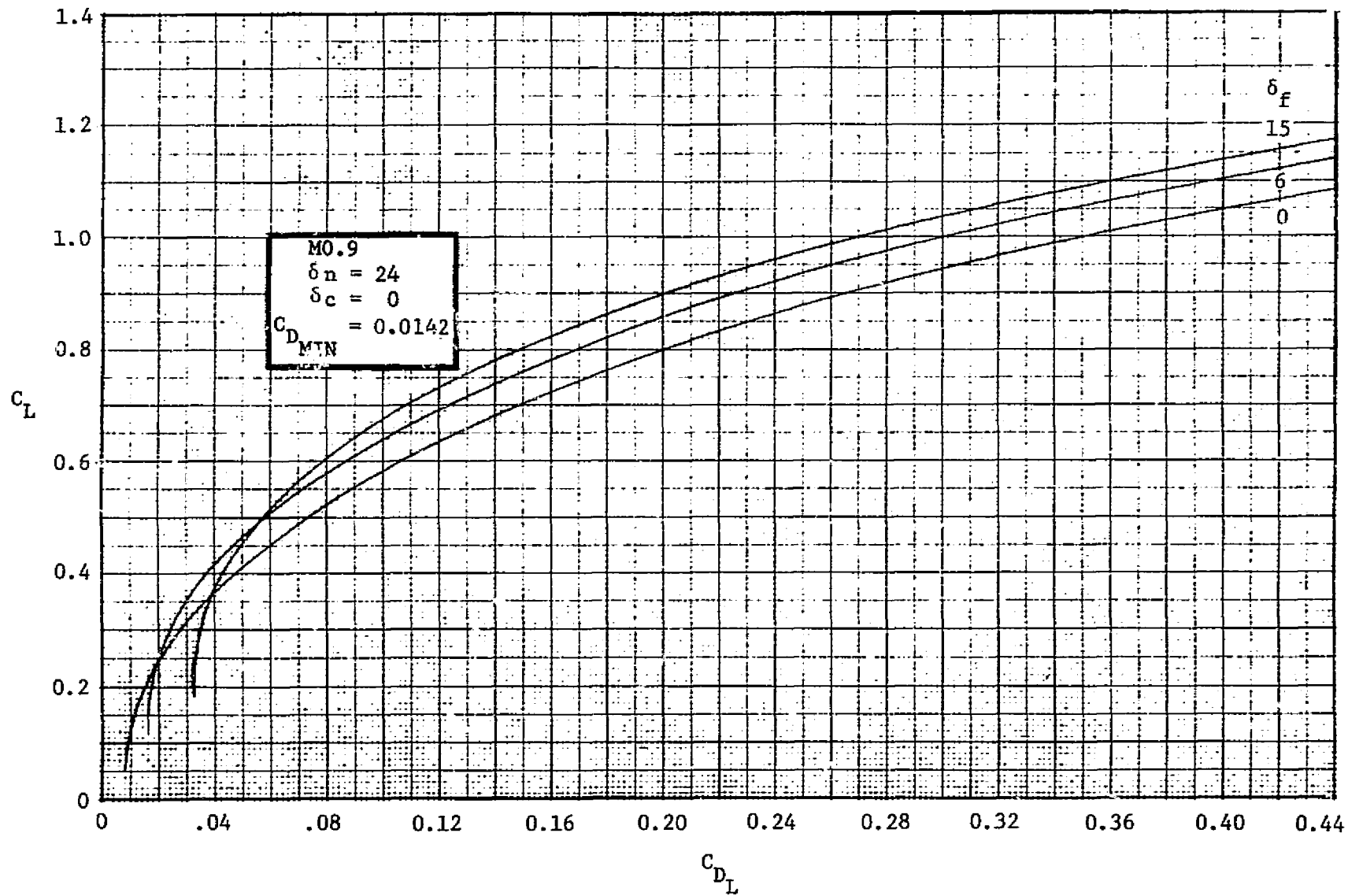


FIGURE 3-20.- DRAG DUE TO LIFT AT  $M_0.9$ ,  $\delta_n = 24$ ,  $\delta_c = 0$

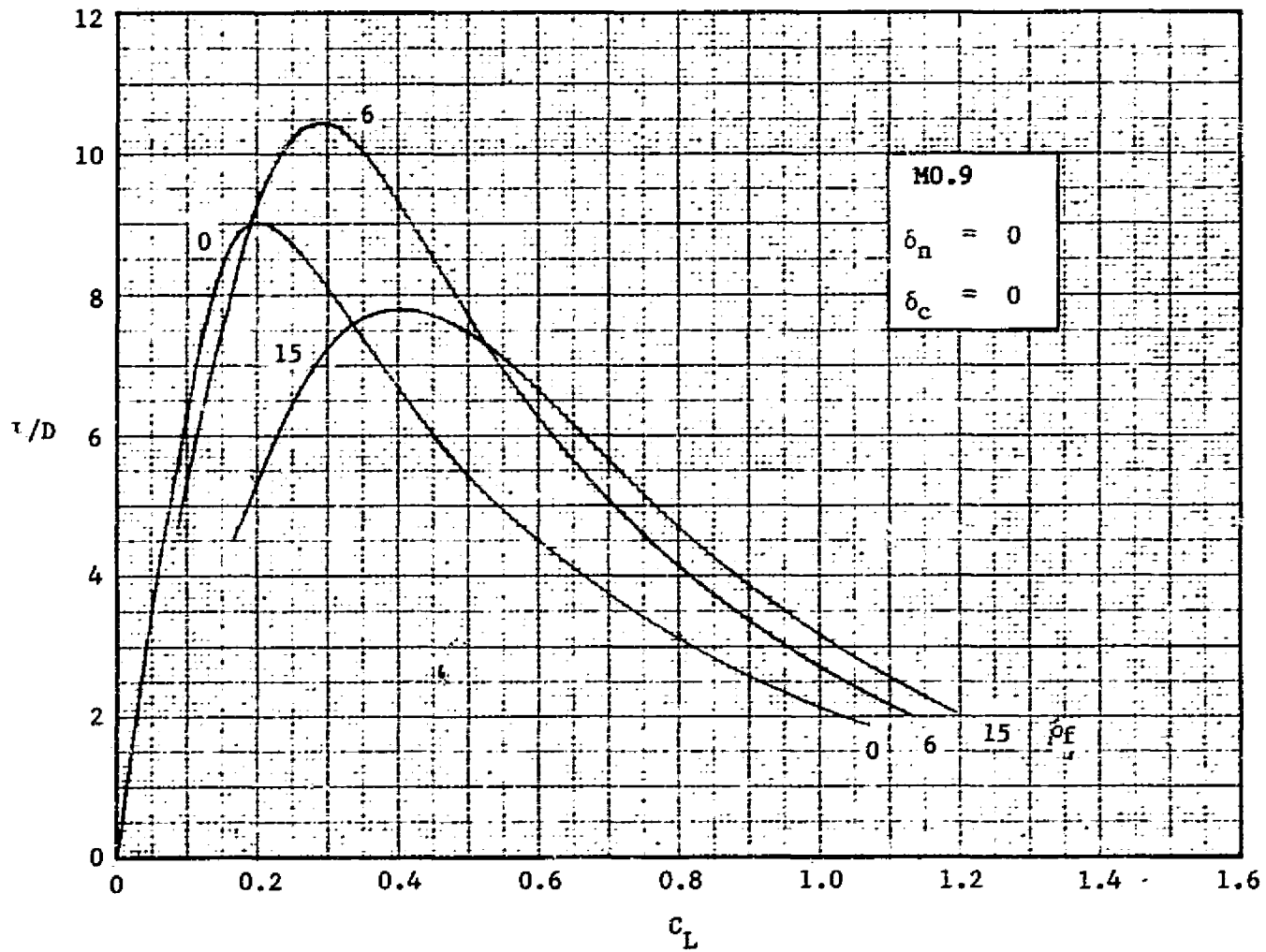
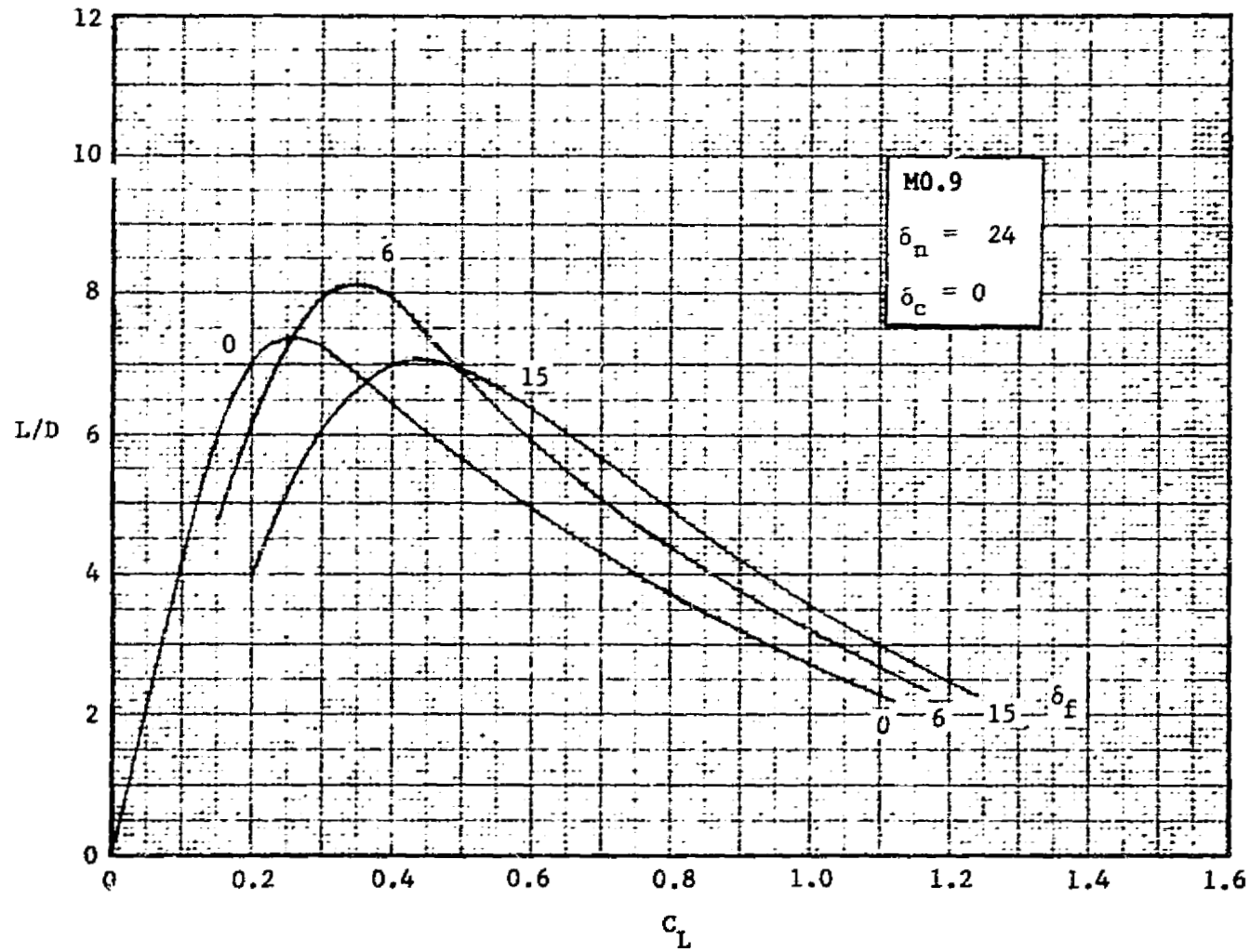


FIGURE 3-21. LIFT-DRAG RATIO AT  $M0.9$ ,  $\delta_n = 0$ ,  $\delta_c = 0$

ORIGINAL PAGE IS  
OF POOR QUALITY

FIGURE 3-22. LIFT-DRAGE RATIO AT  $M_0.9$ ,  $\delta_n = 24$ ,  $\delta_c = 0$

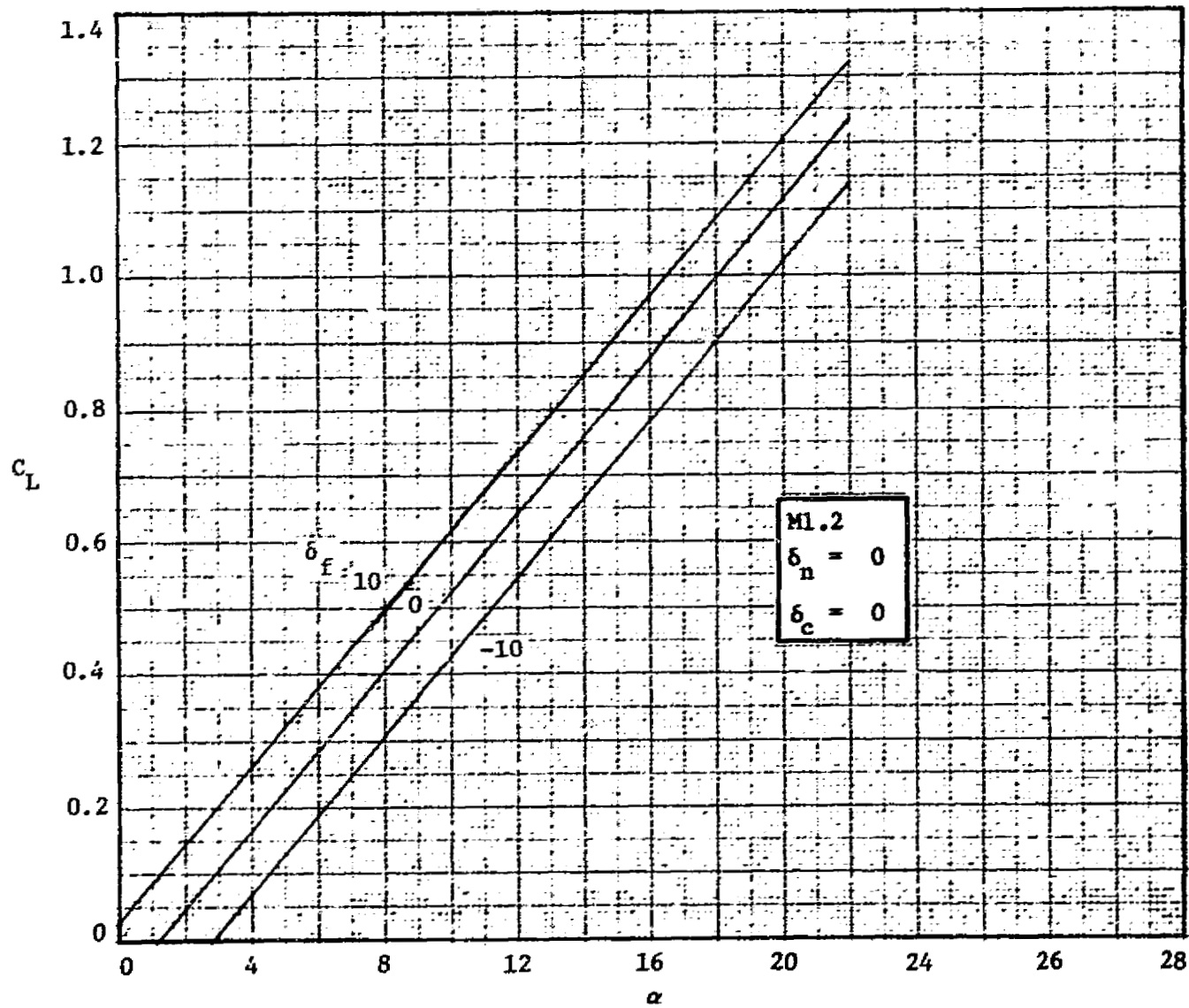


FIGURE 3-23. LIFT VS ANGLE OF ATTACK AT M1.2,  $\delta_n=0$ ,  $\delta_c=0$

ORIGINAL PAGE IS  
OF POOR QUALITY

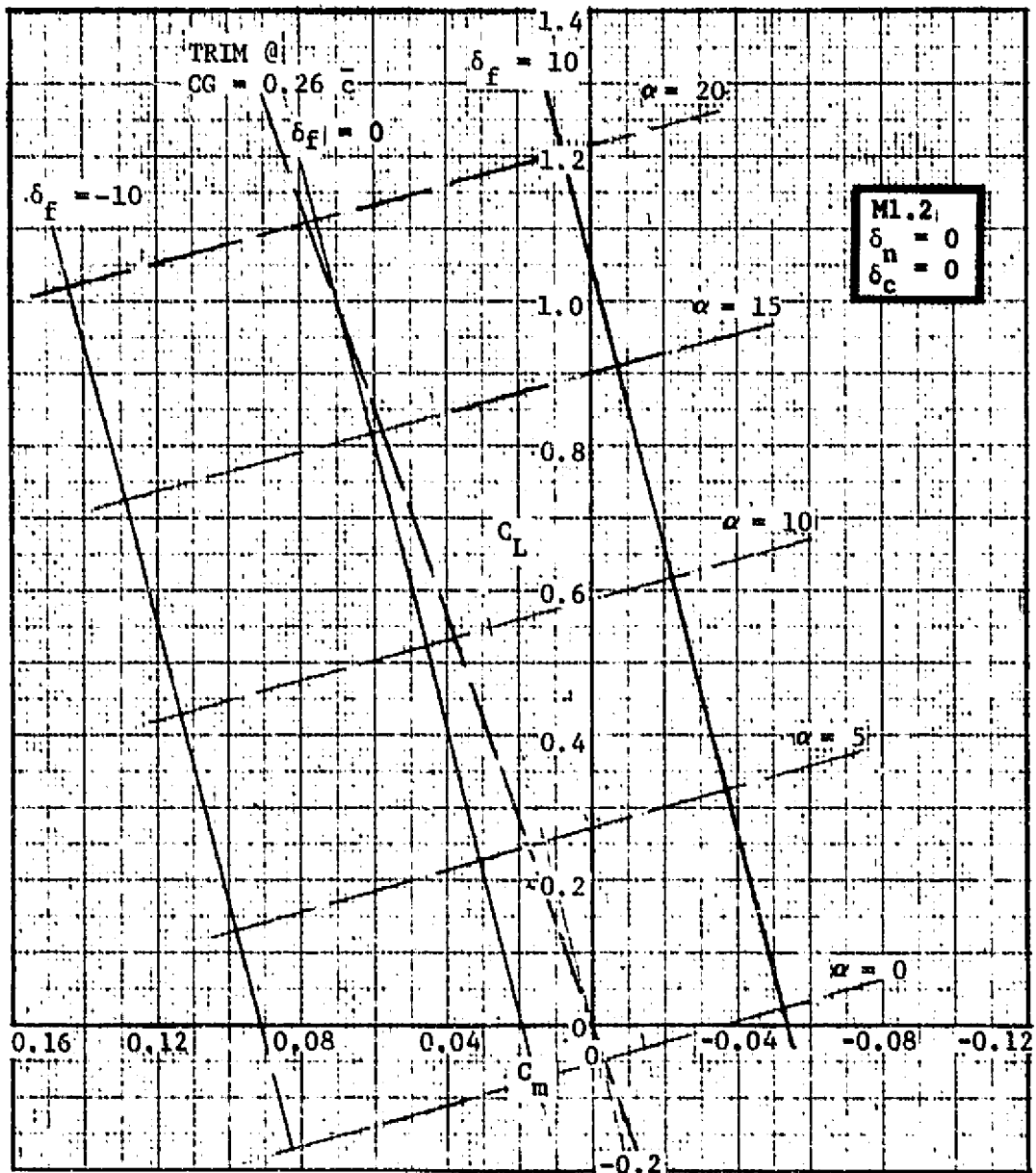


FIGURE 3-24. TRAILING EDGE FLAP EFFECTIVENESS AT  $M1.2$ ,  $\delta_n=0$ ,  $\delta_c=0$

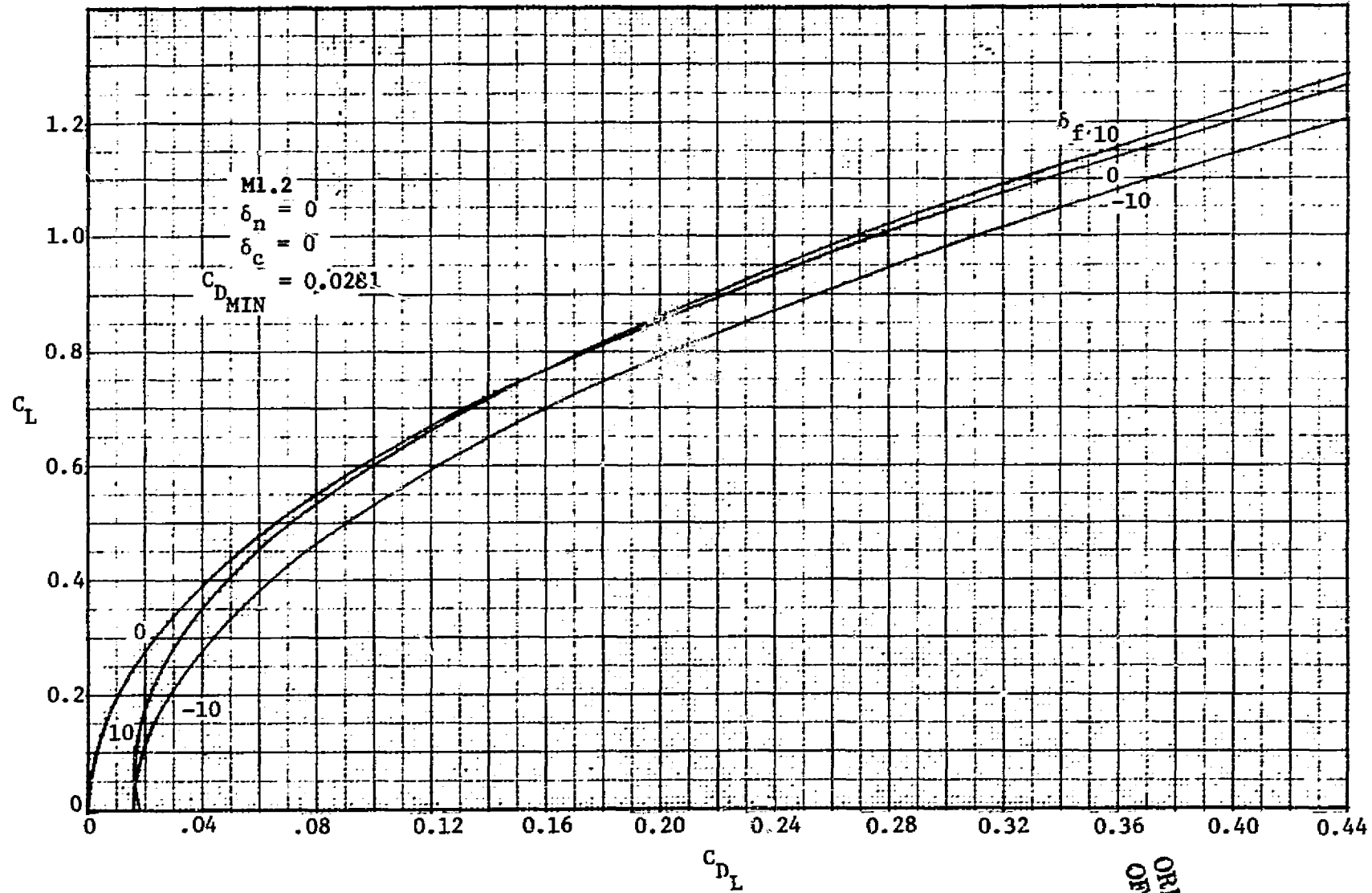
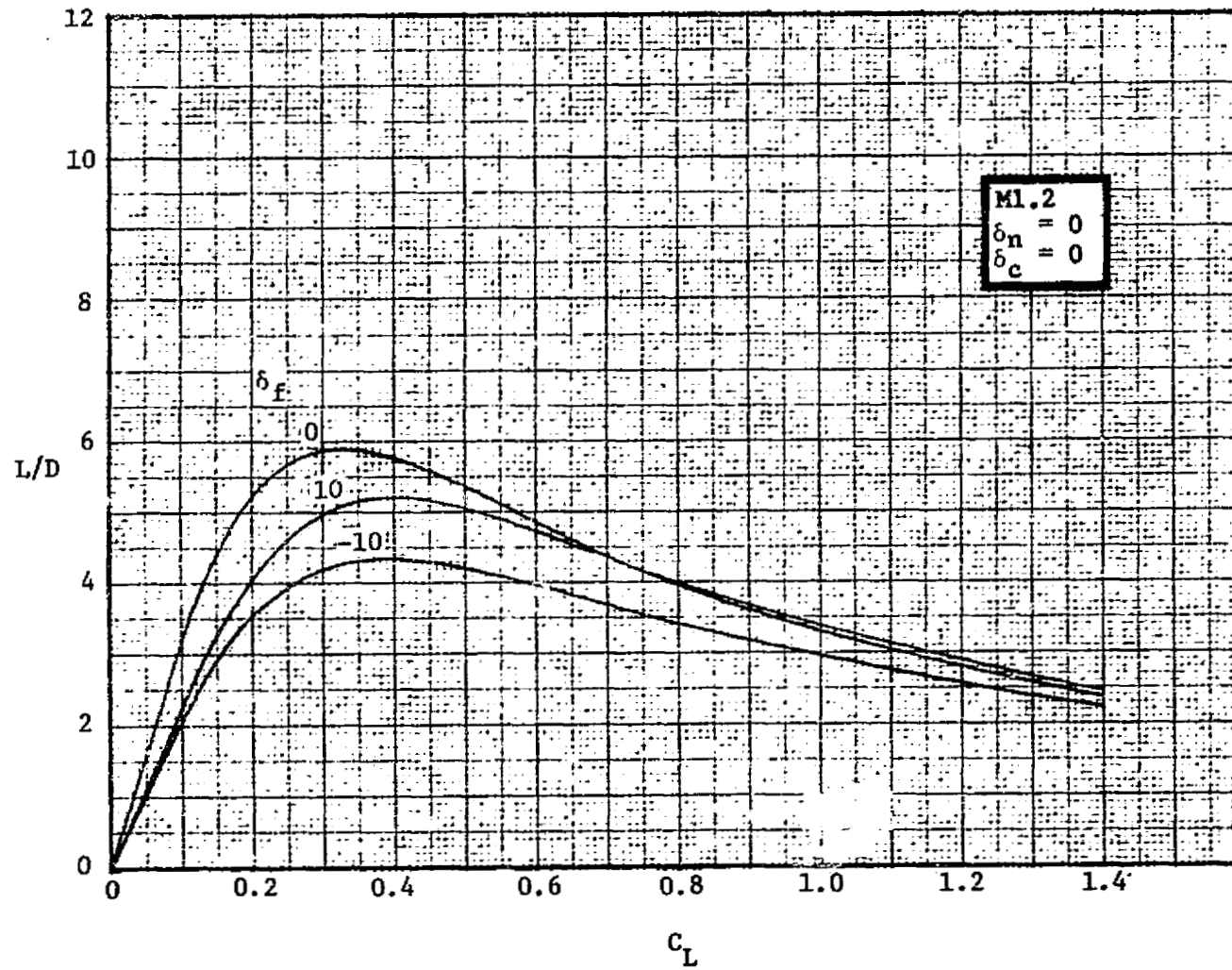


FIGURE 3-25. DRAG DUE TO LIFT AT  $M 1.2$ ,  $\delta_n = 0$ ,  $\delta_c = 0$

ORIGINAL PAGE IS  
OF POOR QUALITY

FIGURE 3-26. LIFT DRAG RATIO AT M1.2,  $\delta_n=0$ ,  $\delta_c=0$

ORIGINAL PAGE IS  
OF POOR QUALITY

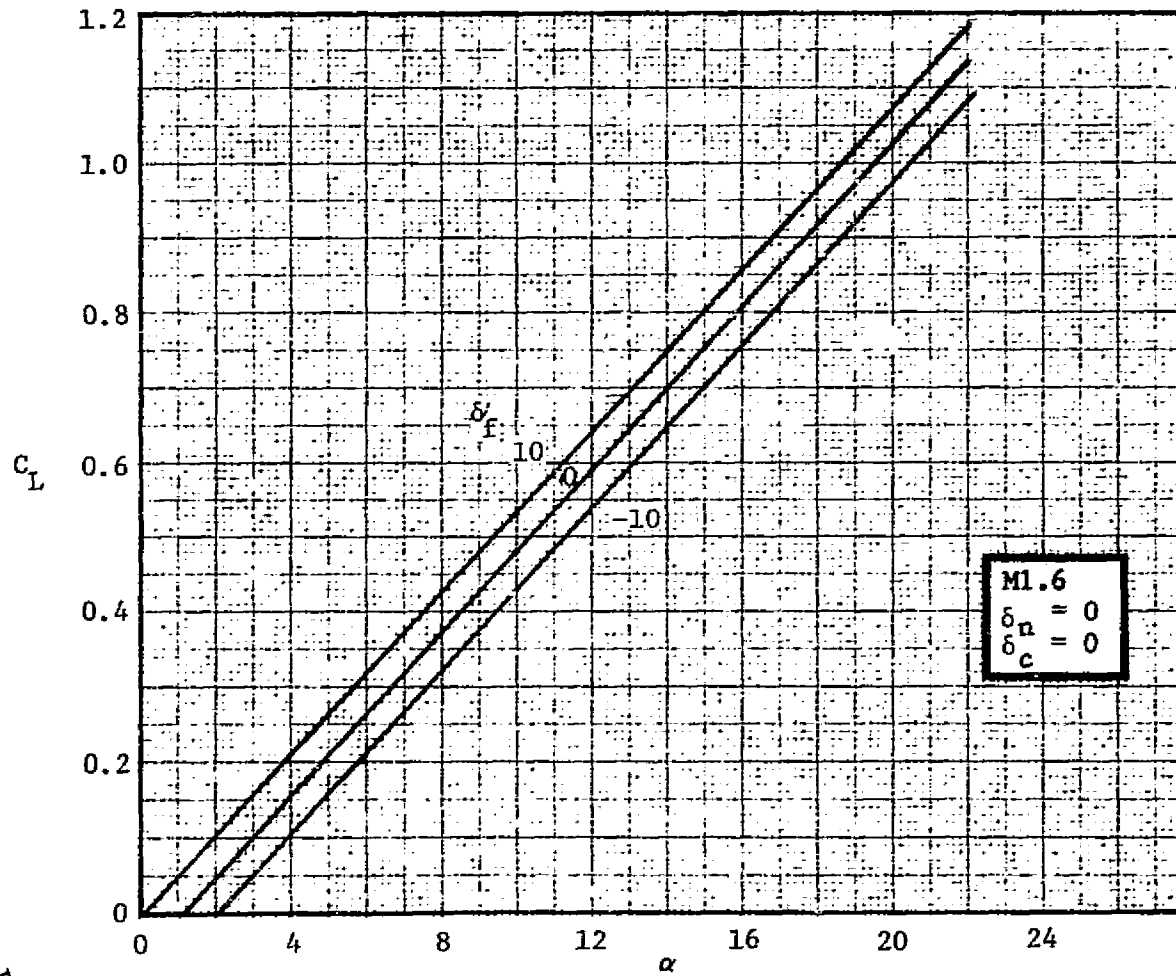


FIGURE 3-27. LIFT VS ANGLE OF ATTACK AT M1.6;  $\delta_n=0$ ,  $\delta_c=0$

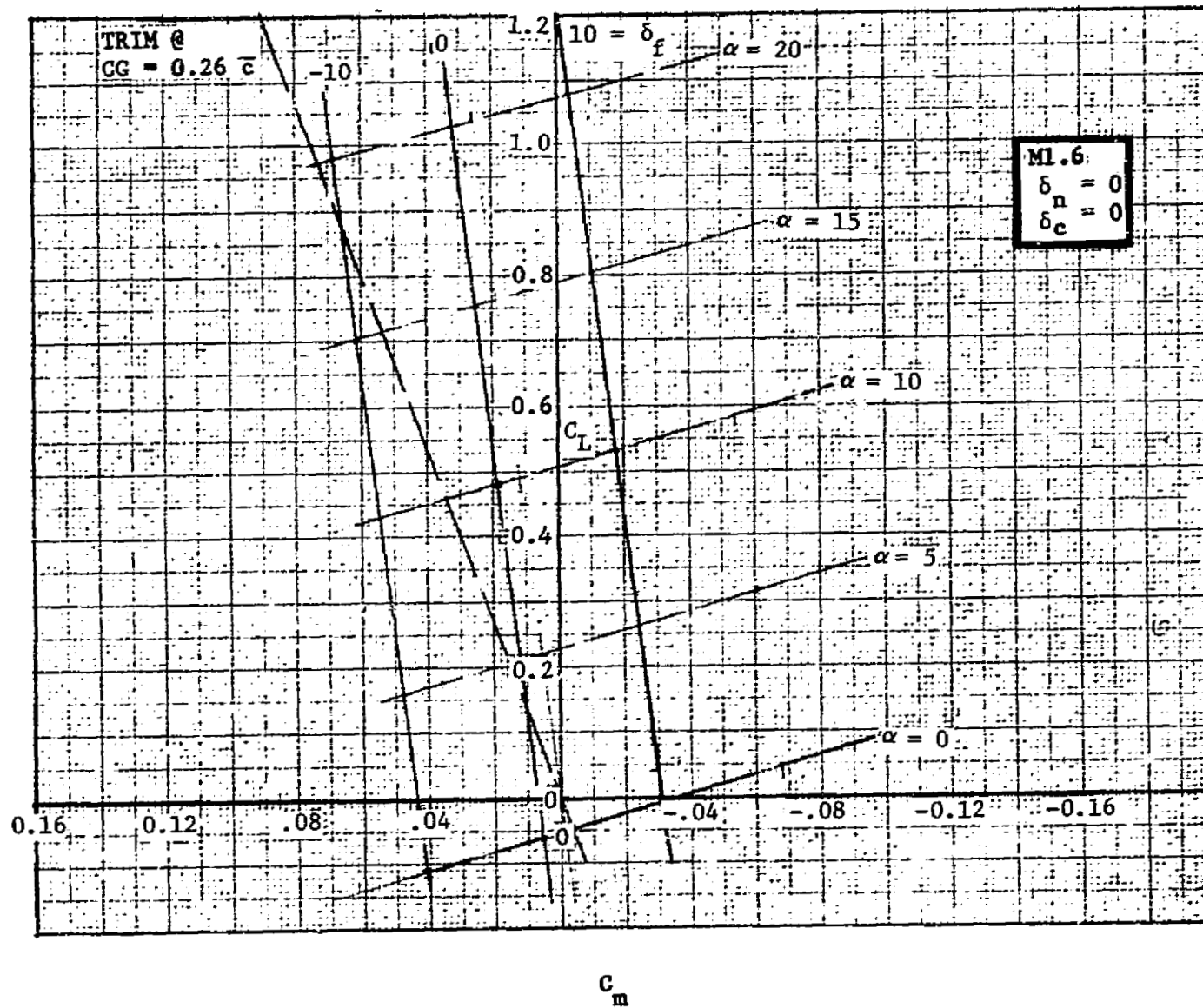


FIGURE 3-28. TRAILING-EDGE FLAP EFFECTIVENESS AT M1.6,  $\delta_n = 0$ ,  $\delta_c = 0$

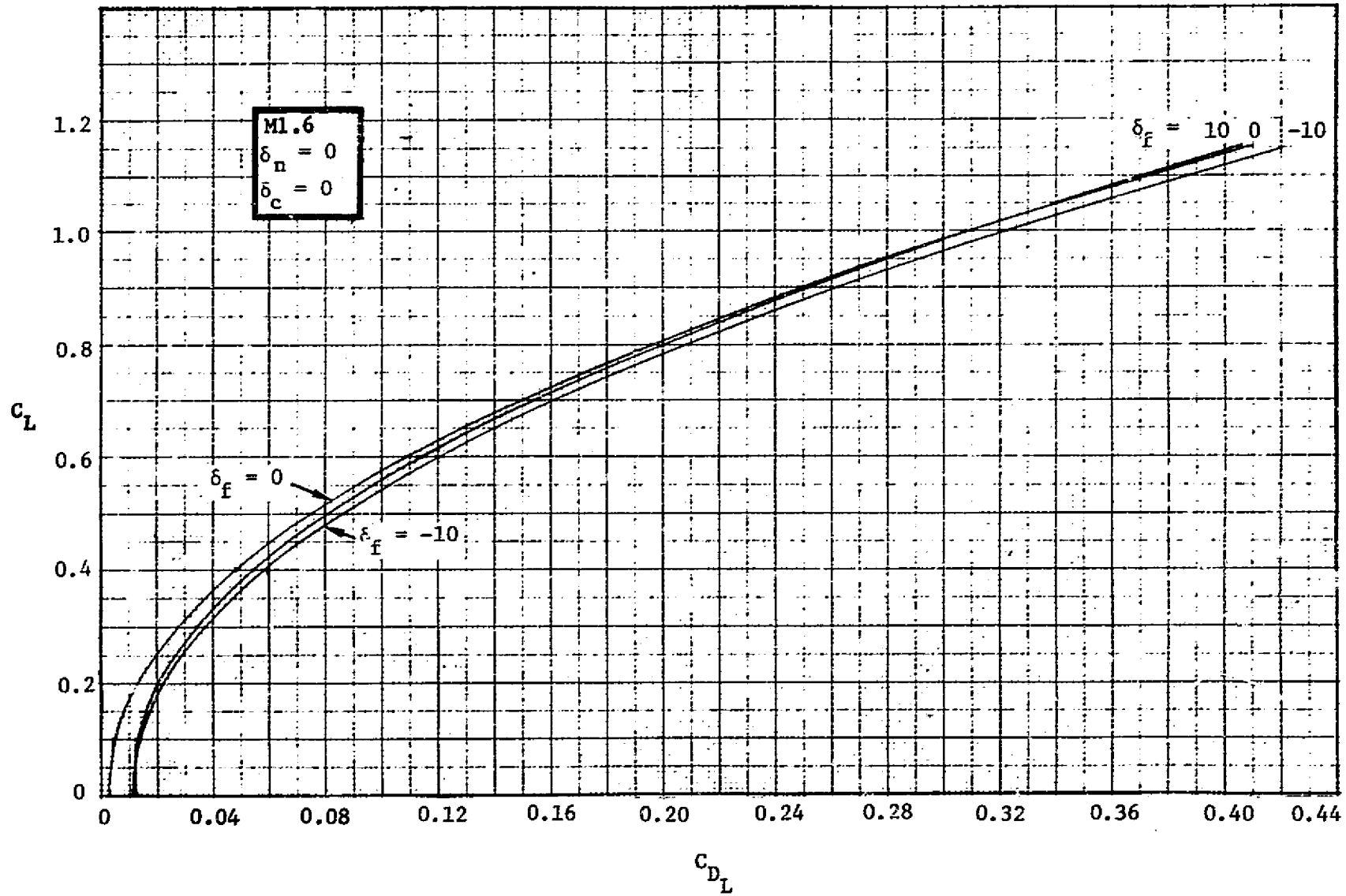
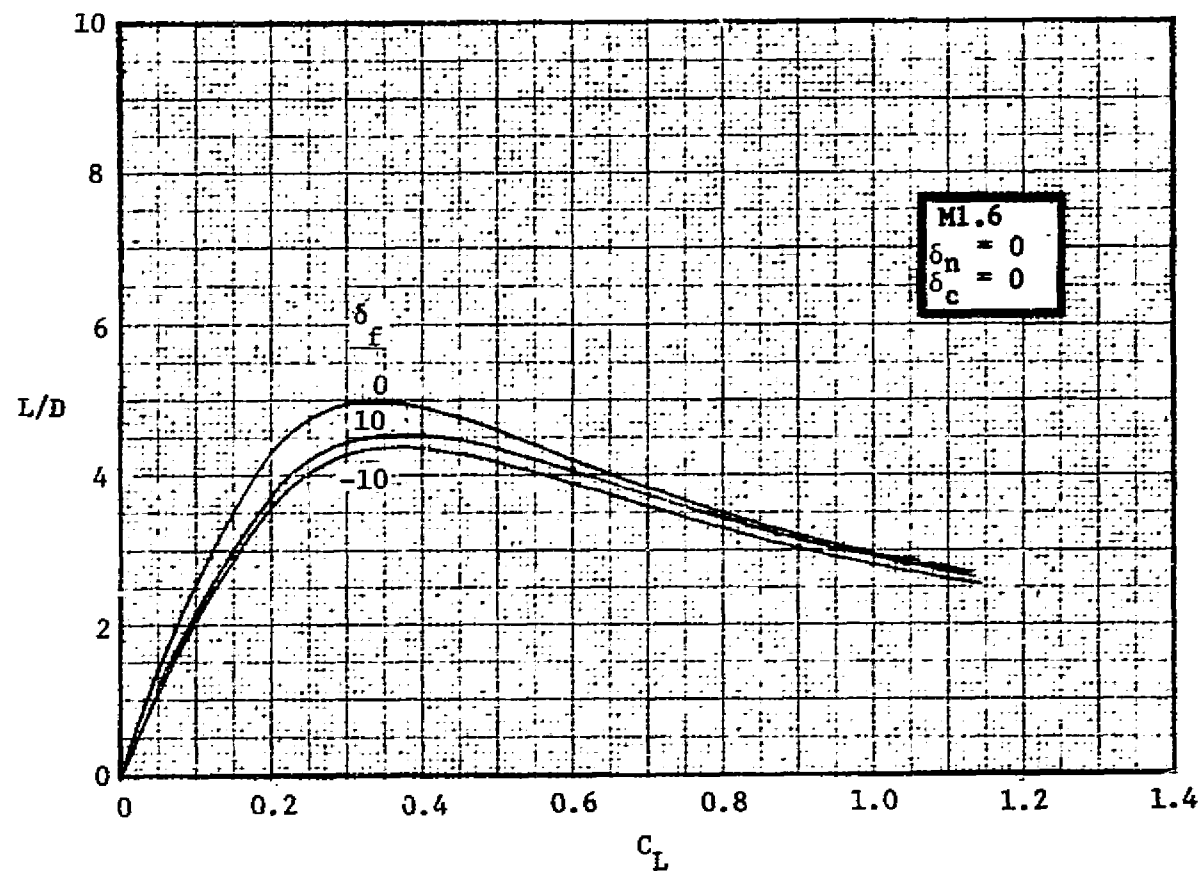


FIGURE 3-29. DRAG DUE TO LIFT AT M1.6,  $\delta_n=0$ ,  $\delta_c=0$

FIGURE 3-30. LIFT/DRAGE RATIO M1.6,  $\delta_n=0$ ,  $\delta_c=0$

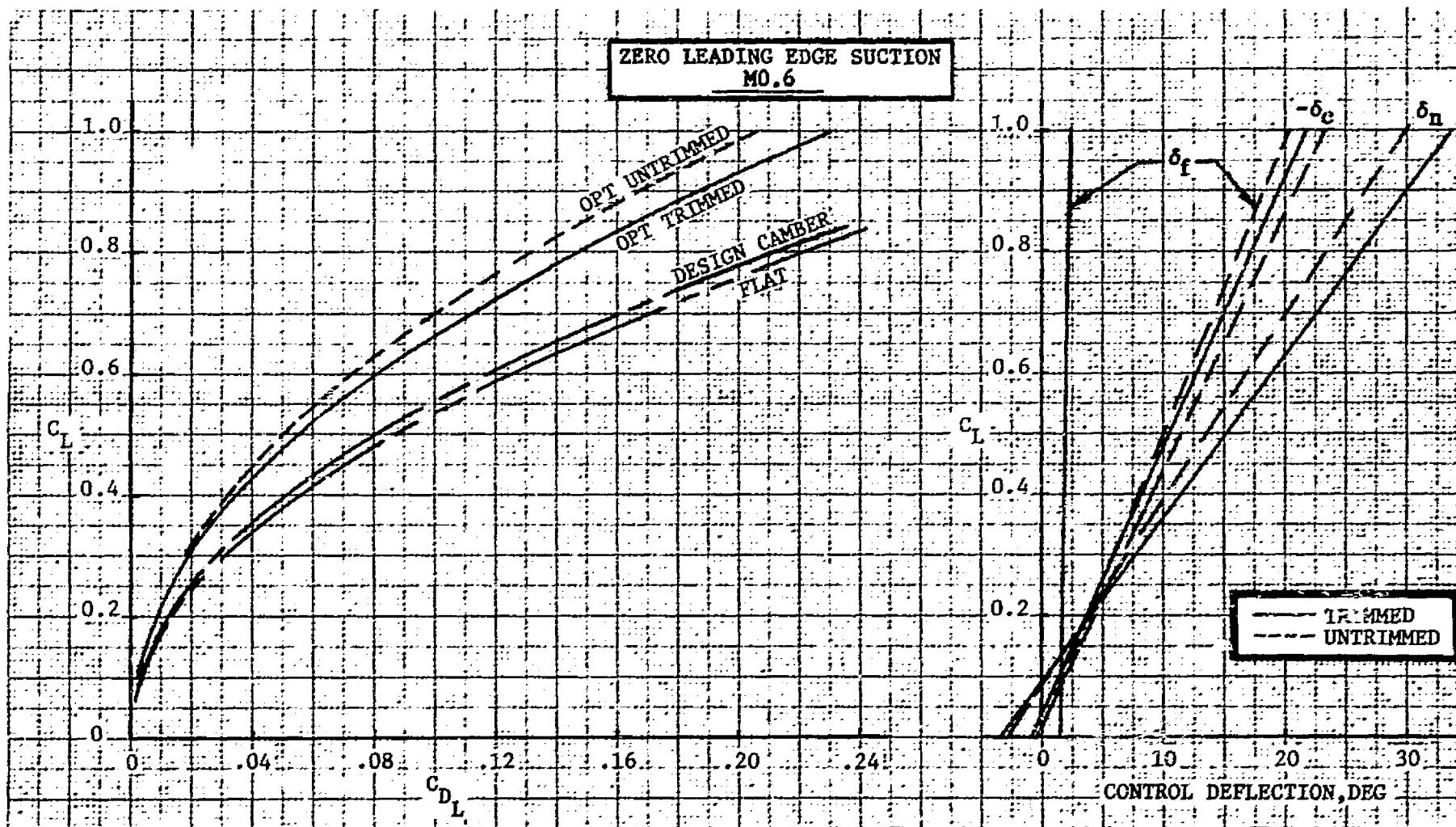


FIGURE 3-31. DRAG DUE TO LIFT

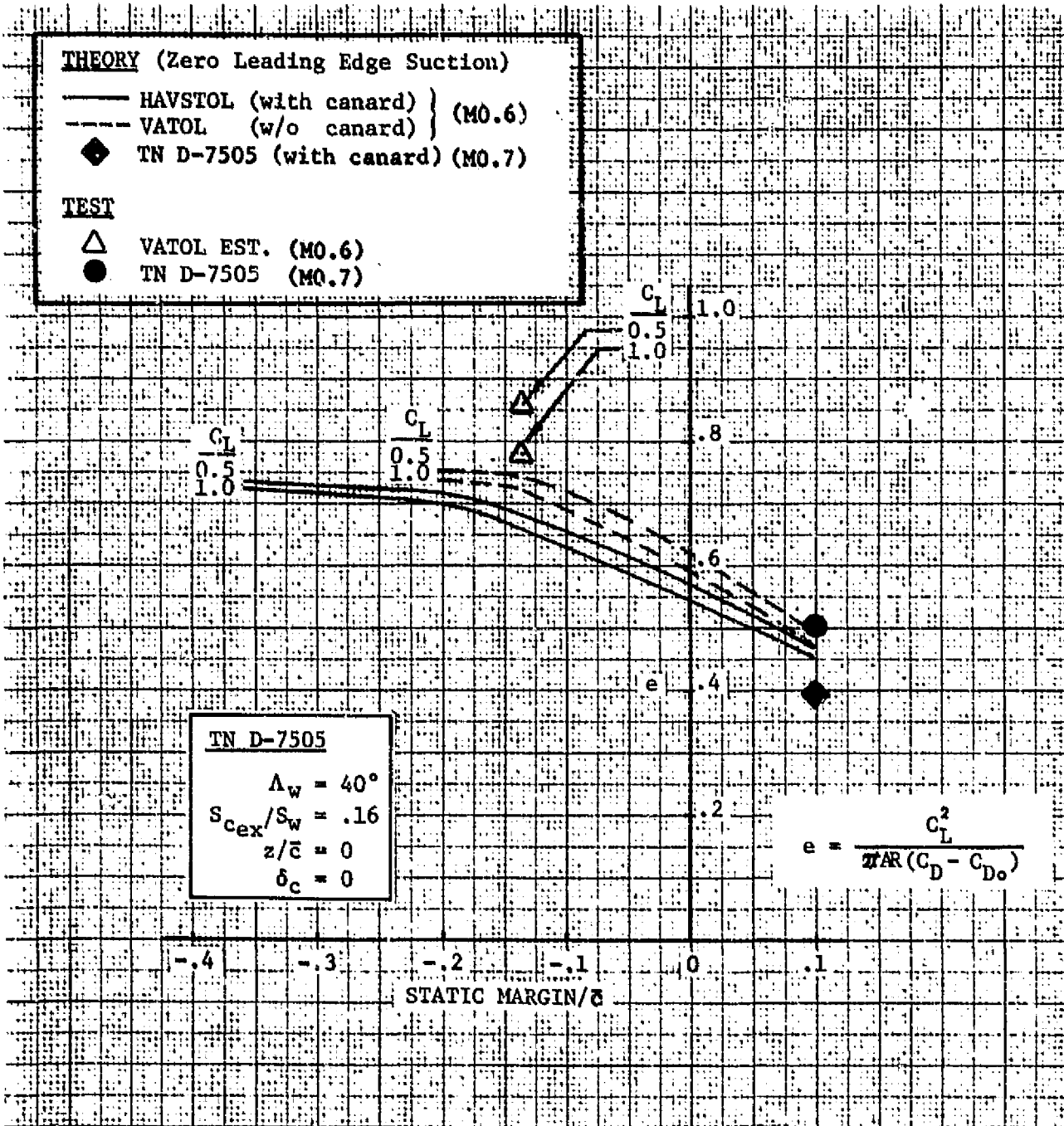


FIGURE 3-32. SPANLOAD EFFICIENCY VS STATIC MARGIN

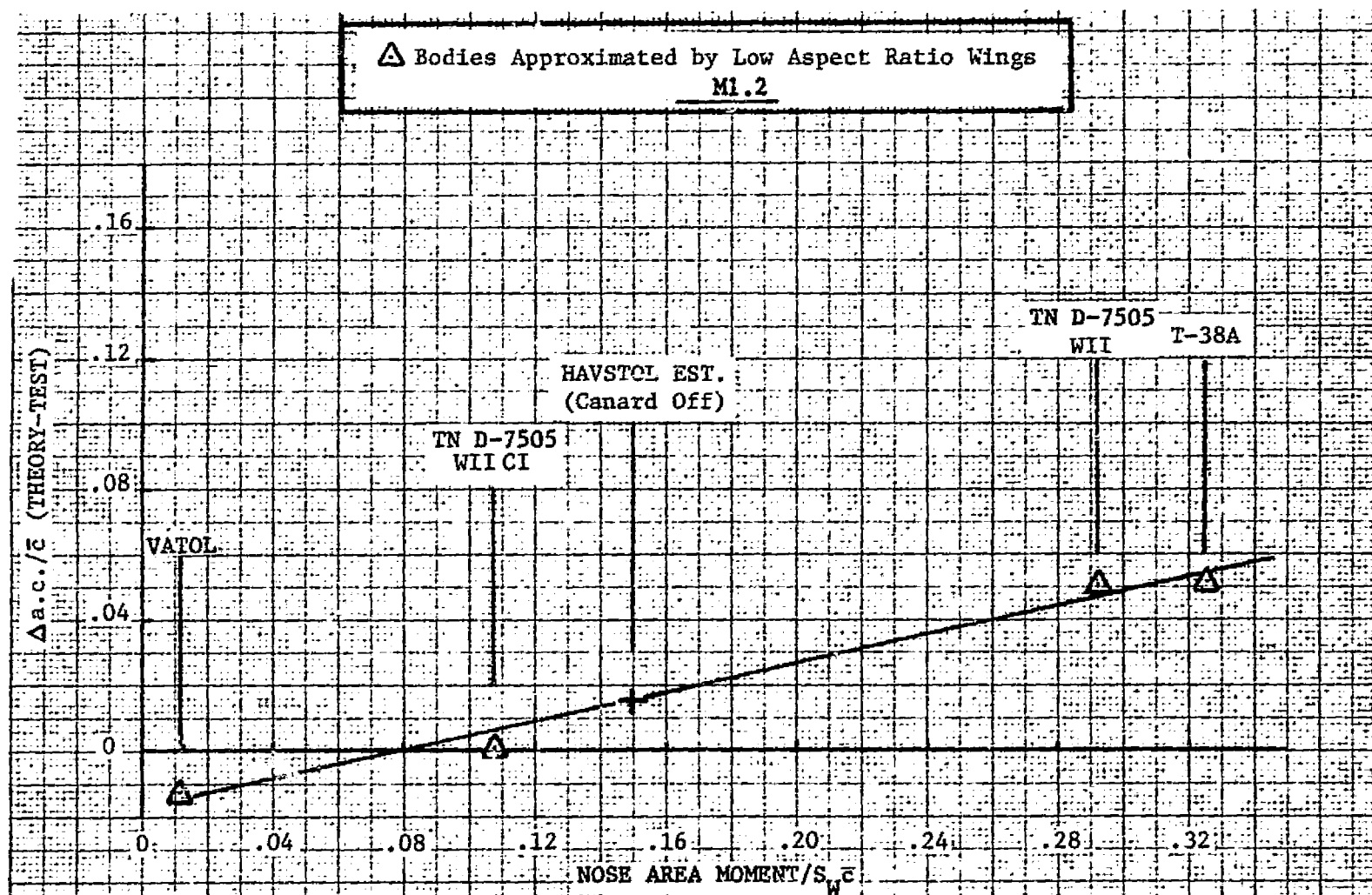
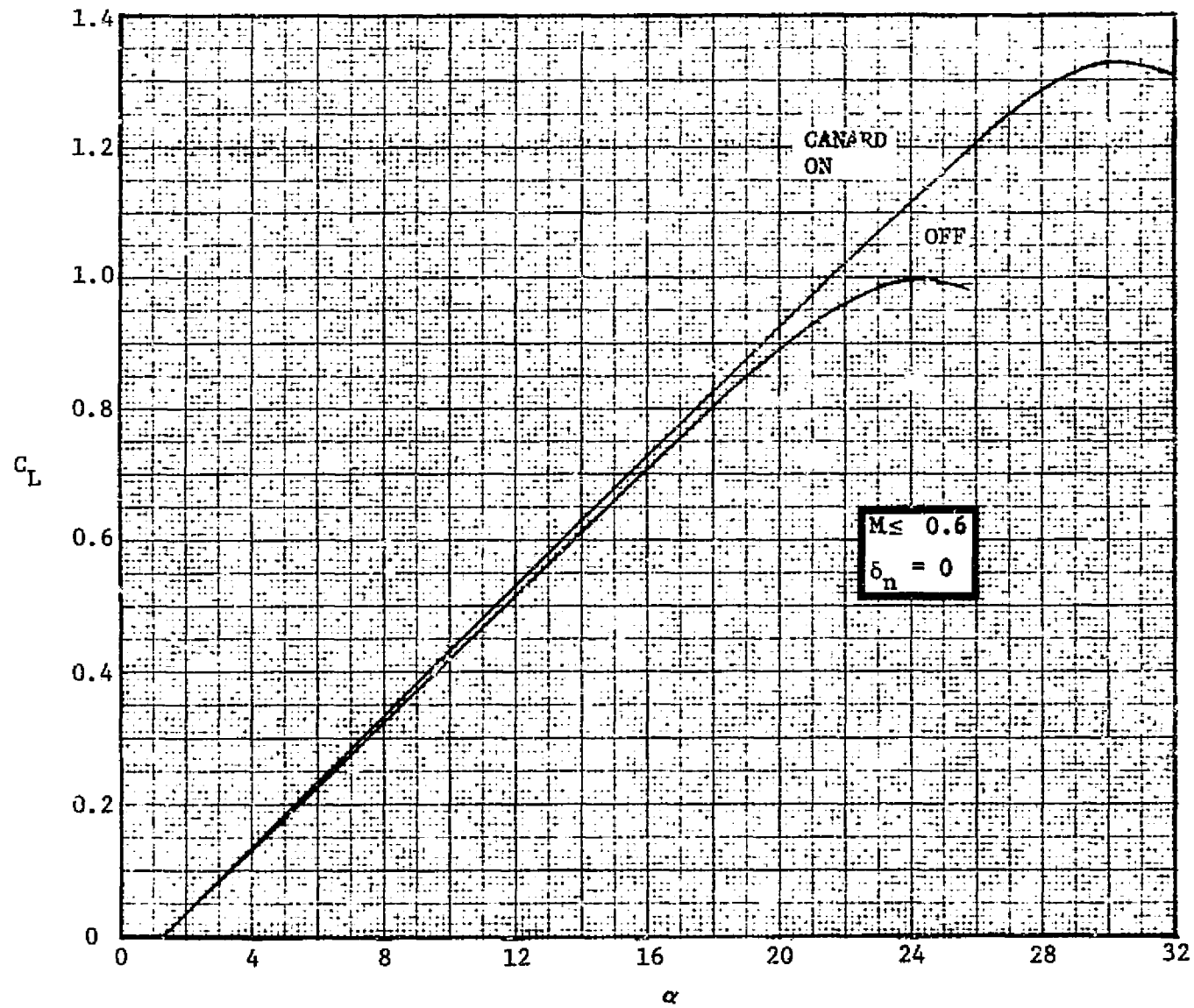


FIGURE 3-33. AERODYNAMIC CENTER ERROR VS NOSE AREA MOMENT COEFFICIENT

FIGURE 3-34. CANARD EFFECTS ON LIFT AT  $M \leq 0.6$

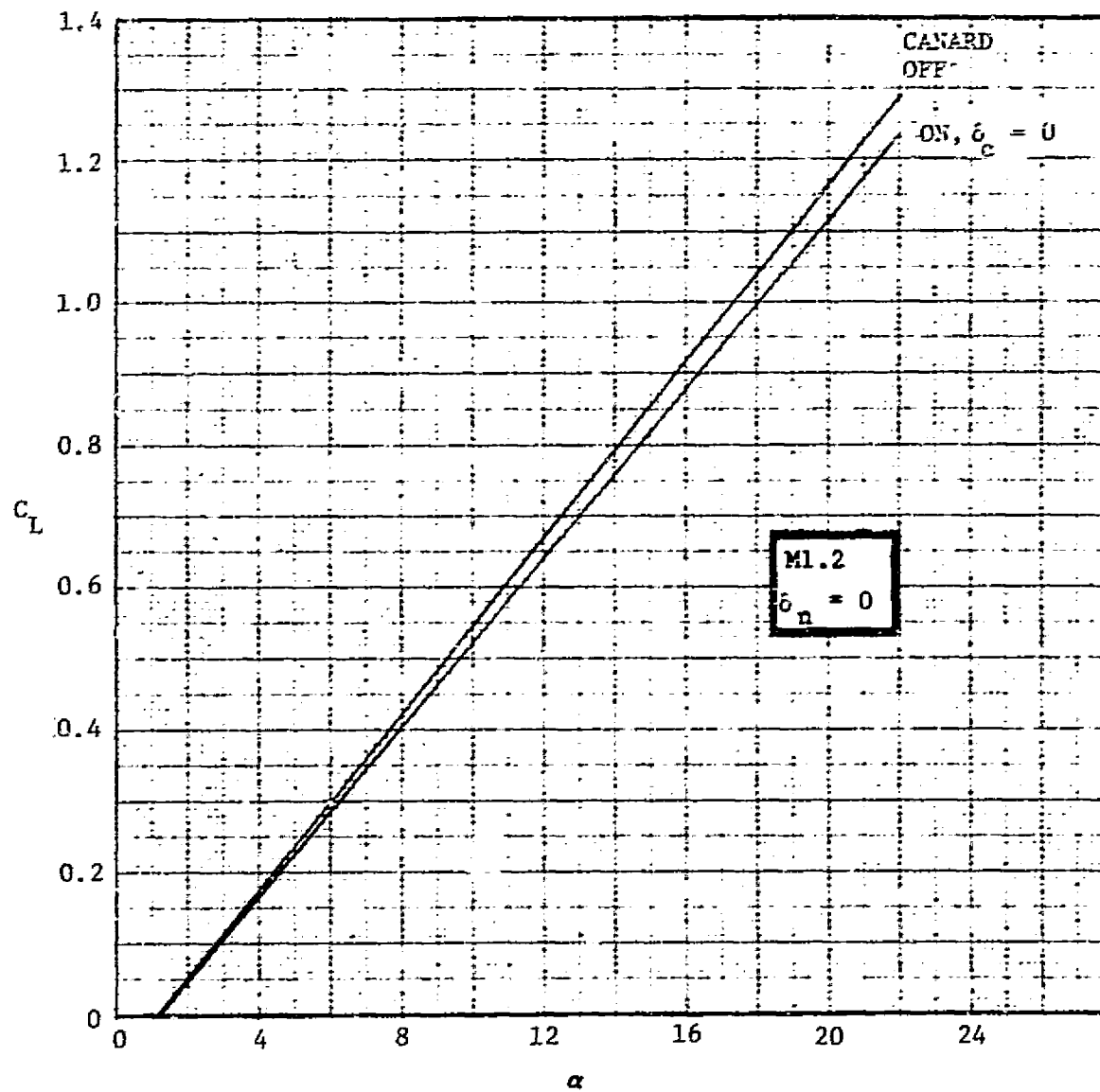
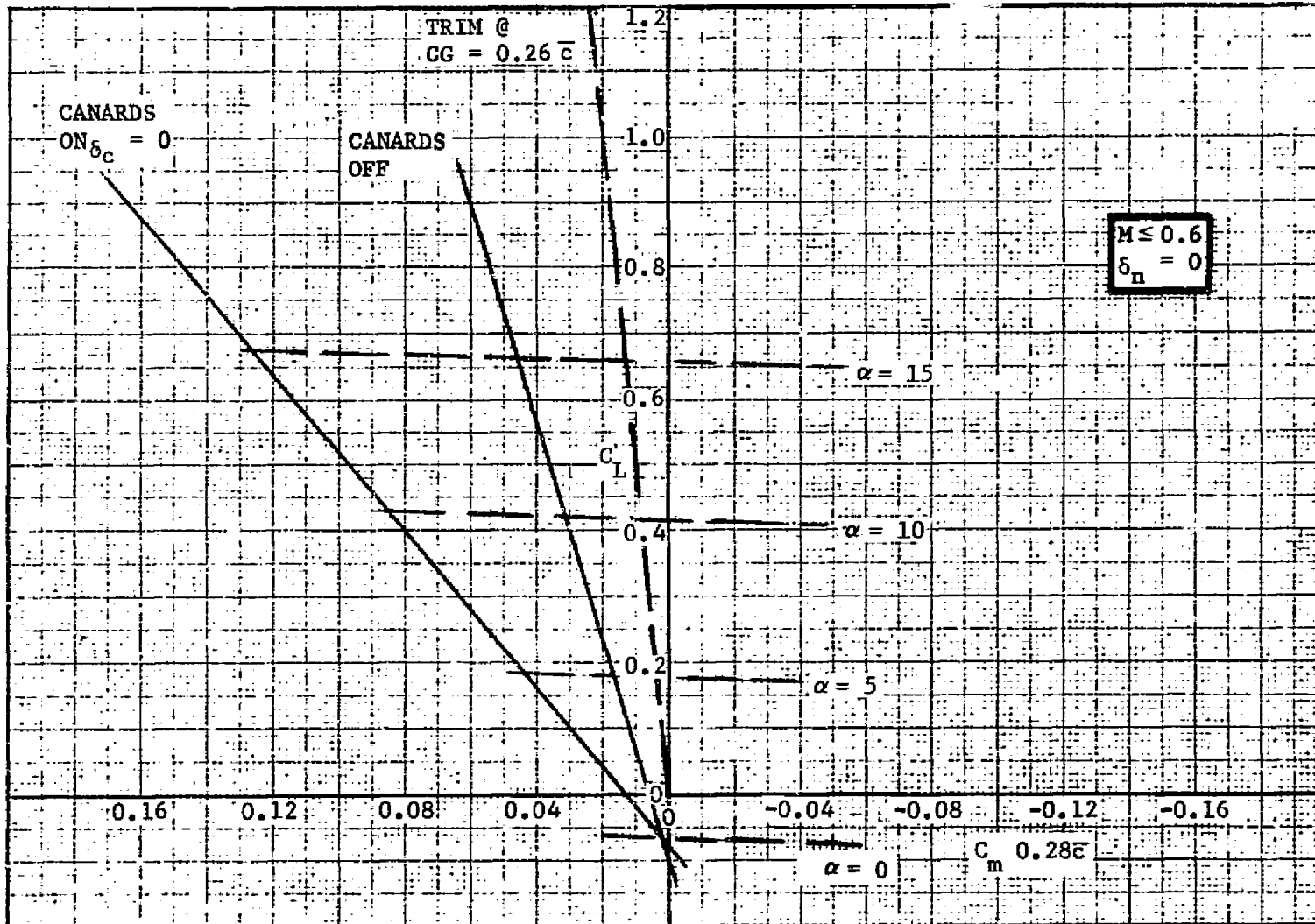


FIGURE 3-35. CANARD EFFECTS ON LIFT AT M1.2

FIGURE 3-36. CANARD EFFECTS ON STATIC STABILITY AT  $M \leq 0.6$

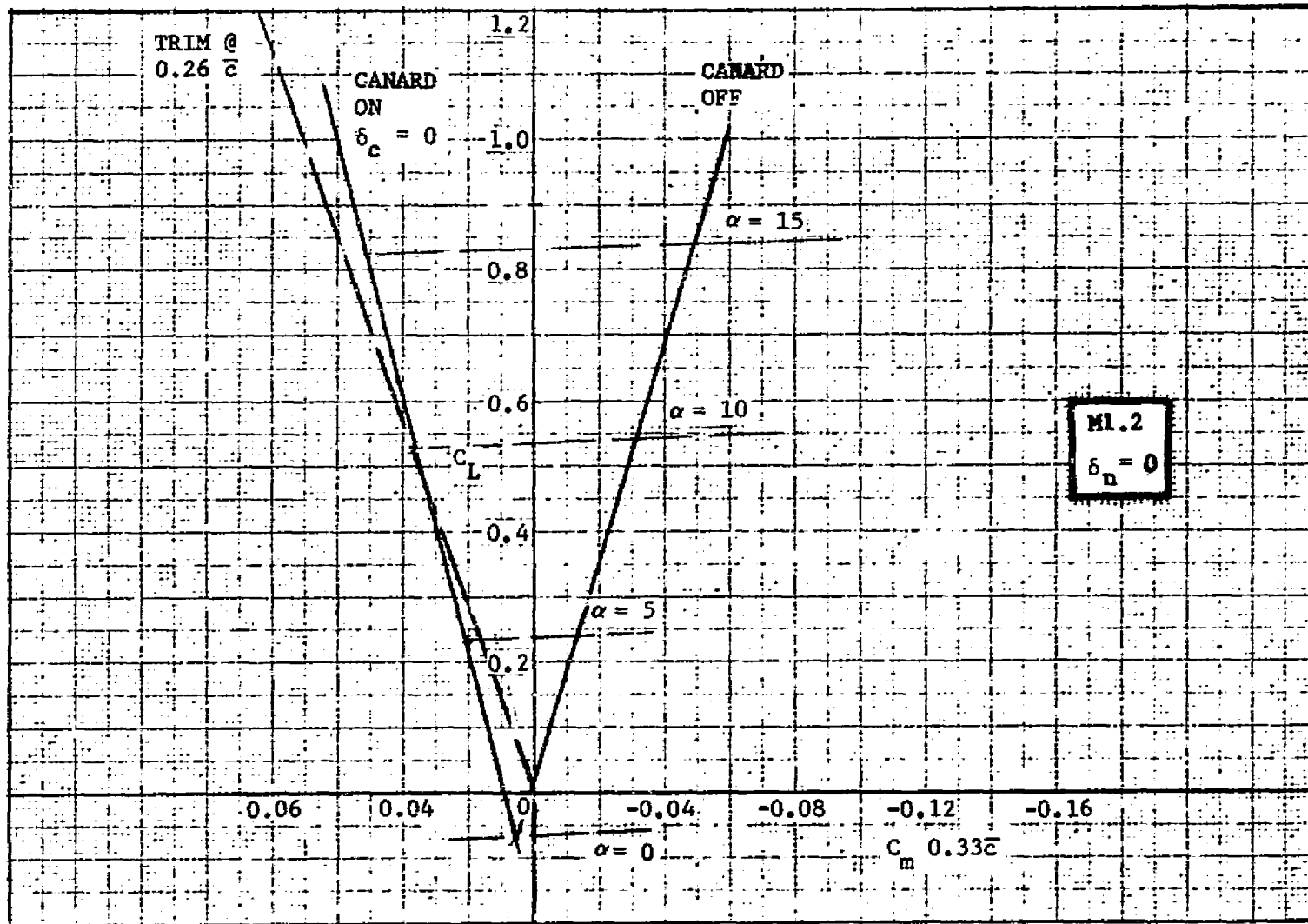


FIGURE 3-37. CANARD EFFECTS ON STATIC STABILITY AT M1.2

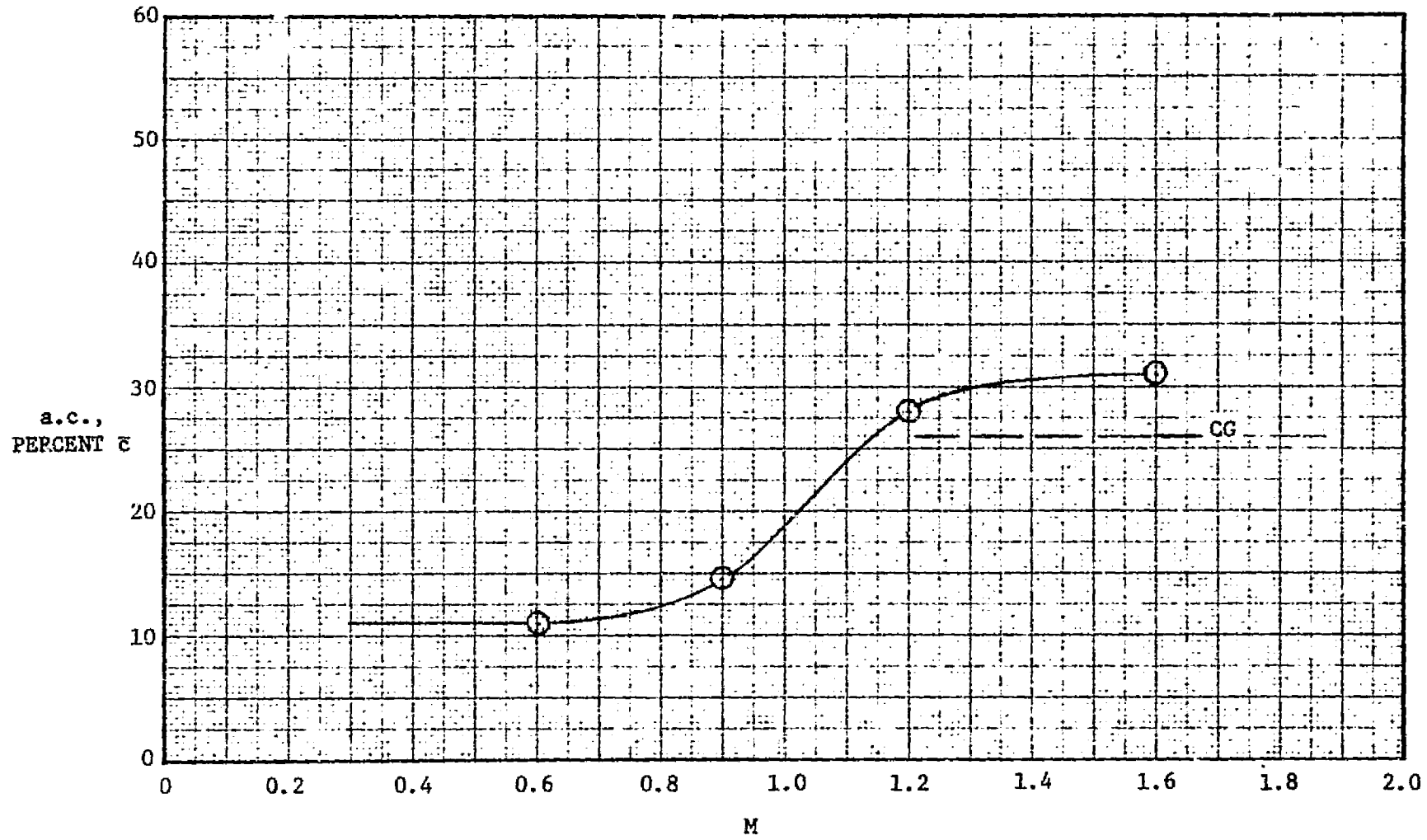


FIGURE 3-38. AERODYNAMIC CENTER LOCATION

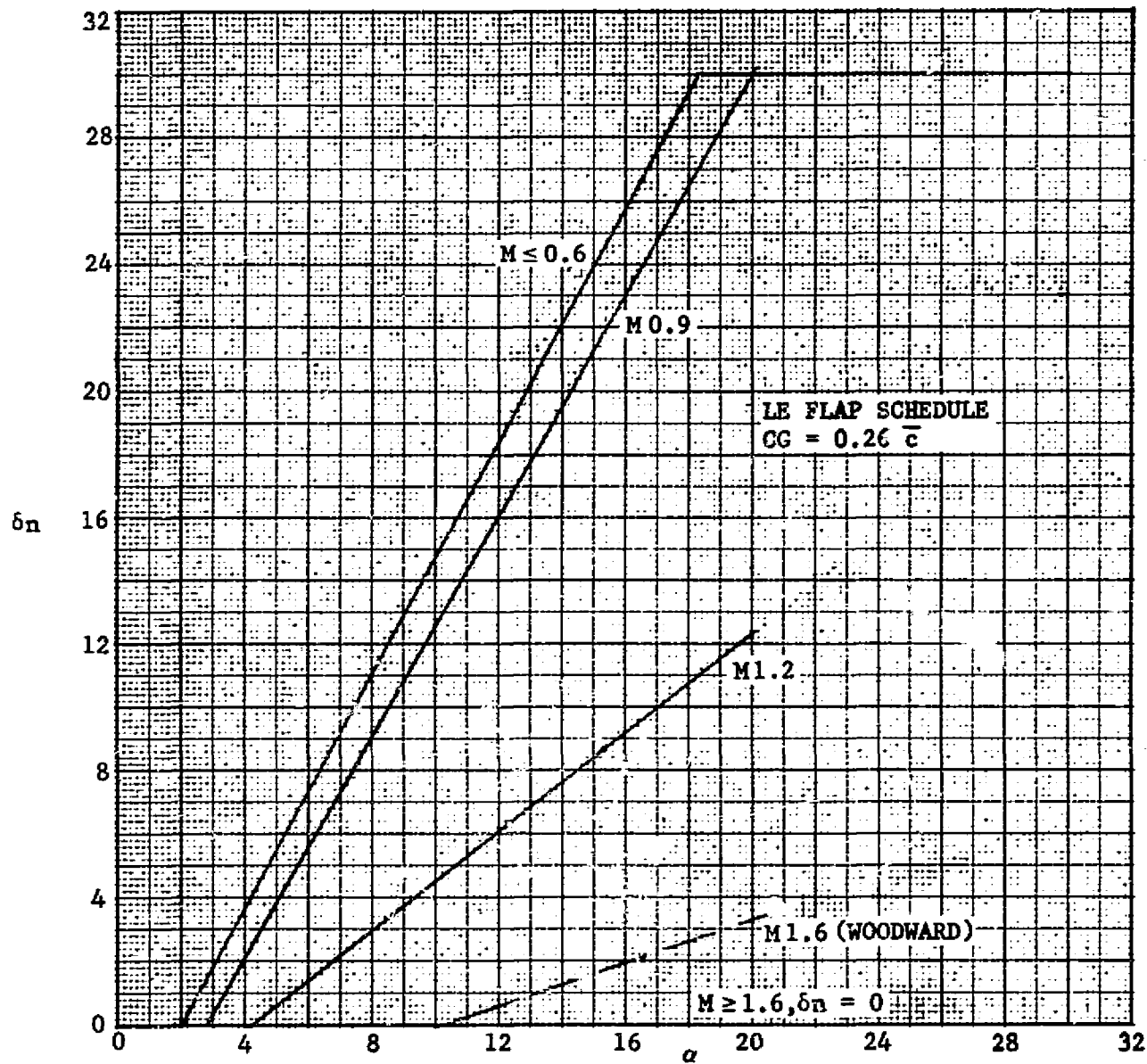


FIGURE 3-39. LEADING EDGE FLAP SCHEDULE,  $CG=0.26 \bar{c}$

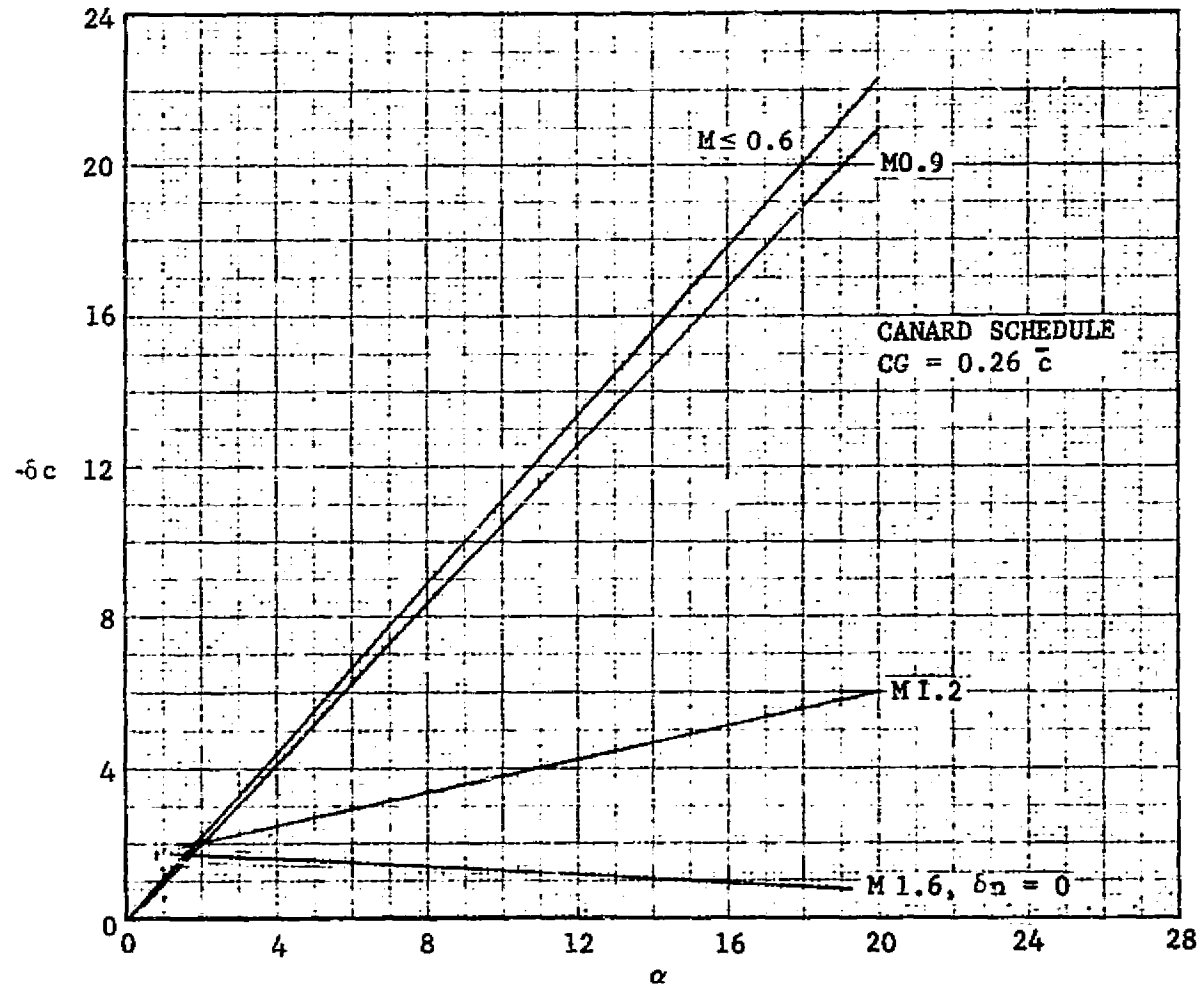


FIGURE 3-40. CANARD DEFLECTION SCHEDULE,  $CG=0.26 \bar{c}$

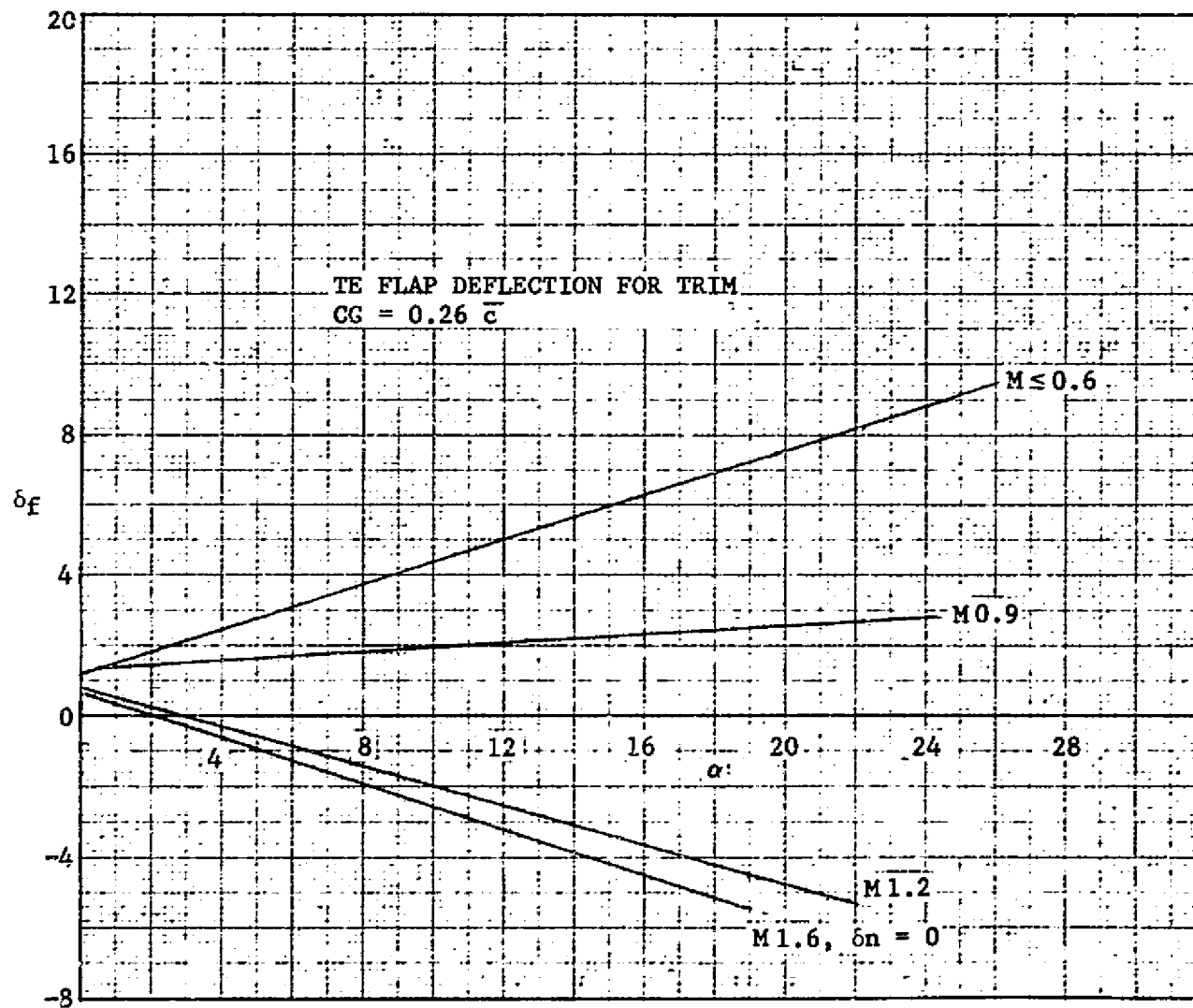


FIGURE 3-41. OPTIMUM TRAILING EDGE FLAP DEFLECTION FOR TRIM

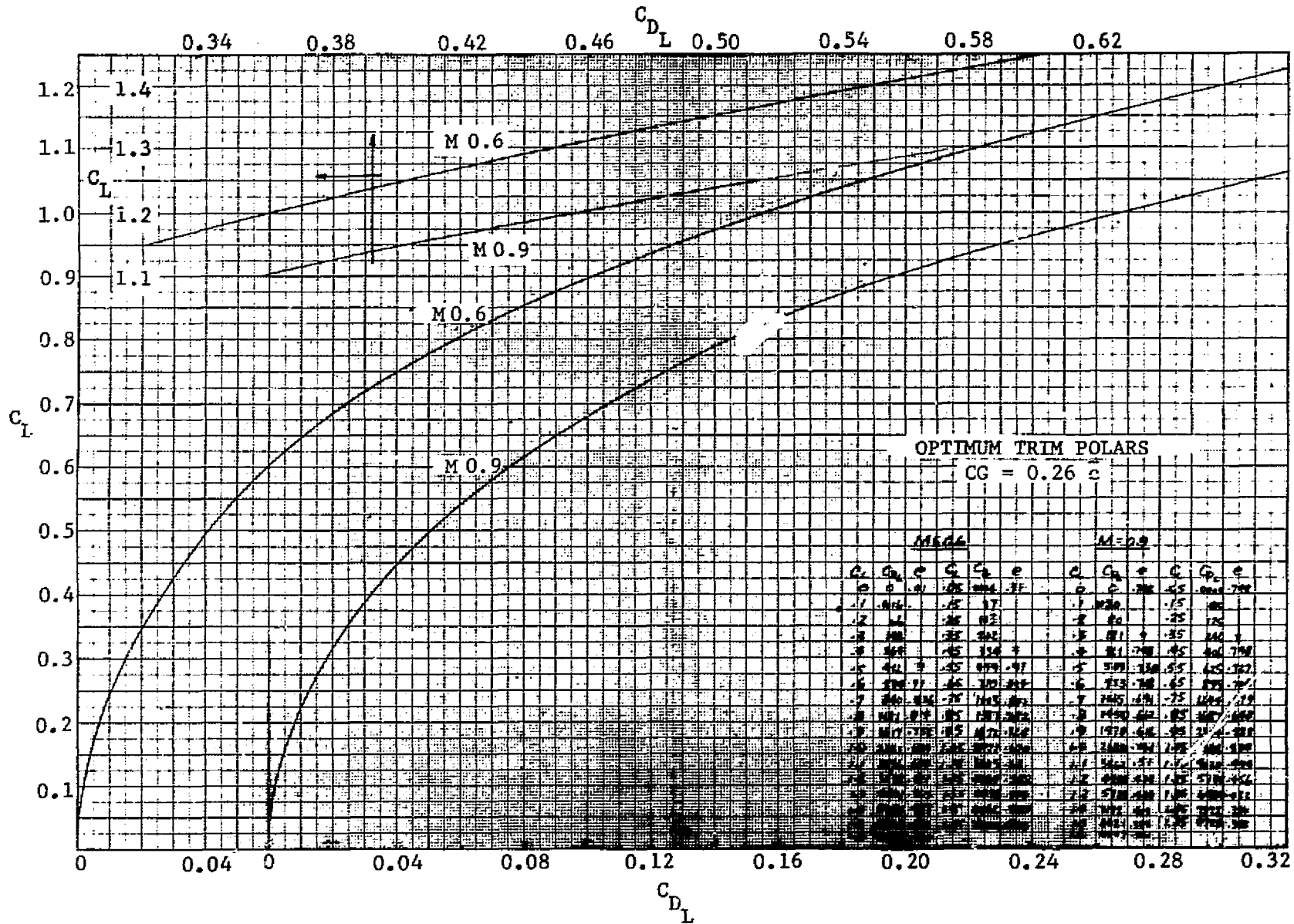


FIGURE 3-42. OPTIMUM SUBSONIC TRIM POLARS

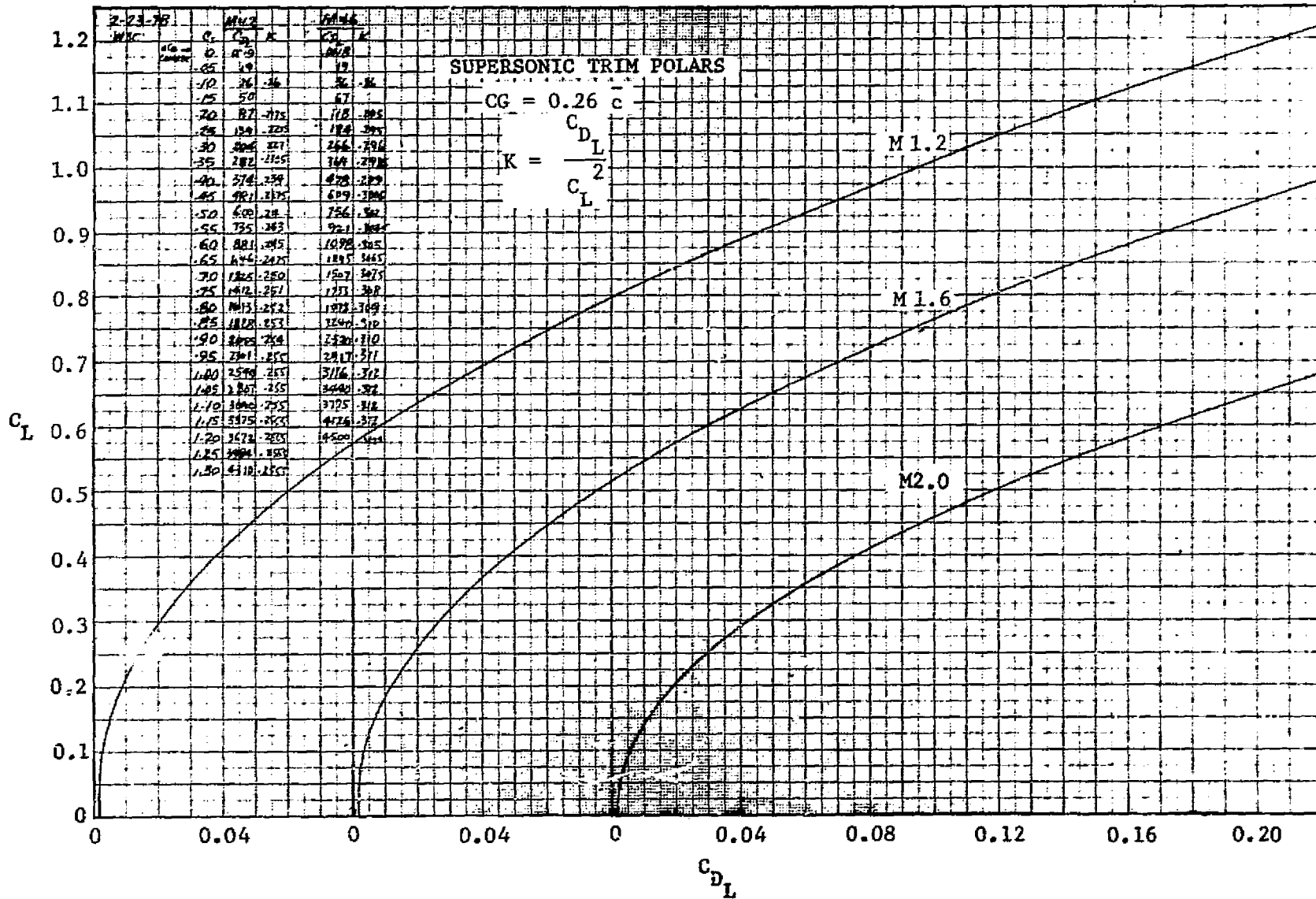


FIGURE 3-43. OPTIMUM SUPERSONIC TRIM POLARS

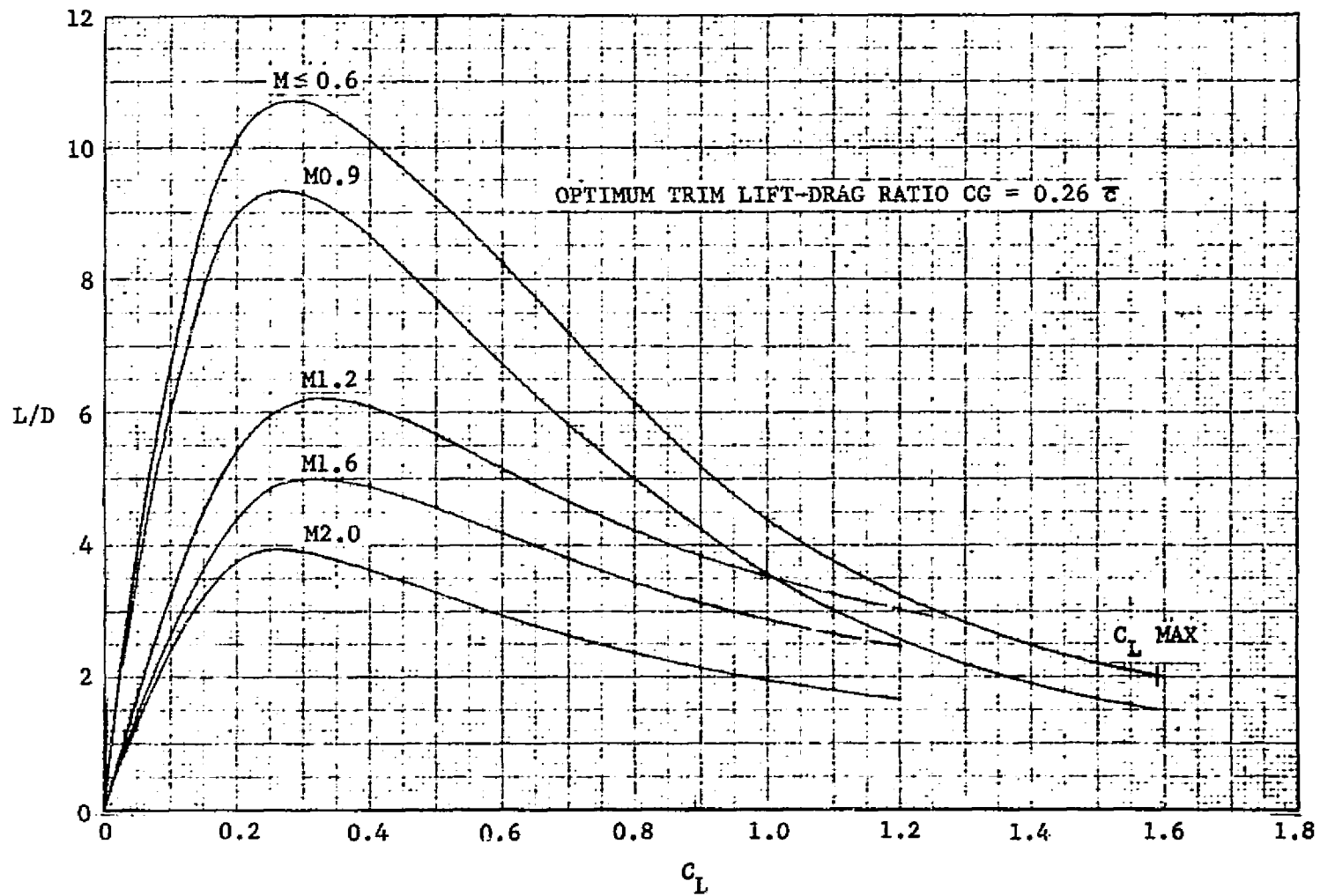


FIGURE 3-44. TRIM LIFT-DRAG RATIO

ORIGINAL PAGE IS  
OF POOR QUALITY

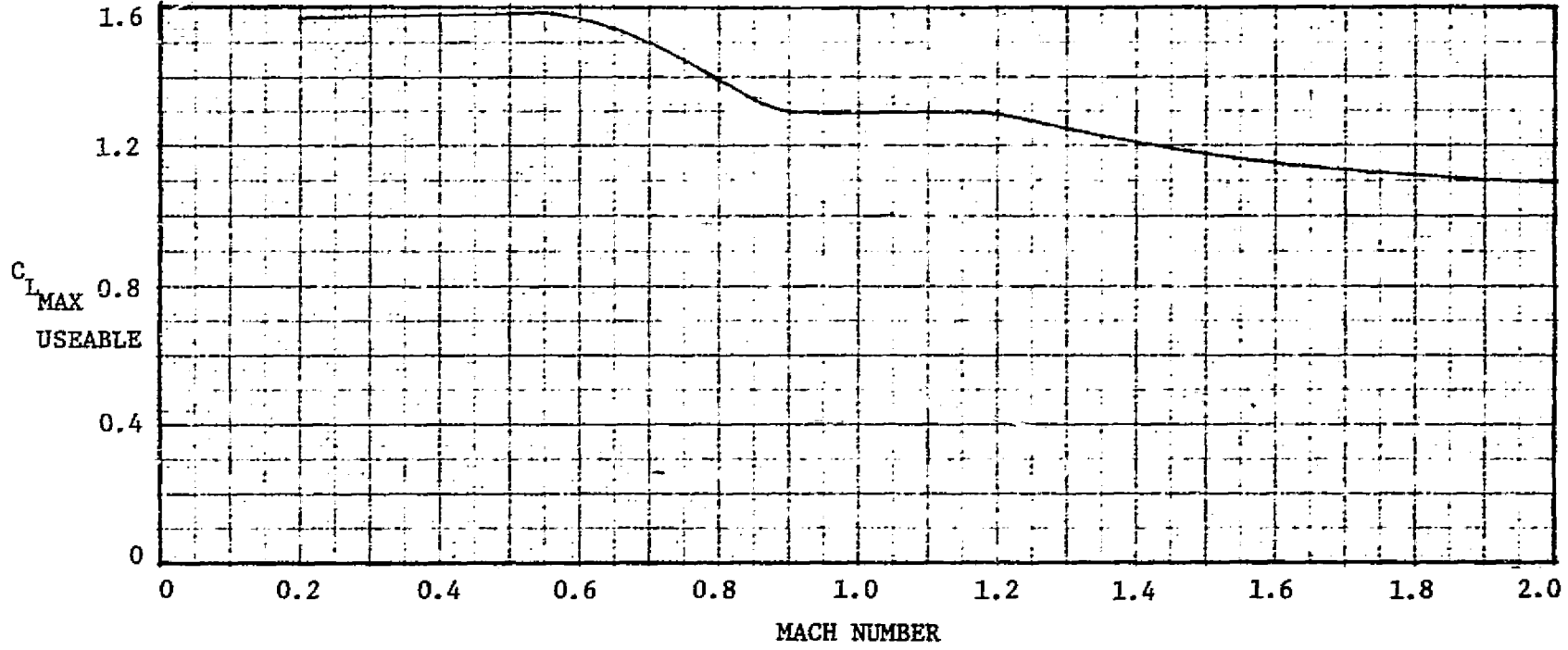


FIGURE 3-45. MAXIMUM USEABLE LIFT

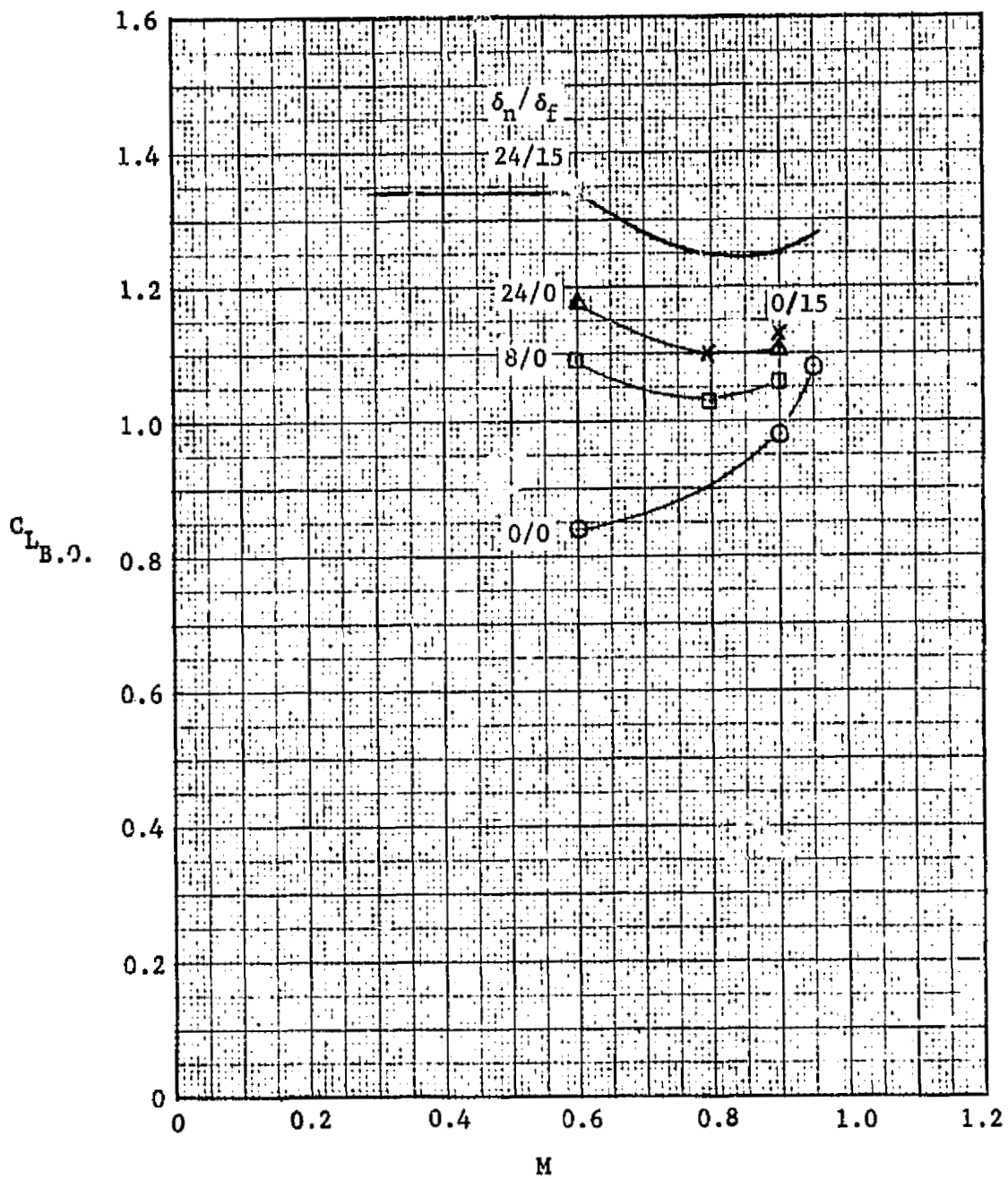


FIGURE S-46. LIFT COEFFICIENT FOR BUFFET ONSET

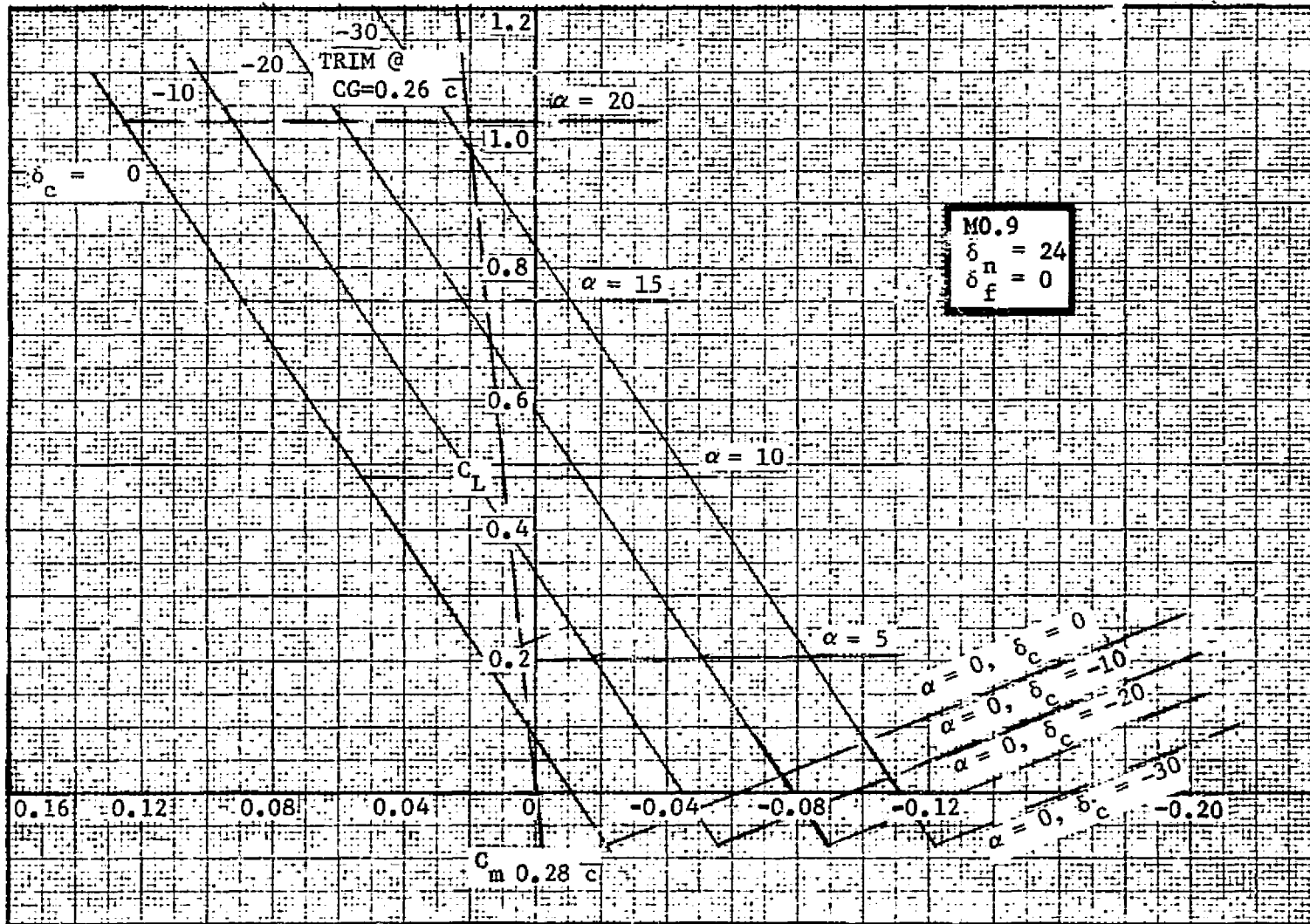


FIGURE 3-47. CANARD EFFECTIVENESS AT  $MO.9, \delta_n=24, \delta_f=0$

ORIGINAL PAGE IS  
OF POOR QUALITY

3-64

C.2

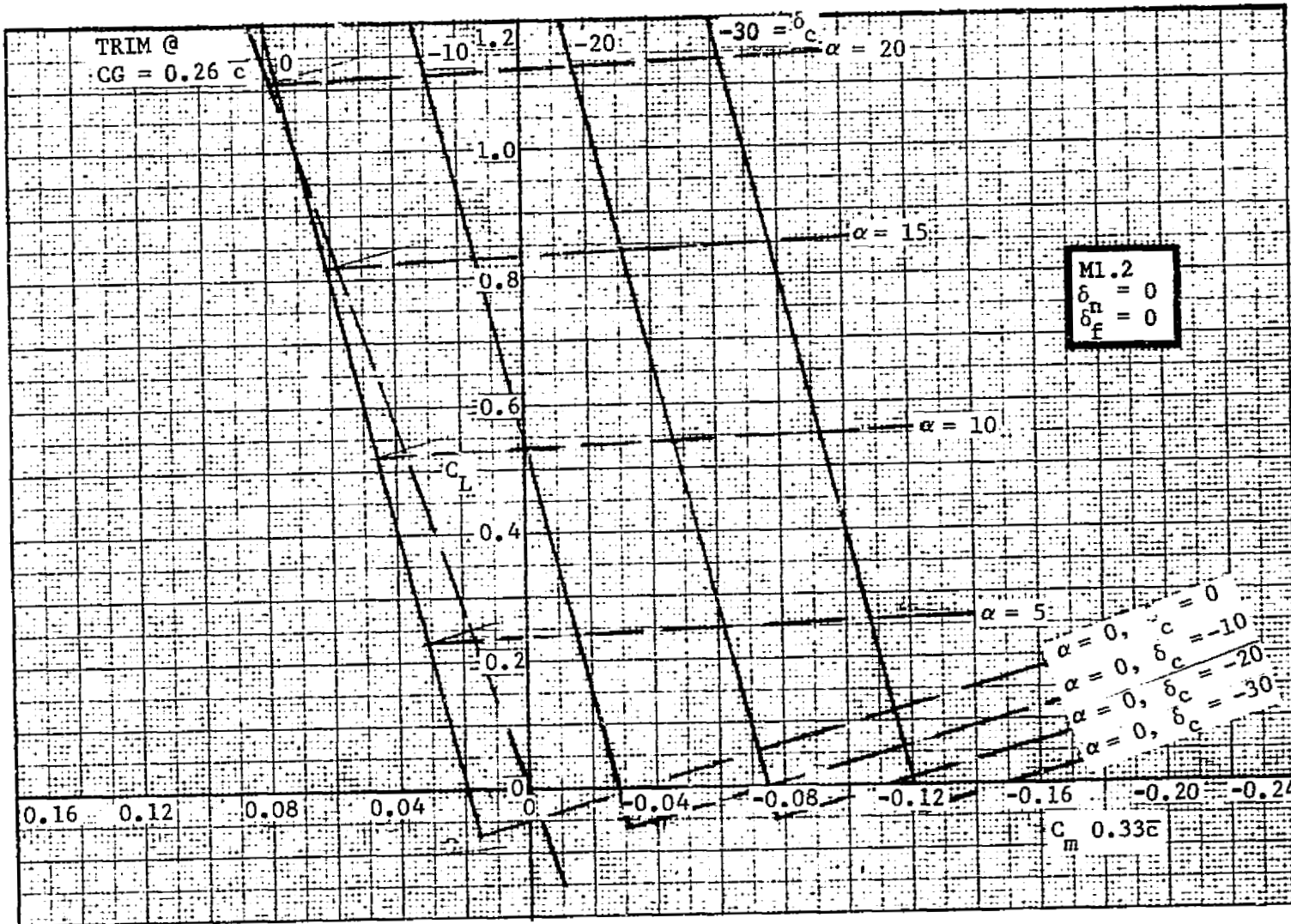


FIGURE 3-48. CANARD EFFECTIVENESS AT  $M 1.2, \delta_n=0, \delta_f=0$

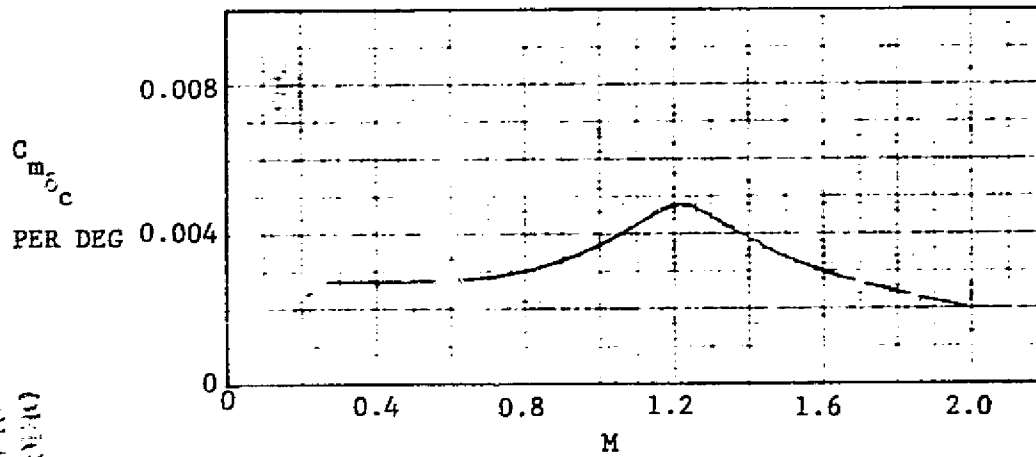
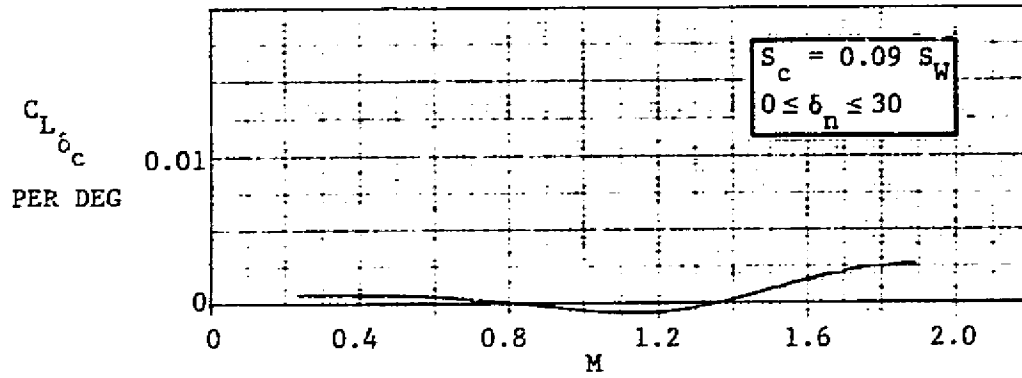


FIGURE 3-49. CANARD CONTROL EFFECTIVENESS

ORIGINAL PAGE IS  
OF POOR QUALITY

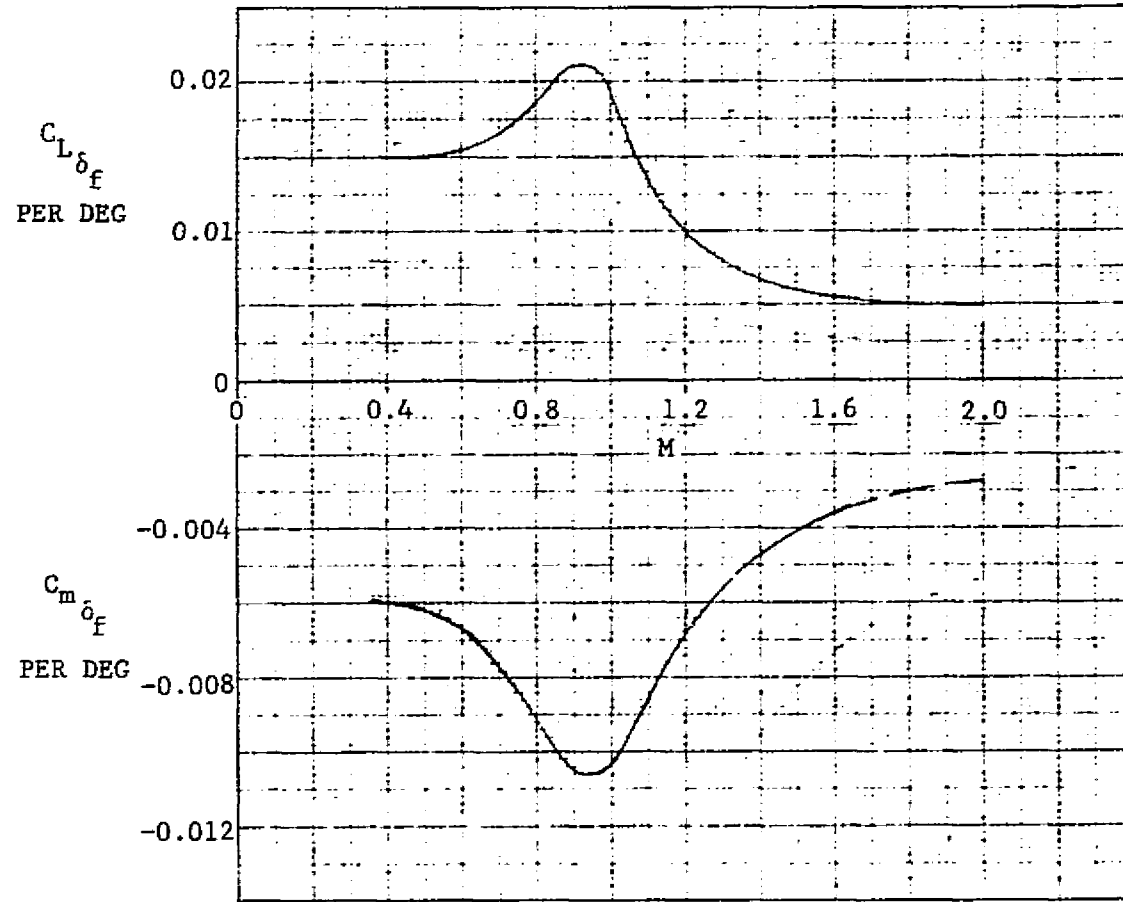


FIGURE 3-50. TRAILING EDGE FLAP CONTROL EFFECTIVENESS

ORIGINAL PAGE IS  
OF POOR QUALITY

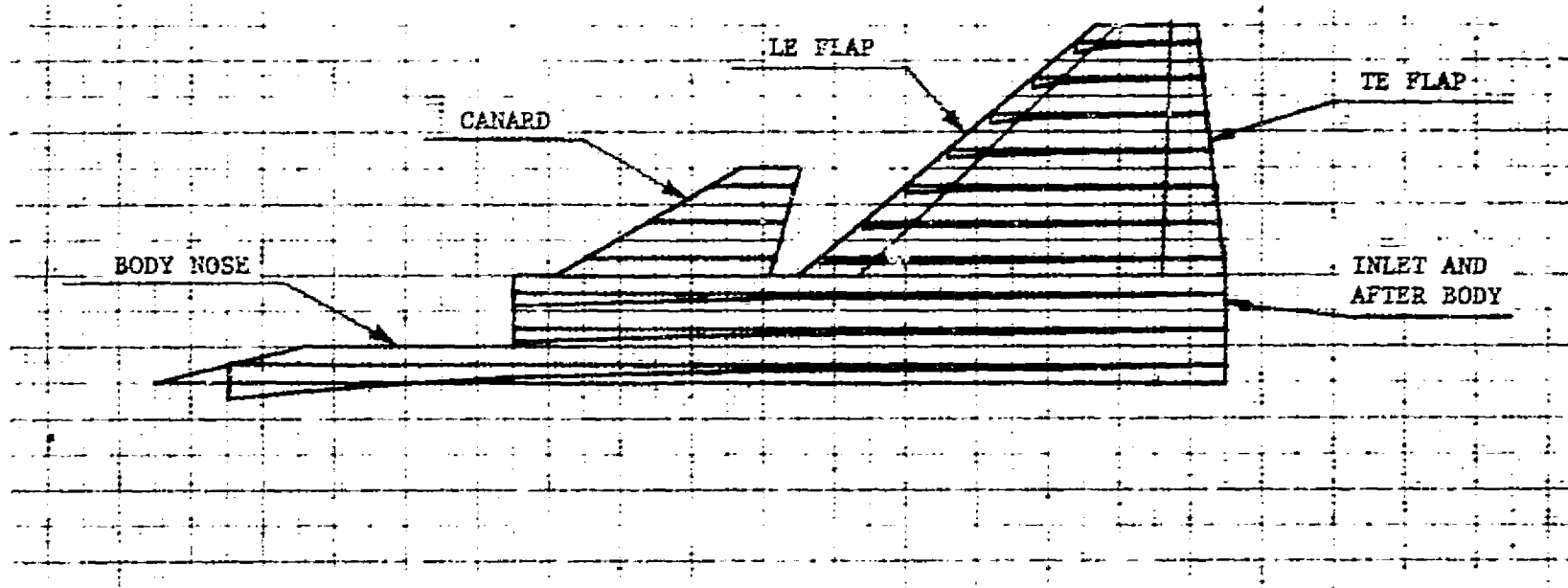


FIGURE 3-51. GEOMETRY MODEL FOR AERODYNAMIC ANALYSIS

ORIGINAL DOCUMENT  
SERIALIZED BY SP-1000 JEN/10/10

### 3.3 LATERAL/DIRECTIONAL ANALYSIS

#### 3.3.1 Lateral/Directional Stability

The coefficients and derivatives presented in this section are essentially derived from wind tunnel test data. The data presented in this section are based on body axes, and are referenced to a moment center at  $0.26\bar{c}$ , and are for a rigid aircraft.

A Northrop transonic wind tunnel test (Reference 7) of a tailless design having the same wing planform and a very similar vertical tail planform compared to the HAVSTOL configuration, was used as a data base which was suitably modified by theory to obtain the estimated lateral/directional data. The test body characteristics,  $\Delta C_Y$  and  $\Delta C_n$ , as a function of  $\alpha$  and  $\beta$ , were estimated and subtracted from the wing body test data. The body-alone  $\Delta C_l$  was assumed negligible (body axes). The HAVSTOL body characteristics were similarly estimated and added back in. The body estimation procedure used modified incremental slender body theory, a technique which has been found to give reasonable approximations in most cases. A self-correcting tendency is inherent in the process just described, provided consistency in the body estimation details is maintained. The wind tunnel test model was nominally a midwing configuration with zero dihedral. Corrections were made to HAVSTOL for the shoulder wing location and five degrees of anhedral, using standard DATCOM procedures.

The vertical tail effects were then estimated, using the test data modified by moment area relationships, and added to the wing body estimates. The effects of the canard surface are difficult to estimate in the absence of specifically applicable test data because of the strong aerodynamic interrelationship of the canard, wing and vertical tail surfaces. The literature shows examples of both positive and negative lateral/directional stability effects due to the addition of a canard surface. For the twin tail configuration, it was assumed that the lateral/directional stability would fall off less rapidly in the presence of the canard surface than without it at angles of attack above twenty degrees. This beneficial effect may require wind tunnel investigation, particularly with regard to vertical tail location.

Wind tunnel test data were available as a base for M 0.6, 0.8, and 1.2, but not at 1.6. As a result the data had to be extrapolated to M 1.6, using trends characteristic of delta wing airplanes, and are therefore not as well substantiated at M 1.6 as at the other Mach numbers.

The static lateral/directional parameters  $C_Y$ ,  $C_n$  and  $C_l$  are plotted at constant angles of attack versus sideslip angle for  $M$  0.6, 0.9, 1.2 and 1.6 in Figures 3-52 through 3-63. Each figure shows the configuration with the vertical tails off (WB) and on (WBCV). In the case of the vertical tails off, the canard surface is also off. The controls are fixed at zero deflection angle in these figures, but will in fact move as required to supplement the aerodynamic stability characteristics via the active control system.

Side force due to sideslip is shown in Figures 3-52 through 3-55. Conventional trends are apparent for the wing-body (WB) and wing-body-canard-vertical tail (WBCV) configurations. The fixed-vertical-tail directional stability of the complete configuration, as seen in Figures 3-56 through 3-59, is positive for the range of Mach numbers, angles of attack and sideslip angles considered except at  $M$  0.6 and  $\alpha = 26$  degrees. Adequate aerodynamic directional control is available via the vertical tail to provide apparent stability even at this condition. The corresponding dihedral effect, Figures 3-60 through 3-63, is mostly favorable without the active control system, although the goal of good flying qualities and control harmony will dictate active control system stability inputs.

As a result of the use of electronic adaptive flight control systems, the stability and control characteristics of the aircraft are not as clearly related to the static aerodynamic parameters as they have been for the more conventional control systems. The apparent aircraft stability is, instead, a combined function of the aerodynamic stability, the aerodynamic control power, and the control system mechanization. Angle of attack or sideslip limitations can be designed into the control system to avoid any situation where the aircraft aerodynamics might lead to an uncontrollable condition. This section of the report does not treat the control system, and the reader is referred to Section 5.2.

### 3.3.2 Lateral/Directional Control Effectiveness

Control effectiveness of the elevons and all movable vertical tails was estimated by correcting the wind tunnel test data described in 3.3.1 using moment area relationships. The vertical tails were sized to satisfy an engine failure condition during a conventional takeoff in accordance with the requirements of MIL-F-8785B (ASG). The

cross wind landing requirement of MIL-F-8785B (ASG) was also investigated, but found not critical.

Vertical tail and elevon roll control effectiveness is presented in derivative form versus angle of attack for M 0.6, 0.9, 1.2 and 1.6.

Figures 3-64 through 3-67 present the control power derivatives of the all movable vertical tail. The vertical tail provides good directional control power to high angles of attack at all Mach numbers. The rolling moment due to vertical tail deflection is small.

Elevon roll control power appears in Figures 3-68 through 3-71. The roll control power holds up well to high angles of attack except at M 0.9 and  $\alpha = 26$  degrees where it falls to about 20 percent of its  $\alpha = 0$  value. The yawing moment due to roll control is very small.

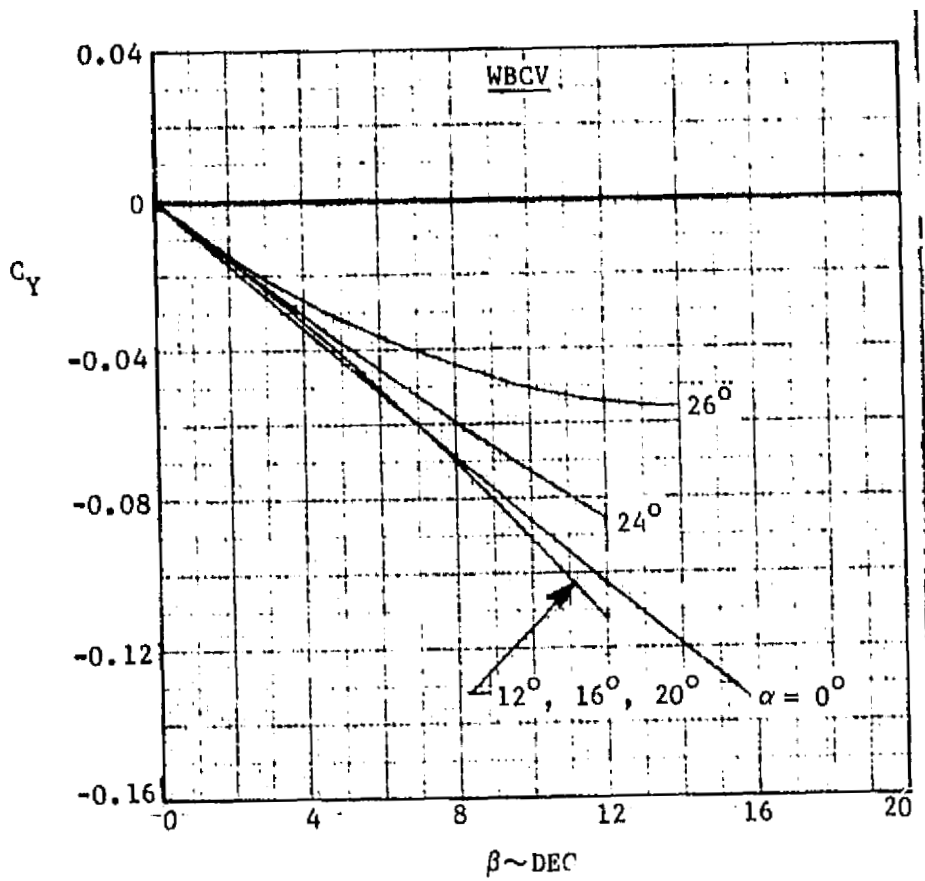
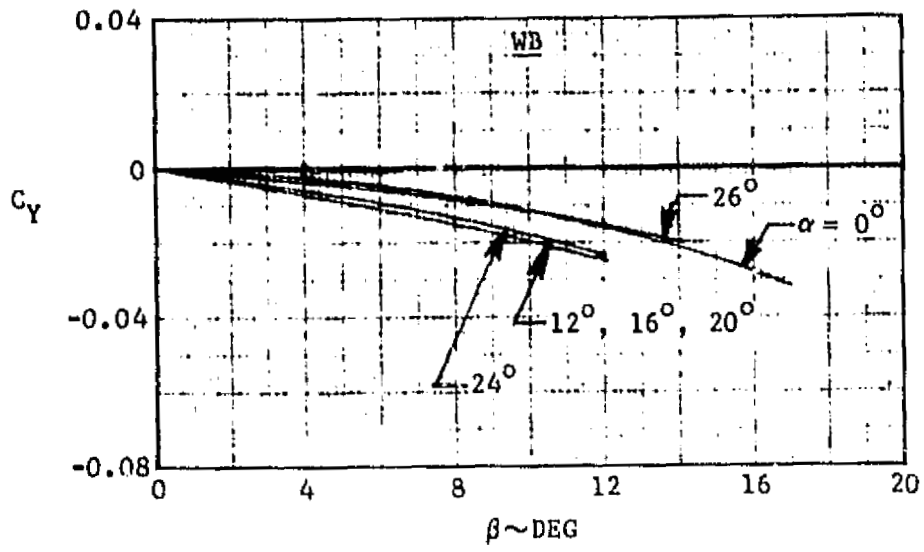


FIGURE 3-52. SIDE FORCE AT M 0.6

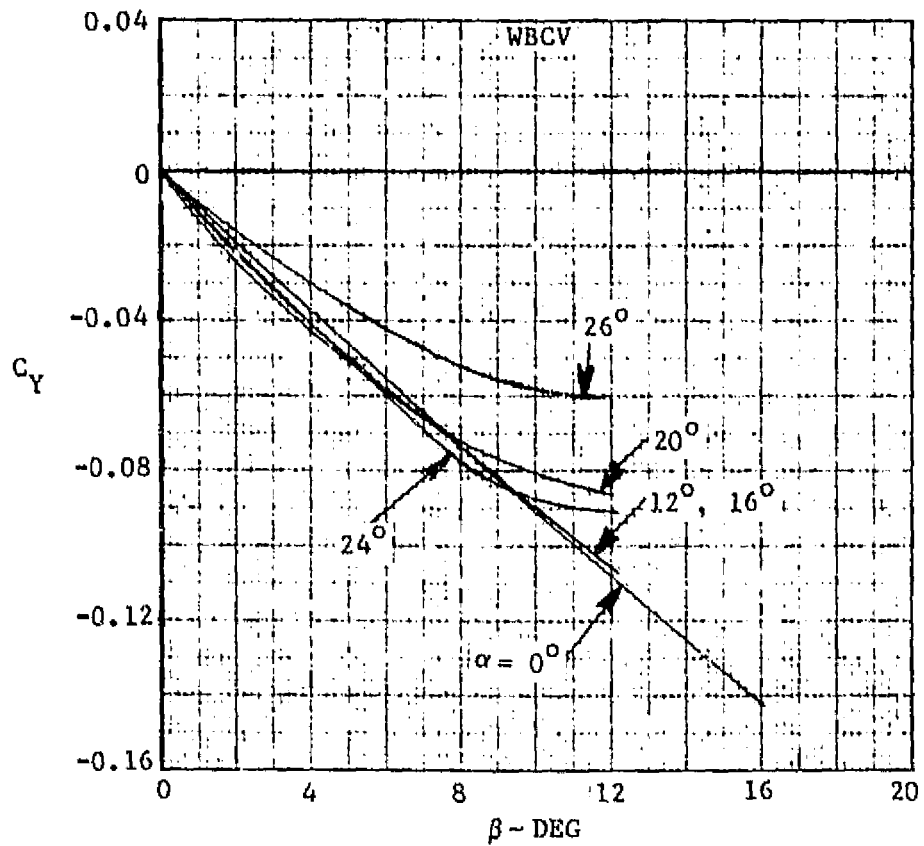
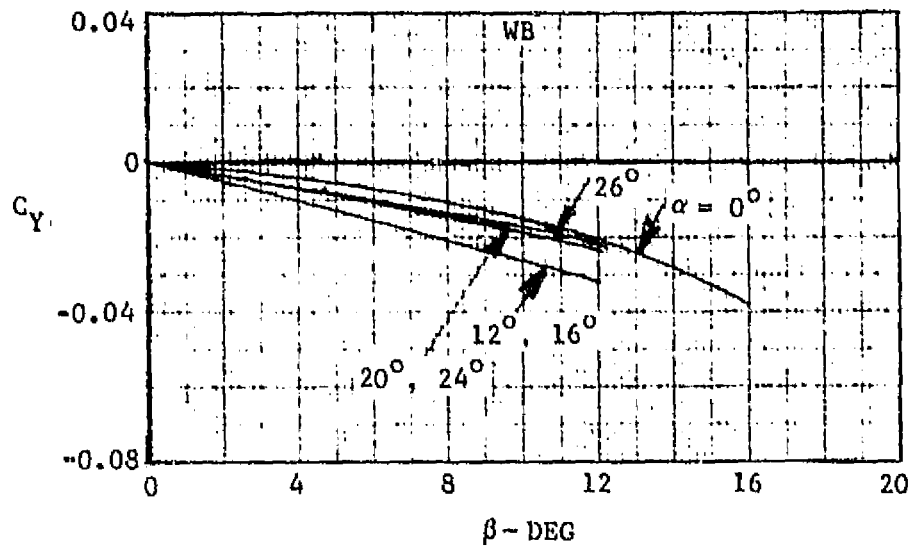


FIGURE 3-53. SIDE FORCE AT M 0.9

ORIGINAL PAGE IS  
OF POOR QUALITY

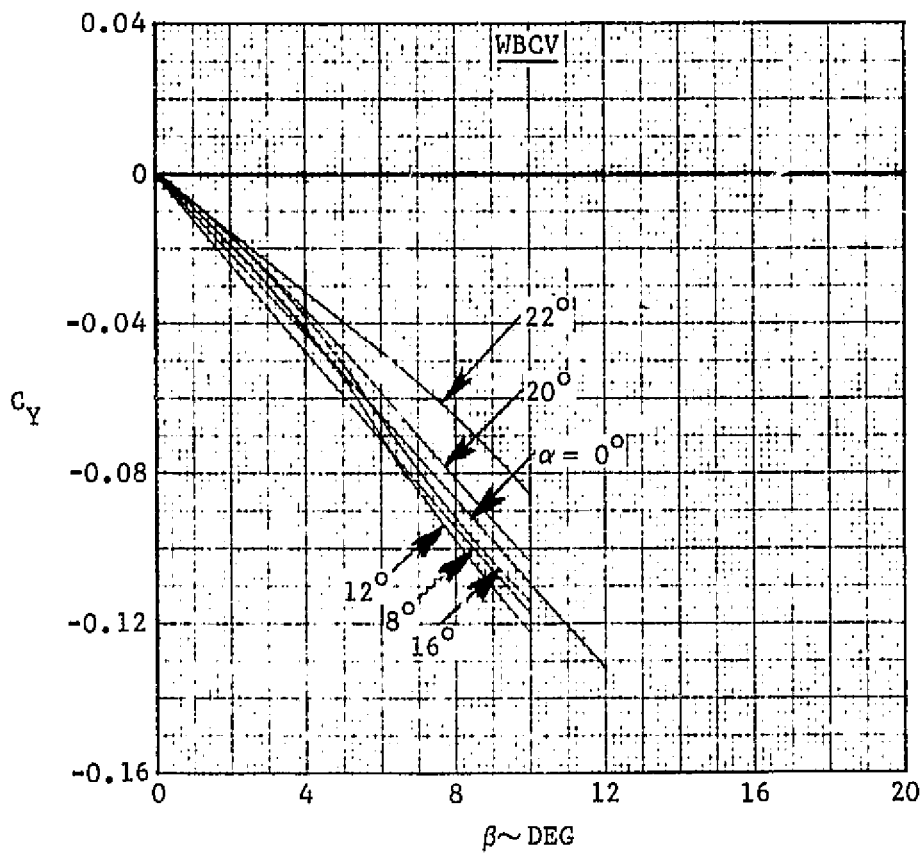
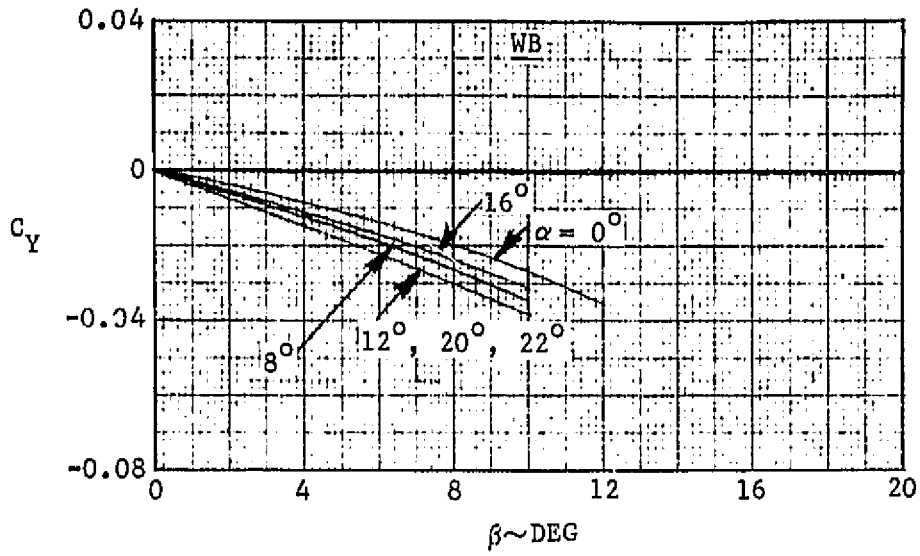


FIGURE 3-54. SIDE FORCE AT M 1.2

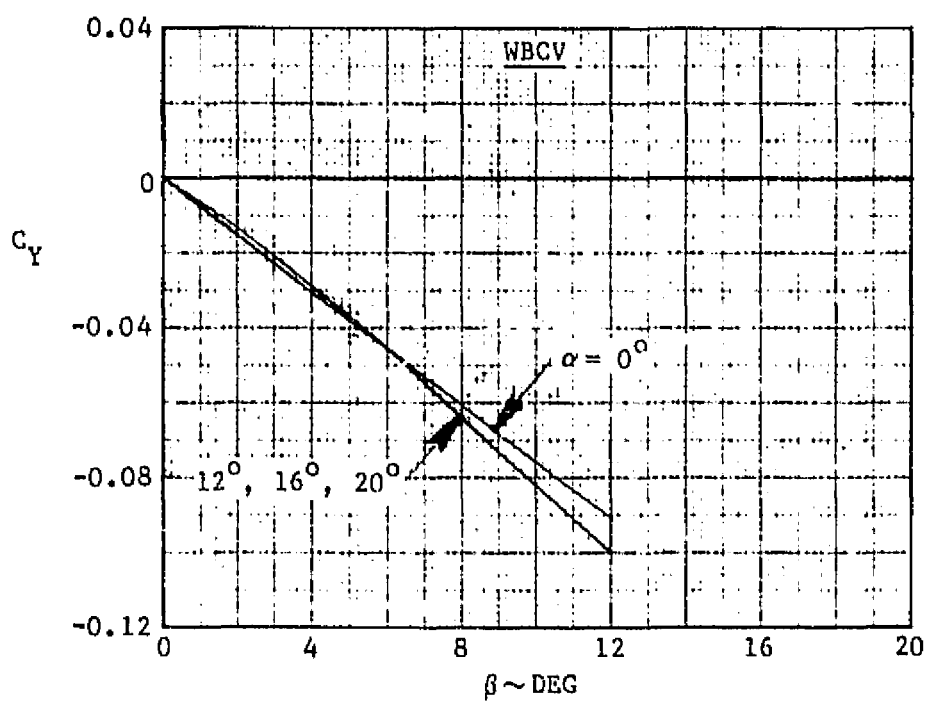
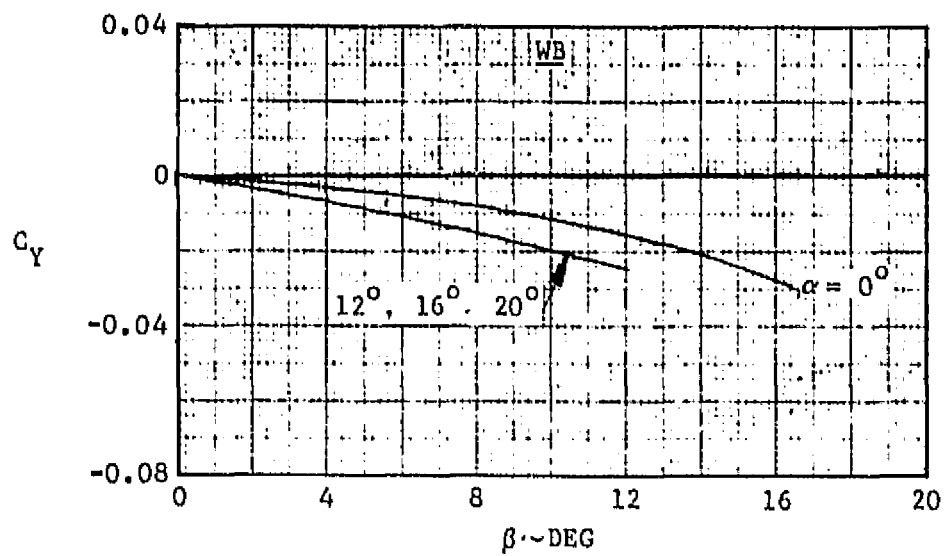


FIGURE 3-55. SIDE FORCE FROM 1.6

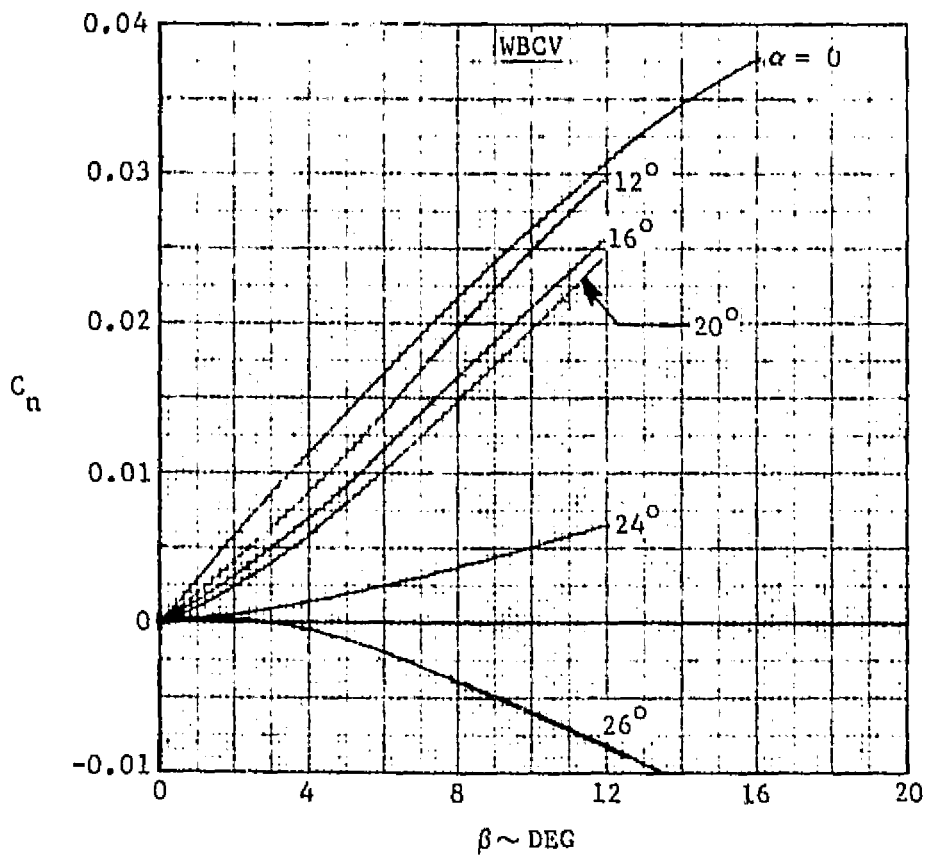
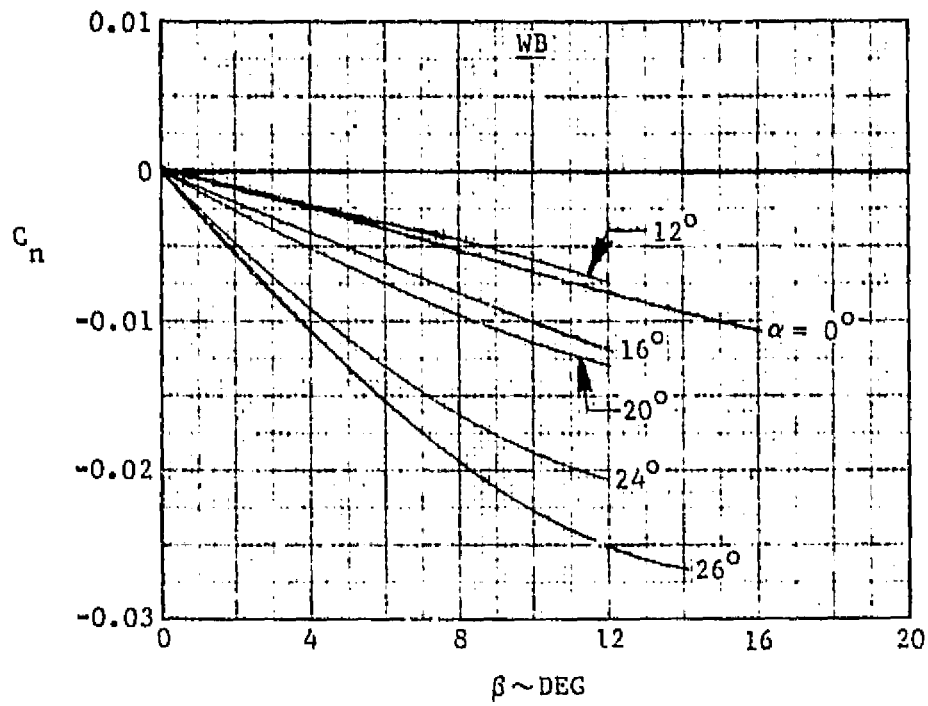


FIGURE 3-56. YAWING MOMENT AT M 0.6

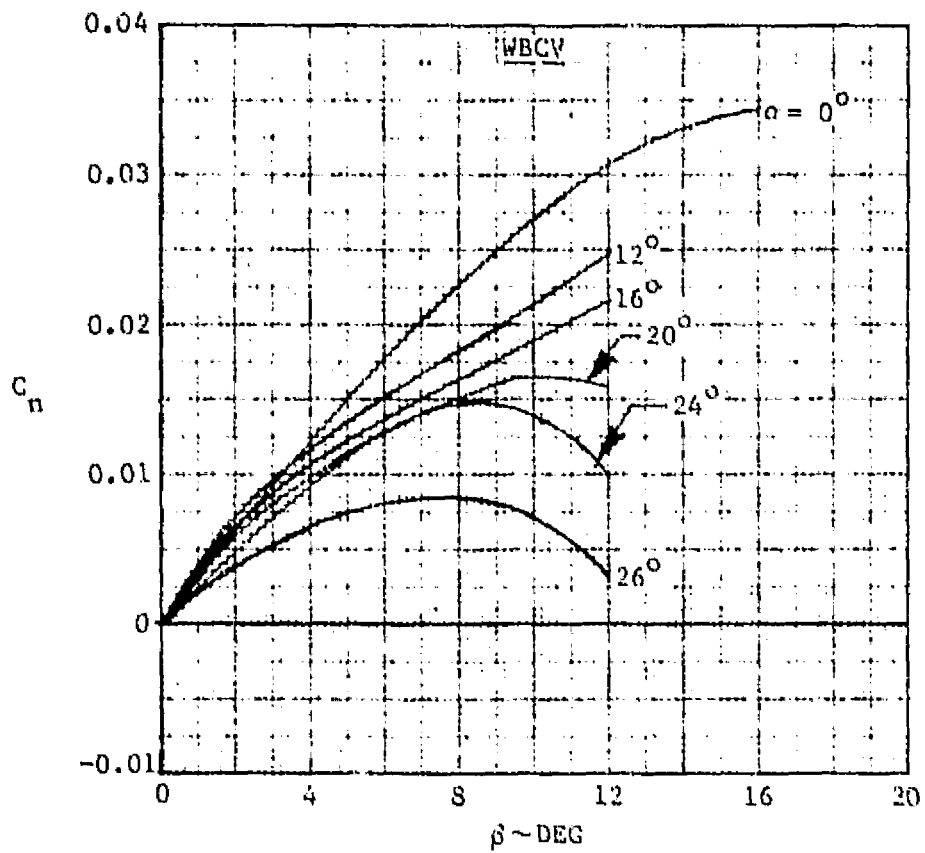
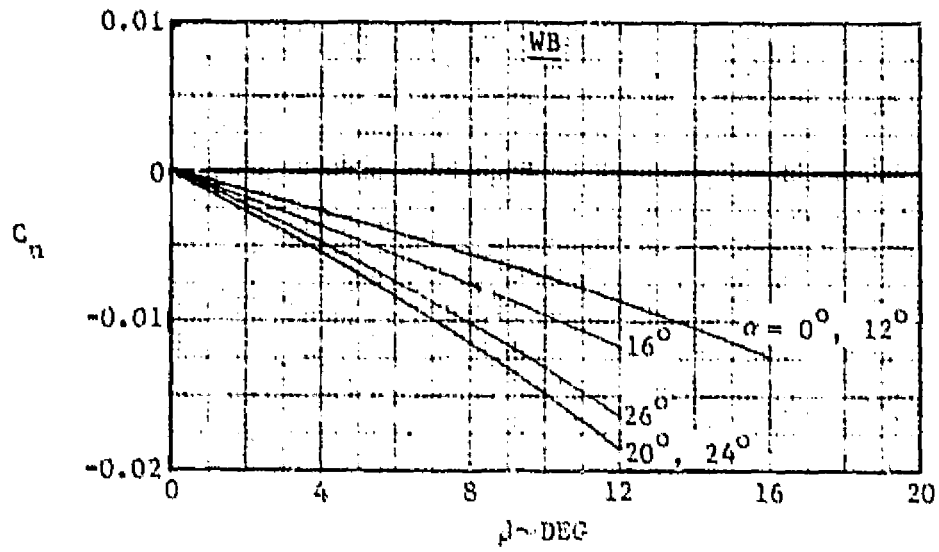


FIGURE 3-57. YAWING MOMENT AT M 0.9

ORIGINAL PAGE IS  
OF POOR QUALITY

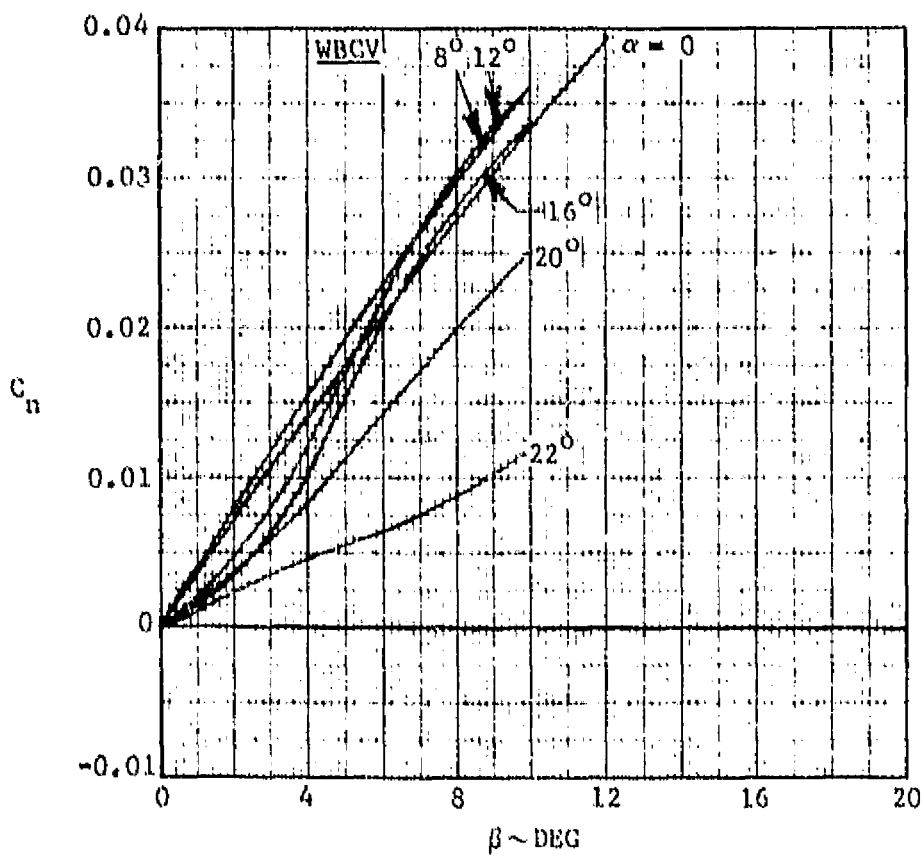
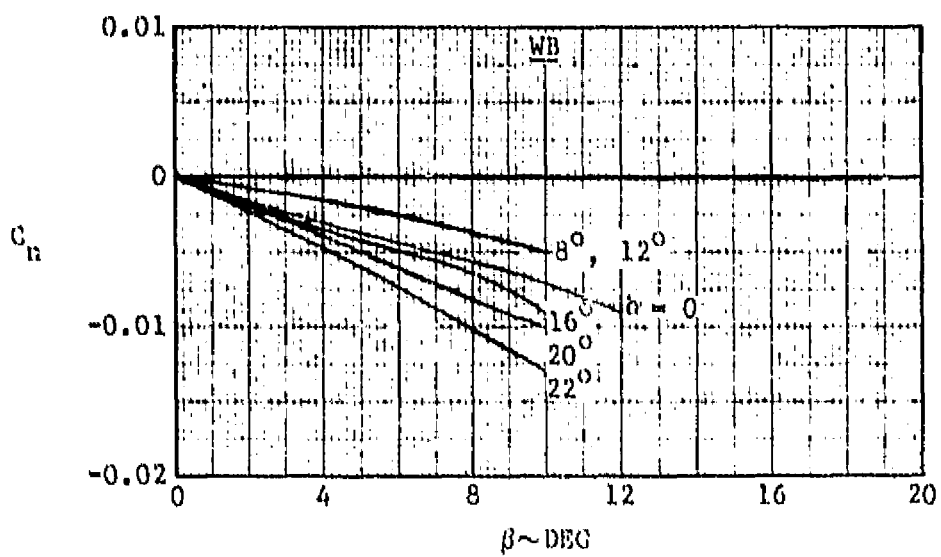


FIGURE 3-58. YAWING MOMENT AT M 1.2

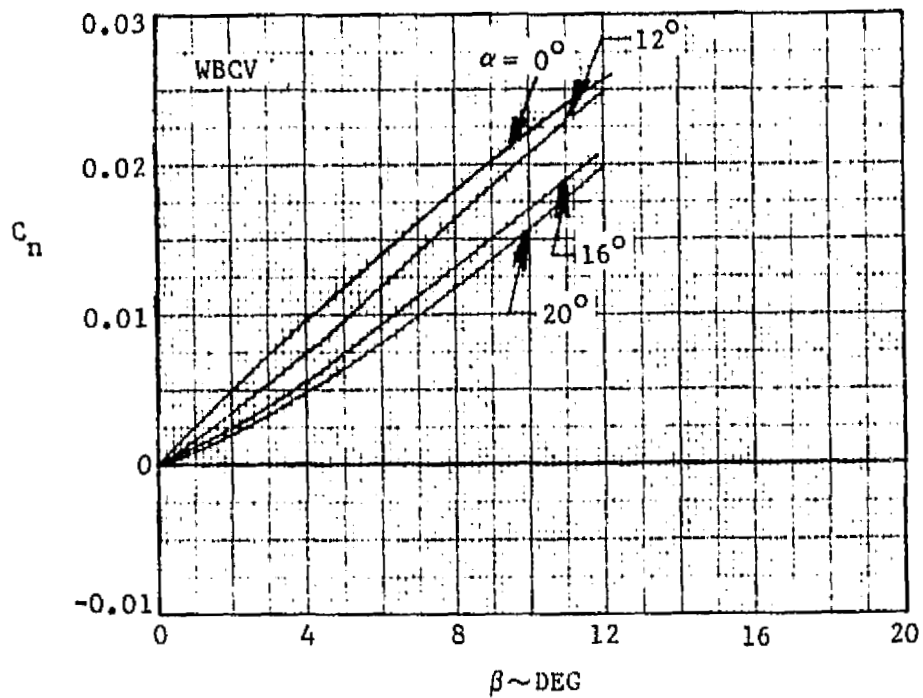
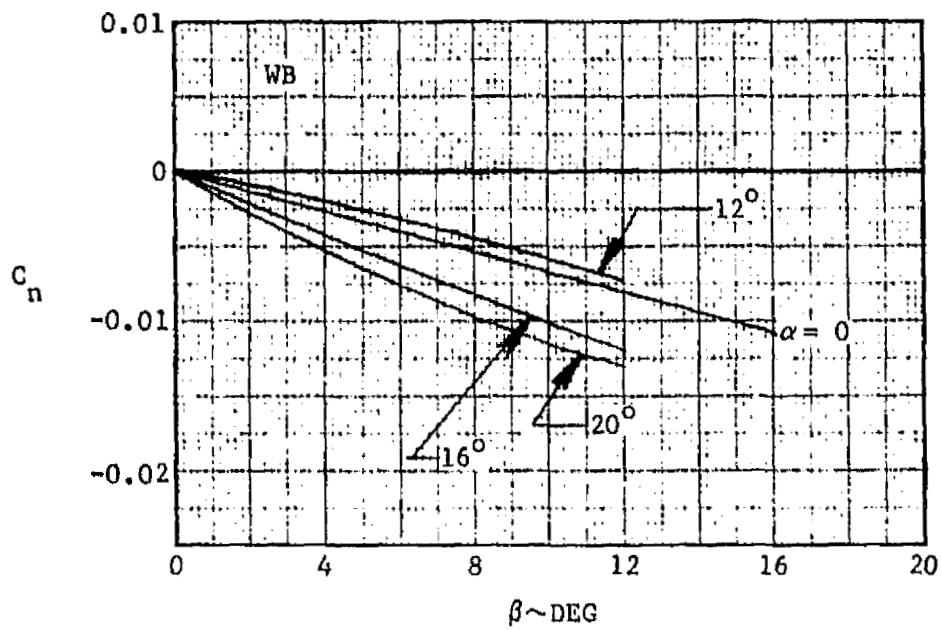


FIGURE 3-59. YAWING MOMENT AT M 1.6

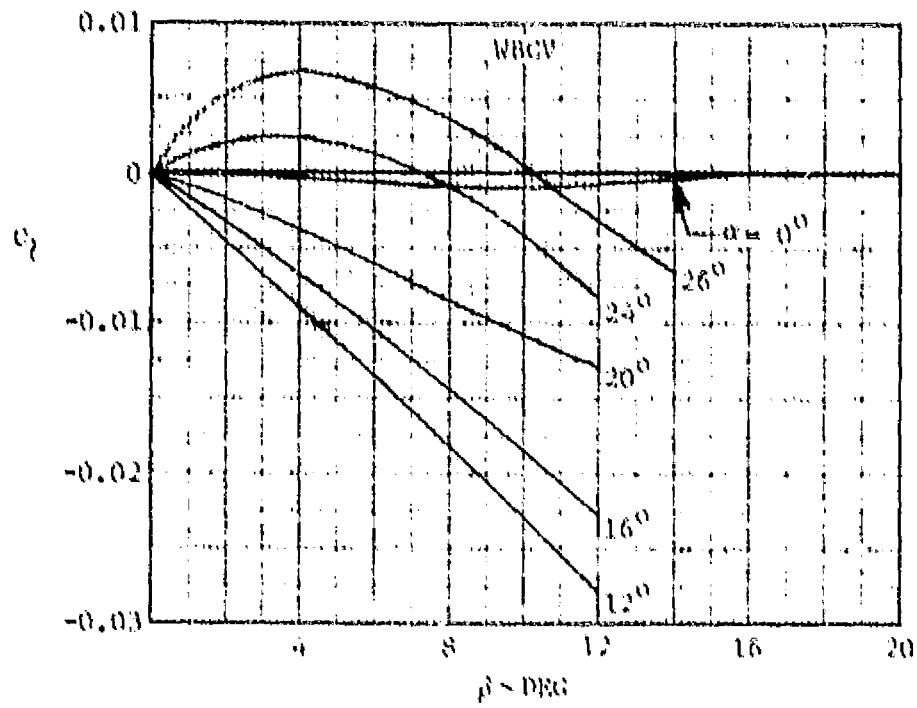
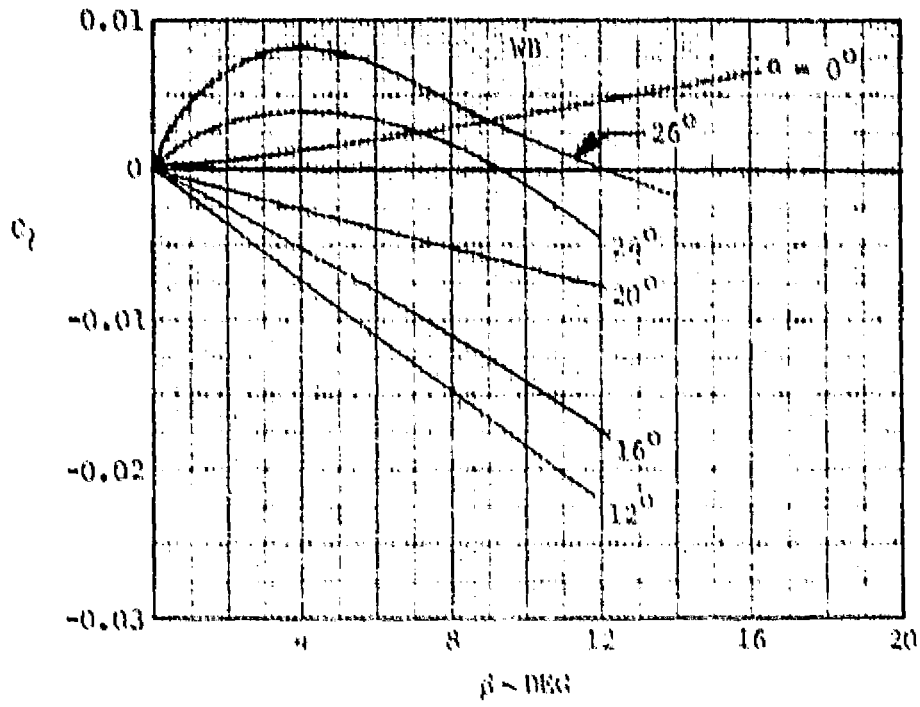


FIGURE 3-60. ROLLING MOMENT AT M 0.6

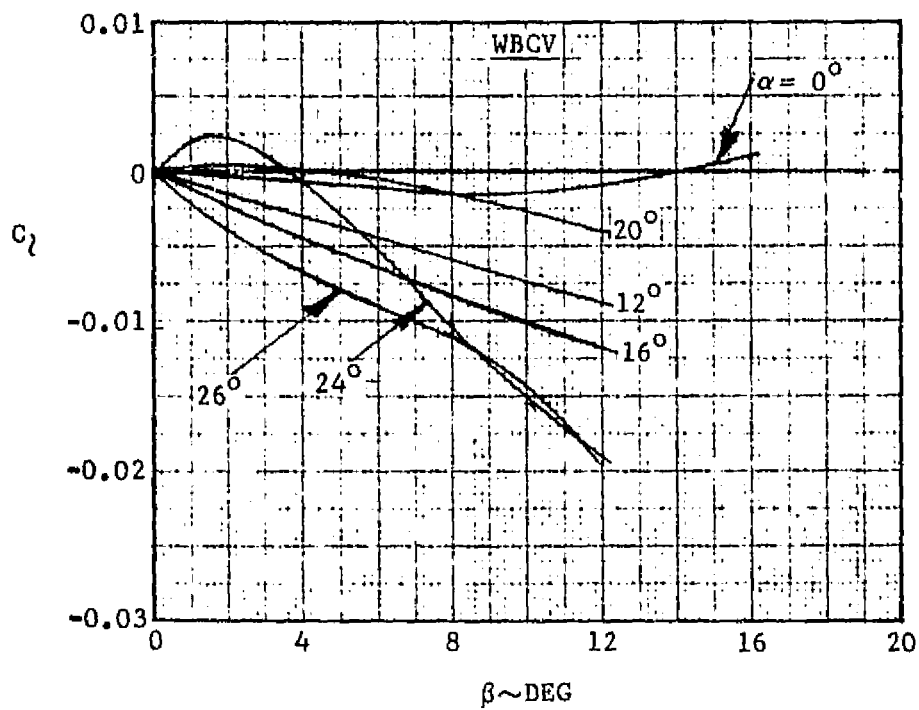
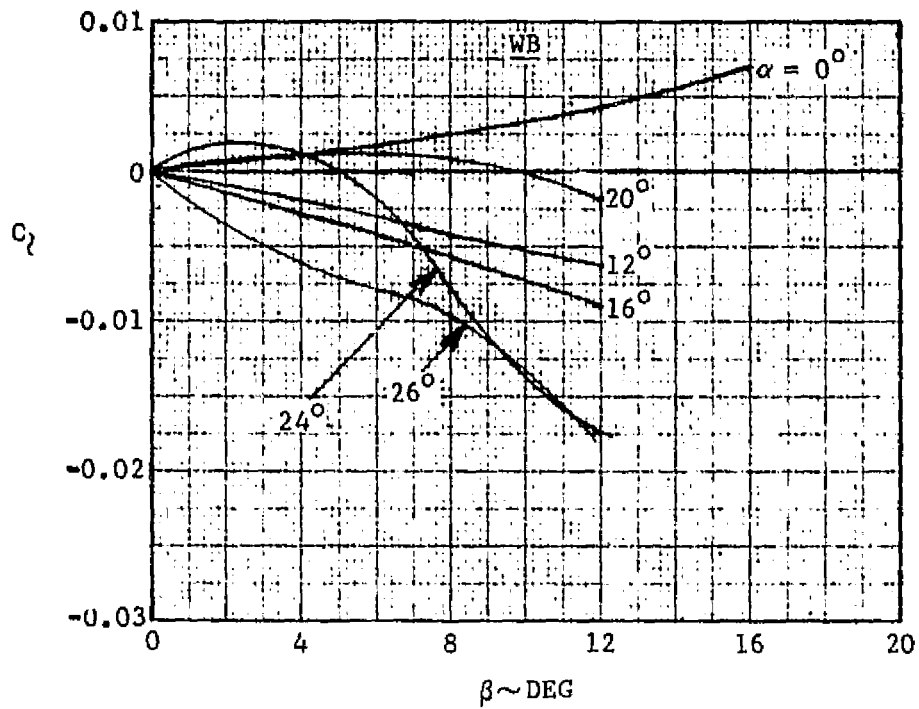


FIGURE 3-61. ROLLING MOMENT AT M 0.9

ORIGINAL PAGE IS  
OF POOR QUALITY

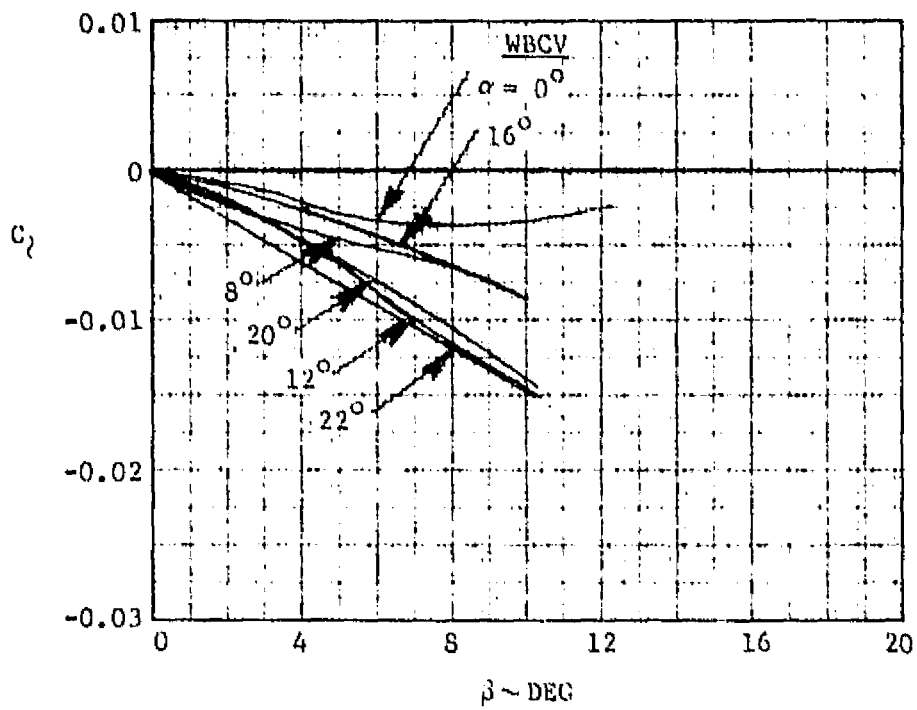
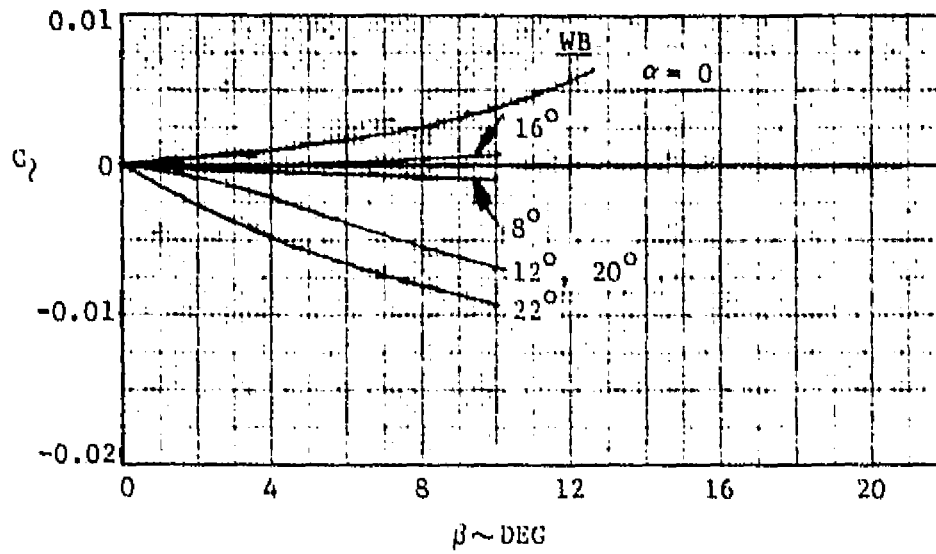


FIGURE 3-62. ROLLING MOMENT AT M 1.2

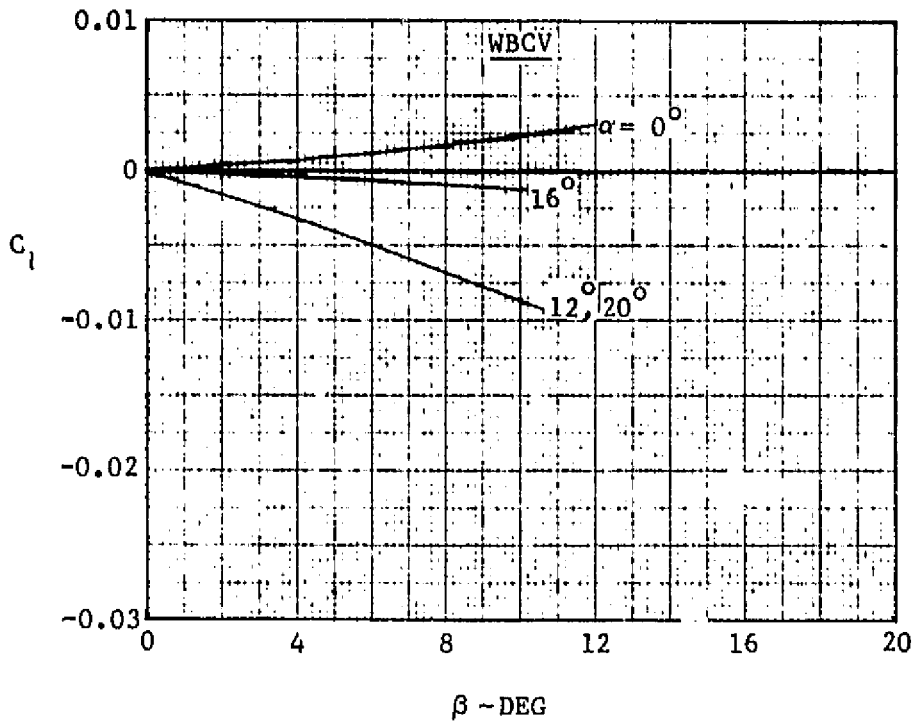
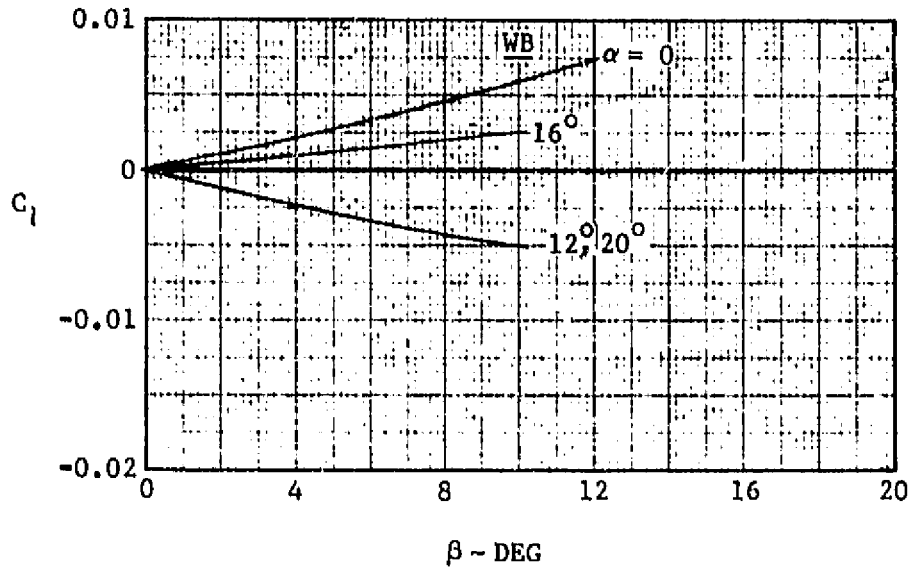


FIGURE 3-63. ROLLING MOMENT AT M 1.6

ORIGINAL PAGE IS  
OF POOR QUALITY

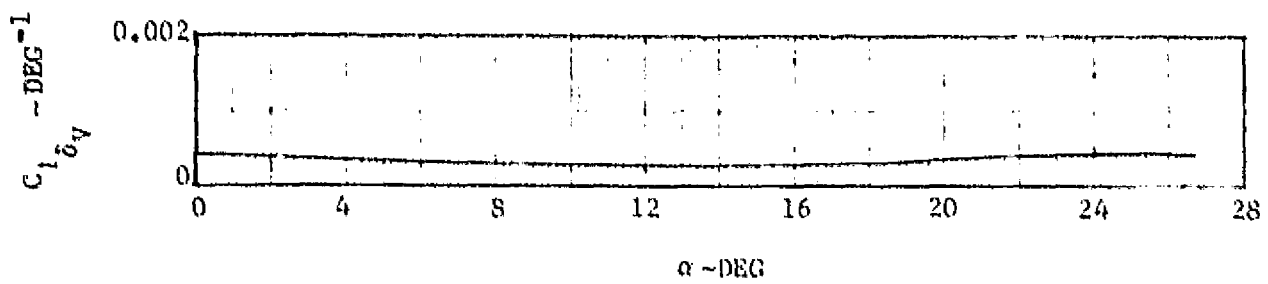
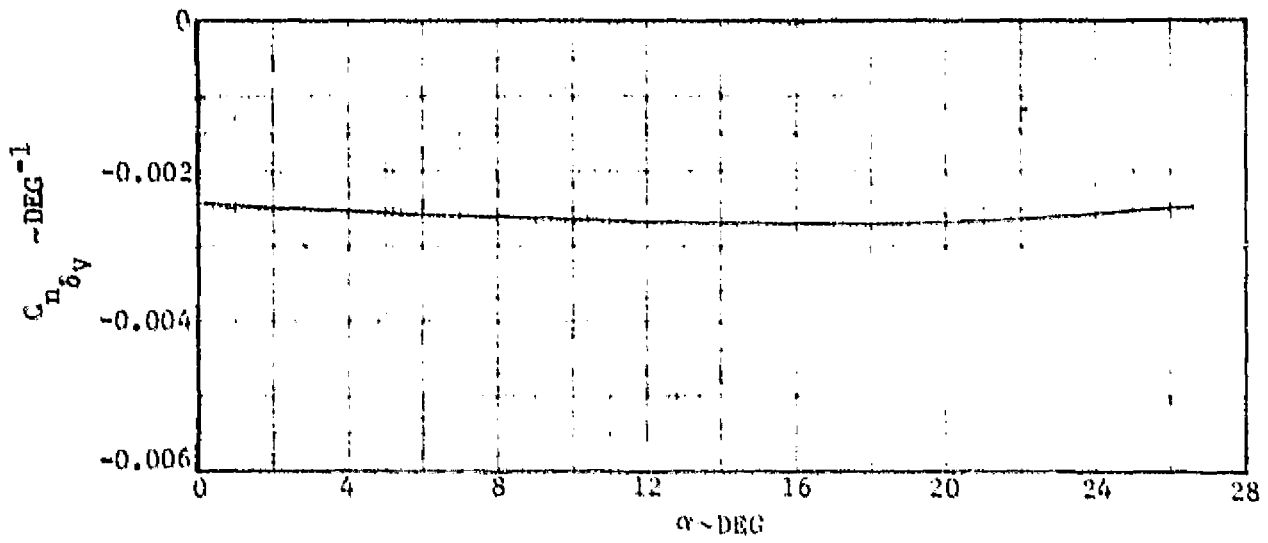
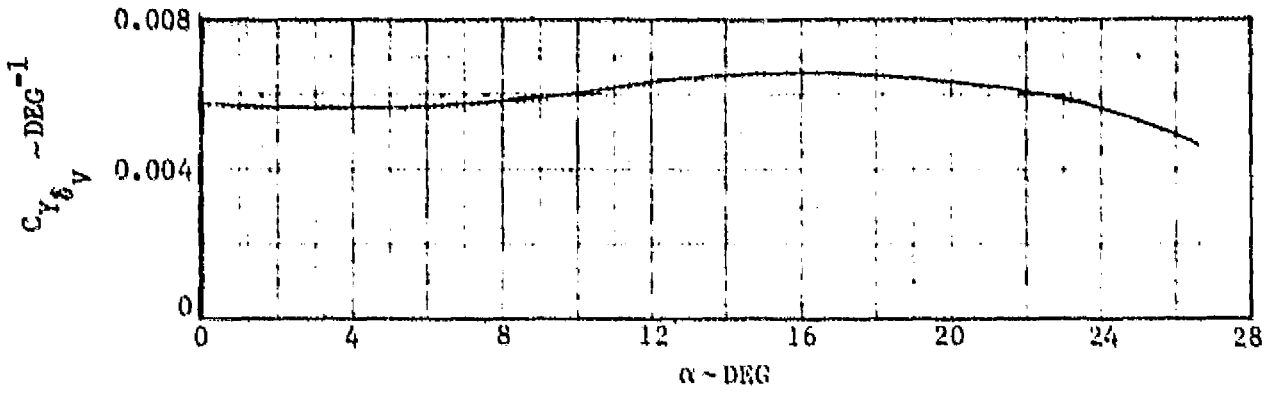


FIGURE 3-64. VERTICAL TAIL CONTROL EFFECTIVENESS AT N 0.6

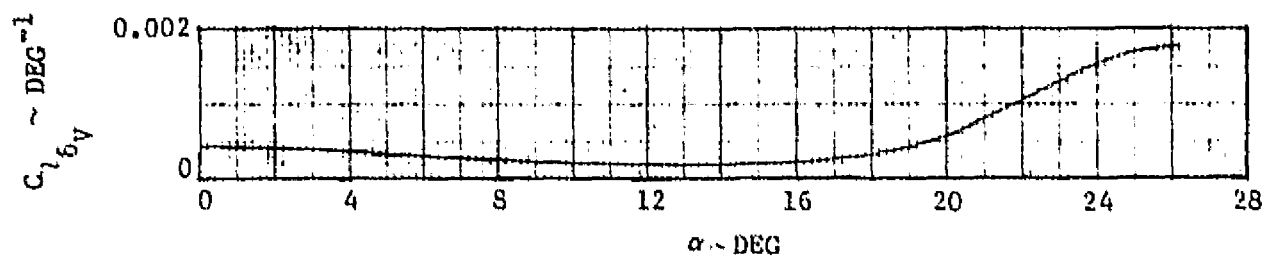
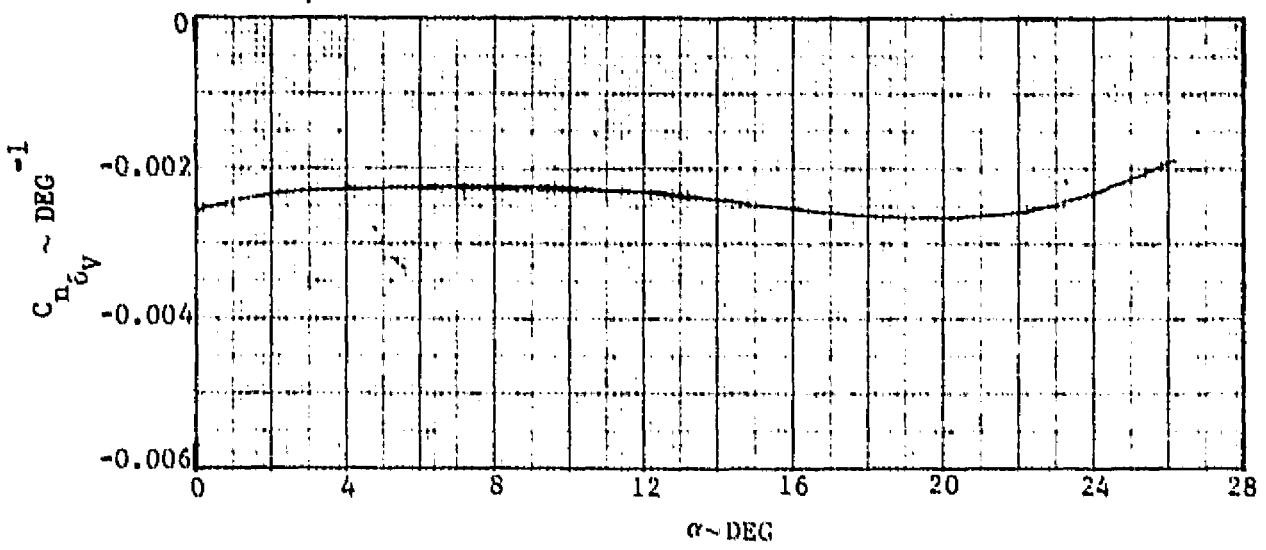
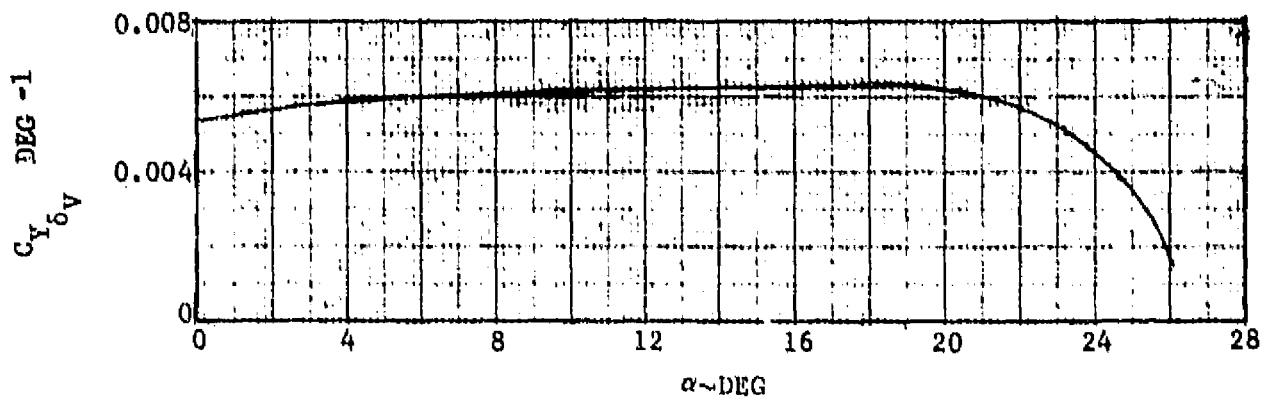


FIGURE 3-65. VERTICAL TAIL CONTROL EFFECTIVENESS AT M 0.9

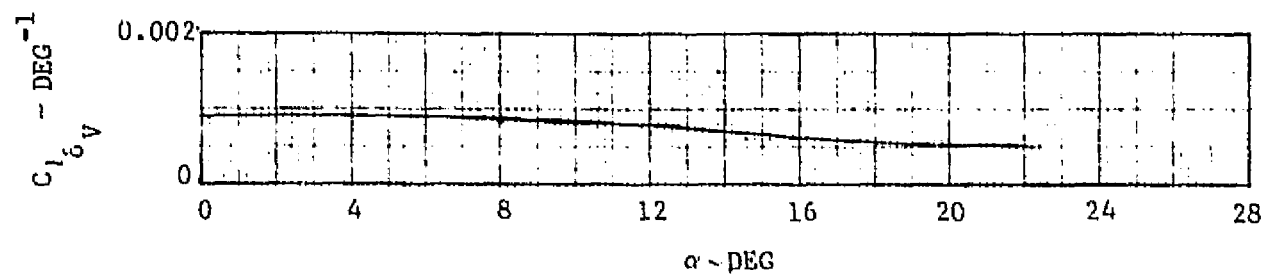
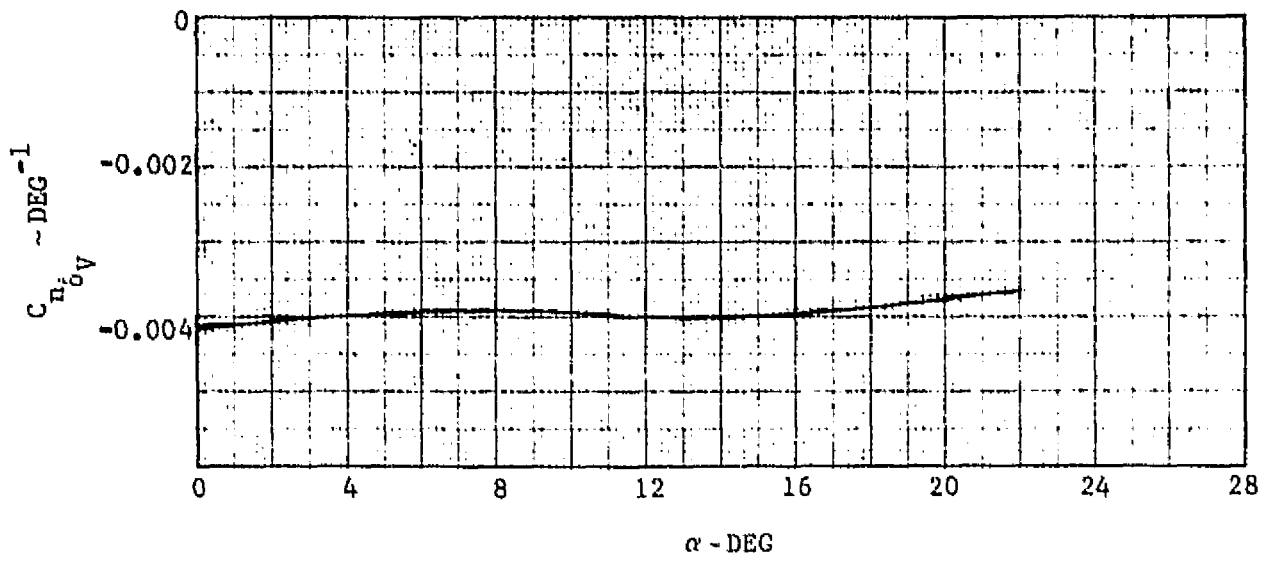
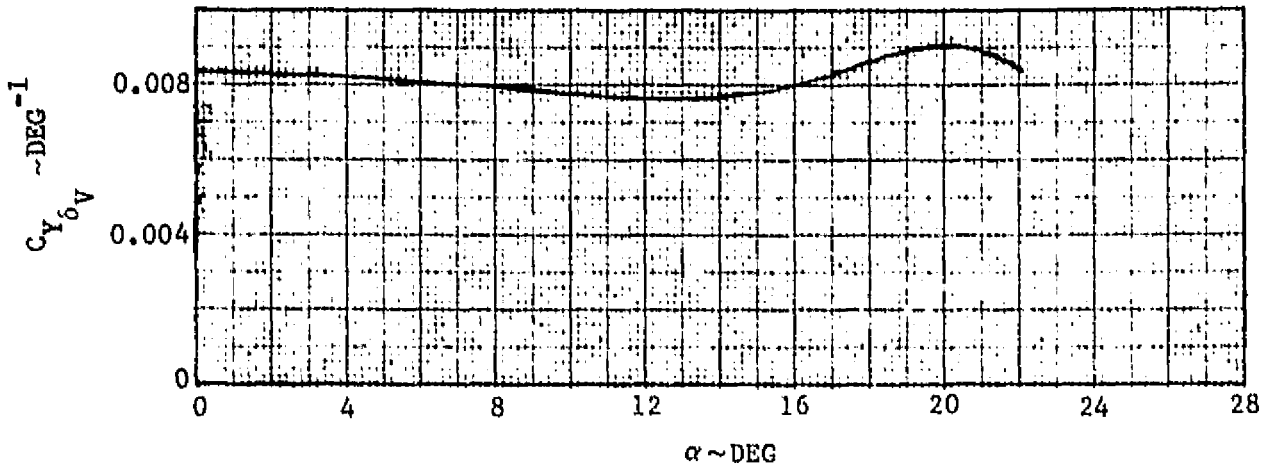


FIGURE 3-66. VERTICAL TAIL CONTROL EFFECTIVENESS AT M 1.2

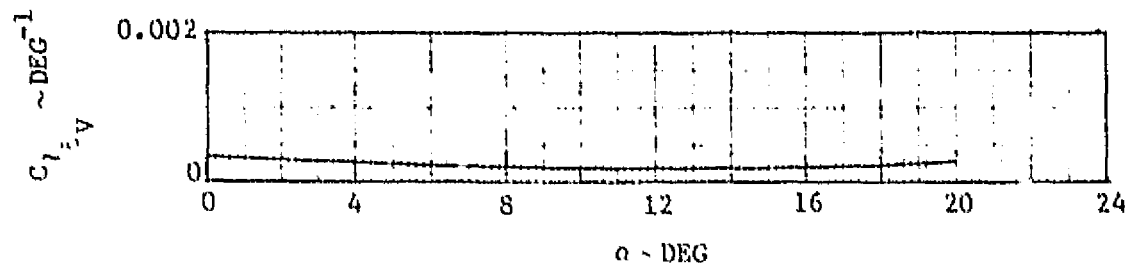
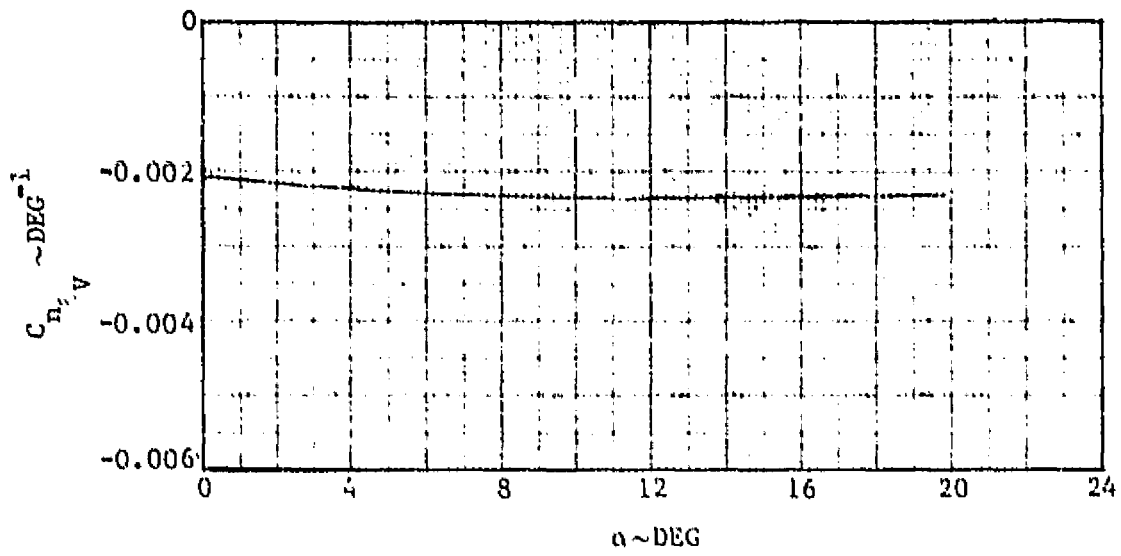
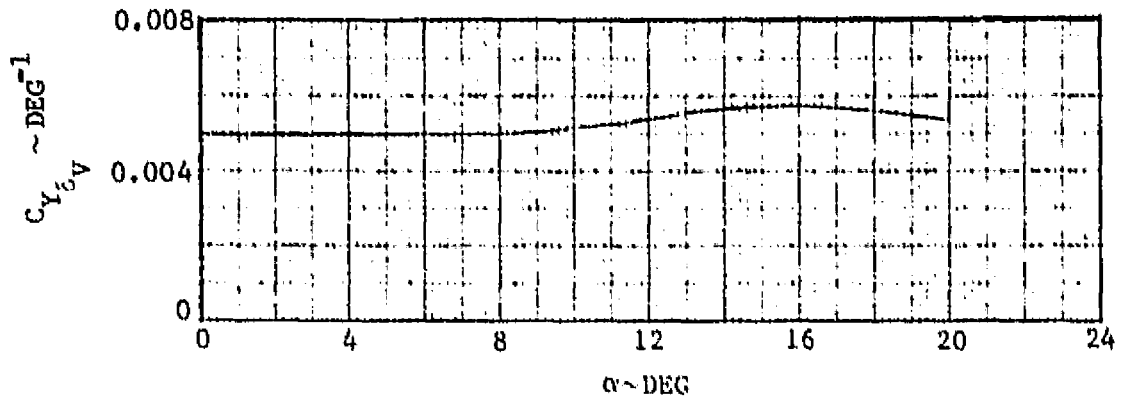


FIGURE 3-67. VERTICAL TAIL CONTROL EFFECTIVENESS AT M 1.6

ORIGINAL PAGE IS  
OF POOR QUALITY

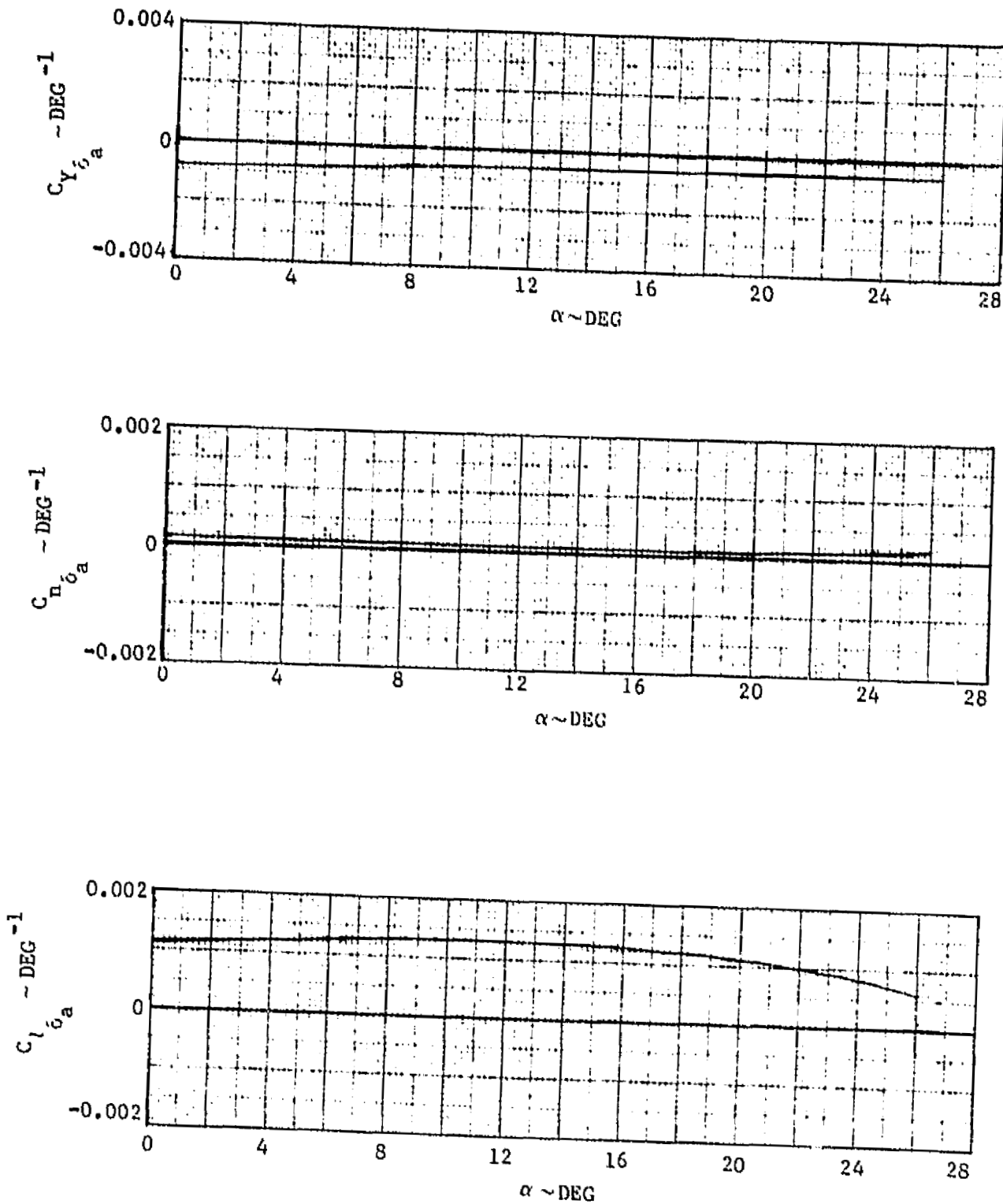


FIGURE 3-68. ELEVON ROLL CONTROL EFFECTIVENESS AT M 0.6

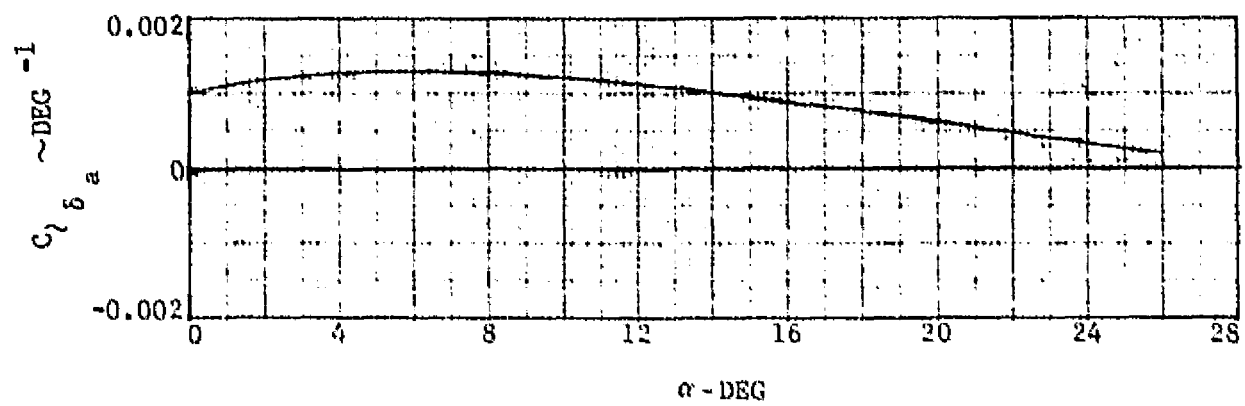
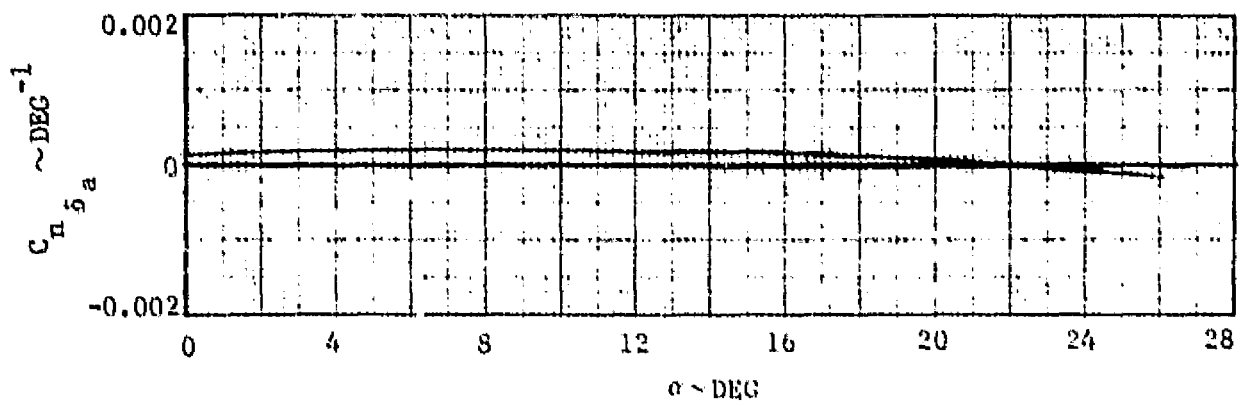
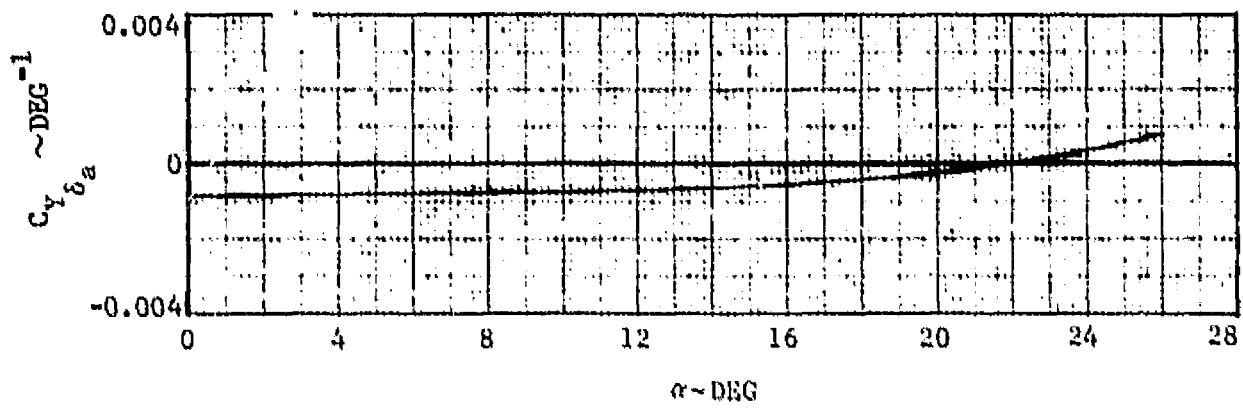


FIGURE 3-69. ELEVON ROLL CONTROL EFFECTIVENESS AT M 0.9

ORIGINAL PAGE IS  
OF POOR QUALITY

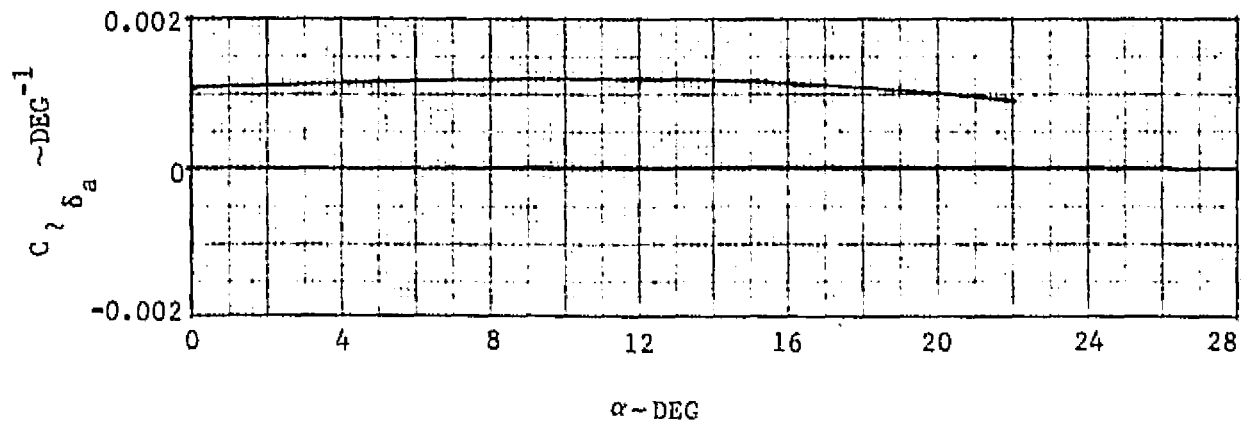
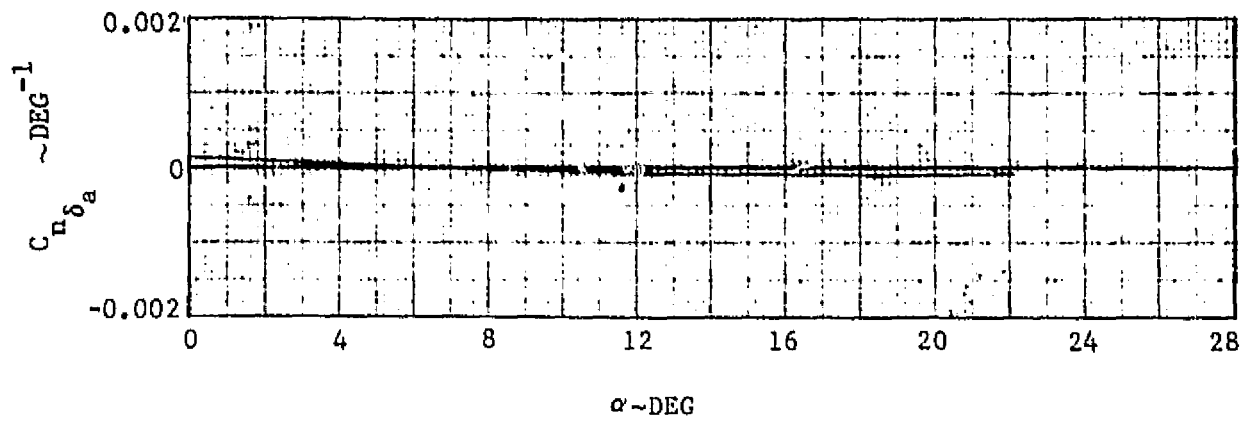
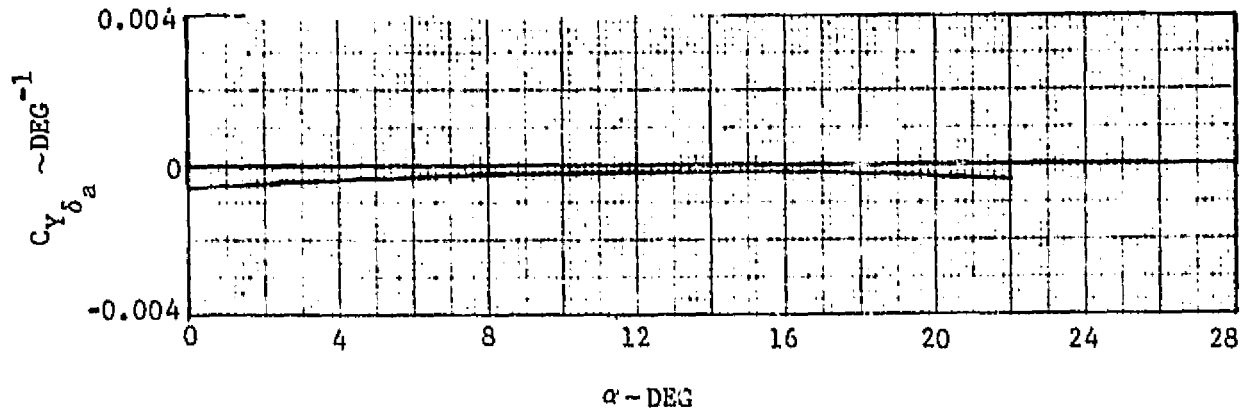


FIGURE 3-70. ELEVON ROLL CONTROL EFFECTIVENESS AT M 1.2

ORIGINAL PAGE IS  
OF POOR QUALITY

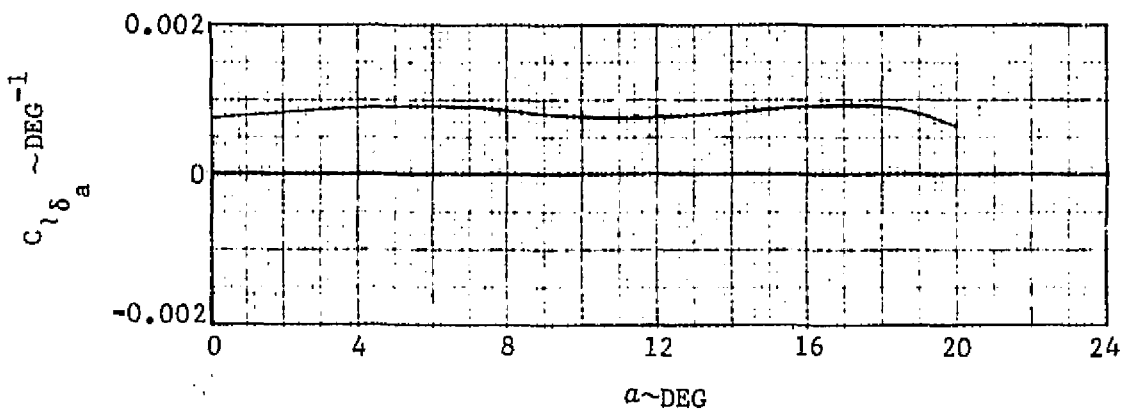
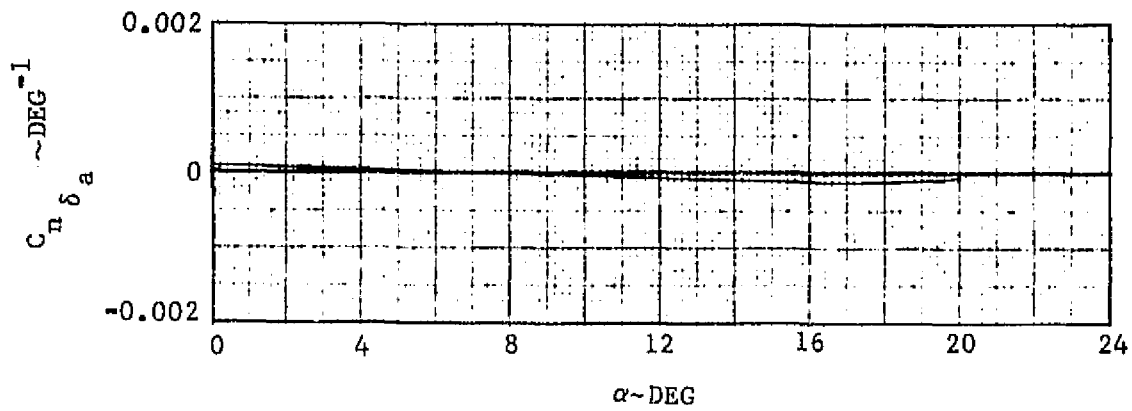
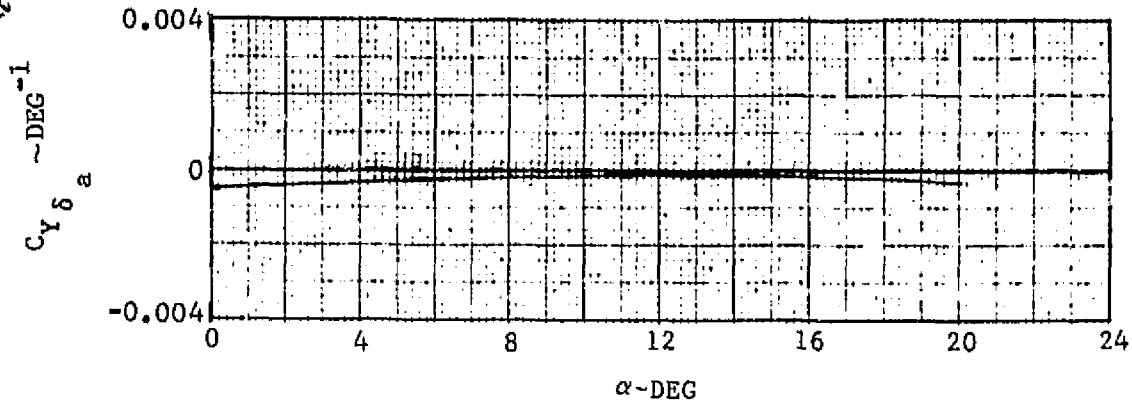


FIGURE 3-71. ELEVON ROLL CONTROL EFFECTIVENESS AT M 1.6

### 3.4 PROPULSION-INDUCED EFFECTS

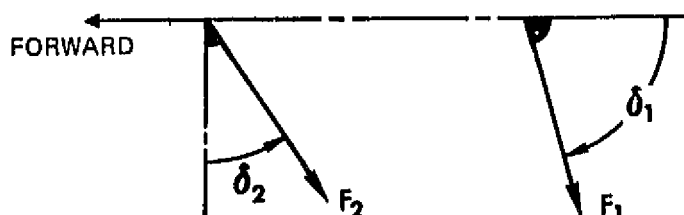
The interaction of the propulsion system exhaust with the freestream can have a significant effect on the aerodynamics of the aircraft. Propulsion-induced force and moment change characteristics, which are a function of jet efflux geometry and arrangements relative to aerodynamic surfaces, in turn impact on the performance, stability and control requirements of the aircraft.

Vectoring the nozzles for maneuvering at angle of attack increases the angle between the vectoring lift/cruise engine efflux and the freestream and tends to magnify these interaction effects. During the transition phase, when the aircraft is not yet fully supported by the aerodynamic forces on the wing as in conventional flight, the jets are directed at large angles to the freestream, leading to significant propulsion induced forces and moments. The evaluation of propulsion-induced aerodynamic characteristics involves the determination of the jet-induced flow field and the computation of the forces and moments on the configuration due to the induced flow field.

The jet-induced flow field was evaluated utilizing the entrainment model for jets exhausting into a crossflow of Reference 13. The continuity and momentum equations were solved for the jet path. The velocity field induced by the jet was evaluated by replacing the jet with a sink-doublet singularity distribution accounting for the entrainment of freestream fluid and the blockage effect on the jet. Continuity and momentum considerations yielded initial conditions for the jet resulting from the coalescence of two individual jets. The jet model of Reference 13 was modified to allow treatment of jets of initial elliptical cross section with a major-to-minor axis ratio of 4:1 as an approximation to the rectangular cross section jets of the present design.

Propulsion-induced forces and moments were evaluated utilizing the vortex-latticed method of representing lifting planforms (Reference 14). To determine power-induced longitudinal aerodynamic characteristics, a camber distribution was introduced on the planform to represent the presence of the jet-induced velocity field. Propulsion-induced aerodynamics for the configuration in cross-wind condition (i. e. at sideslip) were evaluated by applying asymmetric cambering of the platform to reflect the asymmetry of the jet-induced downwash field.

The nomenclature used in the discussion of propulsion-induced aerodynamic characteristics is summarized in the following schematic representation of the efflux from the primary nozzles and the RALS nozzle.



Propulsion-induced effects of thrust vectoring for maneuvering in the cruise/ combat flight regime are presented in 3.4.1. Section 3.4.2 treats induced aerodynamic characteristics in the transition flight phase where the presence of the RALS jet must be accounted for. Since the jet model of Reference 13 is a potential flow model which neglects viscous effects other than entrainment, results presented in Section 3.4.2 were corrected to account for the jet wake effect from the RALS jet.

### 3.4.1 Cruise/Combat Flight Regime

Effects of deflecting the thrust with the two primary nozzles on the longitudinal aerodynamic characteristics of the configuration were evaluated at a fixed deflection angle for a range of angle of attack and velocity ratio representative of thrust vectoring for maneuvering. The velocity ratio is defined in terms of the thrust coefficient ( $C_T$ ) of the two primary nozzles as

$$\frac{U_\infty}{U_{j0}} = \left( \frac{2A_{j1}/S}{C_T} \right)^{1/2} \quad (3.4-1)$$

where  $A_{j1}$  is the total nozzle exit area of the two engines,  $U_\infty/U_{j0}$  is ratio of free stream velocity to jet outlet velocity.

Figure 3-72 shows the effect of thrust deflection ( $\delta_1 = 15^\circ$ ) on induced lift as a function of angle of attack for velocity ratios of 0.3 and 0.4. Experimental data from Reference 15 are included for comparison. Sufficient similarity between the model of the experimental investigation and the present design, in terms of wing-canard planform and relative location of the two-dimensional nozzles with respect to the lifting surfaces, exist to make the comparison meaningful. Computed

induced lift coefficients,  $\Delta C_L$ , are compared with interpolated experimental data from Reference 15. The relative invariance of induced lift coefficient with velocity ratio displayed by the experimental data is also predicted quite well (compare velocity ratios of 0.3 and 0.4 in Figure 3-72).

Induced lift as a function of velocity ratio at constant  $\alpha$  is shown in Figure 3-73. The results are presented in terms of the induced lift coefficient,  $\Delta C_L$ , and non-dimensionalized induced lift thrust ratio,  $\Delta L/T$ , where

$$\frac{\Delta L}{T} = \Delta C_L \frac{S}{2A_{j_1}} \left( \frac{U_\infty}{U_{j_0}} \right)^2 \quad (3.4-2)$$

Figure 3-74 shows induced pitching moment at the same operating conditions. The computation of the nondimensionalized pitching moment follows from Equation 3.4-2, substituting  $C_m$  for  $C_L$ . Trends and magnitudes in computed induced pitching moment are consistent with the experimental data of Reference 15.

### 3.4.2 Transition Flight Regime

In the transition flight phase, the RALS jet contributes to the jet-induced flow field and must be accounted for. The jet model of Reference 11 was utilized to evaluate the induced flow field due to the efflux from the primary nozzles and to the RALS nozzle. Negligible interference effects between the RALS jet and the primary jets due to the large separation permit a direct superposition of the two induced flow fields (Reference 13).

For a fixed velocity ratio of the primary jets,  $U_\infty/U_{j_0}$ , the velocity ratio of the RALS jet is expressed as

$$\left( \frac{U_\infty}{U_{j_0}} \right)_R = \left( \frac{F1/F2}{A_{j_1}/A_{j_2}} \right)^{1/2} \left( \frac{U_\infty}{U_{j_0}} \right) \quad (3.4-3)$$

where  $F1/F2$  is the thrust split between the primary nozzles and the RALS nozzle and  $A_{j2}$  is the exit area of the RALS nozzle. The nondimensionalized induced lift,  $\Delta L/T$ , is now computed as

$$\frac{\Delta L}{T} = \Delta C_L \frac{S}{2A_{j1}} \frac{1}{(1 + F2/F1)} \left( \frac{U_\infty}{U_{j0}} \right)^2$$

All data presented in Figures 3-75 through 3-77 are shown as a function of the velocity ratio of the primary jets,  $U_\infty/U_{j0}$ .

Figure 3-75 shows induced lift as a function of velocity ratio for a number of jet deflection angles and thrust splits representative of the transition flight phase. Pitching moments induced under the same operating conditions are presented in Figure 3-76. Rolling moments induced at a sideslip angle of  $\beta = 10^\circ$  were evaluated for two sets of operating conditions in the transition flight phase and are presented in Figure 3-77.

Immediately downstream of a jet efflux there is a wake region which has not been accounted for in the prior discussions. The primary propulsion exhaust is located at the trailing edge of the wing so that in this case the wake has no significant aerodynamic effect. However, the RALS jet exhausts well forward of the wing and its wake interacts with the fuselage lower surface and at sideslip can be directed over the canard and wing. Theoretical analysis methods are not available but an empirical method (Reference 13) has been developed for estimating these effects. Charts were generated in Reference 13 for the lift and moment increments due to a normally exhausting jet as a function of jet velocity ratio and wake length. These charts were used to obtain the longitudinal aerodynamic increments (Figures 3-78 and 3-79) and the incremental rolling moment (Figure 3-80) for the configuration. There is a lift loss, nose down pitching moment and a negative rolling moment for positive sideslip due to the wake of the RALS jet.

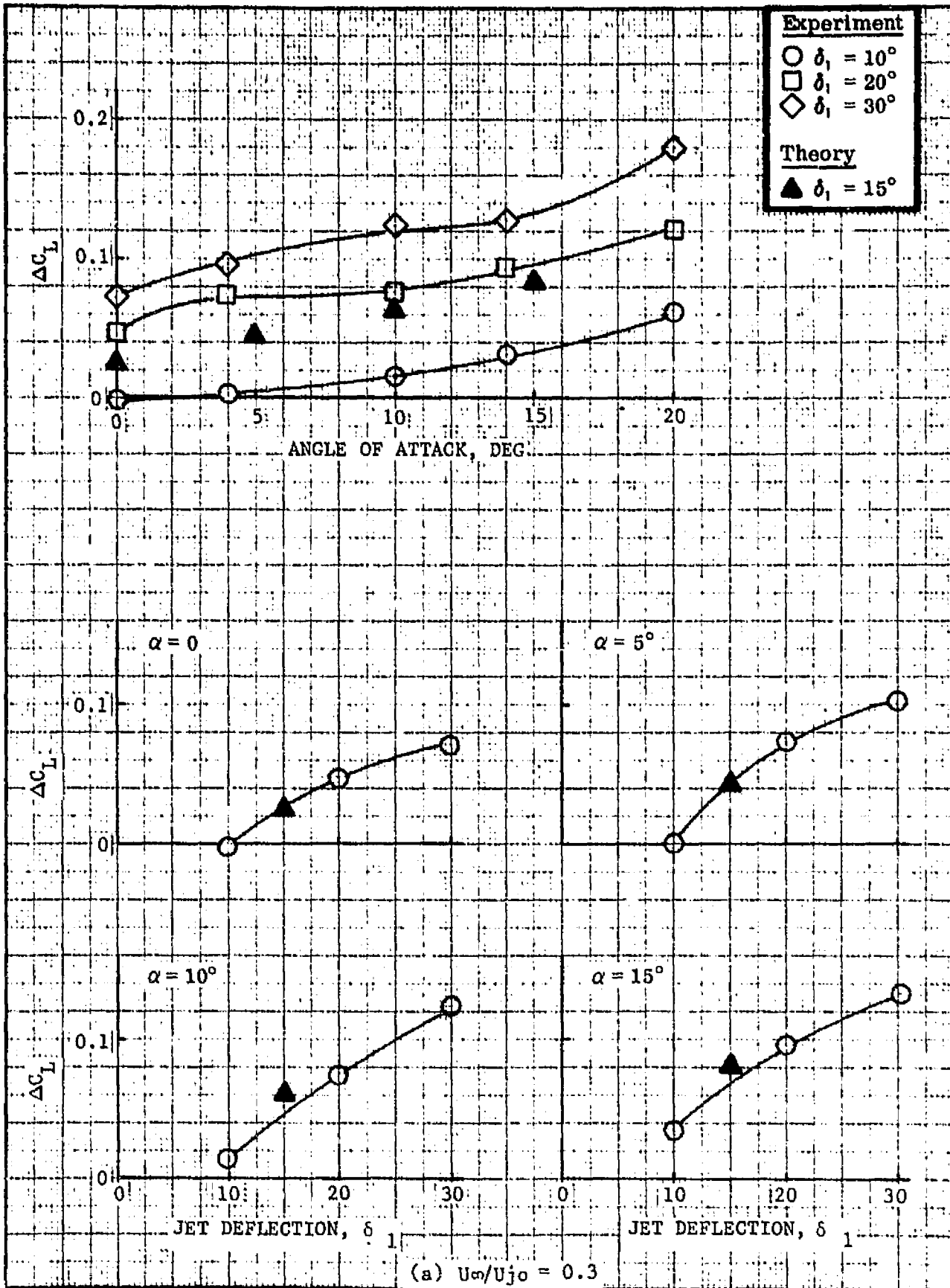


FIGURE 3-72. EFFECT OF DEFLECTED THRUST ON LIFT

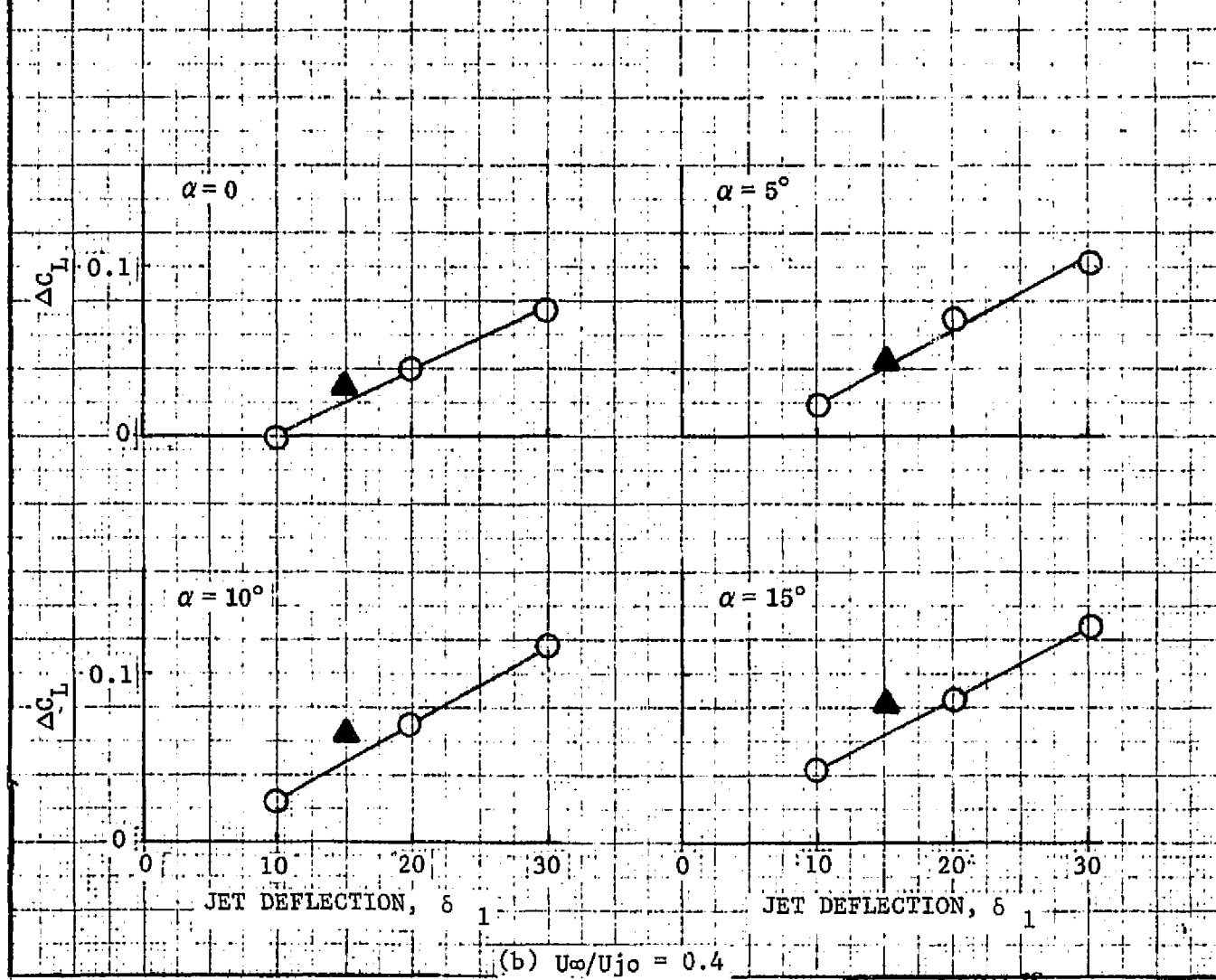
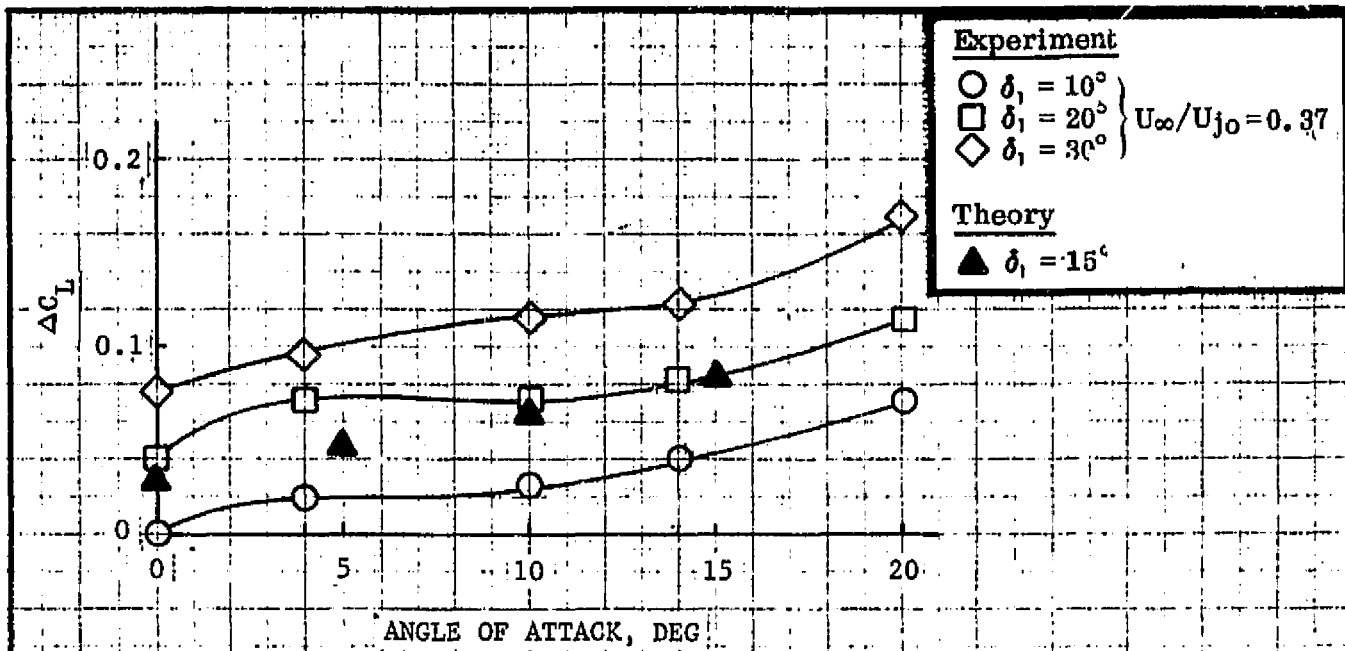


FIGURE 3-72. (CONCLUDED) ORIGINAL PAGE IS OF POOR QUALITY

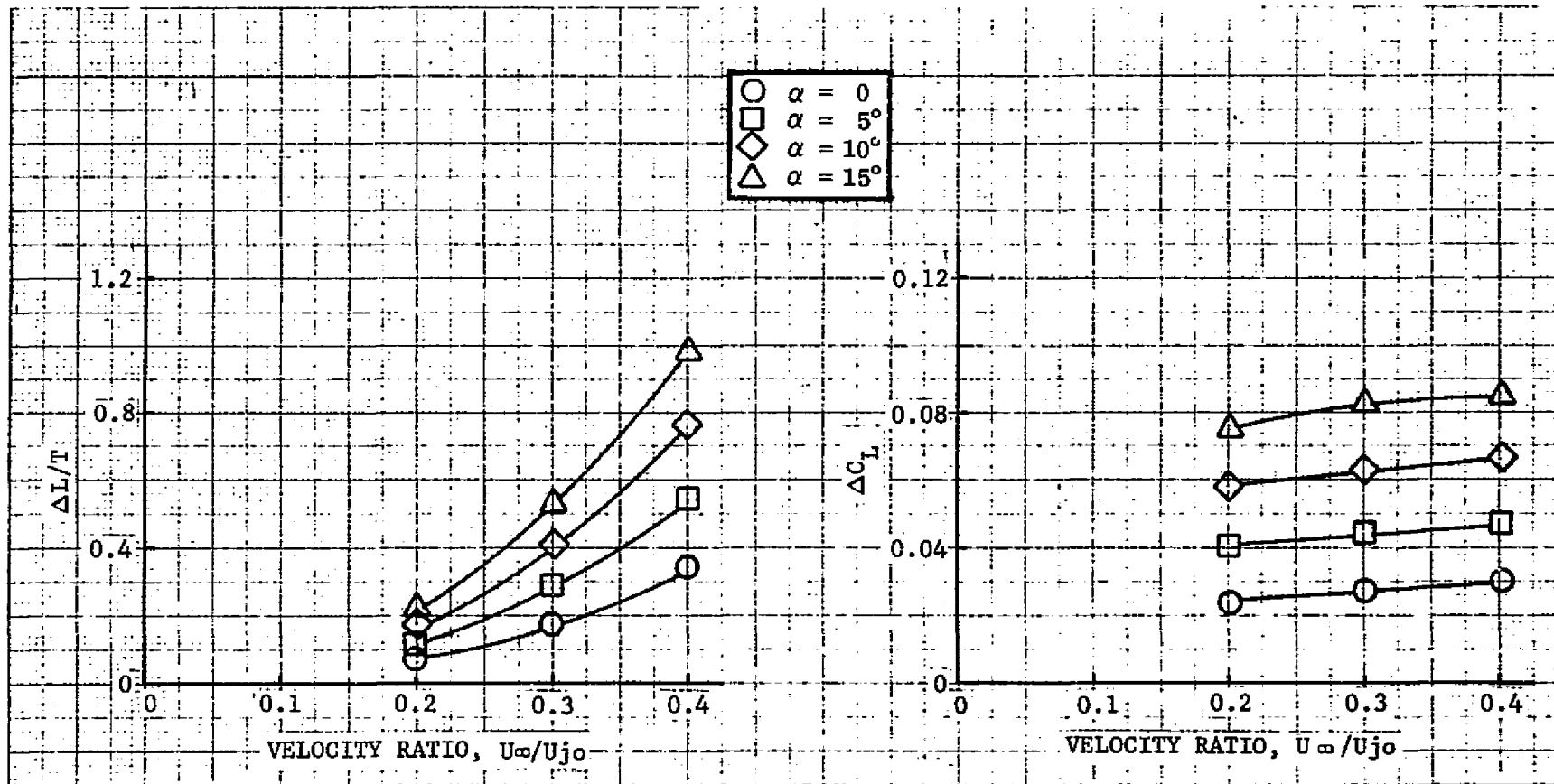


FIGURE 3-73. INDUCED LIFT DUE TO THRUST VECTORING ( $\delta_1 = 15^\circ$ )

ORIGINAL PAGE IS  
OF POOR QUALITY

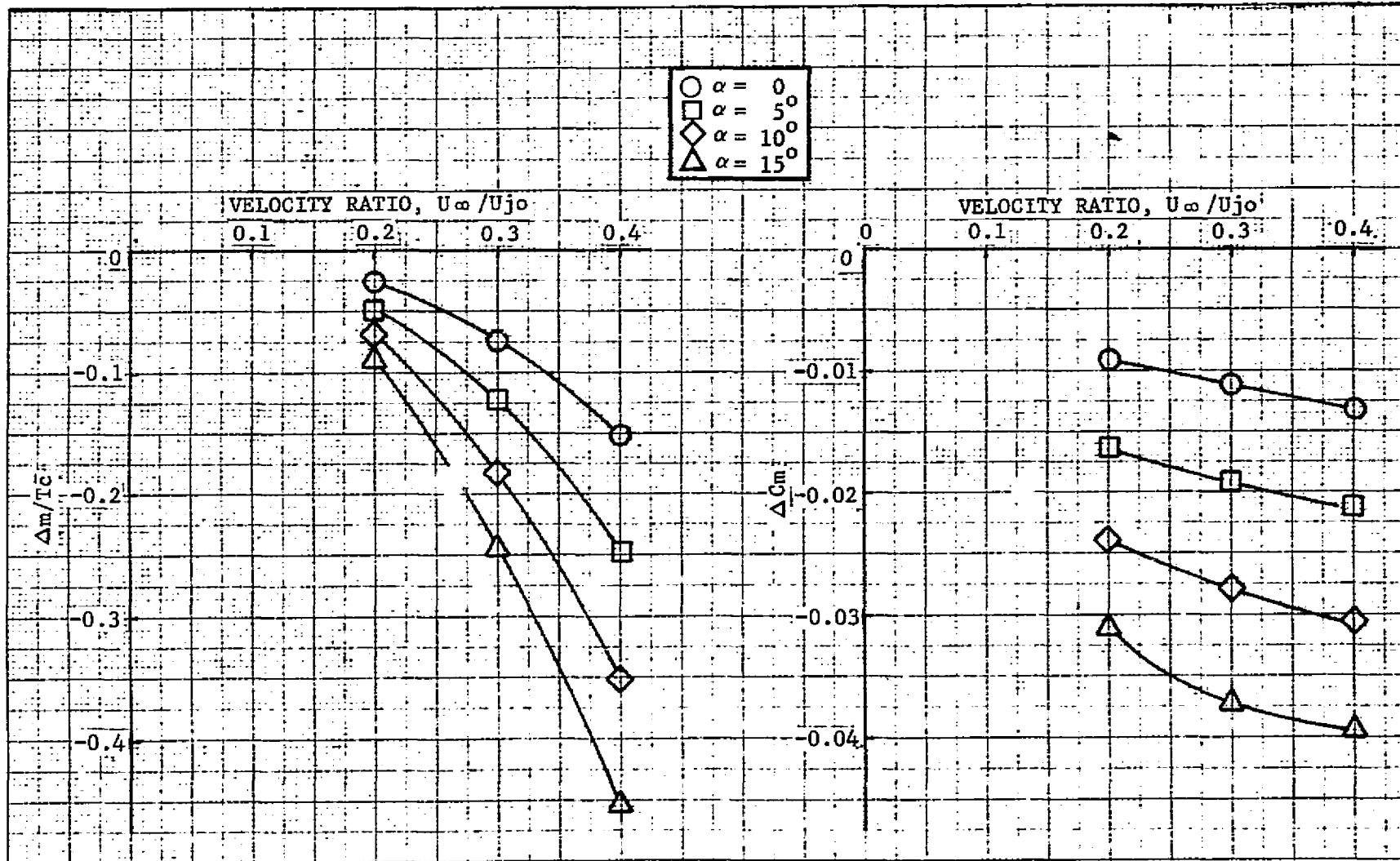


FIGURE 3-74. INDUCED PITCHING MOMENT DUE TO THRUST VECTORING ( $\delta_1 = 15^\circ$ )

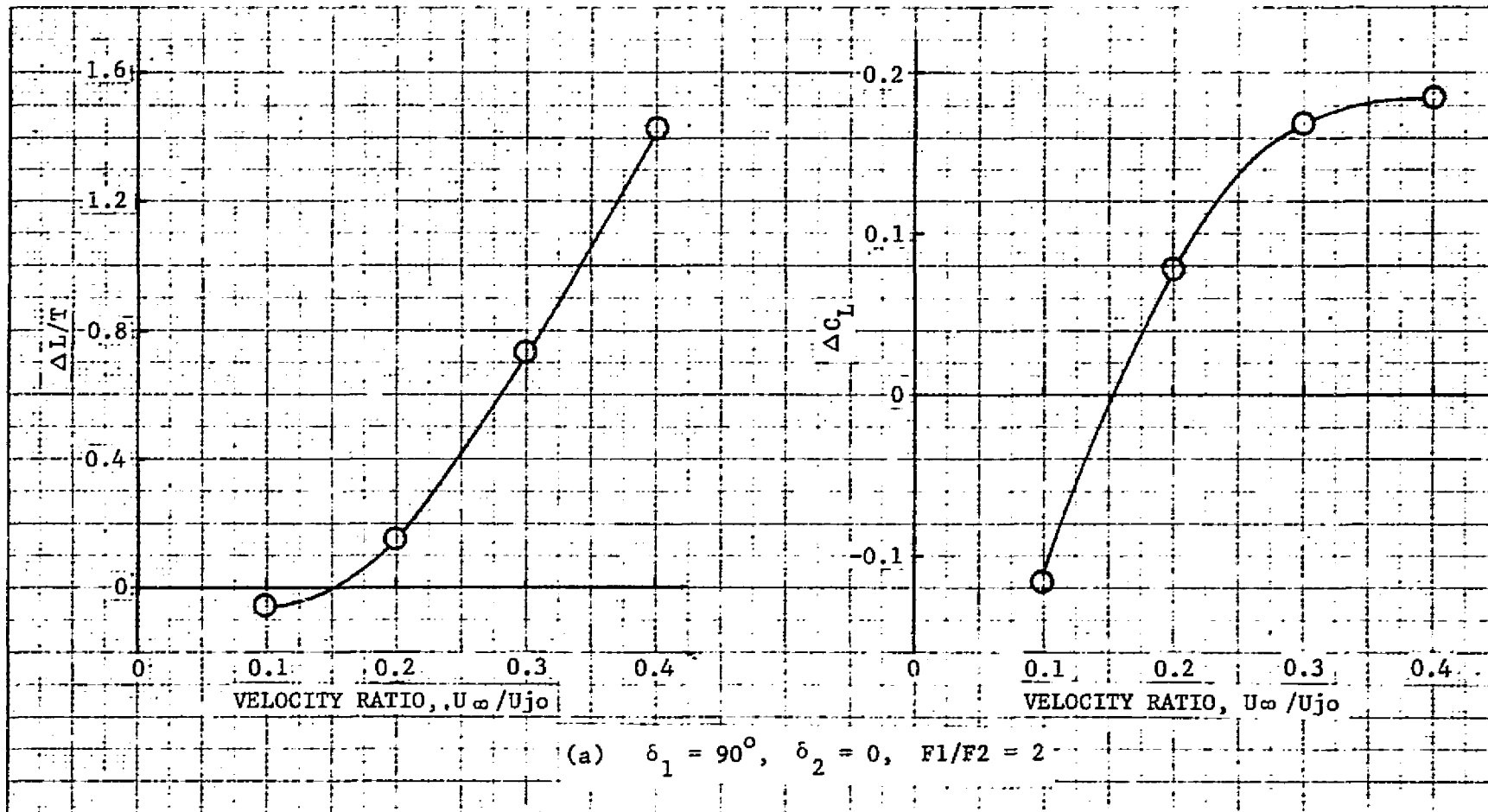


FIGURE 3-75. PROPULSION-INDUCED LIFT IN TRANSITION

ORIGINAL PAGE IS  
OF POOR QUALITY

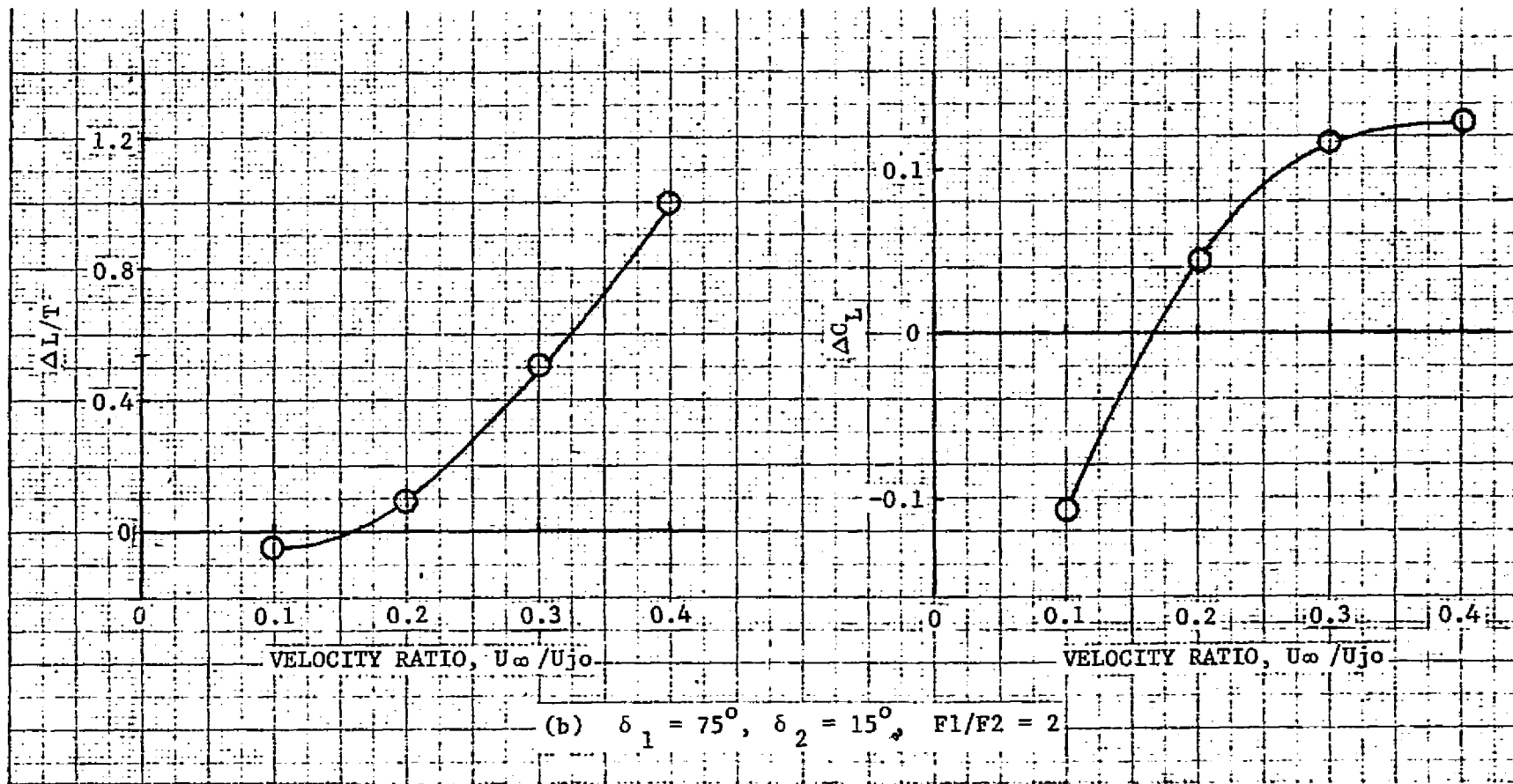


FIGURE 3-75. (CONTINUED)

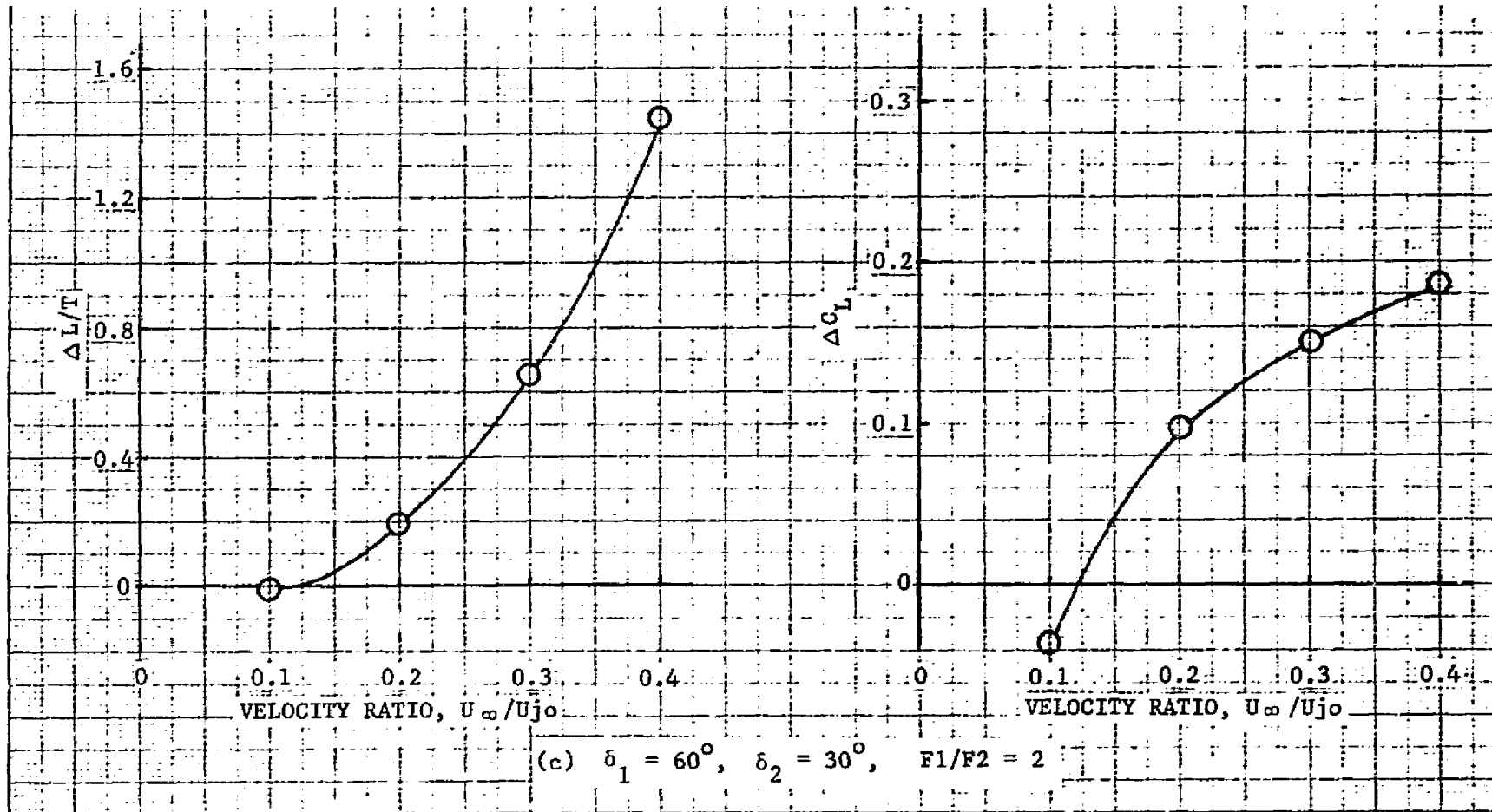


FIGURE 3-75. (CONTINUED)

ORIGINAL PAGE IS  
OF POOR QUALITY

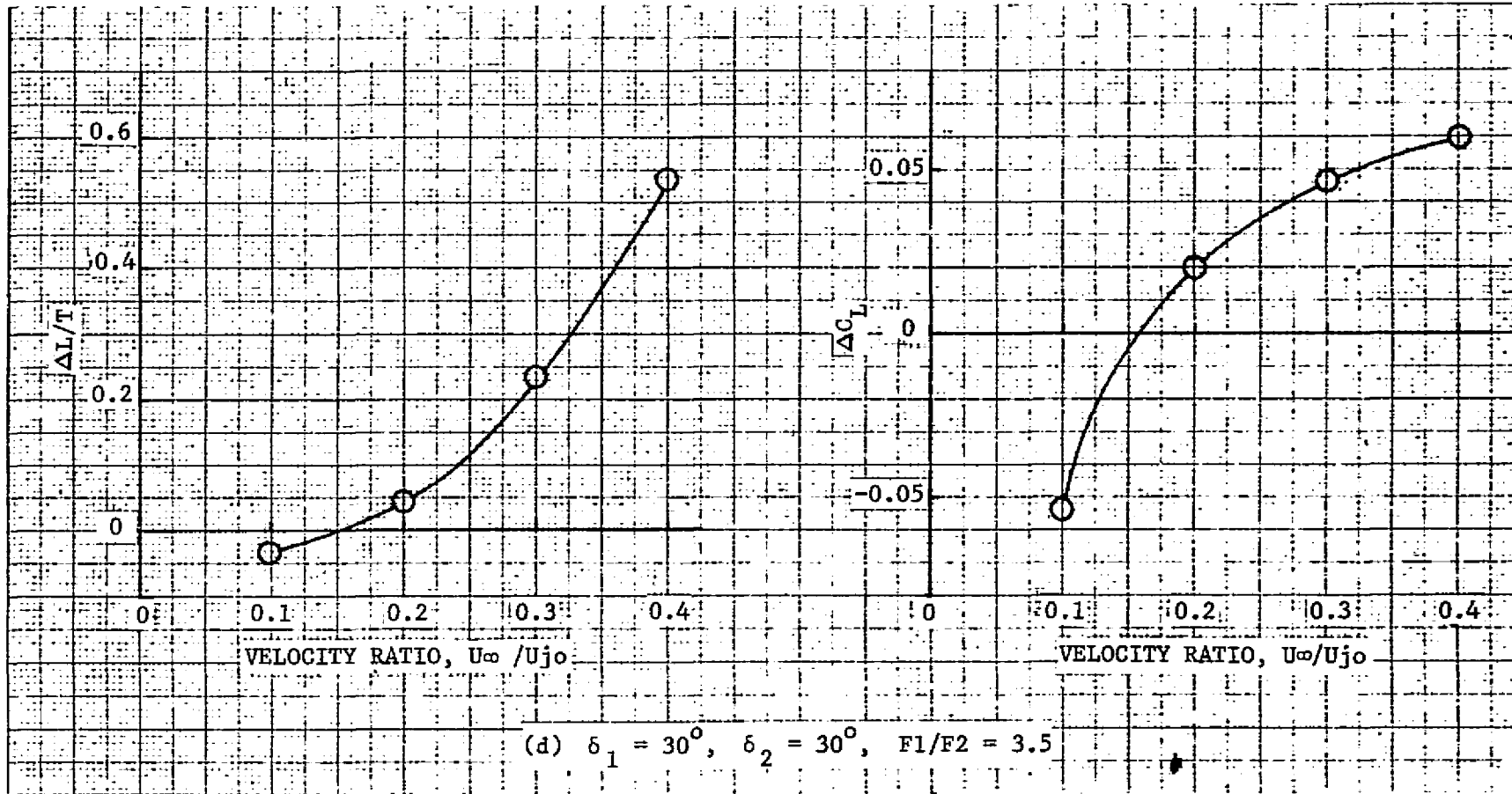


FIGURE 3-75. (CONTINUED)

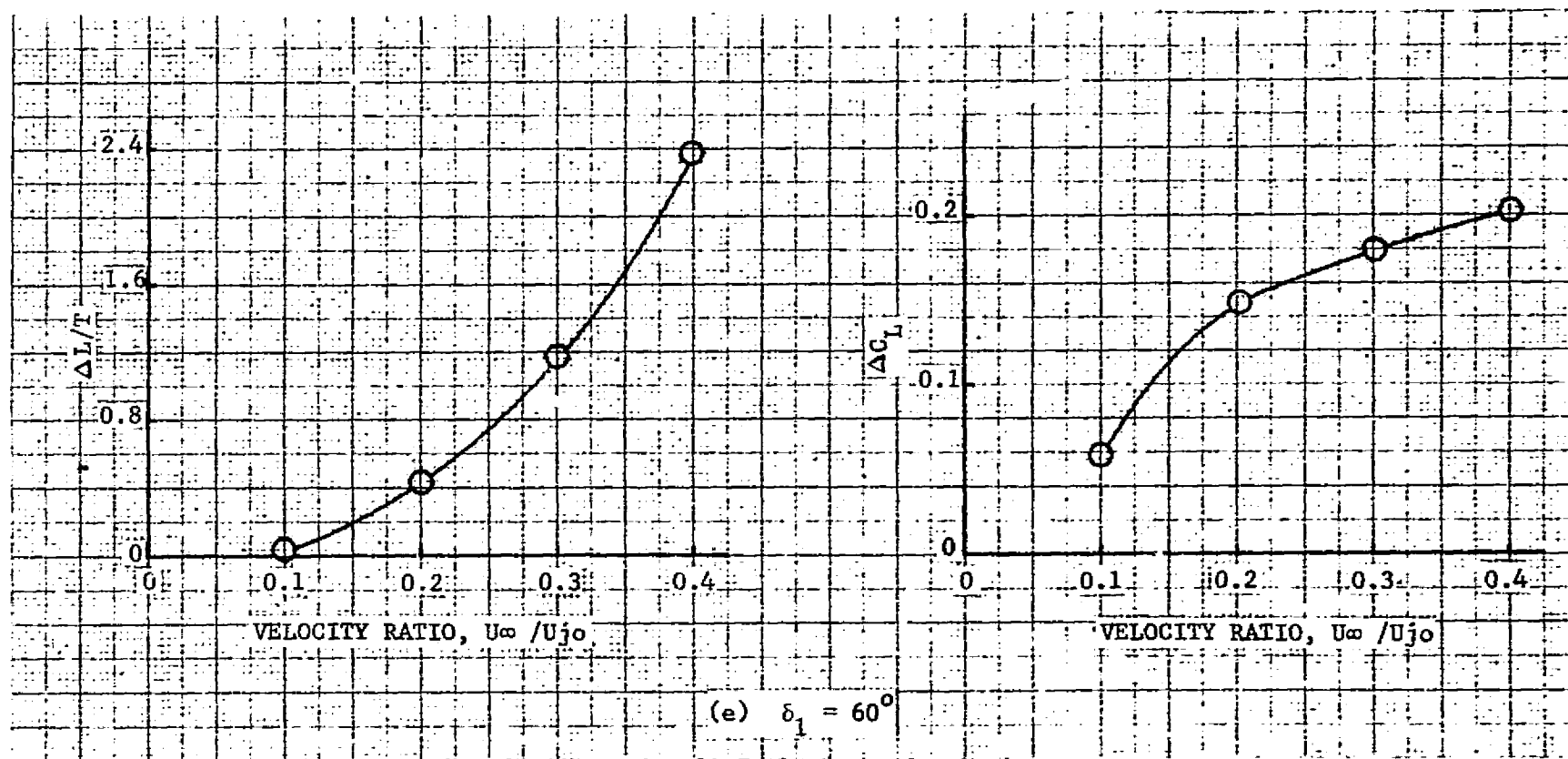


FIGURE 3-75. (CONCLUDED)

ORIGINAL  
OF POOR QUALITY

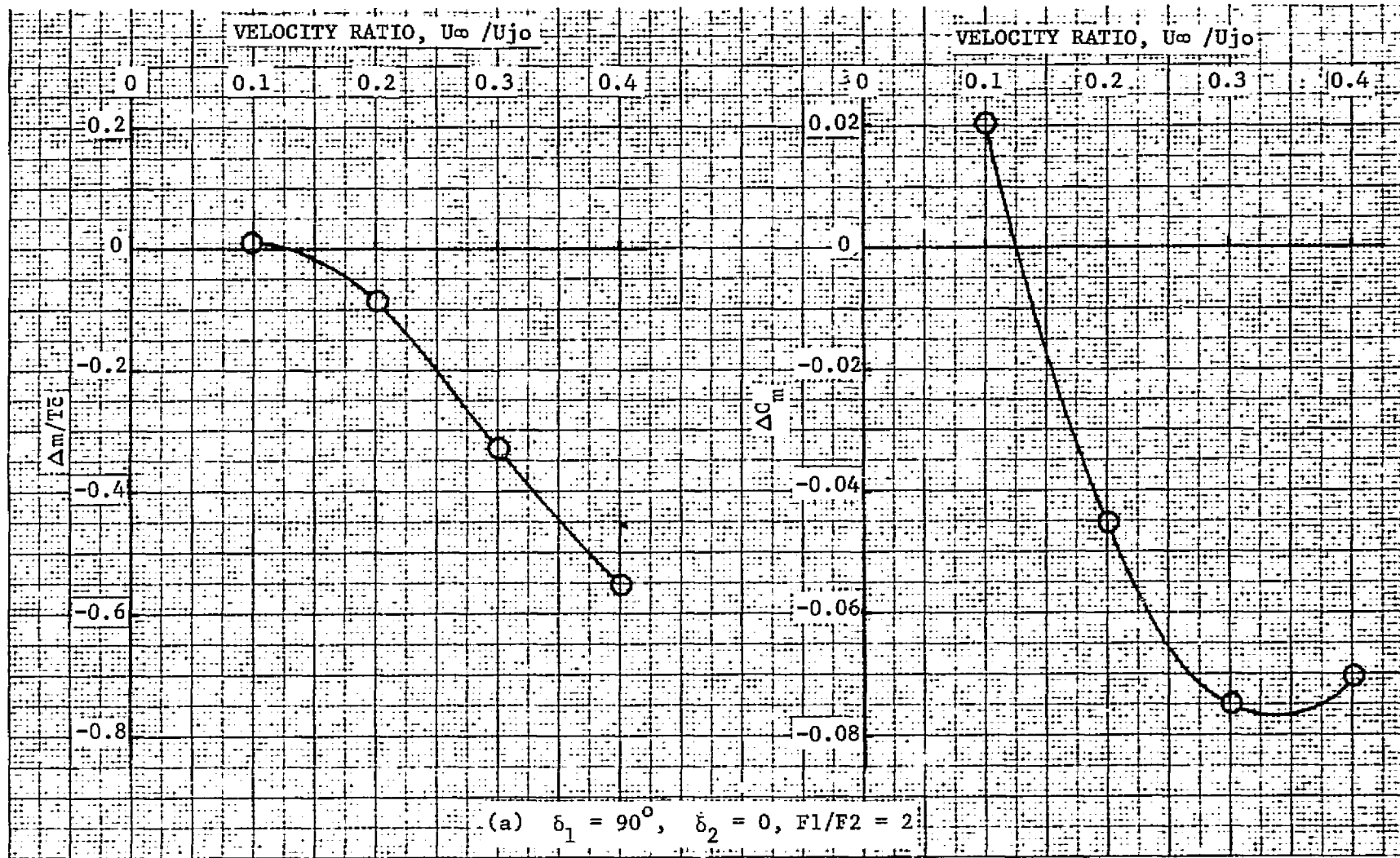


FIGURE 3-76. PROPULSION-INDUCED PITCHING MOMENT IN TRANSITION

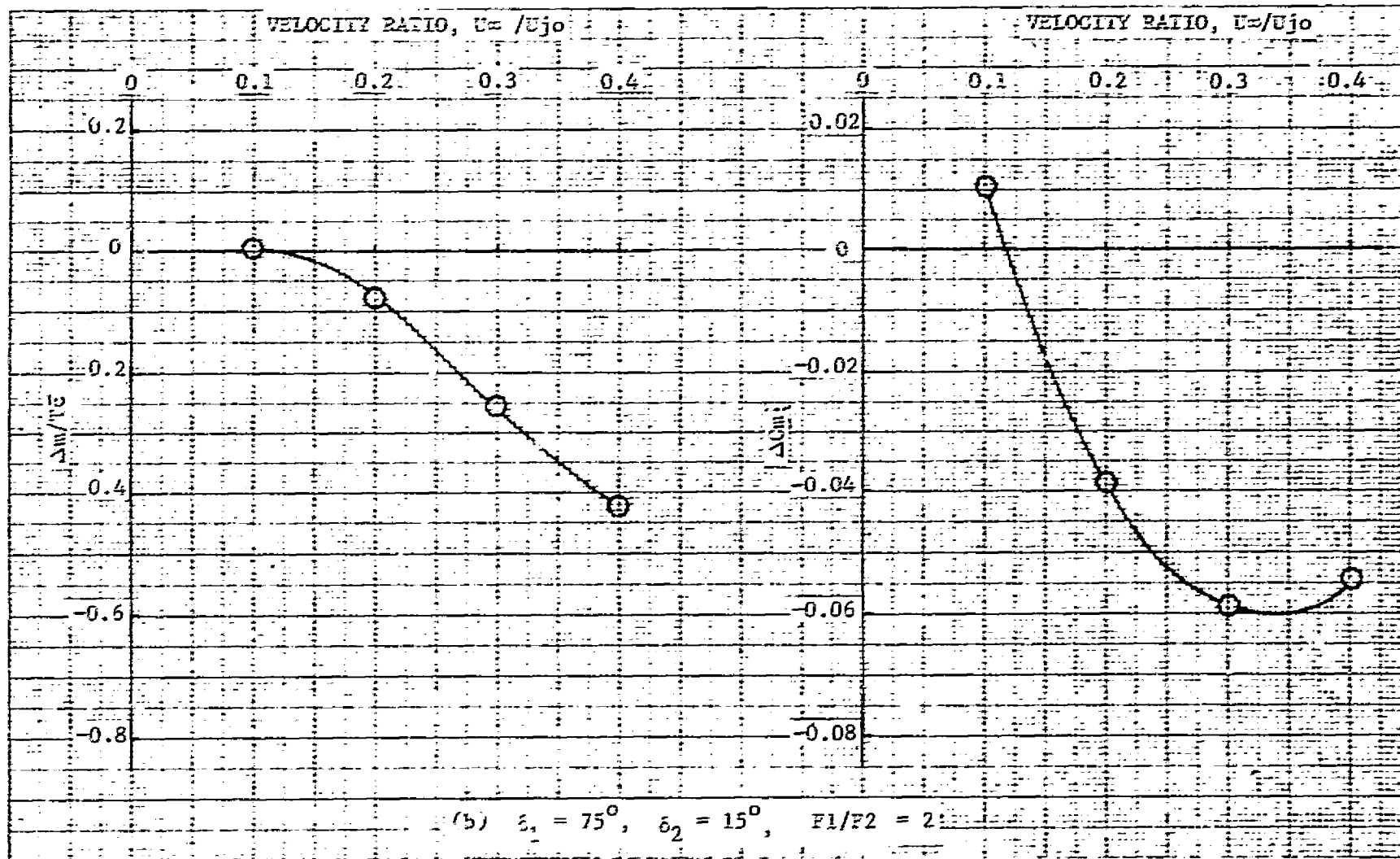


FIGURE 3-76. (CONTINUED)

NATIONAL BUREAU OF  
 STANDARDS

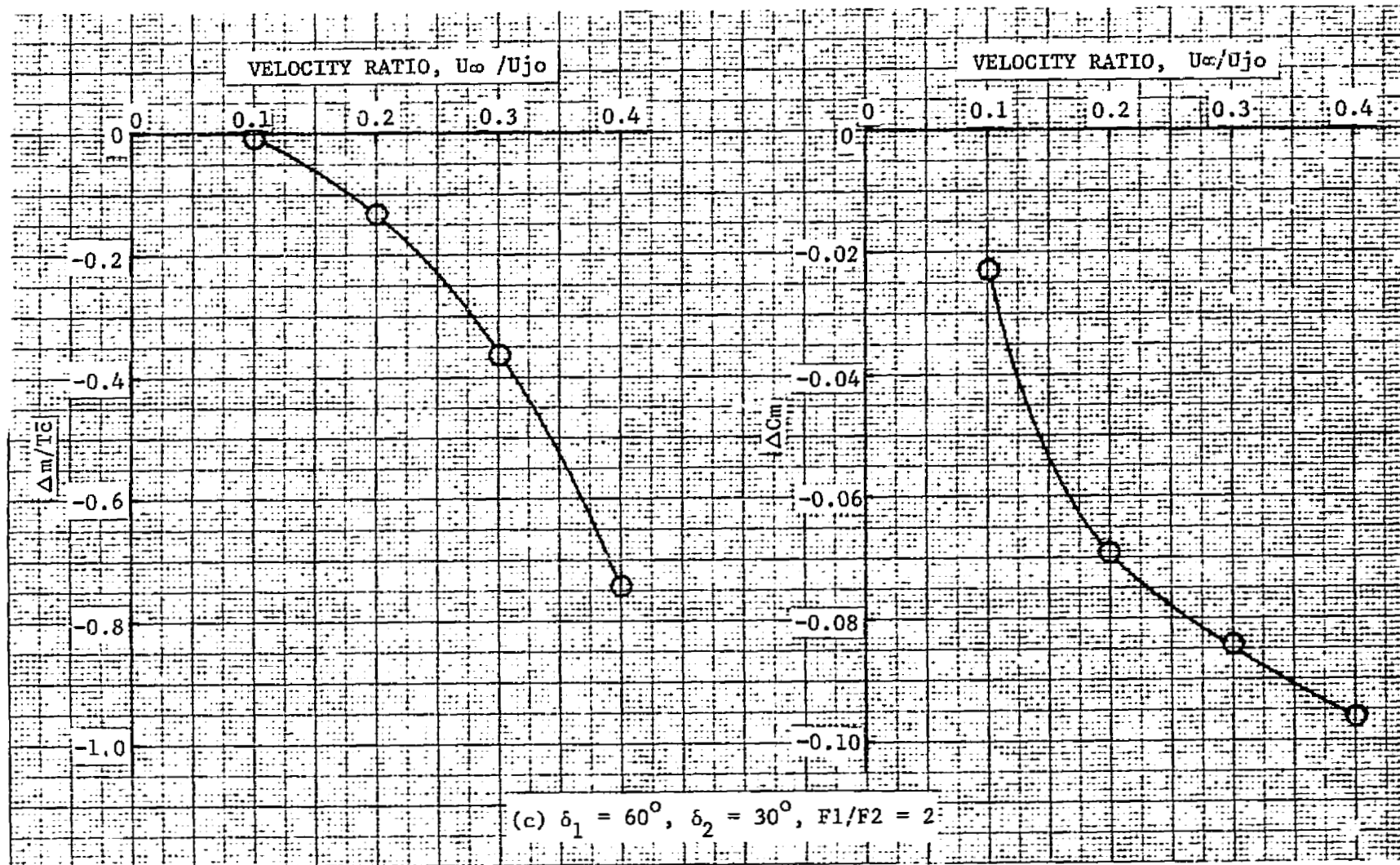


FIGURE 3-76. (CONTINUED)

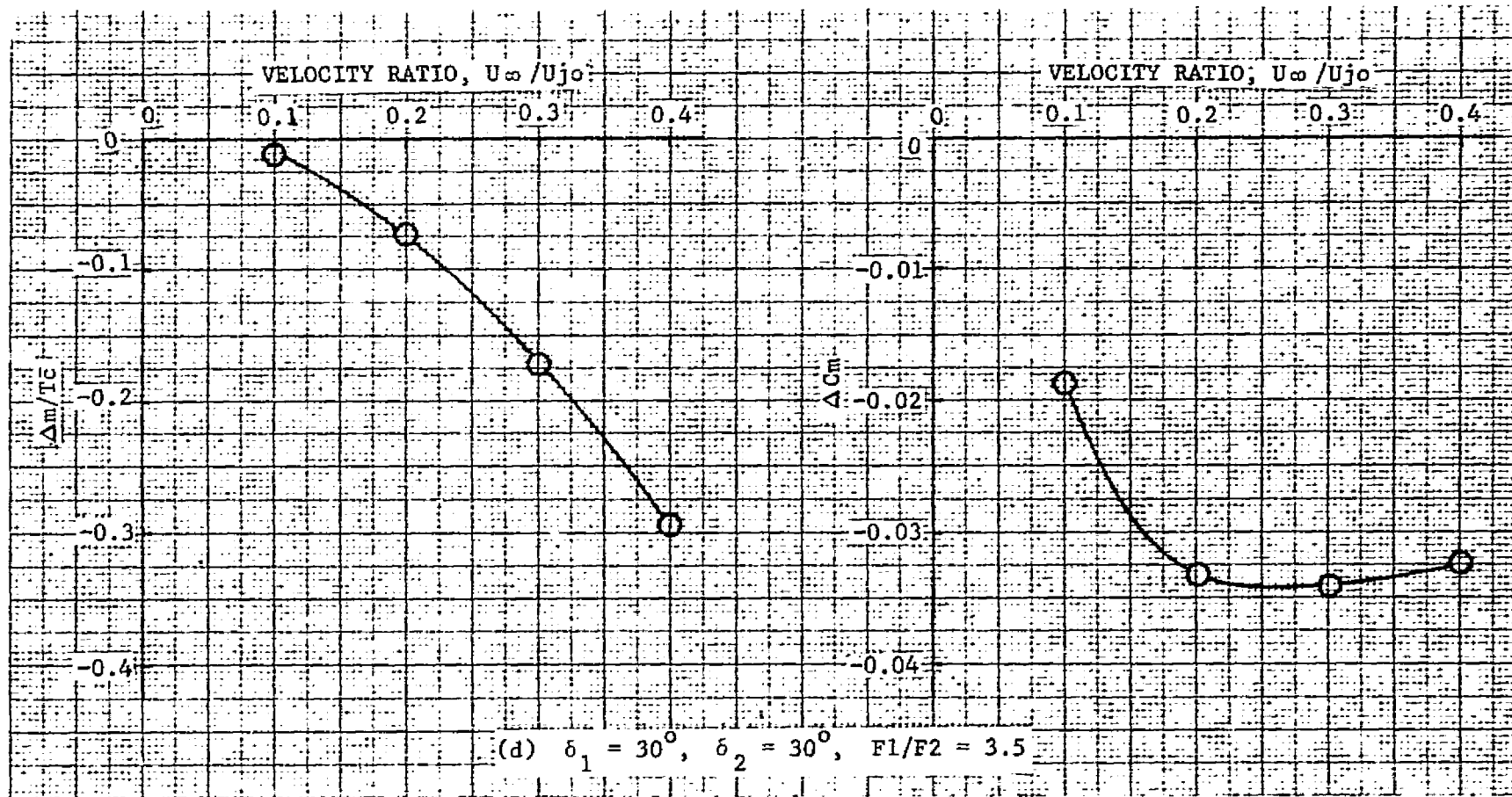


FIGURE 3-76. (CONTINUED)

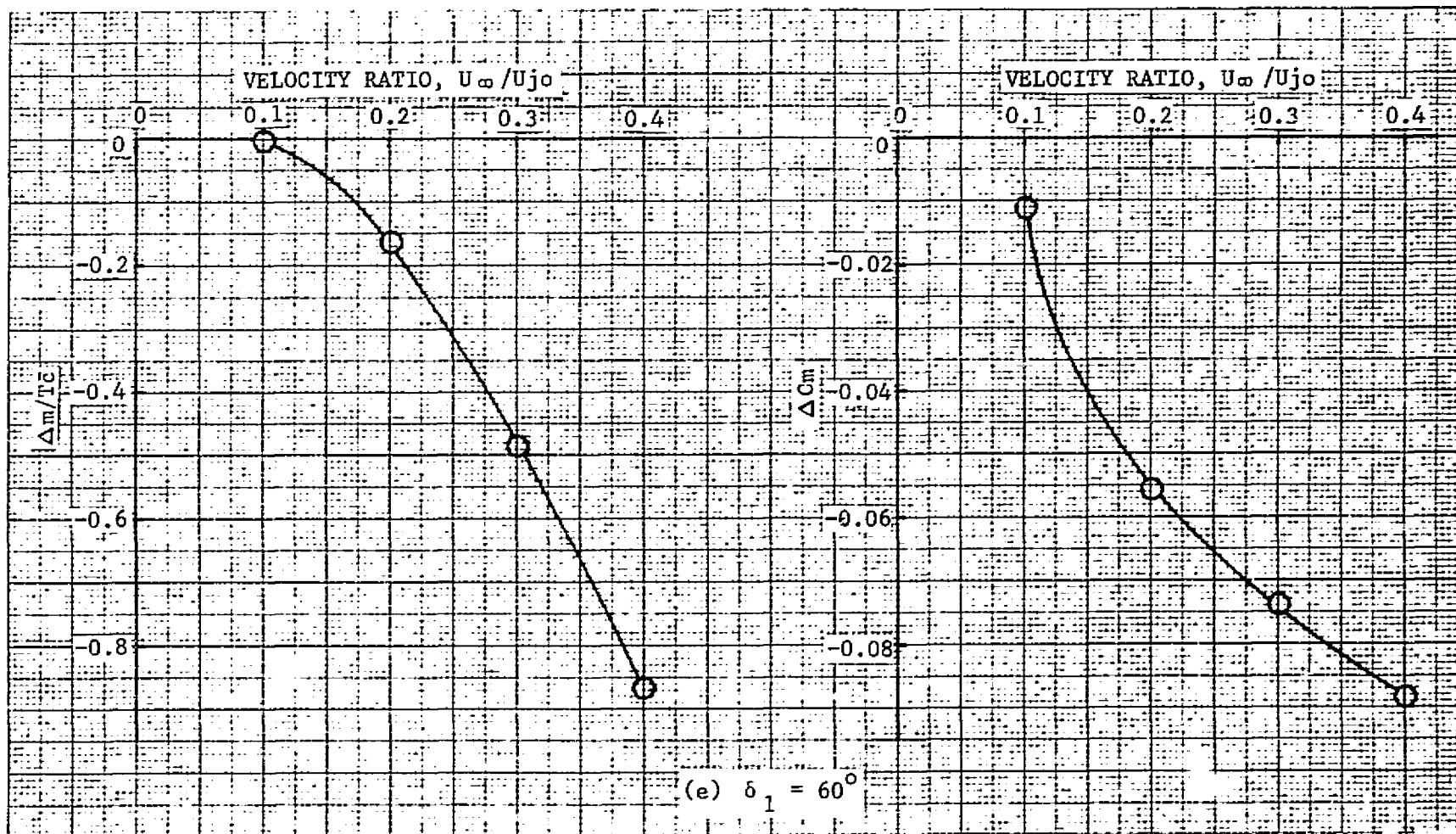


FIGURE 3-76. (CONCLUDED)

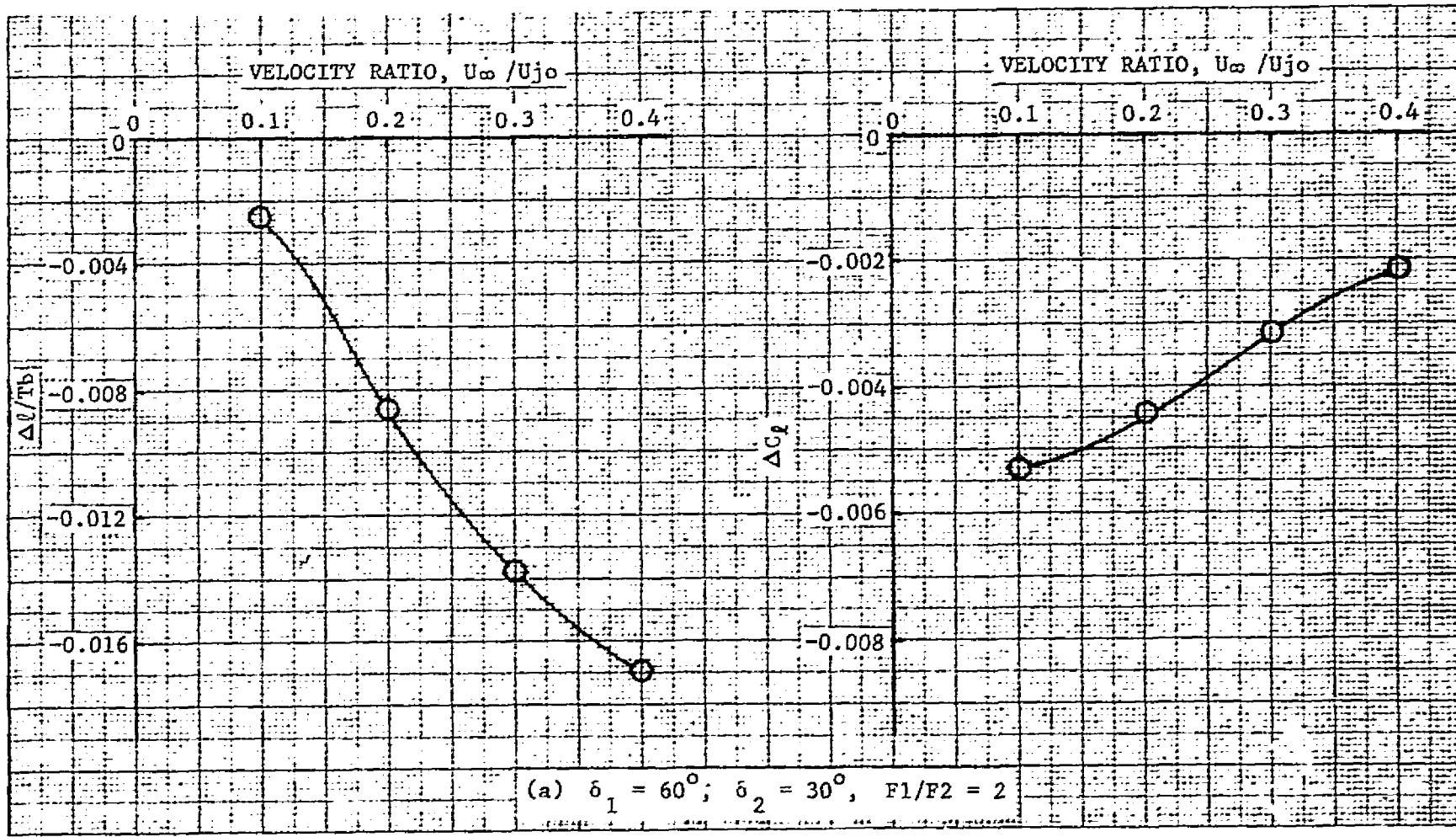


FIGURE 3-77. PROPULSION-INDUCED ROLLING MOMENT IN TRANSITION ( $\beta = 10^\circ$ )

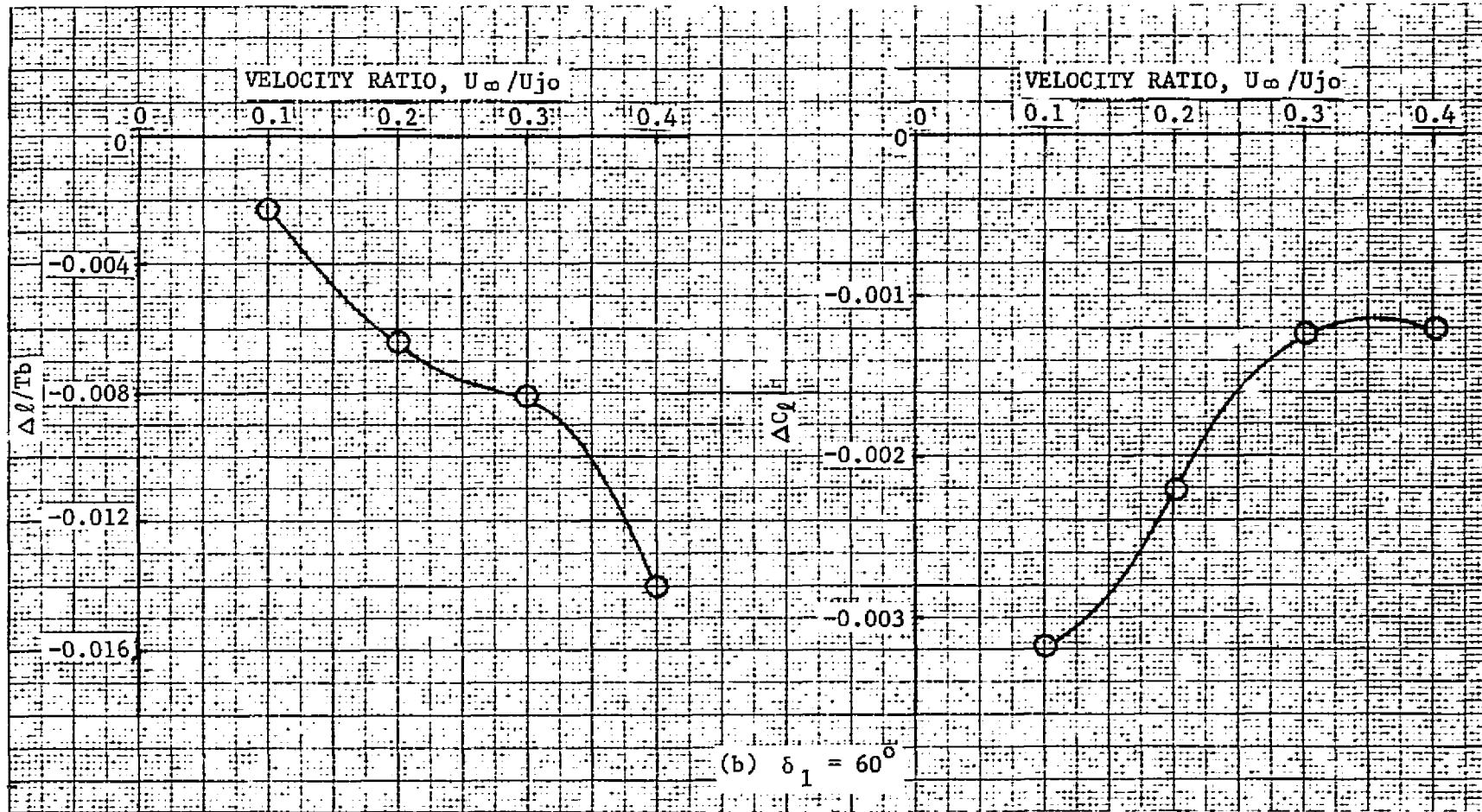


FIGURE 3-77. (CONCLUDED)

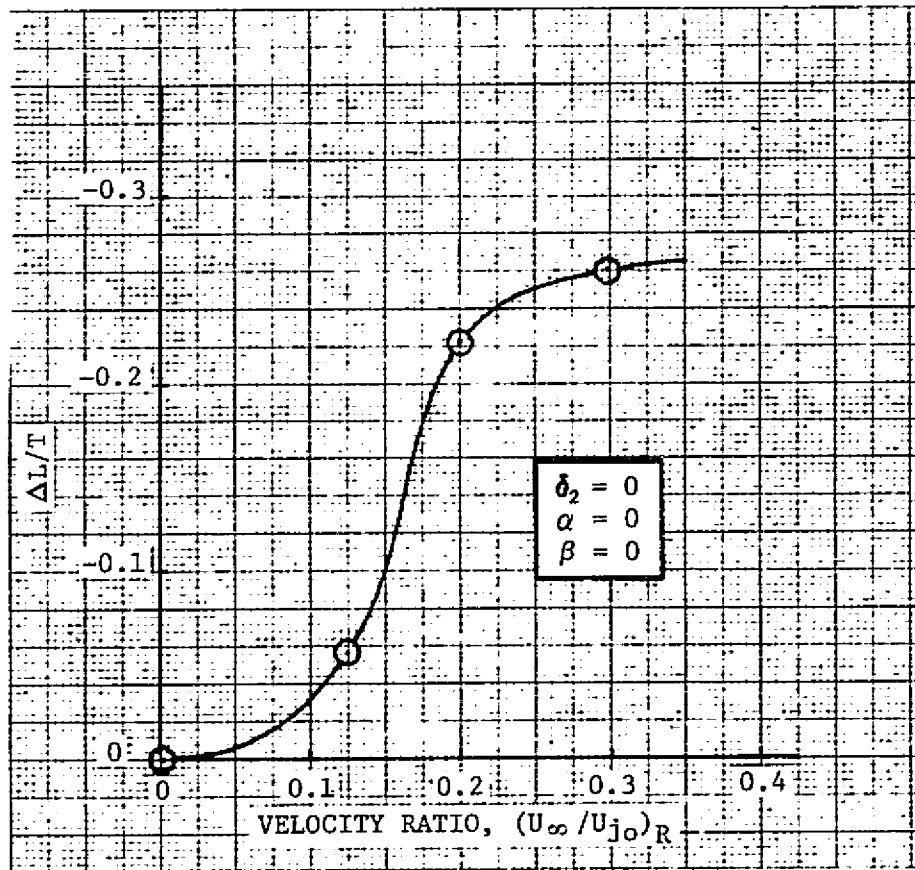


FIGURE 3-78. RALS WAKE CONTRIBUTION TO PROPULSION-INDUCED LIFT IN TRANSITION

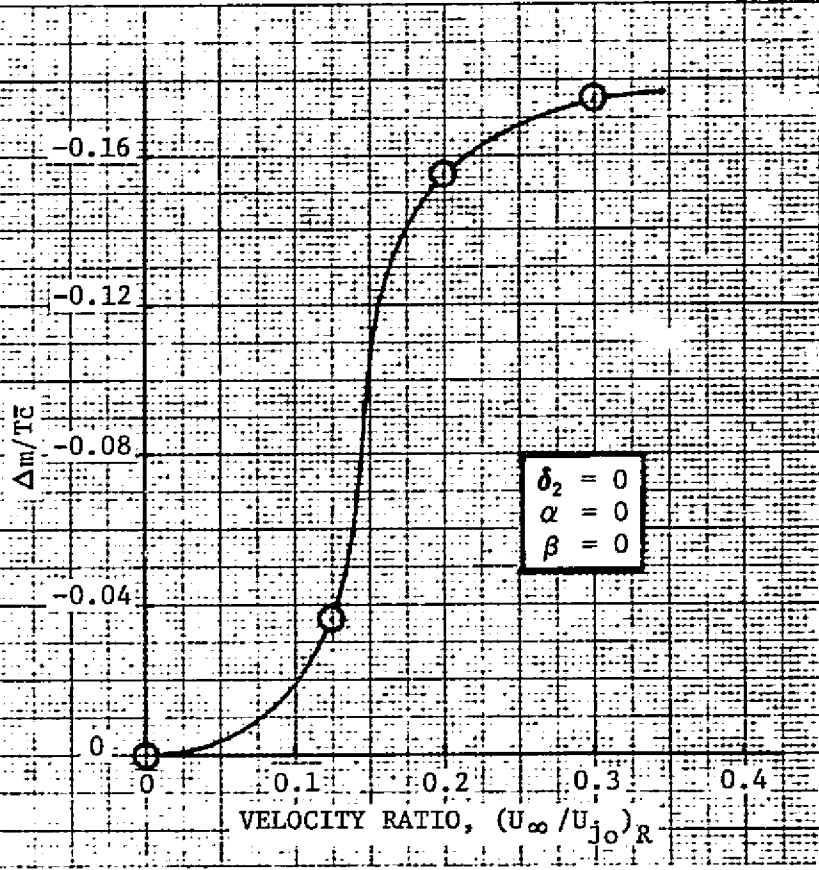


FIGURE 3-79. RALS WAKE CONTRIBUTION TO PROPULSION-INDUCED PITCHING MOMENT

ORIGINAL PAGE IS OF POOR QUALITY

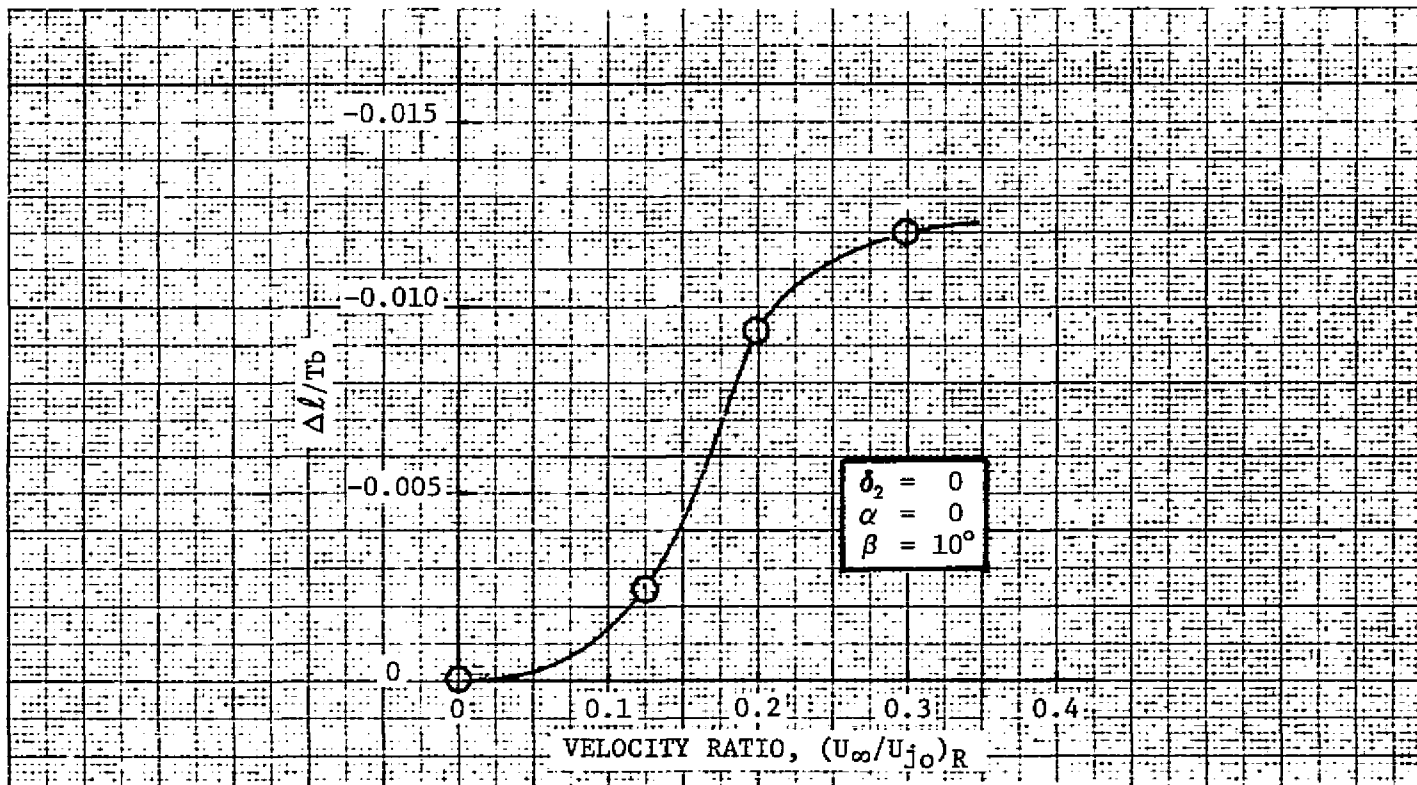


FIGURE 3-80. RALS WAKE CONTRIBUTION TO PROPULSION-INDUCED ROLLING MOMENT

ORIGINAL PAGE IS  
OF POOR QUALITY

### 3.5 CONTROLS BLENDING

Blending of the roll reaction control and the flaperon is considered first, as this axis is probably most critical. Use of RALS duct burning plus vectoring of the aft nozzles for pitch, makes the pitch and yaw axes less critical.

The roll reaction control power has been estimated for a 56 km/hr (35 kt) cross wind as a function of forward velocity. The interference losses from reaction control nozzles and airframe in a crosswind are based on experimental data while the internal duct losses have been estimated at 15 percent. At full thrust (7.26 kg/sec or 16 lb/sec fan air per engine available) takeoff weight and the highest moment of inertia, the reaction control power is slightly over 1.8 rad/sec<sup>2</sup> at all forward velocities to 278 km/hr (150 kts). With the conservative assumption that roll control power is proportional to engine airflow, the flight idle roll control power is slightly over 0.6 rad/sec<sup>2</sup> at all speeds up to 278 km/hr (150 kts.). For an attitude command system, AGARD 577 recommends a value of 0.2 to 2.0 rad/sec<sup>2</sup> for a STOL condition and 0.4 to 1.5 rad/sec<sup>2</sup> for a hover condition. Thus, to meet the mid-point of the AGARD values, the ailerons are required to provide some assistance under low power settings conditions. Low power settings would be most likely during a landing transition above the stall speed of the aircraft in order to commence deceleration to hover. Below stall speed, propulsive lift is essential to maintain the desired flight path. If the combination of reaction control and flaperons can provide the desired control power down to stall speed, and the reaction control can provide the total at hover, the system should be satisfactory.

Figure 3-81 has been developed to show the various roll control factors through a landing transition to hover. Total reaction and flaperon control power ( $40^\circ$  total deflection,  $C_{S\delta\alpha} = 0.0375$  and below stall angle of attack) are shown for both intermediate and flight idle thrust settings. The stall speeds from zero fuel weight to maximum VTOL weight together with the desired control power of about 1.4 rad/sec<sup>2</sup> are also shown.

As the weight of the aircraft decreases, so does the moment of inertia, the thrust required for support, and the available reaction control power. These effects are compensating, and the control power at hover is practically independent of gross weight. Intermediate power is not required for hover, so that roll control power at hover is 1.6 rad/sec<sup>2</sup>. This control power is still available at lighter weights and thrusts as indicated above. The other possible critical point is the lowest stall speed. At speeds higher than stall speed, it is possible that flight idle thrust could be selected. Below stall speed, as stated previously, thrust must increase to support the aircraft.

At the lowest stall speed (lightest weight), the combination of reaction control and aerodynamic control provides a roll control power of  $1.8 \text{ rad/sec}^2$  with thrust at idle. Thus, as shown on Figure 3-81, the minimum control power available varies from  $1.6 \text{ rad/sec}^2$  to  $1.8 \text{ rad/sec}^2$  at stall speed, and then increases rapidly, all compared to  $1.4 \text{ rad/sec}^2$  required.

The midpoint of the AGARD 577 specification for the pitch axis control power is  $0.6 \text{ rad/sec}^2$ . The RALS nominal temperature is  $1366^\circ\text{K}$  for static pitch balance. The temperature may be lowered to  $513^\circ\text{K}$  for nose down pitch and raised to  $2033^\circ\text{K}$  for nose up pitch. The aft nozzles can be deflected suitably or thrust level changed to maintain height. The temperature difference is less for nose up pitch and thus nose up pitch is critical. The nose up pitching hover control power available is  $0.97 \text{ rad/sec}^2$  at maximum moment of inertia and weight and  $0.69 \text{ rad/sec}^2$  at minimum moment of inertia, weight and flight idle power compared to  $0.6 \text{ rad/sec}^2$  required. During transition, a nose down moment will result from the interference effect of flow from both the RALS and aft nozzles. The airframe will have a nose up moment in transition because of flying 15 percent unstable. The moment from both increase with speed. Any small difference is estimated to be handled by aerodynamic control trim.

The mid-point of the AGARD 577 specification for the yaw axis control power is about  $0.5 \text{ rad/sec}^2$ . Available hover control power is  $0.63 \text{ rad/sec}^2$  at maximum weight, inertia and engine thrust while the control power at minimum weight, inertia and flight idle thrust is only  $0.40 \text{ rad/sec}^2$ . If the RALS could be deflected about 3 degrees over the nominal 15 degrees, the control power at flight idle could be raised to  $0.5 \text{ rad/sec}^2$  at flight idle thrust. Since the nozzle can deflect aft 30 degrees, a slight airframe modification would allow 18 degrees to the side. Very small interference on yaw control is estimated during transition, and is not considered at this time.

ORIGINAL PAGE IS  
OF POOR QUALITY

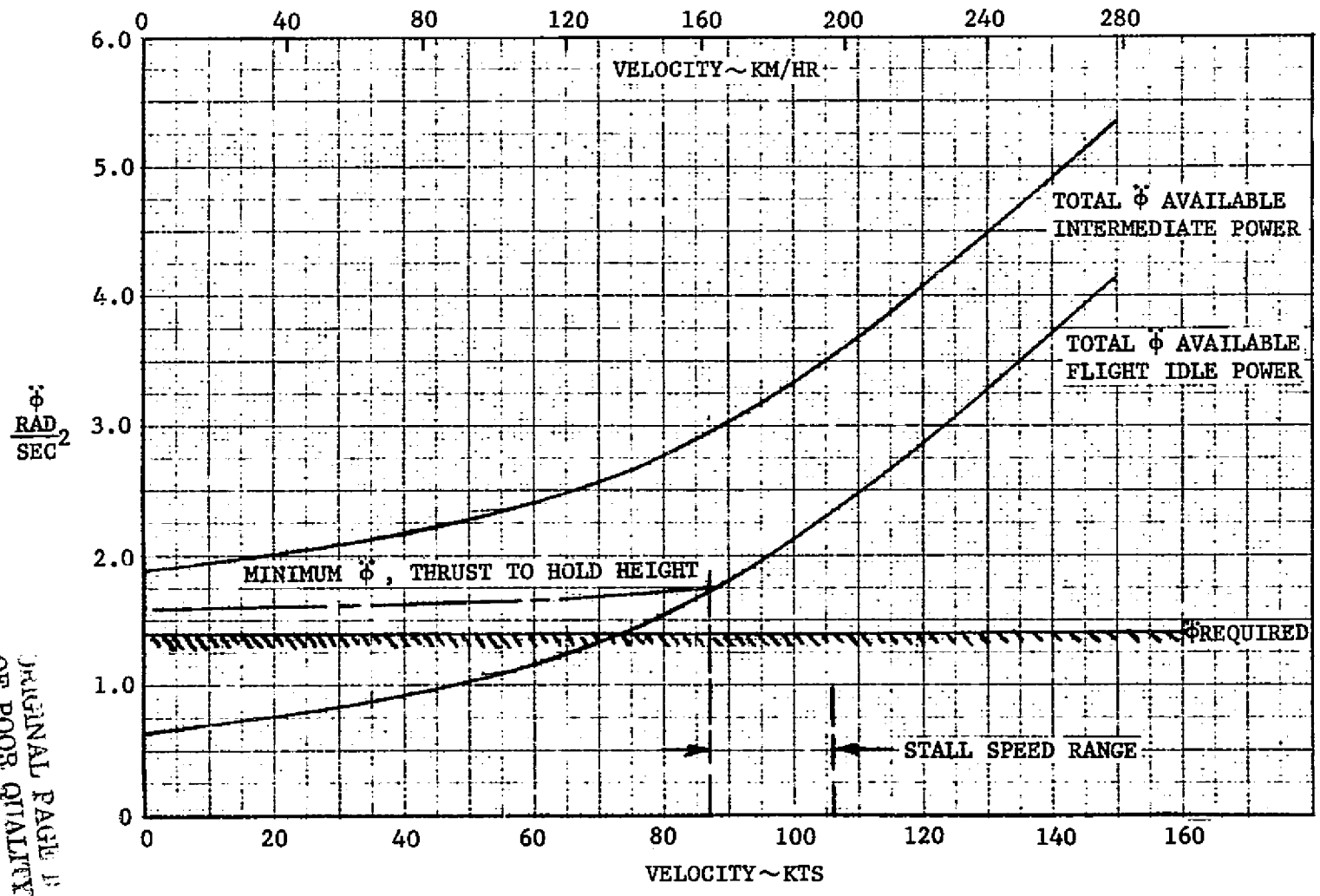


FIGURE 3-81. ROLL CONTROL BLENDING

PRECEDING PAGE BLANK NOT FILMED

## SECTION 4

### PROPULSION CHARACTERISTICS

A Remote Augmented Lift System (RALS), as described by General Electric in their SYS-GE16/VVCE6 study G1, was selected for this study. This concept uses a bypass ratio (BPR) 0.7 fan engine with a variable cycle capability including front and rear variable area bypass injectors, a variable area low pressure turbine, and a double bypass split fan. The front block of the fan is oversized to provide additional airflow for VSTOL and transonic requirements. The engine has a partial afterburner (555°K temperature rise) to provide additional thrust at certain forward flight conditions. This augmentation is not used for vertical takeoff or landing.

#### 4.1 ENGINE DESCRIPTION

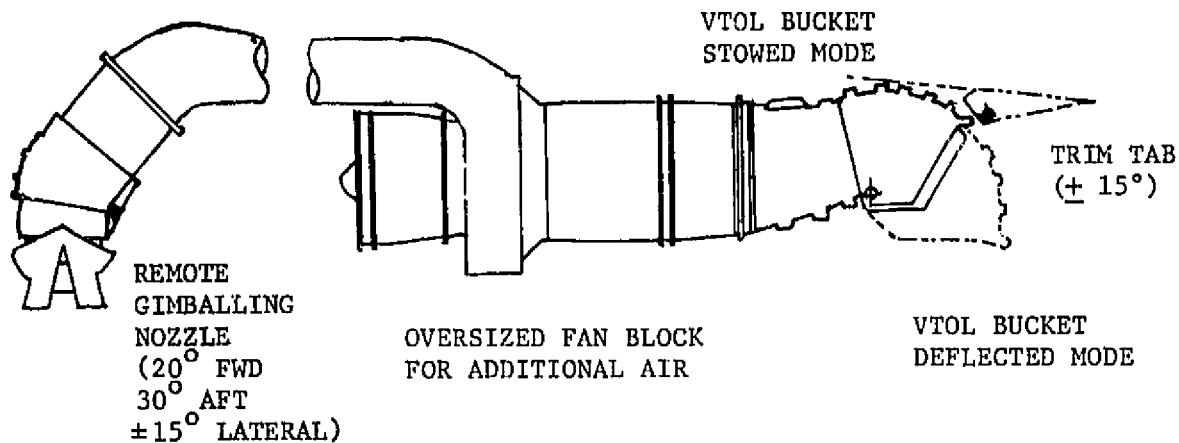
The RALS engine and installation are conceptually illustrated in Figure 4-1. During vertical takeoff and landing, all bypass air from both engines is diverted via common ducting to a forward location, where it is augmented with a simple burner and expanded through a downward exhausting nozzle. The operating temperature of the forward augmentor is normally 1370°K (2000°F). To generate a thrust change for pitch control, this temperature can be varied between 516°K (470°F) and 2033K (3200°F). Finally, the system is designed so that bypass air can be diverted on demand from the engine and used for roll control.

The engine has been sized to provide an installed thrust-to-aircraft weight ratio of 1.20 for VTO on a 305°K (90°F) tropical day in consideration of required vertical acceleration, vectoring necessary for control, and potential secondary interferences. The size necessary for VTOL approximately matches combat requirements at maximum power taking advantage of increased engine airflow at transonic speeds. Some thrust augmentation is provided by partial afterburning, however, to meet combat requirements. As the augmentation ratio is relatively small compared to other engines, the SFC at combat conditions is also relatively small.

A major advantage of using a low augmentation ratio engine is the lower specific fuel consumption (SFC) at maximum power which can significantly reduce the overall

weight of tactical fighters requiring combat persistence. The variable geometry turbine will reduce the SFC rise at reduced power normally associated with engines throttled back for cruise and loiter.

REMOTE  
AUGMENTOR



$$\begin{aligned} \text{BPR} &= 0.7 \\ T_4 &= 2030.0 \text{ K} \\ &= (3200.0 \text{ F}) \end{aligned}$$

TOTAL VTOL THRUST\* = 8296 Kg (18290 LB)

$$T/W = \frac{36580}{30000} = 1.22$$

\*INSTALLED, TROPICAL DAY 305°K OR (90°F)

FIGURE 4-1. REMOTE AUGMENTED LIFT SYSTEM (RALS)

## 4.2 PROPULSION TRADES (BYPASS RATIO STUDY)

The unique VTOL requirement must be considered, i. e. , the bypass ratio must be high enough to allow sufficient augmented remote air for a moment balance about the aircraft c. g. This is in addition to the other mission parameters which drive the cycle selection.

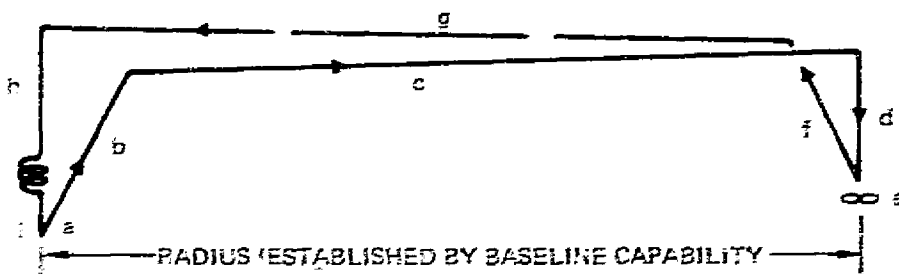
An analysis was made to determine the optimum bypass ratio of the engine for a selected mission. For this analysis, the maximum combustion temperature was held constant ( $T_{4MAX} = 2030^{\circ}K$ ) along with the overall pressure ratio (OPR = 28). The technology of the propulsion system is representative of the post-1990 time period. The GE16/VVCE4/A1 was used as the basis for this study.

The study of the effects of bypass ratio on engine cycle selection was based on the Pratt and Whitney Variable Geometry turbofan (VGT) Computer program (CCD0282). This engine model differs from the General Electric one in that the fan and core gases are exhausted separately. However, it can approximate the effect of bypass ratio on variable cycle turbofan engine performance. The basic cycle design parameters of the engine (bypass ratio, fan pressure ratio, turbine inlet temperature, etc.) were an input to the VGT turbofan deck. The airflow schedule was used to develop a similar schedule for the VGT turbofan deck. It was not possible to use the exact GE16/VVCE4/A1 RALS schedule because the airflow schedule is unique. Once the RALS engine was reasonably modeled on the VGT turbofan deck, some performance data were calculated and compared with actual RALS brochure data. The comparisons are reasonably close.

After simulation of the RALS engine was obtained, the installed engine performance to be used in the bypass ratio study was calculated as described above. The three bypass ratios studied varied from 0.7 to 1.0. The baseline bypass ratio is 0.7.

In order to evaluate the overall effects of bypass ratio on aircraft performance, a mission performance study was made. A fighter Escort sizing mission, as shown in Table 4-1, was selected. In this table, fuel consumption is shown for the various mission segments for aircraft using engines of BPR 0.7 and 1.0.

TABLE 4-1. FIGHTER ESCORT SIZING MISSION



SEGMENT	MISSION EVENT	FUEL REQUIREMENT BASIS	FUEL USED	
			926 KM (500 NM) BPR = 0.7	954 KM (515 NM) BPR = 1.0
A	START, T.O. TRANSITION AND ACCELERATE TO BEST CLIMB SPEED	45 SEC EACH, INTERMEDIATE AND MAX THRUST (VSTOL MODE), 1 MIN INTERMEDIATE THRUST (UP AND AWAY MODE) (S.L. TROPICAL DAY)	755 KG (1665 LB)	714 KG (1575 LB)
B	CLIMB TO BEST CRUISE ALTITUDE	MAX R/C AT INTERMEDIATE THRUST	222 KG (490 LB)	211 KG (465 LB)
C	CRUISE OUT	BEST ALTITUDE AND MACH NO	975 KG (2150 LB)	973 KG (2145 LB)
D	DESCENT TO 30,000 FT	NO DISTANCE OR FUEL CREDIT		
E	TASK ORIENTED COMBAT	1. ACCELERATION FROM MO. 2 TO MO. 2, 30,000 FT 2. 360° SUSTAINED TURNS AT MO. 2, 30,000 FT 4. 360° SUSTAINED TURNS AT MO. 6, 10,000 FT	556 KG (1225 LB)	531 KG (1170 LB)
F	CLIMB TO BEST CRUISE ALTITUDE	MAX R/C AT INTERMEDIATE THRUST FROM 10,000 FT	177 KG (390 LB)	162 KG (370 LB)
G	CRUISE BACK	BEST ALTITUDE AND MACH NO	848 KG (1870 LB)	846 KG (1865 LB)
H	DESCENT TO S.L.	NO DISTANCE OR FUEL CREDIT		
I	RESERVES AND LANDING	VSTOL MODE 1 MIN EACH INTERMEDIATE AND MAX THRUST ALLOWANCE UP AND AWAY MODE 10 MIN AT BEST LOITER SPEED PLUS 5% INTERNAL FUEL RESERVE	1037 KG (2285 LB)	1002 KG (2210 LB)
TOTAL FUEL			4570 KG (10075 LB)	4445 KG (9800 LB)

In making this comparison, aircraft gross takeoff weight was held constant, while the fuel weight was varied as the engine weight varied. A change from the baseline engine to the BPR=1 engine will improve the SFC enough to increase the mission radius by 10%. However, the increased engine weight will reduce this advantage in mission radius to 3% for a constant takeoff weight. As the change in engine bypass ratio will necessitate a larger engine and aircraft, the aircraft wetted area will increase by 3%. This, in turn, will mean an associated aircraft drag increase. The predicted engine weights also increase. Thus, if aircraft performance estimates were refined during the design process, and aircraft drag and weight increases were accounted for, the small 3% mission radius advantage for higher engine bypass ratios would probably vanish. From a mission performance standpoint, then there is no advantage in increasing the engine design bypass ratio above 0.7. The baseline bypass ratio of 0.7 is required for thrust balance during VTOL operations and was retained.

#### 4.3 AIR INDUCTION SYSTEM DESIGN APPROACH AND SIZING

The air induction system (Figure 4-2) is designed to operate efficiently at the critical takeoff, maneuvering, and maximum speed conditions. The design concept has a two-dimensional 7-degree ramp design with shock-on-lip operation at Mach 1.8 and angle of attack of -2 degrees (-1G maneuver at maximum speed). The 7-degree ramp provides a good compromise between recovery and spillage over the required Mach range.

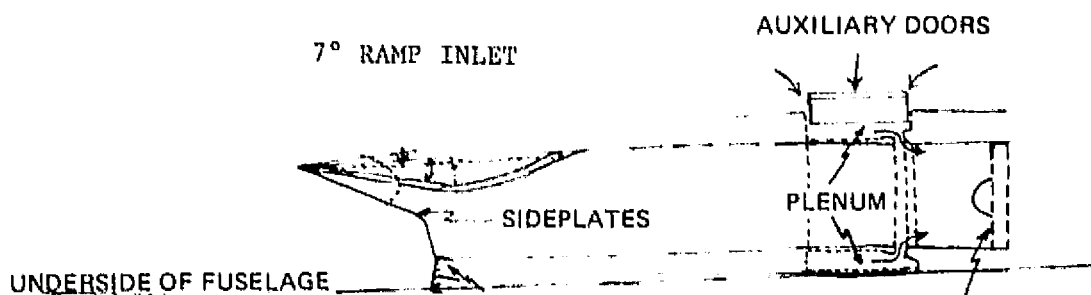


FIGURE 4-2. AIR INDUCTION SYSTEM CONFIGURATION

Inlet pressure recovery at takeoff is enhanced by the use of auxiliary inlet doors located in the duct immediately upstream of the compressor face. These doors are sized to minimize the amount of air passing through the main inlet, thus minimizing lip-induced pressure losses. Spillage drag for the inlet is held to a minimum by proper scheduling of the variable turbine features of the engine.

The baseline air inlet system is sized to match the requirements of the engines. Each main air inlet has the following characteristics:

- 1)  $0.56\text{m}^2$  ( $871\text{ in}^2$ ) capture area
- 2)  $0.45\text{m}^2$  ( $702\text{ in}^2$ ) throat area
- 3) Inlet lip thickness of 1.3 cm (1/2 inch).

The auxiliary inlet doors are sized to provide  $0.42\text{m}^2$  ( $647\text{ in}^2$ ) of flow area. The inlet duct area distribution is shown in Figure 2-3. The inlet system incorporates a ramp bleed system which removes most of the ramp boundary layer, improves pressure recovery, and reduces shock/boundary layer interaction problems. This type of ramp bleed system is used on the YF-17 air induction system. Tests have shown it is capable of providing stable inlet operation to flight speeds of M 2.2.

#### 4.4 EXHAUST NOZZLE/AFT END DESIGN APPROACH

Primary exhaust is through ADEN nozzles with a single remotely located augmentor/nozzle assembly. For normal VTOL, approximately 64 percent of the lift is provided at the primary nozzles and 36 percent by the remote augmentor nozzle. The ADEN nozzle has a vectoring capability through 90 degrees in the pitch plane during VTOL. The remote augmentor nozzle has a vectoring capability of 30 degrees aft, 20 degrees forward and 15 degrees laterally. The forward nozzle is not used in normal flight operation, but the primary nozzle flow can be vectored approximately 15 degrees in flight by the trim tab providing direct lift and fuselage aiming capability in combination with canard deflection.

The ADEN is an external expansion nozzle for which the upper aft slopes are fixed, and the throat geometry requires only minimal modulation due to the variable turbine. For this reason, the throttle-dependent afterbody drag is minimal. The two dimensional nozzle results in smooth contours that integrate easily into the aircraft.

Due to the high aspect ratio of the two nozzles in combination and the side plates on the nozzle, very little expansion and plume mixing will occur on the sides. The interfairings between the nozzle and the twin afterfairings have been shaped to avoid plume interference effects on interfairing flow and minimize scrubbing drag on the afterfairings.

#### 4.5 ENGINE INSTALLATION LOSS ASSESSMENT

Propulsion installation losses were divided into two categories: 1) engine cycle losses, and 2) propulsion-related subsystem losses. Installation factors causing engine cycle performance losses are:

1. Extraction horsepower for aircraft power systems (hydraulic and electrical).
2. Engine air bleed for the environmental control system.
3. Inlet total pressure recovery.

Drag components assigned to the propulsion system are as follows:

1. Environmental Cooling System (ECS) and Avionics System cooling airflow momentum losses.
2. Engine bay ventilation airflow momentum loss.
3. Inlet ramp and throat bleed airflow momentum losses.
4. Throttle-dependent inlet spillage drag.
5. Throttle-affected nozzle/afterbody drag.

A Northrop engine installation computer program was used. The engine data provided by GE were given with specified cycle losses. These included a power extraction of 37 KW (50 HP) and an engine compressor bleed of 0.12-0.48 KG/SEC (0.28-1.07 lbs/sec) as shown in Figure 4-3. The matched inlet recovery schedule used is shown in Figure 4-4. The recovery is almost 95 percent at takeoff, about 98 percent transonically and drops to 89 percent at M1.8. The installation program corrected the net thrust and fuel flow data for any differences between operating inlet pressure recovery and that shown in Figure 4-4. The external installation losses were also calculated by the installation program. The assessments of propulsion loss items are summarized in Table 4-2. The thrust-drag bookkeeping procedure relative to the inlet spillage and afterbody drags is the same as the "Navy" procedure used for the F-18. In this procedure, for Mach numbers of one and above, the critical inlet spillage drag is assigned to the aircraft minimum drag.

Only the subcritical portion of the spillage drag is assigned to the propulsion system. Since the external geometry of the two-dimensional ADEN nozzle doesn't vary with throttle setting, and since afterbody slopes are low, it is assumed that the throttle-dependent nozzle/afterbody drag is negligible.

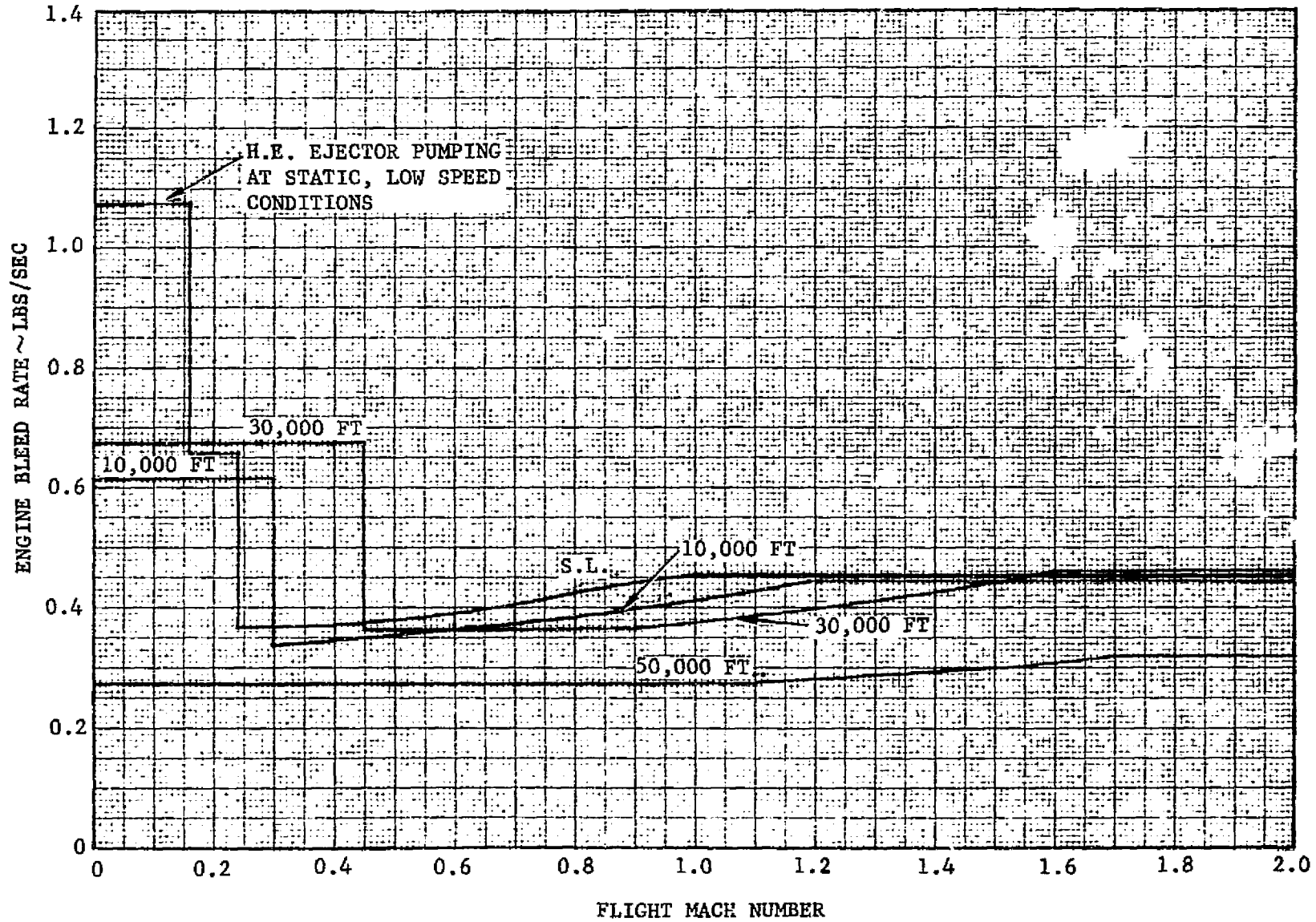


FIGURE 4-3. ENGINE COMPRESSOR BLEED RATES.

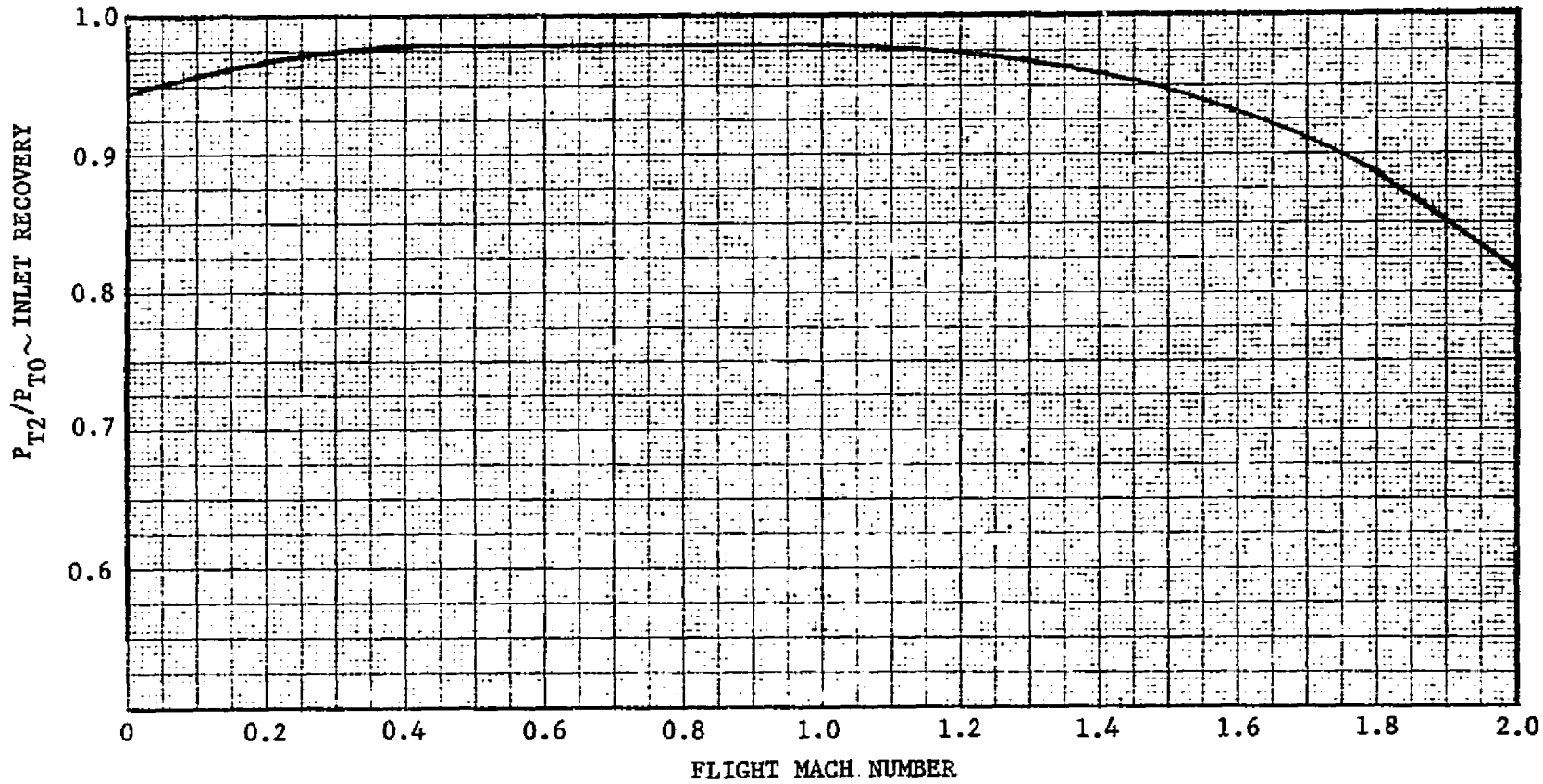


FIGURE 4-4. MATCHED INLET RECOVERY

ORIGINAL PAGE IS  
OF POOR QUALITY

TABLE 4-2. AIRCRAFT PROPULSION LOSS ASSESSMENT

ITEM	ASSESSMENT
POWER EXTRACTION	37 KW (50 HP) per engine except for certain takeoff, landing, and combat conditions where 63 KW (85 HP) is assumed.
ENGINE BLEED AIR	F-18 requirements.
INLET RECOVERY	Use modified F-17 7° ramp inlet data. Modification made for use of auxiliary inlet doors.
ECS, AVIONICS SYSTEM DRAG	ECS and Avionics ram airflows equal to three times engine air bleed. Drag equal to 1/2 freestream momentum.
ENGINE BAY VENTILATION DRAG	F-17/F-18 procedure with ventilation airflow scaled to engine size. Cooling air velocity change determined with semi-empirical technique. Drag proportional to product of airflow and velocity change.
RAMP BLEED DRAG	Scaled F-17 7° ramp bleed data used for airflow and bleed airflow velocity change. Drag proportional to product of airflow and velocity change.
INLET SPILLAGE DRAG	Calculated with Sibulkin method. For Mach numbers $\leq 1$ only the subcritical inlet spillage drag is assigned to the propulsion system. The critical spillage drag is assigned to the aircraft minimum drag.
THROTTLE- DEPENDENT NOZZLE/ AFTERBODY DRAG	Nozzle is a 2-D ADEN type. Throttle-Dependent drag is assumed negligible.

The effects of the tropical day atmosphere ( $T = 305^{\circ}\text{K}$ , sea level) on installed engine takeoff performance was supplied by G. E.

#### 4.6 INSTALLED ENGINE PERFORMANCE

Engine performance is proprietary to General Electric and is not presented in this report.

#### 4.7 ROLL REACTION CONTROL

In the hover and transition flight regimes, roll control is provided by wingtip mounted reaction nozzle jets. The roll reaction control system is composed of left and right-hand subsystems. Each subsystem consists of (1) a feeder pipe which transfers bleed air from the engine fan duct through the wing to (2) a wingtip plenum chamber and then exhausts it through (3) a reaction nozzle to create thrust and rolling moment. The reaction control subsystem for each wing has been designed for a maximum flow rate of 7.2 kg/sec (16 lb/sec). The fan duct air is supplied at a stagnation temperature of 516°K (930°R) and pressure of 4.3 bars (62 psia). To ensure low feed pipe pressure losses, the pipe is sized so that the pipe flow is  $M = 0.4$  at the maximum flow rate. To keep pipe diameter reasonable, a dual parallel pipe system is used. The pipe inner diameters are 8.3 cm (4.0 in.). The wingtip reaction nozzle is of the convergent type and has an exit diameter of 11.5 cm (4.5 in.). The maximum reaction thrust from each wingtip nozzle is 420 kg (925 lb).

PRECEDING PAGE BLANK NOT FILLED

SECTION 5  
AIRCRAFT DESIGN

The aircraft structural design and various systems were investigated to a limited depth. The intent was to insure that the configuration was sufficiently credible to justify a more detailed aerodynamic and propulsion integration analysis.

5.1 STRUCTURAL DESIGN AND ANALYSIS

5.1.1 Design Criteria

Current military specifications were reviewed to establish the applicability of available requirements for structural design of VSTOL aircraft. Results indicated that although current MIL-SPEC requirements provide adequate criteria for operation as a conventional airplane; appropriate criteria must be developed to provide a basis for structural design during both hover and transition modes of flight. Criteria for hover require specification of thrust forces, inertia effects, engine gyroscopic effects, and crosswind forces. Control requirements for maximum load factor maneuvers and for maneuvers induced with maximum control deflection must be defined to provide for evaluation of the effects of rapid changes in trim, moment shifts, and interactions between aerodynamics and propulsion forces during transition.

The thermal environment of structure in areas exposed to propulsion system effects has been reviewed utilizing F-18A design experience and available data. Temperature limitations were established as follows:

1. RALS and Engine Compartments were designed with appropriate cooling flows such that the temperature distribution did not exceed the design limits of adjacent structure. Engine cooling airflows were sized such that aluminum airframe components were not exposed to temperatures in excess of 120°C (250°F) with titanium used in areas where higher temperatures may be experienced. Steel structural components were not exposed to temperatures greater than the design thermal level.

2. Reaction control duct walls were considered exposed to the same temperature as bleed air from the fan duct; approximately 240°C (470°F).

### 5.1.2 Structural Materials

Advanced composite materials were selected as the primary materials of construction for both strength and stiffness-critical applications. Not only are lightweight structural components possible through efficiently tailored properties and higher specific strength/stiffness, but lower fabrication costs result through integral or one piece design concepts.

Advanced metallic materials were selected for areas of extremely localized loading as well as severe thermal, acoustic, moisture, and corrosive environmental/operational conditions. A proper blend of the application of aluminum powder metallurgy, titanium superplastic forming plus diffusion bonding will result in lightweight, low cost, and durable advanced metallic material airframe components in the 1990's.

### 5.1.3 Structural Description

The aircraft structure is shown in Figure 5-1. Major structural components include a fuselage with integrated nacelles, side tie wing panels, and twin, pivoted, vertical stabilizers and canard panels.

Fuselage Structure. The fuselage is a semi-monocoque structure of stressed skin panels stabilized by edge members, bulkheads, and frames. Frame spacing is based on trade studies made for both honeycomb sandwich and integrally stiffened skin panel designs. Typical of most airframe designs, a common frame spacing is not achievable due to support frame or compartment bulkhead location constraints. However, studies have shown that by optimizing honeycomb panel thickness or integral stiffener heights within any specific bay based on local loading conditions, near optimum panel weight is obtainable for frame spacings varying from 38 cm (15 in) to 102 cm (40 in). An average frame spacing of approximately 51 cm (20 in) has been selected for this design based on system routing support and battle damage considerations.

For ease of producibility the fuselage is divided into three major sections: a forward section from FS 25 (10) to FS 610 (240), a center section from FS 610 (240) to FS 1020 (401.5), and an aft section from FS 1020 (401.5) to FS 1453 (572).

The Forward Fuselage contains radome, radar bay, nose landing gear, cockpit, remote augmentor, and avionics bay.

The Center Fuselage contains all main body fuel tankage and access provisions. Fuselage fuel is contained in two balanced fuel bays, with the forward bay bounded by bulkheads at FS 610 (240) and FS 793 (312) and an aft fuel bay bounded by the FS 793 (312) and FS 968 (381) bulkheads. The Center Fuselage also contains left and right hand canard torque tube and actuator support provisions, left and right hand upper missile bays, ECS bay, leading edge flap actuator, wing forward attach provisions, left and right hand auxiliary engine inlets, and the forward engine bay bulkhead at FS 1020 (401.5).

The Aft Fuselage contains engine bays, engine mount provisions, engine bay and engine accessories access doors, hydraulic reservoirs, and wing attach provisions.

Wing Structure. The wing consists of left and right hand panels attached to the fuselage with twenty-six shear pins, thirteen each side. Forward and aft-most attachments at FS 968 (381) and FS 1342 (528.5) react vertical shear only. Attachments at FS 1020 (401.5), FS 1109 (436.5), FS 1171 (461.0), FS 1226 (482.5), and FS 1287 (506.5) react both vertical shear and wing bending moment. Wing drag loads are reacted by separate fittings located between FS 1109 (436.5) and FS 1171 (461.0). Each wing panel consists of a fuel containing main structural box, leading edge flap, segmented trailing edge flaperons, and afterfairings which house the main landing gear, integral fuel tanks, inboard flaperon actuator and avionics.

The main structural box is a thick skin, multispar construction fabricated of advanced composite materials. Spar axes are swept three and one-half degrees aft to allow inline drilling of all wing bending moment attach holes. Outboard flaperon actuators and bootstrap members at WS 305 (120) are located below the wing negating the need for internal ribs within the wing fuel bay. The front spar supports leading edge flap rotary actuator loads through canted ribs attaching to a forward auxiliary spar. The area between the forward auxiliary spar and front spar is used for routing hot air ducts to wingtip reaction control nozzles. Upper surface access doors are provided forward of the main structural boxes for access to

wing fuel systems. Main landing gear trunnions attach directly to the FS 1109 (436.5) main spars.

Leading edge flaps and trailing edge flaperon panels are of full depth honeycomb sandwich construction fabricated of advanced composite materials. Metallic inserts, cocured with the panel, are at hinge or actuator attach locations. Each afterfairing is cantilevered aft of the main wing structural box, supported with moment ties to the rear spars and vertical tension ties to the main spars through the wing lower surfaces. Sidewalls on each side of the main landing gear wheel well act in differential bending to provide both vertical shear and side moment reaction. An integral fuel tank is contained between FS 1349 (531.0) and FS 1483 (584.0). Vertical stabilizer torque tubes are supported between aft fuel bulkheads and frames at FS 1504 (592.0), with vertical stabilizer actuators and bootstrap beams extending forward along the upper fuel decks. Inboard flaperon actuators are mounted to the inboard wheel well sidewalls. The area between FS 1504 (592.0) and FS 1600 (630) houses avionics.

Canard and Vertical Stabilizer Panels. Left and right hand canard and vertical stabilizer panels are similar in construction. The panels are single spar, full depth honeycomb, bonded assemblies with advanced composite facings. A single piece, machined steel detail forms each bending/torque tube, root rib splice, and inboard spar segment. Advanced composite outboard spar segments and composite root rib details can be cocured with the steel details after which metallic leading and trailing edge darts, core and facing layups can be added and each assembly cocured in a final operation.

#### 5.1.4 Structural Analysis

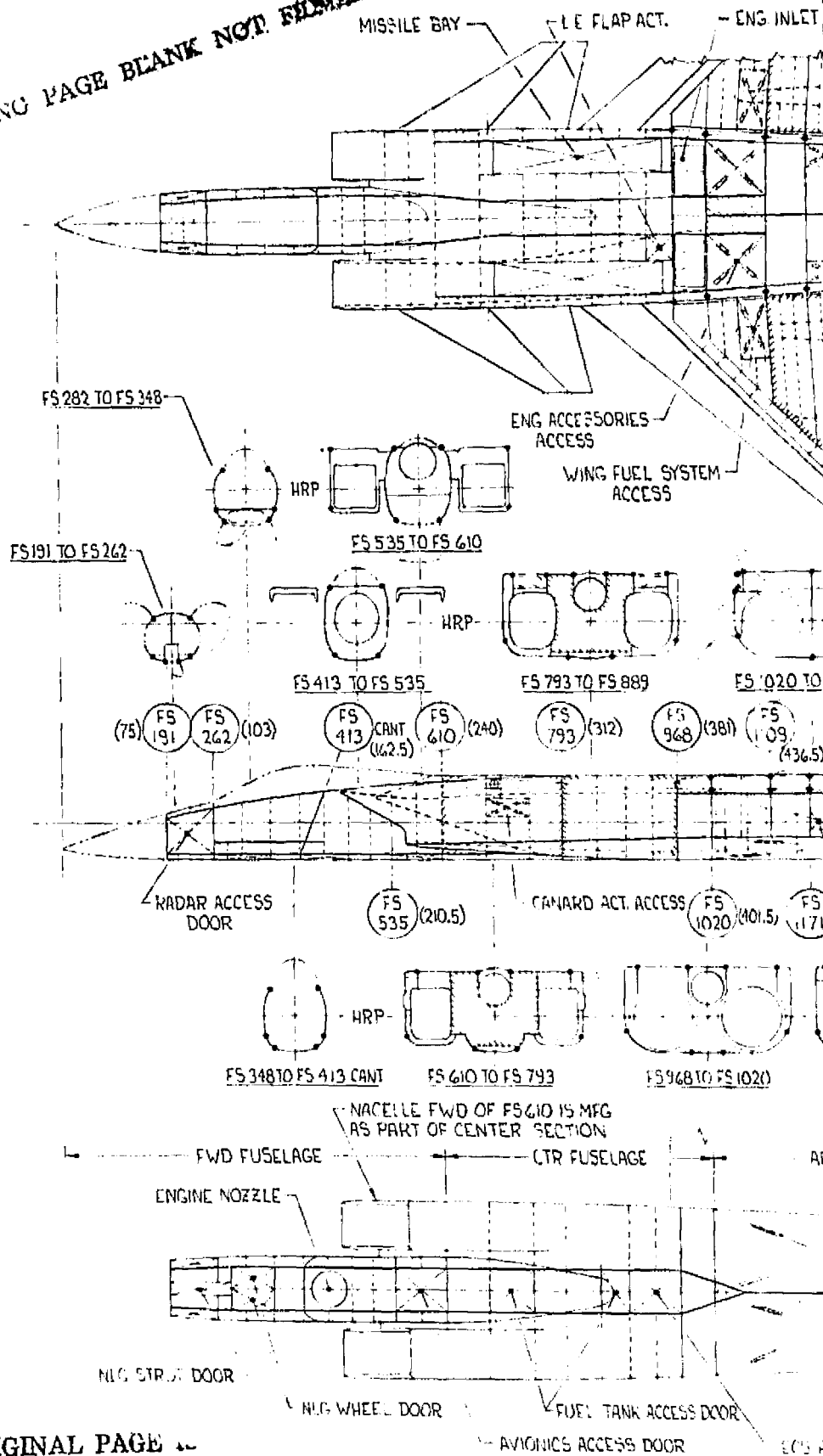
The basic structural concepts used are standard military aircraft approaches and can be adequately substantiated using current military specifications established for structural integrity. Construction of the aircraft is such that compliance with the appropriate manufacturing and process requirements together with adequate stress/damage tolerance analysis and static/fatigue testing will result in unrestricted service operation within the strength envelope.

Twin afterfairings which are installed on the inboard trailing edge portion of the wing carrying 10,700 N (2,400 lb) of fuel could create a potential flutter problem. Motion of each afterfairing would be further complicated by forces acting on the vertical stabilizer placed upright on the rear portion of each afterfairing.

Investigation of the flutter problem was initiated by comparison with a similar known configuration. In the past, Northrop experienced a possible flutter problem in designing the X-21A wing, which was equipped with a laminar flow control pumping system nacelle in the inboard trailing edge portion of the wing. Comprehensive analytical work along with flight tests were performed to evaluate reduction of flutter speeds of the airplane due to the nacelle pitch frequency in the anti-symmetric modal behavior.

Modal characteristics of the twin afterfairings on the study aircraft wing were estimated using data from an existing finite element wing model. The lowest uncoupled afterbody pitch frequency was found to be 14 Hz, considerably higher than 8 Hz of the X-21A nacelle pitch frequency. Since the analysis was conducted using a low elastic-to-rigid ratio delta wing structure, the frequency in the actual design could be 30 percent higher than the above mentioned value. Consequently, this would increase the flutter speed.

THIS PAGE BLANK NOT FILMED

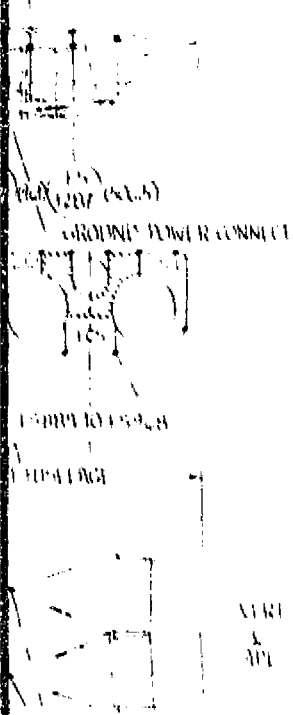
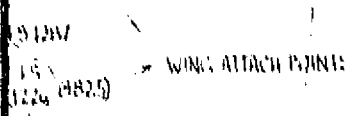
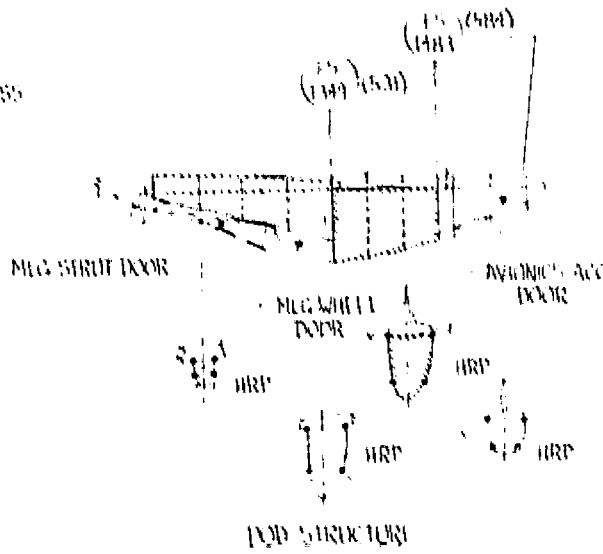
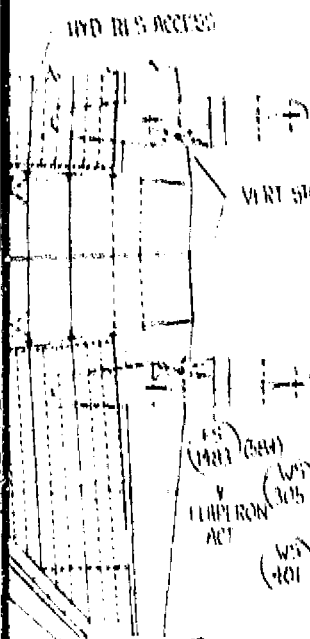


ORIGINAL PAGE OF POOR QUALITY

FIGURE 5-1. STRUCTURAL DIAGRAM

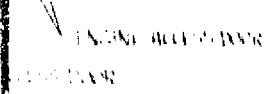
FOLDOUT FRAME

ALL DIMENSIONS  
 "A" DIMENSIONS ARE IN INCHES UNLESS OTHERWISE NOTED  
 CONVERTED DIMS TO METRIC



- 1. [Symbol] DENOTES EQUIVALENT INCHES
- 2. [Symbol] DENOTES LONGITUDINAL CONTINUITY SHEAR PANEL
- 3. [Symbol] DENOTES TIE-BRICK BOUNDARIES
- 4. [Symbol] DENOTES STRUCTURAL ACCESS DOOR
- 5. [Symbol] DENOTES NON-STRUCTURAL ACCESS DOOR

SCALE: 1" = 10" INCHES  
 1:100 CENTIMETERS



2. **BOLDOUT FRAME**  
**ORIGINAL**  
**OF POOR QUALITY**

## 5.2 FLIGHT CONTROL SYSTEM

### 5.2.1 Hover and Transition Regimes — Normal Operation

One of the most frequent complaints about previous VSTOL aircraft is the excessive pilot workload during the transition between aerodynamic and powered-lift configurations and during the hover period. The aircraft described in this report has 11 parameters available at the beginning of the landing transition (and end of the takeoff transition) to control its forces and moments, and 8 controllable parameters when solely in the powered-lift configuration. Such a large number of controls, along with their mutual interactions, would make extraordinary demands on the abilities of even a highly-skilled pilot. Consequently, the control system shown conceptually in Figure 5-2 was conceived to reduce pilot workload. Its main features are:

1. The number of cockpit controls is reduced to the familiar five (pitch and roll stick, rudder pedals, and left and right throttle controls) plus a new sixth control which commands vertical speed;
2. The cross-axis coupling between controls is greatly reduced;
3. The aircraft response to cockpit controls is "natural"; i. e., similar to its response when in the conventional aerodynamic-lift mode.
4. The transition phase is fully automated;
5. The system readily lends itself to expansion to fully automated landings and takeoffs, depending upon the quantity of earth-referenced data available.

The heart of the control system is the Crossfeed Matrix and the two Augmentation blocks. These blocks, in the Manual mode, achieve the following. 1) make pitch rate proportional to fore-aft stick movements; 2) make roll attitude proportional to lateral stick displacement; 3) Maintain zero lateral speed (via bank angle) when no stick input is present; 4) make altitude rate proportional to closure time of the Speed Control switch; 5) make fore-aft speed proportional to throttle lever position; 6) make heading-rate proportional to pedal inputs. Appropriate crossfeed terms are provided to minimize coupling between the three-attitude command and 2 speed command loops.

The details of the Attitude Augmentation block are shown in Figure 5-3. Fore-aft stick motions,  $\Delta Sp$ , in excess of threshold "b" command pitch rates proportional to stick displacement (or force) from neutral. In the neutral position, the system is a pitch attitude hold system. The high gains used for  $K\theta$ ,  $Kq$  and  $KaN$  will result in a

rapid, wide-bandwidth system. The prefilter slows the system down to a level comfortable to the pilot and maintains this response for a wide range of flight conditions. Not shown is the gain scheduling which may be required as a function of dynamic pressure or an appropriate alternate parameter.

Lateral stick movements above threshold "a" command attitude proportional to force (or displacement). For stick inputs below the threshold, the loops act to drive lateral speed to zero. This keeps yaw accelerations caused by lateral deflections of the forward nozzle from causing lateral speed changes. The lateral accelerometer signal  $a_y$ , including its  $g \sin \phi$  component, is approximately integrated by the large time constant lag to form an approximate lateral speed signal  $V_{APPX}$ . This signal is then passed through a gain and an integration and forms a roll command signal. Appropriate gain scheduling will be provided.

In the aero-lift regime, the rudder is driven to achieve turn coordination. In the powered-lift regime, pedal movements command a heading rate-heading hold system similar to the pitch axis.

The details of the Speed Augmentation block, which controls fore-aft speed and vertical speed, are shown in Figure 5-4, while Figure 5-5 gives the overall view of events occurring during the landing transition. Fore-aft speed is controlled as follows. As the airspeed falls below a certain value, the Land-Takeoff switch is transferred to the land position and a 90 degree step is applied to Rate Limit 1, whose output, about 5 deg/sec, generates the main command to rotate the rear nozzle to 90 degrees. As the airspeed drops below about  $1.1 V_{STALL}$ , SW1 transfers to the -0.1 g position and commands a -0.1 g longitudinal deceleration. The acceleration error signal, softened by Rate Limit 2, then modulates the rate at which the rear nozzle is deflecting.

During this period, only the rear nozzle is being driven, but thrust is also available from the forward nozzle, whose angle is essentially vertical at this time.

After the aircraft decelerates to about 30 knots, SW1 returns to the center position and the deceleration command is removed. When the rear nozzle is within 10 degrees of vertical ( $\theta + \lambda_R > 80^\circ$ ) or  $V_a < 56.2$  km/s (30 kts), SW2 transfers and a ground speed or airspeed hold loop is activated. Speed errors out of  $K_u$  drive the fore and aft nozzles together. The pilot can alter the automatic deceleration profile at any time by positioning his throttle levers, which now vary fore-aft speed via nozzle angle position, rather than by thrust level as in conventional flight.

The pitch attitude signal fed to the fore and aft nozzle-angle command signals maintains the nozzle angles fixed with respect to earth (not aircraft body axis) and thus decouple pitch attitude from the fore-aft speed loop. The speed error and longitudinal acceleration signals also decouple the modes, but the pitch signal provides more anticipation in the event it is needed.

Operation of the vertical speed portion of the Speed Augmentation block is as follows. Prior to the transition initiation point, SW4 is in the position shown and the K4/S block is synchronizing any altitude rate and normal acceleration signals to zero. At the beginning of transition, SW4 transfers to the center position and the commanded thrust magnitude, TRC and TLC, is varied to maintain the altitude rate existing at the beginning of transition (which is stored on K4/S). When the rear nozzle is within 10 degrees of vertical or the altitude becomes less than 15.2 m (50 ft). SW4 moves to position A and the output of the K4/S block decays to zero to command zero sink rate. The pilot now establishes the landing sink rate with his Speed Command switch. This is a 3-position spring-loaded-to-center switch (the dive brake switch can be used for this function) which is active during all landing and takeoff transitions. The commanded vertical speed is proportional to the duration the switch is held off-center.

Since the thrust level required prior to transition is small (especially if a steep descent angle is being flown), and a large thrust level is required during hover, a means must be provided to maintain the thrust difference. The output of integrator  $K_{lh}/S$  can provide the required difference, but since its input is the altitude rate error, relying solely upon the integrator forces the aircraft's sink rate to be greater than the commanded value. To reduce the demands upon the integrator, a bias whose magnitude increases as the rear nozzle deflection increases is introduced at the integrator's output. The bias would provide about 2/3 of the increased thrust level required, with the integrator providing the remainder.

Nozzle motions away from the vertical are passed through absolute value circuits and increase the thrust level, thus providing additional decoupling (over what the normal accelerometer provides) between changes in fore-aft speed and altitude rate.

Note that in the above discussion, parameter values such as  $-1 g$ , 15.2m (50 feet),  $1.1 V_A$ , etc., were chosen arbitrarily to illustrate the control system concept and to provide ball-park estimates. More exact values will be obtained from simulator studies. Note also that switching details to lock the system out during combat

conditions when, for example,  $V_A$  might drop below  $1.1 V_S$ , are not shown. Finally, it was assumed that all of the pilot's cockpit controls only move as a result of his inputs, and that electrical signals generated by the control system do not move the pilot's controls.

During the takeoff transition, the reverse sequence occurs with some of the switching occurring at slightly different points than shown in Figures 5-3 and 5-4 which are drawn to mainly show a landing sequence. Since takeoff is generally less demanding than landing, fully automated takeoffs can readily be provided without having to add additional earth-referenced signals. One easily implemented profile might be to command a 0.1 g upward acceleration for about 4 or 5 seconds, and then maintain the existing climb rate while commanding a forward accelerations of about 0.1 g until stall speed is exceeded.

Figure 5-6 shows the details of the crossfeed Matrix. Its 7 inputs, which are the various error signals from the two augmentation blocks, are distributed to its 11 force and angle outputs as shown. To illustrate its use, consider input  $\delta_{ec}$ , which is commanded elevator position. Reading down the fifth column to the first non-zero element,  $a_{65}$ , and then reading to the left end of the row, we see that the primary effect of  $\delta_{ec}$  in the powered-lift regime is on thrust from the forward nozzle,  $T_f$ . Continuing down, elements  $a_{75}^s$  and  $a_{85}^s$  show that  $\delta_{ec}$  also produces pitching moments to a lesser degree by varying the thrust from the rear nozzles,  $T_{RR}$ ,  $T_{RL}$ . Finally,  $a_{95}$  indicates that  $\delta_{ec}$  also drives the elevator, whose effectiveness goes to zero as airspeed goes to zero. In combat conditions,  $\delta_{ec}$  only affects the elevator. Although the matrix elements are shown as constants, most of these elements have first or second order denominators representing the transfer functions of the surface and nozzle actuators, and the engine dynamics. Also, gain scheduling might be required for some of these gains.

The Outer Loop Control Laws block and the Auto-Man switch in Figure 5-2 provide the means of readily adding modes such as Altitude Hold, VOR, glide slope and localizer and even a fully automated landing mode. The main restriction on these modes is the availability of the appropriate earth-referenced and air-data signals. Although the Auto-Man switch is shown as having all signal paths either from the pilot or from the Outer Loop Control Laws Block, the actual hardware could easily be implemented to permit split-axis operation.

### 5.2.2 Engine Failures in Hover or Transition

Since the maximum thrust level from each engine is less than the landing weight of the aircraft, an engine loss in a certain range of altitudes with airspeed below some critical value will result in loss of the aircraft. The problems now become one of ejecting the pilot before the aircraft gets to an attitude where ejection is impossible.

Consider first the effect of an engine loss on pitch attitude. Referring to the sketch in Figure 5-2, just prior to engine loss the pitching moment due to  $T_F$  was exactly balanced by the moments due to the rear thrust,  $T_{RR}$  and  $T_{RL}$ . Since  $T_F$  is derived by mixing air equally from both engines, a loss of one engine will half the pitching moment from the rear and forward nozzles equally, so even without the attitude hold loop very little net pitching would result from an engine loss. The engine-out situation for the roll axis is shown in part A of Figure 5-7, which assumes that the left engine is lost and that the mass flow producing  $R_L$  and  $R_R$  normally comes equally from each engine. Therefore, loss of one engine will half the maximum value of  $R_L$  and  $R_R$  available. For zero rolling moment, the following must be achievable:

$$T_{RRMAX} \ell_1 < R_{LMAX} \ell_2 + R_{RMAX} \ell_2$$

$$R_{LMAX} = R_{RMAX} = R_{MAX}$$

$$R_{MAX} > (T_{RRMAX}) (\ell_1 / 2 \ell_2)$$

$T_{RRMAX}$ , the maximum thrust from the right engine, is used because the control system will increase thrust levels to maximum in attempting to halt the downward acceleration.

For  $T_{RRMAX} = 4990$  kg (11,000 lbs) and  $\ell_1 / \ell_2 = 9.8$ , the force level required at each wing tip with one engine out to prevent roll divergence must be at least 254 kg (561 lbs).

Consider now Figure 5-7B which assumes that the mass flow to each reaction jet is fully obtained from the opposite engine. Therefore, loss of the left engine will result in no output from the right reaction jet, but the maximum force available from the left jet will be unchanged from the no-failure case, and equal to twice the value available when each reaction jet gets half its air from each engine. Using

$T_{RRMAX} = 4990$  kg (11,000 lbs) and  $t_1/t_2 = 9.8$ ,  $R_{LMAX}$  must exceed 508 kg (1122 lbs) to prevent roll divergence. So, from a rolling moment consideration, either ducting arrangement produces the same result, but the situation shown in part B of Figure 5-7 results in additional upward force of 508 kg (1122 lbs). This reduces the sink rate buildup and gives the pilot valuable extra time to eject.

If the required reaction jet maximum force levels cannot be provided because of the thru-wing restrictions on the maximum size of ducts carrying air to the jets, then a lost-engine monitor must be provided which will warn the pilot to eject.

Even if sufficient roll control power is available, the monitor is probably still desirable to minimize the time required for the pilot to recognize the resulting rapid increase in sink rate.

### 5.2.3 Conventional Flight Regime

The aircraft is designed to operate with 15 percent negative static margin in pitch. With this level of static instability, the aircraft cannot be flown augmented with mechanical controls. Hence, a full authority fly-by-wire stability and command augmentation system (SCAS) with proper redundancy is used to provide good flying qualities and to ensure flight safety.

With static instability, the amount of control power available at high angles of attack is insufficient to counteract moments due to inertial and aerodynamic cross-coupling, engine gyroscopic effects, and thrust offset. Hence, high angle of attack maneuvering capability has to be restricted to prevent uncontrolled departures from which the aircraft cannot be recovered. An automatic departure prevention system has been designed for an aircraft having a 15 percent negative static margin and a wing planform similar to that used for the HAVSTOL concept. The automatic departure prevention system is integral with the SCAS so that the pilot can use any combination of control inputs without the danger of the aircraft becoming uncontrollable, and he can fly with "head out of the cockpit." Nonlinear control laws are used to maximize the lift and turn rate capability. For structural protection, the SCAS limits the maximum load factor that the pilot can command.

The performance at low dynamic pressures is enhanced by using the thrust vectoring capability of the trim tab (see Figure 4-1). The Thrust Vector Control System (TVC) is designed integral with SCAS and is phased in automatically at low dynamic pressures. With additional control power available, the angle of attack flight envelope and roll rate

capability are substantially expanded. The inputs to the TVC are provided, along with inputs to aerodynamic control surfaces, by pitch and roll stick displacement. The pilot task is thus made easier by not requiring extraordinary control input.

An extensive air combat simulation was recently concluded, using an aircraft in which this flight control system was modeled, in which the pilot on a moving base simulator was engaged with an interactive target. This target, computer controlled, took defensive as well as offensive action. The resulting maneuvering was very realistic, with the aircraft driven to its performance limits. In a total of 500 combat engagements, not a single departure from controlled flight occurred.

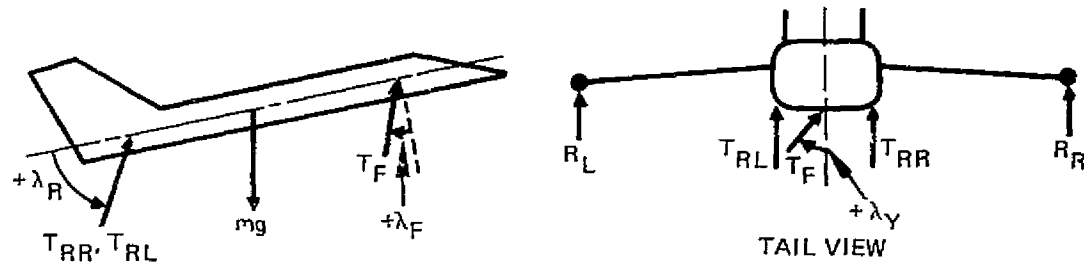
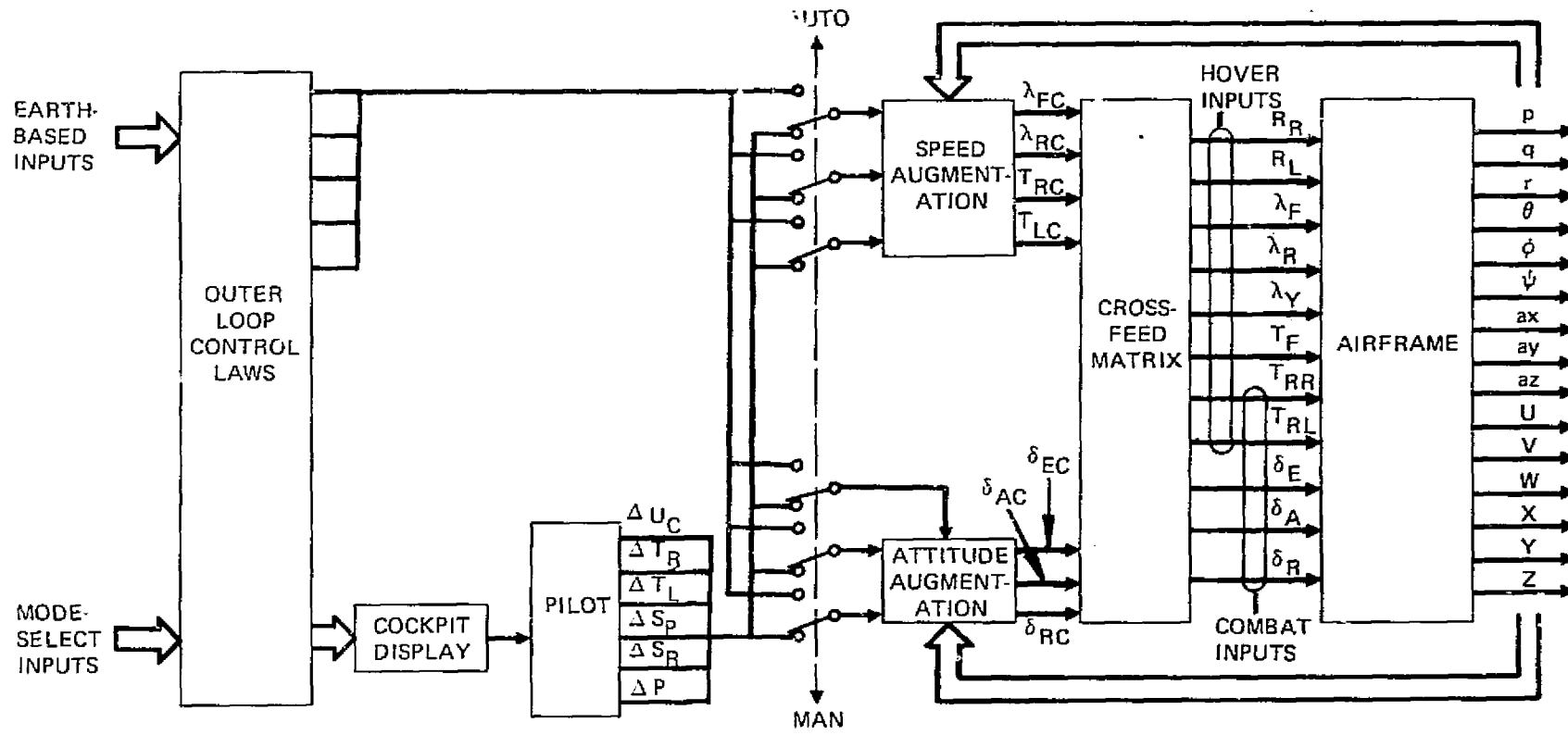


FIGURE 5-2. AIRFRAME - FLIGHT CONTROL SYSTEM CONFIGURATION

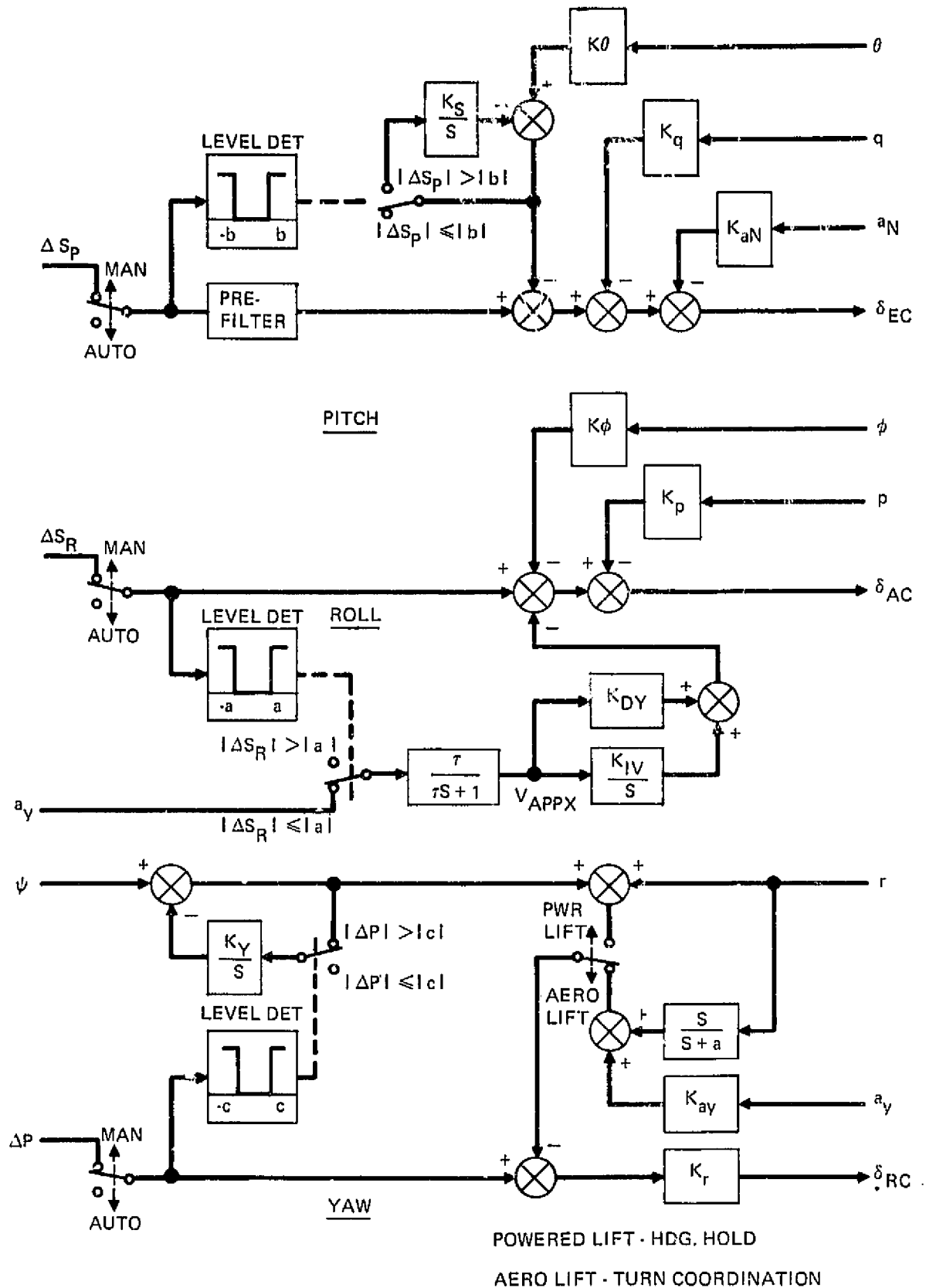
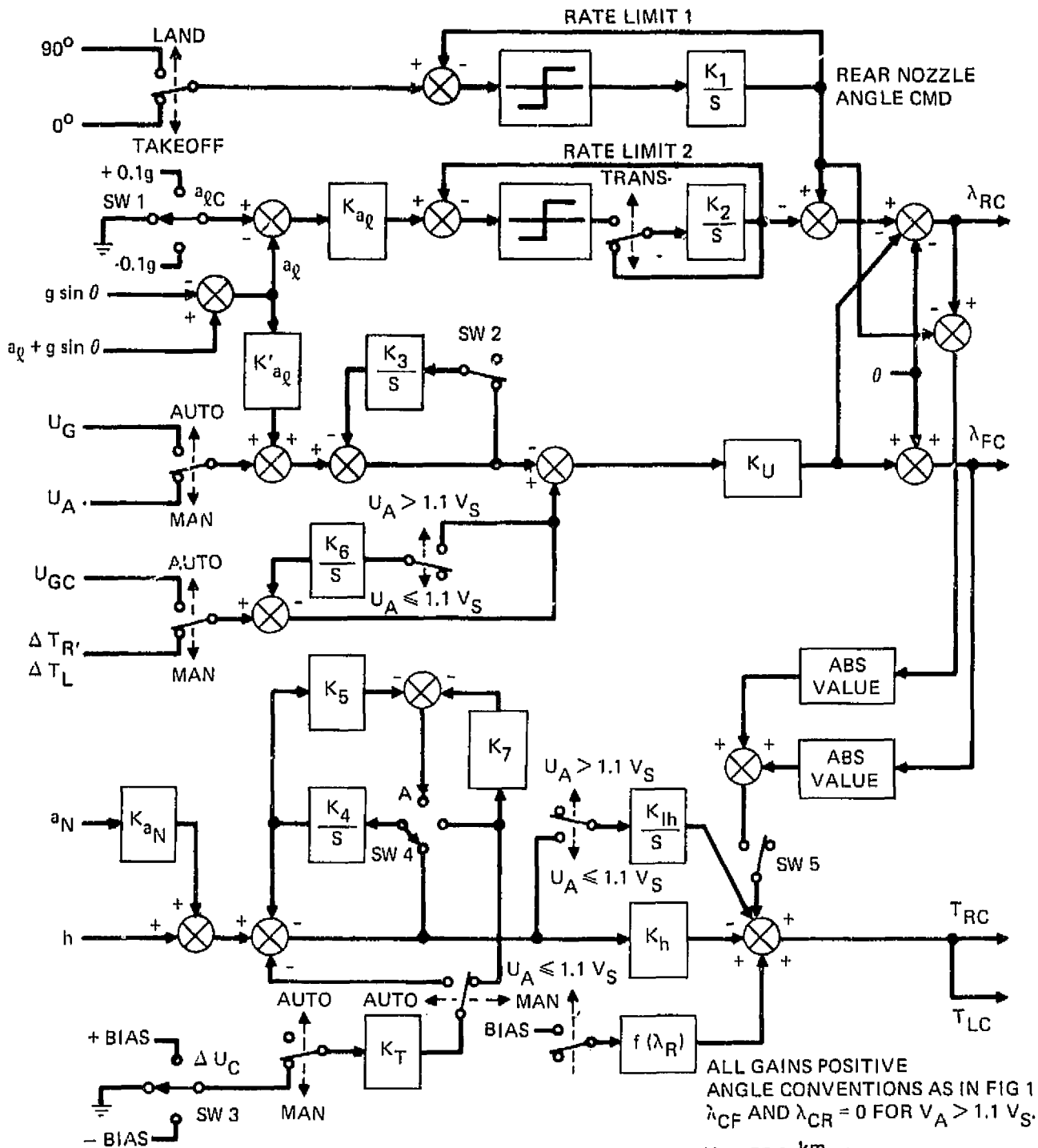
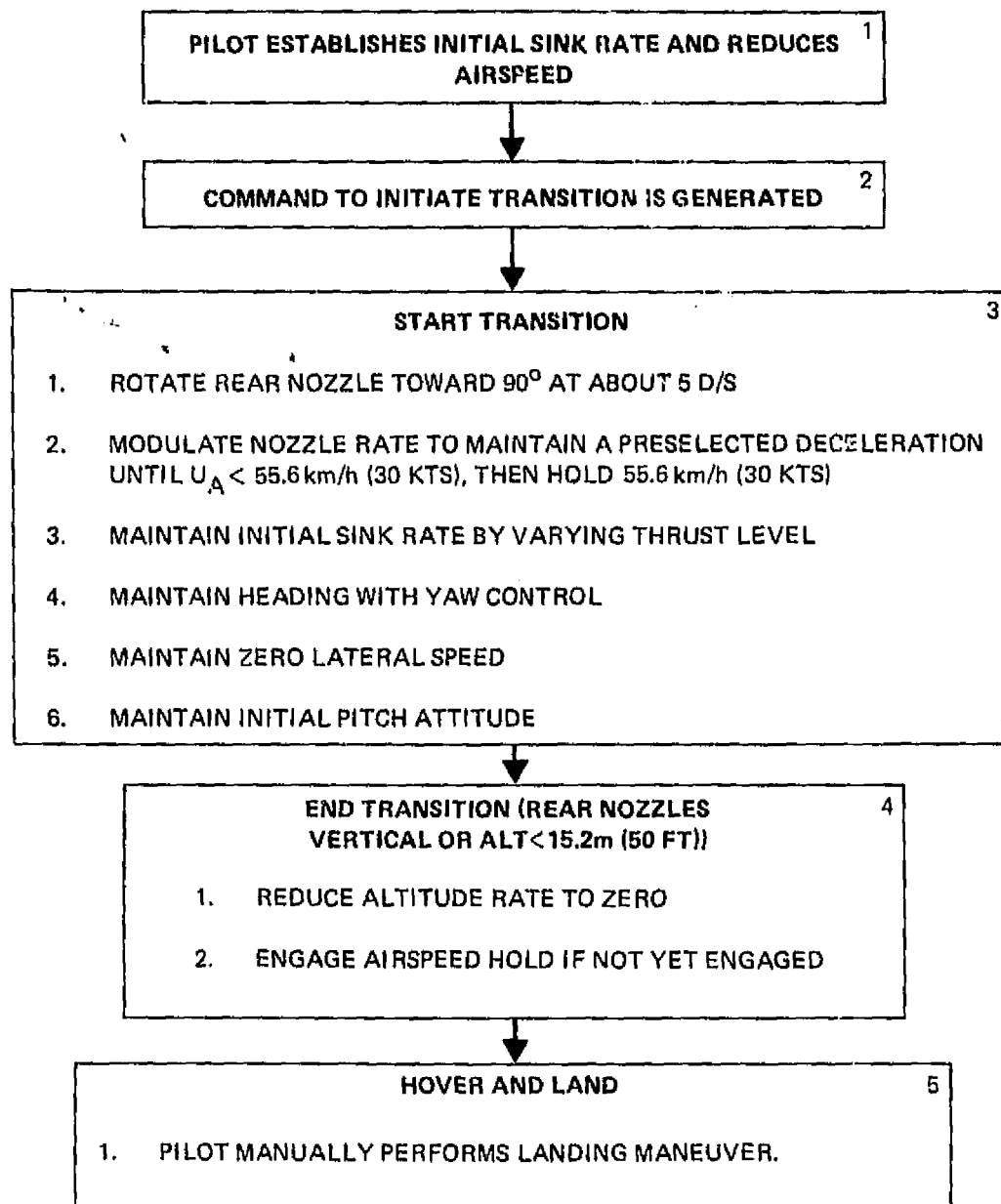


FIGURE 5-3. ATTITUDE AUGMENTATION



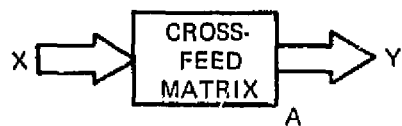
- 1) SW 1 TO  $-0.1g$  WHEN ( $U_1 < U_A \leq 1.1 V_S$ ) AND LAND  
 SW 1 TO  $+0.1g$  WHEN ( $U_1 < U_A \leq 1.1 V_S$ ) AND TAKEOFF
- 2) SW 2 LATCHES OPEN WHEN  $\theta + \lambda_R > 80^\circ$  OR  $U_A \leq U_1$  UNTIL AIRSPEED EXCEEDS  $1.1 V_S$
- 3) SW 3 - SPEED COMMAND SWITCH
- 4) SW 4 OPENS WHEN AIRSPEED LESS THAN  $1.1 V_S$  UNTIL  $\theta + \lambda_R > 80^\circ$  OR  $h < 15.2\text{m}$  (50 ft)  
 THEN CLOSES, TO POSITION A
- 5) SW 5 LATCHES CLOSED WHEN  $\theta + \lambda_R > 80^\circ$  UNTIL AIRSPEED EXCEEDS  $1.1 V_S$

FIGURE 5-4. SPEED AUGMENTATION



NOTE: FUNCTIONS IN BLOCKS 3 AND 4 PERFORMED AUTOMATICALLY

FIGURE 5-5. TRANSITION - LANDING SEQUENCE



$$Y = AX$$

$$Y = [R_R \ R_L \ \lambda_F \ \lambda_R \ \lambda_Y \ T_F \ T_{RR} \ T_{RL} \ \delta_E \ \delta_A \ \delta_R]^T$$

$$X = [\lambda_{FC} \ \lambda_{RC} \ T_{RC} \ T_{LC} \ \delta_{EC} \ \delta_{AC} \ \delta_{RC}]^T$$

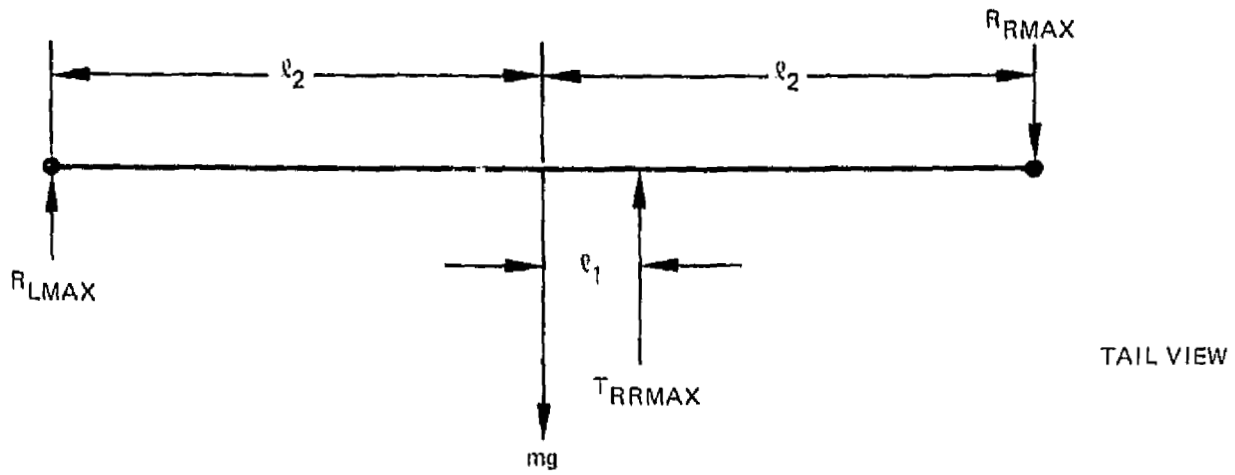
MATRIX A

Y \ X	$\lambda_{FC}$	$\lambda_{RC}$	$T_{RC}$	$T_{LC}$	$\delta_{EC}$	$\delta_{AC}$	$\delta_{RC}$	
$R_R$	0	0	0	0	0	$a_{16}$	0	$a_{16} = -a_{26}$
$R_L$	0	0	0	0	0	$a_{26}$	0	
$\lambda_F$	$a_{31}$	0	0	0	0	0	0	
$\lambda_R$	0	$a_{42}$	0	0	0	0	0	
$\lambda_Y$	0	0	0	0	0	0	$a_{57}$	
$T_F$	0	0	$a_{63}^S$	$a_{64}^S$	$a_{65}$	0	0	$a_{63}^S = a_{64}^S$
$T_{RR}$	0	0	$a_{73}$	0	$a_{75}^S$	$a_{76}^S$	0	$a_{75}^S = a_{85}^S$
$T_{RL}$	0	0	0	$a_{84}$	$a_{85}^S$	$a_{86}^S$	0	$a_{76}^S = -a_{86}^S$
$\delta_E$	0	0	0	0	$a_{95}$	0	0	
$\delta_A$	0	0	0	0	0	$a_{106}$	0	
$\delta_R$	0	0	0	0	0	0	$a_{117}$	

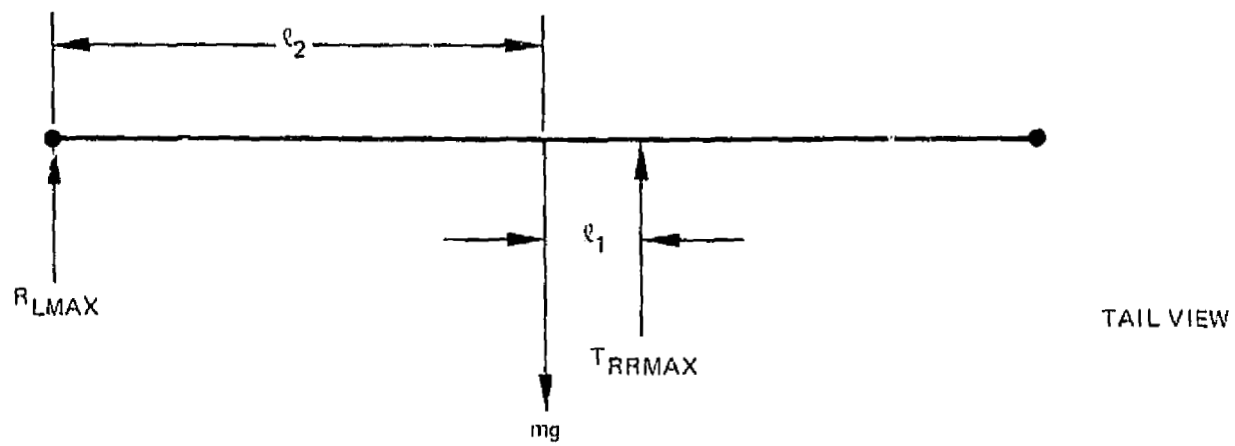
ALL ELEMENTS EXCEPT THESE EQUAL ZERO IN CONVENTIONAL FLIGHT

SUPERSCRIT S INDICATES THIS TERM IS OF SECONDARY IMPORTANCE, BUT NOT NECESSARILY NEGLIGIBLE.

FIGURE 5-6. CROSSFEED MATRIX DETAILS



(A)



(B)

FIGURE 5-7. ROLLING MOMENTS AFTER ENGINE LOSS. EACH WINGTIP JET DRIVEN BY  
 (A) BOTH ENGINES EQUALLY, (B) ONLY THE OPPOSITE-SIDE ENGINE

### 5.3 MASS PROPERTIES

A parametric weight estimation procedure in conjunction with the Northrop D-SYN sizing program was used for the sizing and sensitivity studies of the aircraft under study. The weight prediction equations are of the rational-empirical type applicable to conventional aircraft configurations, and supplemented to include the appropriate increments and penalties peculiar to VSTOL aircraft (e.g., reaction controls, thrust vectoring, high lift devices). Factors are applied to the structural weight estimates to account for different materials, fatigue life and thermal environment.

The resulting individual group weight estimates are then accumulated for several assumed design gross weights, including the effect of fuselage sizing for the required fuel volume. The corresponding fuel available is then found from mission performance computations and is subsequently used to iterate for a take-off gross weight (fuel required = fuel available).

Identical weight computations may also be performed by a stand-alone computer program utilizing the formulas to estimate the weights of individual design groups (wing, tail, body flight controls, etc.) for a specific aircraft and design mission. Each formula employs significant design parameters affecting weight: such as, design weight, load factor, basic dimensions, and yields a predicted weight for a particular design group.

Commensurate with the 1990 time period, service introduction advanced composite materials was reflected in the use of the following structural weight savings: wing and tail surfaces 26 percent, fuselage 25 percent, and landing gear 18 percent.

#### 5.3.1 Weight Estimates

The estimated weights are presented in the group weight statement shown on Table 5-1.

#### 5.3.2 Balance

The baseline configuration is balanced for the center-of-gravity position (corresponding to 13,608 kgf [30,000 lb] T.O.W.) at 26 percent MAC, which satisfies the conditions for a specified static margin and for thrust vector coincidence. At zero fuel weight of 8,650 kgf (19,323 lb) the C.G. location is at 22.9 percent MAC.

ORIGINAL PAGE IS  
OF POOR QUALITY  
ORIGINAL PAGE IS  
OF POOR QUALITY

TABLE 5-1. GROUP WEIGHT STATEMENT

SHORT GROUP WEIGHT STATEMENT  
NAVY AIR FORM 13060/3 (4-72)

DATE

STRUCTURE	MODEL	Lbf	Kgf	% TOW		
		7,940	3,603	26.74		
1.	WING (inc. 200 Lb LG. Nacelles)	2,868	1,301			
2.	Canard	160	73			
3.	TAIL (Vertical)	300	136			
4.	BODY	2,493	1,131			
5.	ALIGNING GEAR	1,035	470			
6.	ENGINE SECTION (inc. Exh. Flap)	1,084	492			
7.	PROPULSION	7,011	3,180	23.37		
8.	ENGINE INSTALLATION	5,662	2,568			
9.	ACCESS. GR. BOXES & DRIVE	IN 8				
10.	EXHAUST SYSTEM	IN 8				
11.	ENGINE COOLING	IN 8				
12.	WATER INJECTION					
13.	ENGINE CONTROLS	IN 8				
14.	STARTING SYSTEM	IN 8				
15.	PROPELLER INSTAL					
16.	SMOKE ABATEMENT					
17.	LUBRICATION SYSTEM	IN 18				
18.	FUEL SYSTEM	948	430			
19.	DRIVE SYSTEM	Duct 205	93			
20.	JET DRIVE	RALS nozzle + Cont 196	89			
21.	FLIGHT CONTROLS	IN 24				
22.	AUX POWER PLANT	IN 8				
23.	INSTRUMENTS	120	54			
24.	HYDRAULICS & PNEUMATICS (inc. Roll RCS)	1,630	739	5.43		
25.	ELECTRICAL	IN 24				
26.	AVIONICS	1,177	534			
27.	ARMAMENT (inc. missile launcher)	167	76			
28.	FURNISHINGS & EQUIPMENT	250	113			
29.	AIR CONDITIONING	260	118			
30.	ANTI-ICING					
31.	PHOTOGRAPHIC					
32.	LOAD & HANDLING					
33.	MANUFACTURING VARIATION					
34.	WEIGHT EMPTY	18,555	8,417	61.85		
35.	CREW (NO )	215	98			
36.	PASSENGERS (NO )					
37.	FUEL-UNUSABLE	130	59			
38.	FUEL-INTERNAL	10,677	4,843	34.6		
39.	FUEL-EXTERNAL					
40.	OIL	50	23			
41.	FUEL TANKS, AUX					
42.	BAGGAGE					
43.	CARGO, TROOPS					
44.	GUNS					
45.	AMMUNITION					
46.	EQUIPMENT (O <sub>2</sub> ) SURVIVAL KITS	IN 23 13	6			
47.	WEAPONS INSTALLATION					
48.	BOMBS					
49.	ROCKETS, MISSILES	360	163			
50.						
51.						
52.						
53.	PHOTOGRAPHIC					
54.	MISCELLANEOUS					
55.	USEFUL LOAD	11,445	5,192	38.15		
56.	GROSS WEIGHT	30,000	13,608	100.0		

### 5.3.3 Moments of Inertia

Moments of inertia of the baseline configuration were calculated for two loading conditions and are given in Table 5-2.

TABLE 5-2. MOMENTS OF INERTIA

Loading Condition	$I_{yy}$ (Pitch)	$I_{xx}$ (Roll)	$I_{zz}$ (Yaw)	Units
Take-Off Weight, 13,608 kgf (30,000 lb)	140,325	19,935	178,102	Kg. m <sup>2</sup>
	103,500	14,703	131,361	sl. ft <sup>2</sup>
Zero-Fuel Weight 8,765 kgf (19,323 lb)	90,027	12,789	11,362	Kg. m <sup>2</sup>
	66,401	9,433	83,806	sl. ft <sup>2</sup>

#### 5.4 CREW STATION

The design and development of a crew station for use in a VSTOL aircraft must identify and solve the unique problems associated with vertical flight.

In a vertical takeoff and landing (VTOL) aircraft, the critical function of pilot operation at the different attitudes is of primary concern. The pilot must be afforded excellent visibility and comfort so that he can operate his aircraft at the extreme attitudes required in the liftoff and touchdown maneuvers. The unique problem facing VSTOL operations is the necessity to maximize pilot vision while still maintaining a good supersonic area distribution. An overnose vision angle of 15 degrees in conjunction with overside vision of 40 degrees was deemed necessary for operation during liftoff and touchdown as well as transition. High attitude angles, in the order of 20 degrees, are obtained during transition and approach, thus requiring good forward and side vision to maintain contact with the landing platform.

As this VSTOL aircraft is a high performance fighter, it is essential that the pilot has good aft visibility (360 degrees) and maintains a high level of proficiency during air combat high "G" maneuvers. The requirement for high "G" tolerance tends to conflict with VSTOL visibility. Greater proficiency results from a reclined seat position in the former case, and an upright position for the latter.

Pilot safety is of primary concern during VSTOL operations with a necessity that the aircraft provide an escape system for all modes of flight. This escape criteria is referred to as the "pilot ejection envelope" and, in the case of VSTOL aircraft, must cover the flight regime from low altitude no speed to high altitude high speed. In some cases, the extreme attitude of the aircraft will require some kind of "vertical seeking seat" so that altitude may be gained before chute deployment. During liftoff and touchdown, aircraft control is supplied by the engine power system and so is dependent on the engines operating. The twin-engine configuration has an inherent level of safety in an engine-out condition if the remaining engine thrust can be redirected through the center-of-gravity and the reaction controls system remains operational.

One of the most demanding tasks a pilot has is during the landing and take-off phase of flight. This phase is even more demanding in VSTOL flight when it is

necessary that the pilot's total attention be focused outside the cockpit. Also associated with this critical phase of flight is a high level of pilot workload required inside the cockpit monitoring critical controls and positions to insure safe operations. The aircraft attitude and speed must be displayed to the pilot during the transition flight in order that he can stay within the safe flight envelope, and during the landing phase so that he can judge his relative speed and position with the landing craft. Engine health must be monitored to assure sufficient thrust for safe vertical flight; consequently, any instrument operation that must be completed during the vertical flight mode must be operable from either the control stick or the throttle.

The horizontal attitude VSTOL aircraft incorporates a Remote Augmented Lift System (RALS) which divides the engine airflow into separate exhausts forward and aft of the center of gravity. This aircraft utilizes a liftoff and touchdown concept which features rotation to a high attitude (20 degrees) prior to application of full VTOL thrust. Because this angle will be additive with the seat back angle, any large degree of seat back angle will result in a reduction in visibility with an associated loss in orientation. Northrop studied two crew station concepts for the horizontal attitude aircraft: one with a fixed seat back angle and the other with a high "G" articulating seat and selected the former for the present.

The fixed seat concept has an 18-degree seat back angle, center control stick, and an instrumentation system that is operated from the stick or throttle. A seat back angle of 18 degrees was selected to best fulfill the VSTOL requirement for pilot attitude and visibility as well as the combat requirements for high "G" tolerance. This position seat allows for a conventional center control stick with maximum size instrument panel.

The instrumentation system incorporates cathode ray tubes for displays with selection and control being made from the control stick and throttle. This system is referred to as "Hands on Stick and Throttle" (HST) and is currently being installed in the F-18A aircraft. HST allows the pilot to always remain in complete control of his aircraft while operating in the critical modes of flight; thus, for this reason, it is being considered for application on each of the crew station concepts. A general arrangement of the crew station is shown in Figure 5-8. This arrangement meets Navy requirements of visibility and pilot size; i. e., 3 percent to 98 percent.

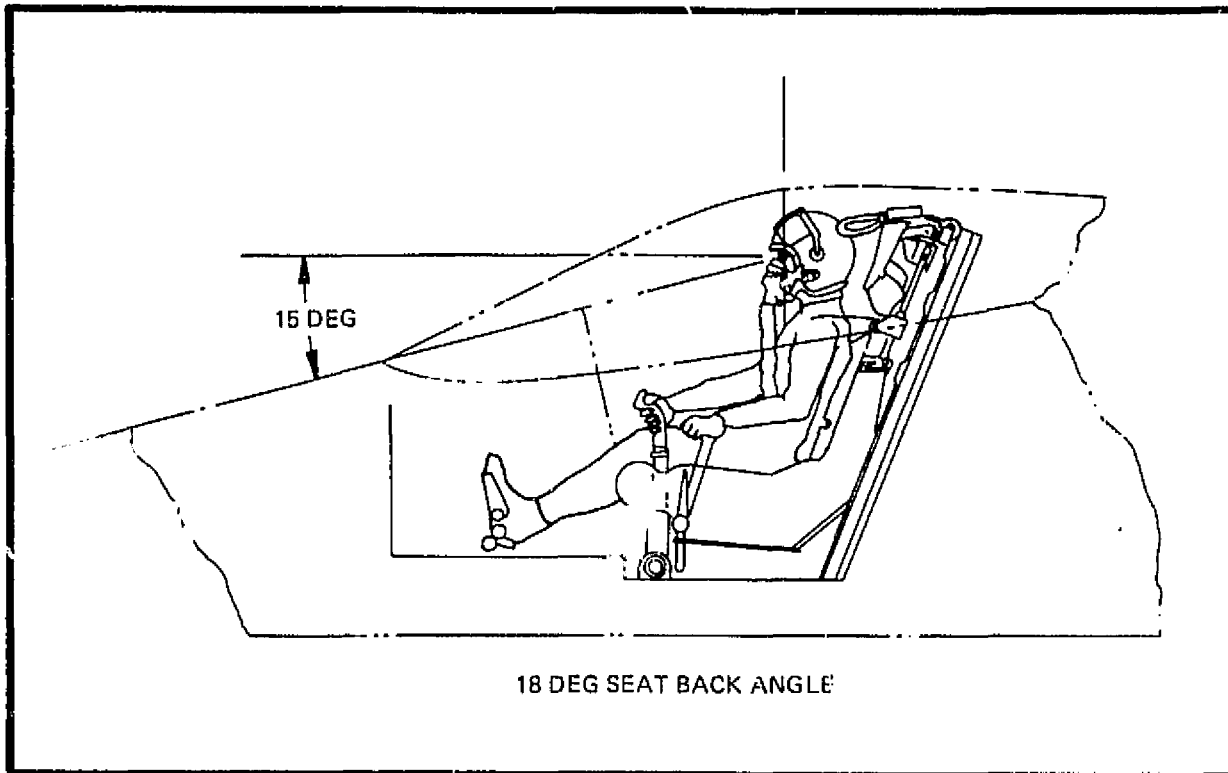


FIGURE 5-8. FIXED SEAT - GENERAL ARRANGEMENT

The escape system utilized in this crew station is an advanced 0=0 ejection seat. The maximum aircraft attitude of 20 degrees allows safe crew ejection during liftoff and touchdown.

## 5.5 SUBSYSTEMS

Primary study effort for aircraft subsystems was to define preliminary concepts to support the configuration development. Specific systems such as landing gears and propulsion installation were evaluated in more depth than other systems since they had a major impact on the configuration development. Other systems discussed below include hydraulics, environmental control, fuel, and electrical. General location of system components are shown on the inboard profile drawing, Figure 2-4.

The propulsion installation utilizes two General Electric variable cycle engines mounted in the aft fuselage with a single forward Remote Augmented Lift System (RALS). A four point mount system is used to attach each engine to the airframe. The air induction system consists of rectangular fixed geometry inlets positioned on each side of the fuselage forward of the canards, internal ducting terminating at each engine compressor face, and a plenum with auxiliary air inlet doors located forward of the engine compressor face. A variable C-D, Augmentor Deflected Exhaust Nozzle (ADEN), capable of providing fully vectorable thrust for VTOL operation is provided for each engine. Fan discharge air from both engines is manifolded into a single RALS duct that is routed forward to provide vectorable downward thrust for VTOL operation. A three point mount system is used to support the RALS augmentor and exhaust nozzle. Aircraft accessories consisting of a generator and hydraulic pump are mounted on and driven by the engine gearbox which is located on top of the engine. Firewalls, fire detection, and extinguishing systems are provided. Access doors are located on the underside of the aft fuselage to facilitate engine servicing and engine installation/removal. Doors on top of the fuselage provide access for servicing and maintenance to the airframe and engine accessories.

Fuel is carried in two bladder cells in the fuselage, two integral wing tanks and two integral wing afterfairings. The two fuselage cells are engine feed tanks, one supplying each engine. Booster pumps installed in inverted flight compartments within the bladder cells provided pressurized fuel to the engines. Cross feed fuel capability is provided. All other tanks supply fuel to the feed tanks by automatic sequence transfer of fuel. Other fuel system components include a vent system, fuel quantity and flow measurement, pressure fueling, fuel dumping, and external fuel provisions.

The environmental control system conditioning unit is located in the lower center fuselage forward of the engines. The system provides air to the cockpit for pressurization and defog, anti-G suit, canopy seal and to the avionics equipment

compartment for avionics cooling. Hot air anti-icing and rain repellent/removal systems are provided for the windshield. Closed loop air cycle environmental control concepts are proposed and require further study to define specific system arrangements and performance capabilities.

Aircraft electrical power is provided by two alternating current generators, transformer rectifiers, a battery, and the power distribution system. The generating system is of the constant hertz type with the generators mounted on and driven by the engine gearbox. Use of electrical technology concepts such as solid state switching, multiplexing, power monitoring, fibre optics for signal transmission and use of advanced permanent magnet materials in generator and electric motor construction, provide for an efficient lightweight electrical system.

Dual independent high pressure (8,000 psi) hydraulic systems are used. Primary flight control actuators are dual and receive one-half of their power from each system. Each system consists of multiple circuits which can be isolated from the main system in the event of a leakage failure. An engine-driven pump, sealed pressurized reservoir, return pressure sensing switching valves, filters, and ground power connections are provided for each system. High strength steel and titanium lines and low flammability fluid are used. Adequate power is provided in each system to control the airplane in the event of a complete failure of a single system.

The landing gear is compatible with the horizontal attitude takeoff and landing concept as well as necessary ground operation requirements. Adequate tip-back and turn-over angle are provided, as are wheel brakes and nose wheel steering, for ship-board maneuvering and taxi. The gear is not designed for standard carrier catapulting or arrested landings.

A baseline avionics suite, is shown in Table 5-3 which also lists certain options and alternatives. Options are additions to the baseline which provide significant supplemented capability and may be adopted either through missionizing a single version of the aircraft, or in alternate versions of the fighter/attack aircraft.

The avionics have been configured to support the anticipated missions of the aircraft. The multi-mode radar has a full air-to-air search and track capability along with an air-to-ground synthetic-aperture high-resolution ground-mapping and target-designating capability. It would be capable of detecting a 5-square meter target at a range of 35 to 45 NMI in a look-down situation over  $\pm 60^\circ$  azimuth coverage and track up to 10 targets simultaneously. The radar will include reduced probability-of-intercept

features and have its emissions controlled by the Observables Control and Management system. The avionics will be covert, i.e., designed to minimize observables throughout the rf, IR and visible spectrum. The air-to-air features and characteristics of the avionics suite are only gross estimates at this time and would be refined as the capabilities and characteristics of the supporting functions (GCI, AEW, Defense Suppression, etc.) and the advanced weapons are better defined.

TABLE 5-3. BASELINE AVIONICS SUITE

	BASELINE		OPTIONS
COMMUNICATIONS NAVIGATION IDENTIFICATION	JTIDS TERMINAL UHF RADIO MMW RADIO INTERCOM INTEGRATED INERTIAL ASSEMBLY LANDING/TAKE OFF SENSORS	68KG (150 LBS)	GPS TERMINAL  TF/TA (IN RADAR)
TARGET ACQUISITION/ WEAPON DELIVERY	SYNTHETIC APERTURE MULTIMODE RADAR GUN FIRE CONTROL & DISPLAY WEAPON LAUNCH CONTROL  ARMAMENT CONTROL FIBER OPTICS TERMINAL DAMAGE ASSESSMENT SET	122KG (270 LBS)	FLIR (MULTICOLOR) TARGET DESIGNATOR LASER/MMW MMWAVE SENSOR TVSU
CONTROLS & DISPLAYS	WIDE ANGLE HEAD-UP DISPLAY MASTER MONITOR DISPLAY  MULTIMODE SITUATION DISPLAY VOICE ACTUATED/SIGHT LINE ACTUATED & MANUAL CONTROLS HELMET SIGHT UNIT	45KG (100 LBS)	INTEGRATED IMAGING/MAP DISPLAY
DATA PROCESSING & DISTRIBUTION	MISSION COMPUTER AIR DATA/FLIGHT CONTROL & NAVIGATION COMPUTER FIBER OPTICS/MUX BUS CONTROL TERMINAL	23KG (50 LBS.)	
DEFENSIVE SYSTEMS (ELECTRONIC WARFARE)	THREAT WARNING RECEIVERS ECM/EOCM/IRCM OBSERVABLES REDUCTION & CONTROL INTERFERENCE & POWER MANAGEMENT EXPENDABLES	152KG (335 LBS)	
	TOTAL	410KG (905 LBS)	

**PRECEDING PAGE BLANK NOT FILLED**

## SECTION 6

### AIRCRAFT PERFORMANCE

Aircraft performance is divided into two parts, Flight Performance and Takeoff and Landing Performance.

#### 6.1 FLIGHT PERFORMANCE

The study performance goals were at least M 1.6 and at 3,048 meters (10,000 ft) a sustained load factor of 6.2 g at M 0.6 and a specific excess power of 274 mps (900 fps) at M 0.9. All performance was to be achieved at 88 percent gross weight. Since no mission was originally specified, a 13608 kg (30,000 lb) VTO gross weight was selected for the baseline study aircraft. The aircraft was also sized in order to provide an idea of the minimum gross weight aircraft meeting or exceeding all of the performance goals and able to perform a typical fighter escort mission. All performance is quoted for the aircraft without external stores. The two air-to-air missiles are carried internally as shown in Section 2. Four missiles could be carried internally, if required.

##### 6.1.1 Baseline Aircraft Combat Performance

All combat performance data are presented at 88 percent of takeoff weight or 11,985 kg (26,400 lb) and maximum power. The specific excess power performance capabilities, as a function of load factor, for the 13,608 kg (30,000 lb) baseline configuration are provided in Figures 6-1 through 6-3 for 3048; 6096; and 9144 m (10,000, 20,000, and 30,000 ft), respectively. Data for M 0.5, 0.6, 0.9, and 1.2 are presented for each altitude with M 1.6 data at 6096 and 9144 m (20,000 and 30,000 ft) only. Sustained load factor capabilities decrease with altitude for all Mach numbers except M 1.6. At each altitude the sustained load factor capability increases with Mach number in the subsonic region (M 0.9) and through the transonic region (M 1.2) at 6096 and 9144 m (20,000 and 30,000 ft). The maximum instantaneous load factor available is limited by the maximum usable lift coefficient for M 0.5 at all altitudes and for M 0.6 at 6096 and 9144 m (20,000 and 30,000 ft). The structural design load factor of 8 g can be attained at all other Mach numbers. At 3048 m (10,000 ft), M 0.9 and 1.2, the specific excess power capabilities are greater than 86 m/sec (250 fps) at 8 g's.

Additional flight performance data is presented in Figures 6-4 and 6-5 in terms of flight envelope contours. Figure 6-4 gives specific excess power contours of 0, 91, 183, and 374 m/sec (0, 300, 600 and 900 fps) for 1 g flight. Figure 6-5 provides 1 g, 3 g, 6 g and 8 g sustained load factor contours.

The baseline configuration at 88 percent takeoff weight can accelerate from M 0.8 to M 1.6 at 9144 m (30,000 ft) in 49.1 sec with maximum capability of M 1.86 (see Figure 6-4). The absolute ceiling is approximately 20,000 m (65,000 ft). The 1 g specific excess power goal of 274 m/sec (900 fps) at M 0.9 at 3048 m (10,000 ft) can be attained at 6096 m (20,000 ft). The structural design load factor level of 8 g can be achieved from M 0.75 to 1.25 at 3048 m (10,000 ft) and at M 1.15 at 5500 m (18,000 ft). The sustained load factor goal of 6.2 g at M 0.6 at 3048 m (10,000 ft) can be attained.

#### 6.1.2 Thrust Loading and Wing Loading Trades/Aircraft Sizing

A representative Fighter Escort mission depicted and defined in Table 6-1 was selected to determine the baseline configuration radius capability and for the T/W, W/S trades sizing studies discussed below. The baseline configuration can perform the mission at 870 km (470 nm) radius. A radius of 926 km (500 nm) was selected as a more representative Navy radius requirement for the T/W and W/S trades. The take-off and landing allowances reflect Navy specified allowances. The RALS propulsion system is similar in some respects in operation to a lift/cruise plus lift engine concept. Therefore, the RALS burner is treated as a lift engine for determining the take-off fuel allowance.

The effects of T/W and W/S variations on the size of aircraft capable of performing the 962 km (500 nmi) mission can be seen in Figure 6-6. For this matrix of sized aircraft, specific excess power and sustained load factor matrices are presented in Figures 6-7 and 6-8 for combat weights at 88 percent of the takeoff weights of Figure 6-6. The thrust to weight values shown in these subsequent Figures are based on installed, intermediate thrust (maximum unaugmented primary thruster) values on a tropical day with the RALS in operation at the mean exhaust temperature of 1093°C (2000°F). The T/W required for VTO has been established as 1.22 in consideration of providing 0.1g excess vertical acceleration and propulsion induced losses. The rated T/W (uninstalled at sea level static on a standard day with afterburner) is 1.51. The T/W of 1.22 required to perform a VTO at sea level on a tropical day, the 274

m/sec (900 fps) specific excess power line from Figure 6-7; and the 6.2 g sustained load factor line from Figure 6-8 (performance goals) have been superimposed on the sizing matrix of Figure 6-6 and are shown in Figure 6-9.

The intersection of the takeoff line and the 6.2 load factor goal line indicates that a wing loading of approximately 3,060 N/M<sup>2</sup> (64 psf) is the highest that could be used to provide the performance goals. The aircraft weight would be approximately 14,500 kg (32,000 lb). A slightly lighter weight aircraft results between wing loadings of approximately 2.63 to 2.87 kN/m<sup>2</sup> (55 to 60 psf). The highest wing loading 2.87 kN/m<sup>2</sup> (60 psf), in the range of minimum weight was selected to provide the best acceleration and highest specific excess power capabilities. The takeoff weight is 14,400 kg (31,800 lb); 100 kg (200 lb) less than the aircraft just meeting the takeoff and sustained load factor goal. The selected aircraft has a 6.4 g sustained load factor and 350 m/sec (1160 fps) specific excess power performance level. The acceleration time from M0.8 to M 1.6 at 9144 M (30,000 ft) is 48 seconds.

Data shown in Figure 6-10 have been transferred from the specific excess power matrix, Figure 6-7, to the aircraft sizing matrix, Figure 6-6. The same procedure for sustained load factor levels gives the data of Figure 6-11.

Figures 6-10 and 6-11 can be used to perform additional trade studies to determine the effects of various levels of specific excess power and sustained load factor combinations on aircraft size and T/W-W/S. For example, if the performance goals were 7 g and 366 m/sec (1200 psf), the aircraft weight would be approximately 15,650 kg (34,400 lb) with a T/W of 1.27 and wing loading of 2.55 kN/m<sup>2</sup> (53 psf). Compared to the minimum weight aircraft of 14,400 kg (31,800 lb) selected.

### 6.1.3 Sensitivity Studies

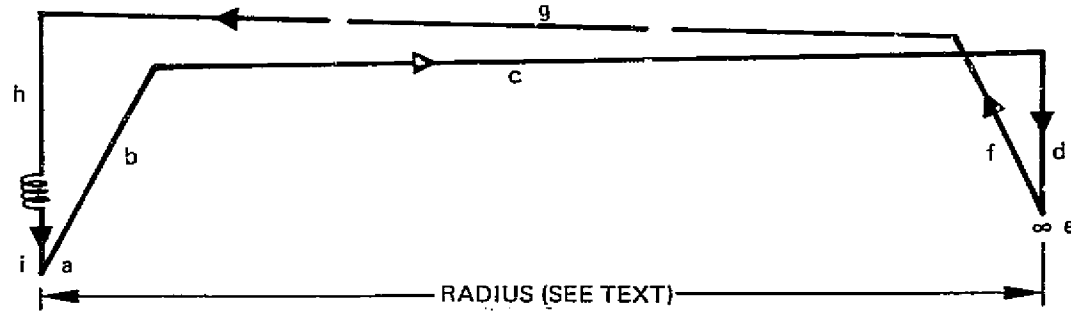
Studies were conducted to determine the aircraft sensitivity to variations in empty weight, minimum drag, drag-due-to-lift, specific fuel consumption and rated thrust. The performance sensitivities are based on 70 percent fuel rather than 88 percent take-off weight for calculating convenience.

Changes in mission radius, specific excess power, sustained load factor and acceleration time at the specified flight conditions to the sensitivity parameters for the fixed weight, 14,400 kg (31,800 lb) aircraft are shown in Figure 6-12. The empty weight variation and the minimum drag variation are approximately 5 percent and 8 percent of the empty weight and drag at M0.8 and 9144m (30,000 ft) respectively.

The other sensitivity factors are shown in percentages. A change in empty weight produces almost twice the effect on radius capability as a similar percentage change in SFC. SFC is almost three times as significant as the other sensitivity parameters with respect to radius. As expected, thrust variation is the most significant parameter affecting specific excess power, sustained load factor and acceleration time.

Sensitivity to the various parameters was also determined holding mission radius, T/W and W/S constant as apposed to holding takeoff weight constant as was the case above and in Figure 6-12. The data for constant mission radius are shown in Figure 6-13. The takeoff weight is affected twice as much by a change in empty weight as a change in SFC and has five times the effect as changes in drag as thrust. Thrust variation has the most powerful effect on specific excess power, sustained load factor and acceleration time as was the case with the fixed size aircraft. However, some of the other sensitivity factors are significant.

TABLE 6-1. TYPICAL FIGHTER ESCORT MISSION



SEGMENT	MISSION EVENT	FUEL REQUIREMENT BASIS
a	START, T.O., TRANSITION AND ACCELERATE TO BEST CLIMB SPEED	1) 2.5 MINUTES AT INTERMEDIATE POWER 2) 1 MINUTE WITH RALS SYSTEM AT 80% POWER 3) 30 SECONDS WITH RALS SYSTEM AT 100% POWER ALL AT SEA LEVEL STATIC CONDITIONS, 32.1°C (89.8°F), TROPICAL DAY.
b	CLIMB FROM SEA LEVEL TO BEST CRUISE ALTITUDE	MAX R/C AT INTERMEDIATE POWER
c	CRUISE OUT	BEST ALTITUDE AND MACH NO.
d	DESCENT TO 9144 METERS (30,000 FEET)	NO DISTANCE OR FUEL CREDIT
e	TASK ORIENTED COMBAT	(1) ACCELERATION FROM M 0.8 TO M 1.2; 9144 METERS (30,000 FEET) AT MAXIMUM THRUST (2) 360° SUSTAINED TURNS AT M 1.2; 9144 METERS (30,000 FEET) (4) 360° SUSTAINED TURN AT M 0.6; 3048 METERS (10,000 FEET)
f	CLIMB FROM 3048 METERS (10,000 FEET) TO BEST CRUISE ALTITUDE	MAX R/C AT INTERMEDIATE POWER
g	CRUISE BACK	BEST ALTITUDE AND MACH NO.
h	DESCENT TO SEA LEVEL	NO DISTANCE OR FUEL CREDIT
i	RESERVES AND LANDING	1) 10 MINUTES LOITER AT SEA LEVEL AT MAXIMUM ENDURANCE SPEED – ALL ENGINES OPERATING, STANDARD DAY 2) 45 SECONDS AT INTERMEDIATE POWER AT SEA LEVEL STATIC CONDITIONS, ALL ENGINES OPERATING, 32.1°C (89.8°F), TROPICAL DAY 3) 5% OF INITIAL FUEL

6-5

6-3

ORIGINAL PAGE IS  
OF POOR QUALITY

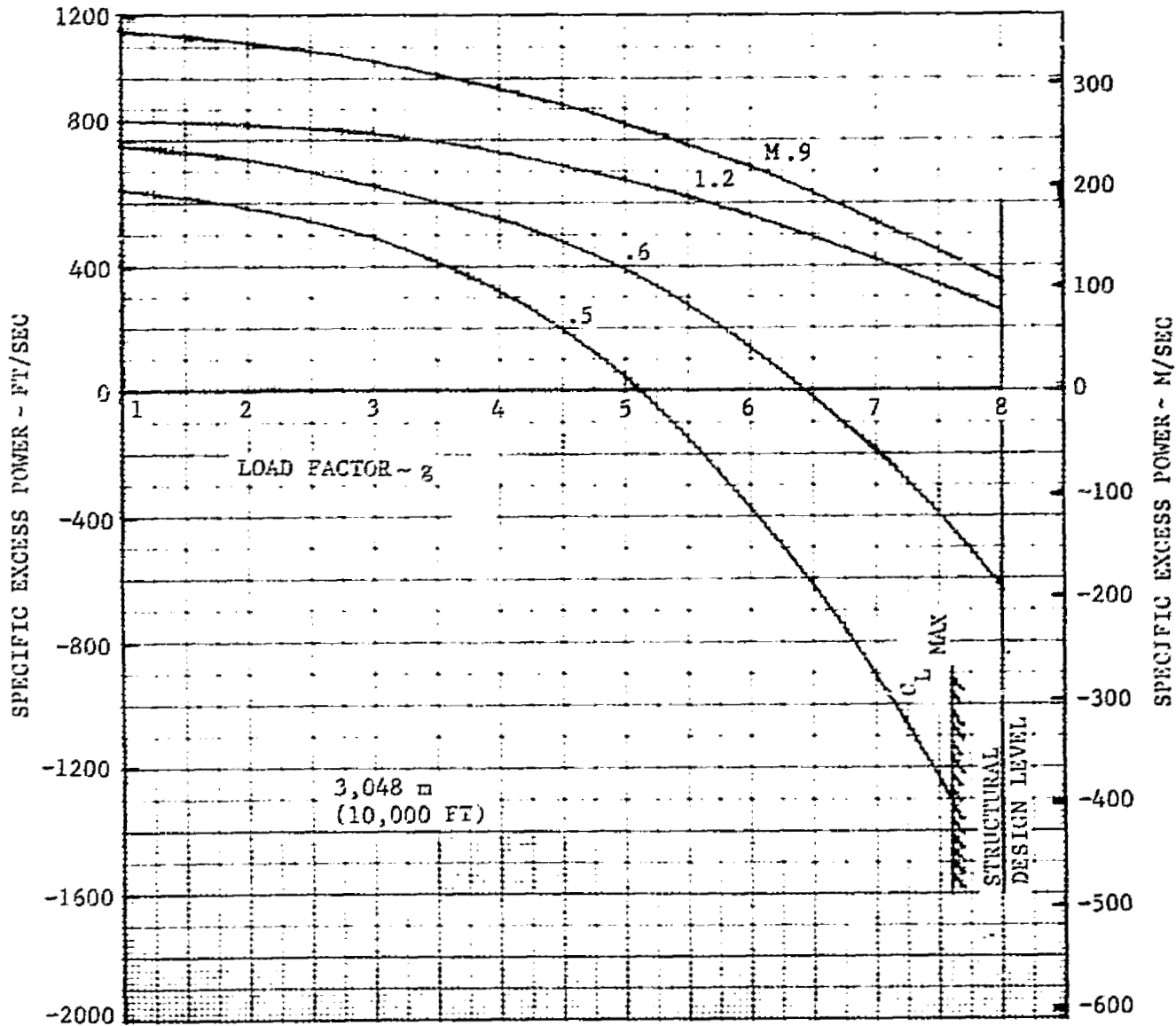


FIGURE 6-1. EFFECT OF LOAD FACTOR AND MACH NUMBER ON SPECIFIC EXCESS POWER AT 3048 METERS (10,000 FT)

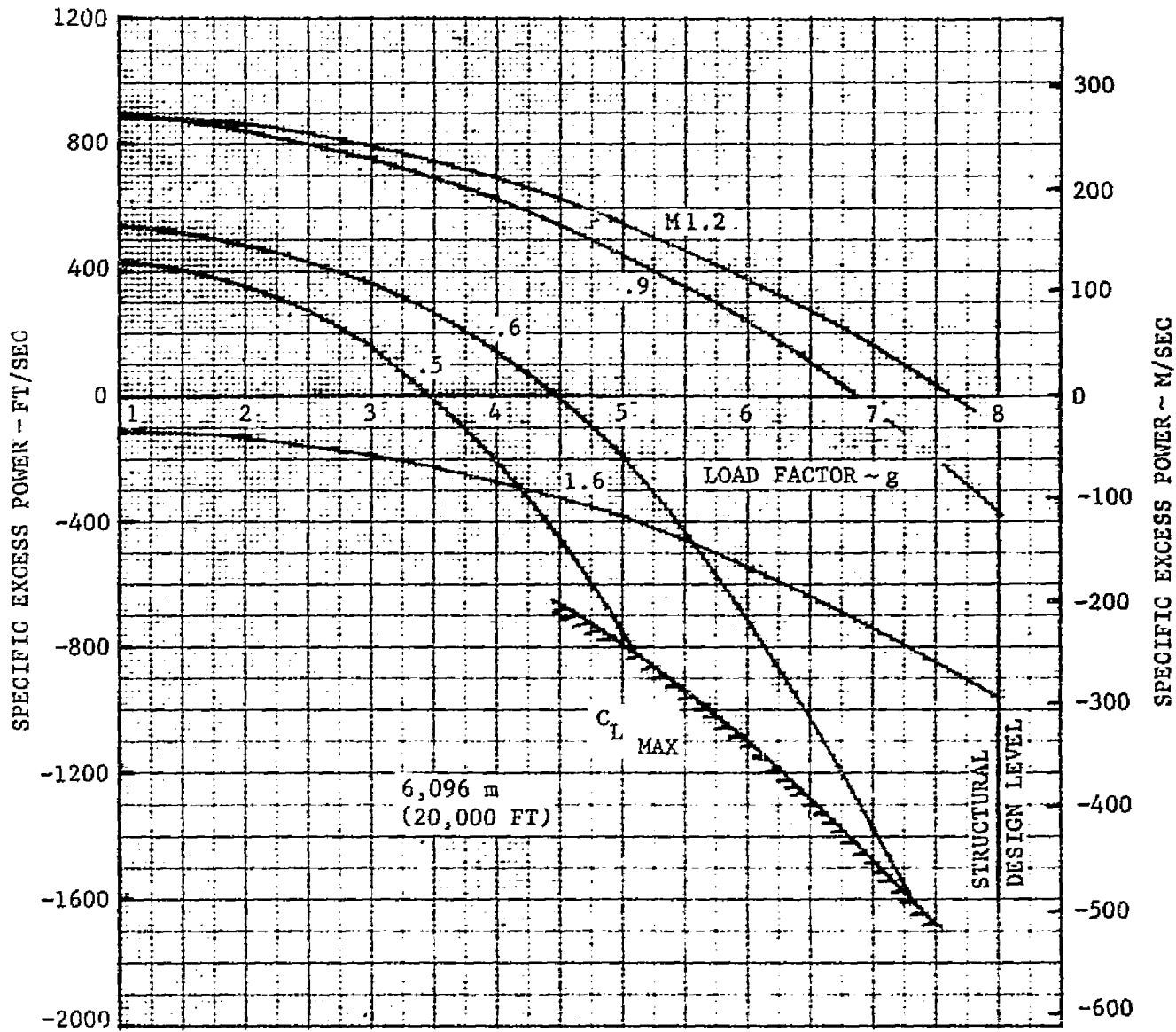


FIGURE 6-2. EFFECT OF LOAD FACTOR AND MACH NUMBER ON SPECIFIC EXCESS POWER AT 6096 METERS (20,000 FT)

ORIGINAL PAGE IS  
OF POOR QUALITY

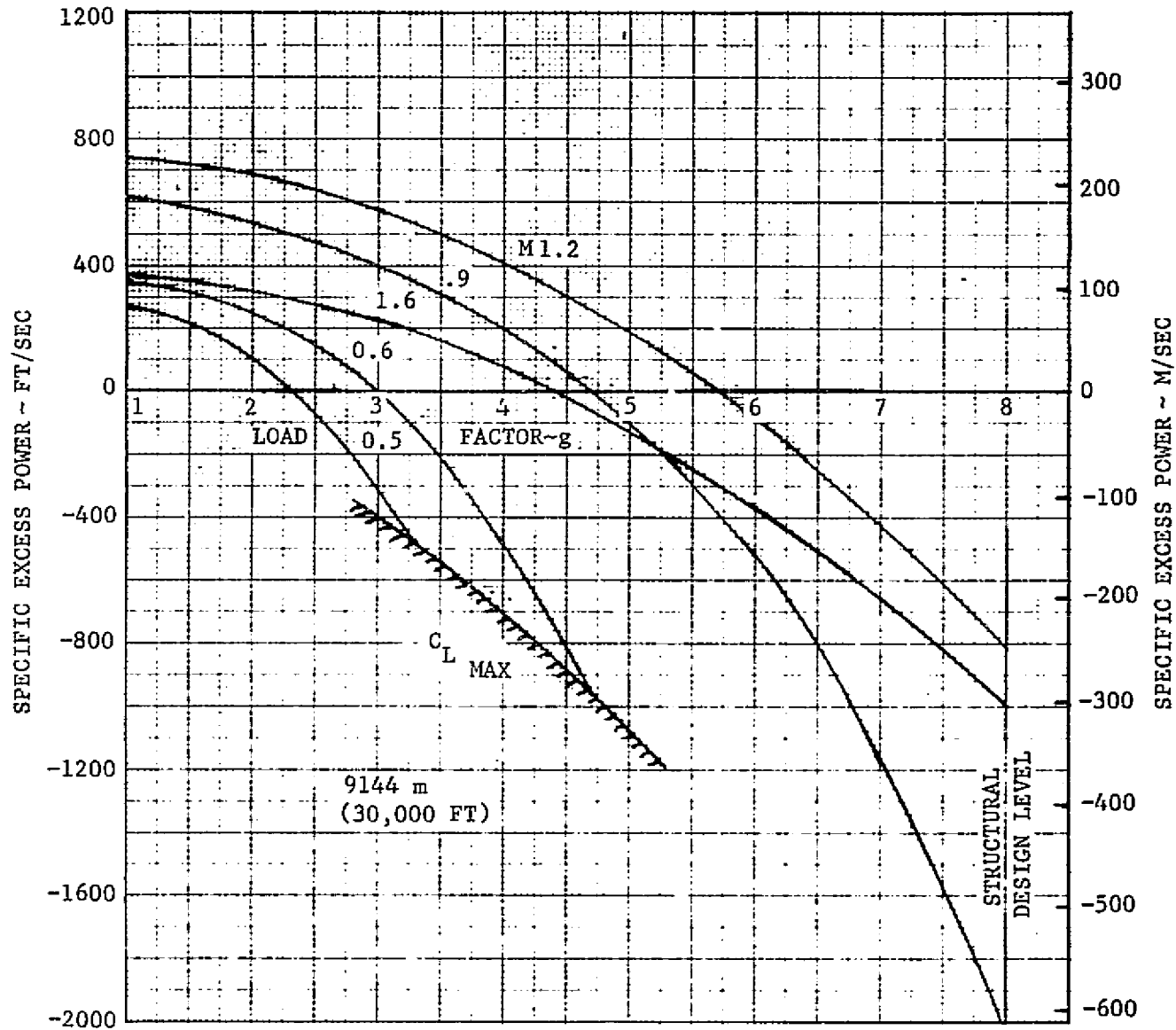
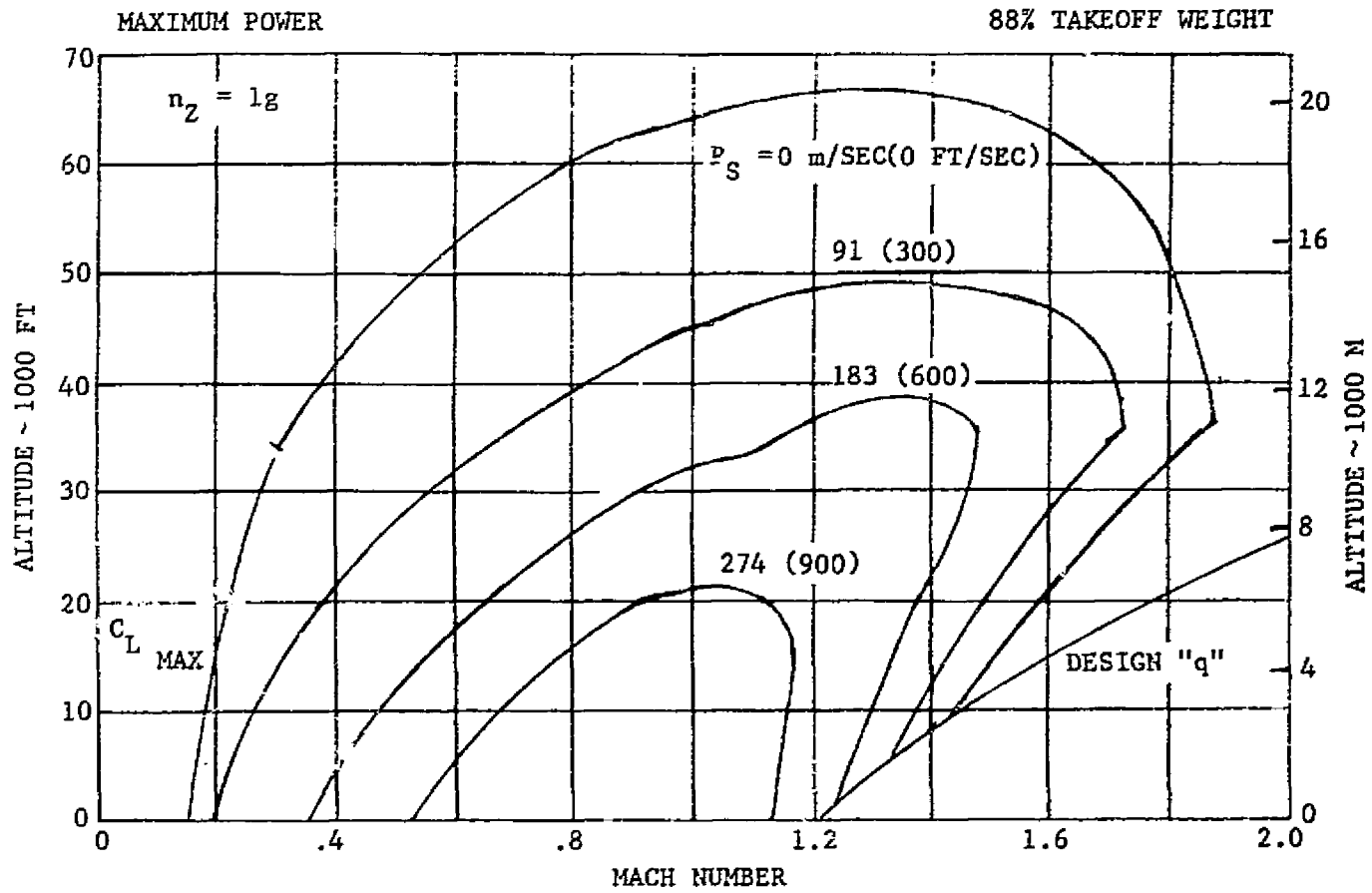


FIGURE 6-3. EFFECT OF LOAD FACTOR AND MACH NUMBER ON SPECIFIC EXCESS POWER AT 9144 METERS (30,000 FT)



ORIGINAL PAGE IS  
OF POOR QUALITY

FIGURE 6-4. SPECIFIC EXCESS POWER CONTOURS AT 1G

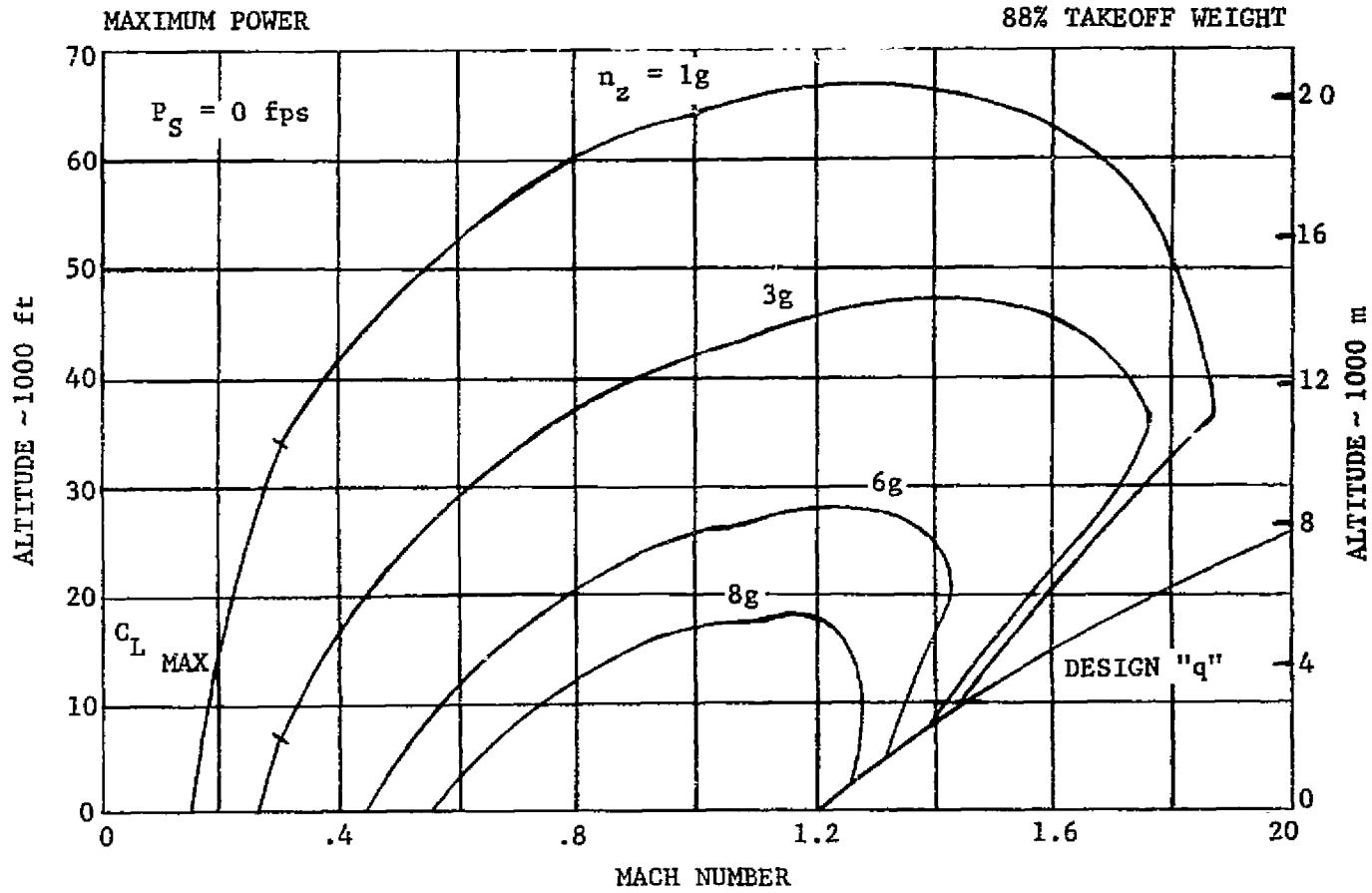


FIGURE 6 -5. SUSTAINED MANEUVER CAPABILITY

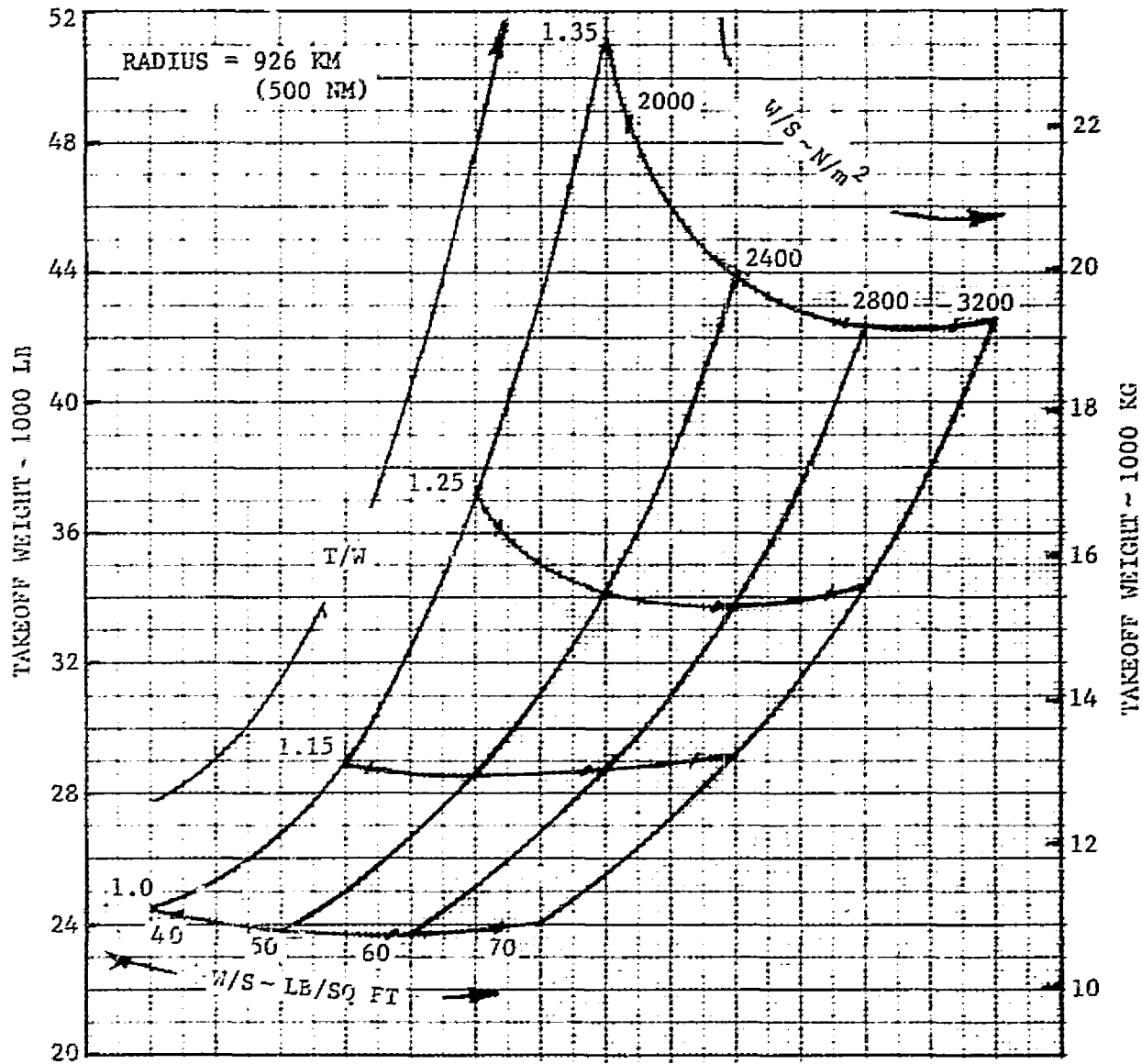


FIGURE 6-6. AIRCRAFT SIZING MATRIX

ORIGINAL PAGE IS  
OF POOR QUALITY

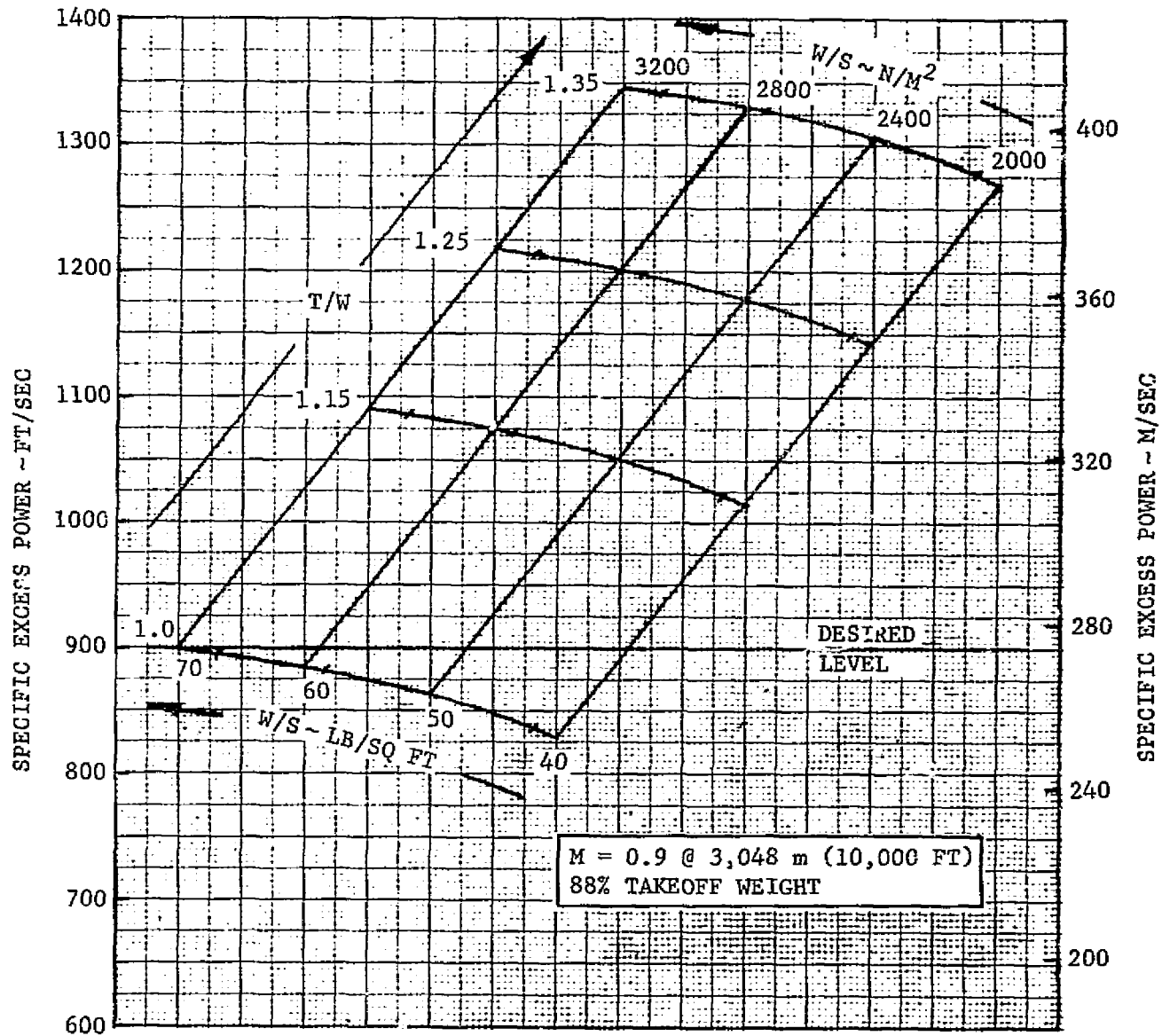
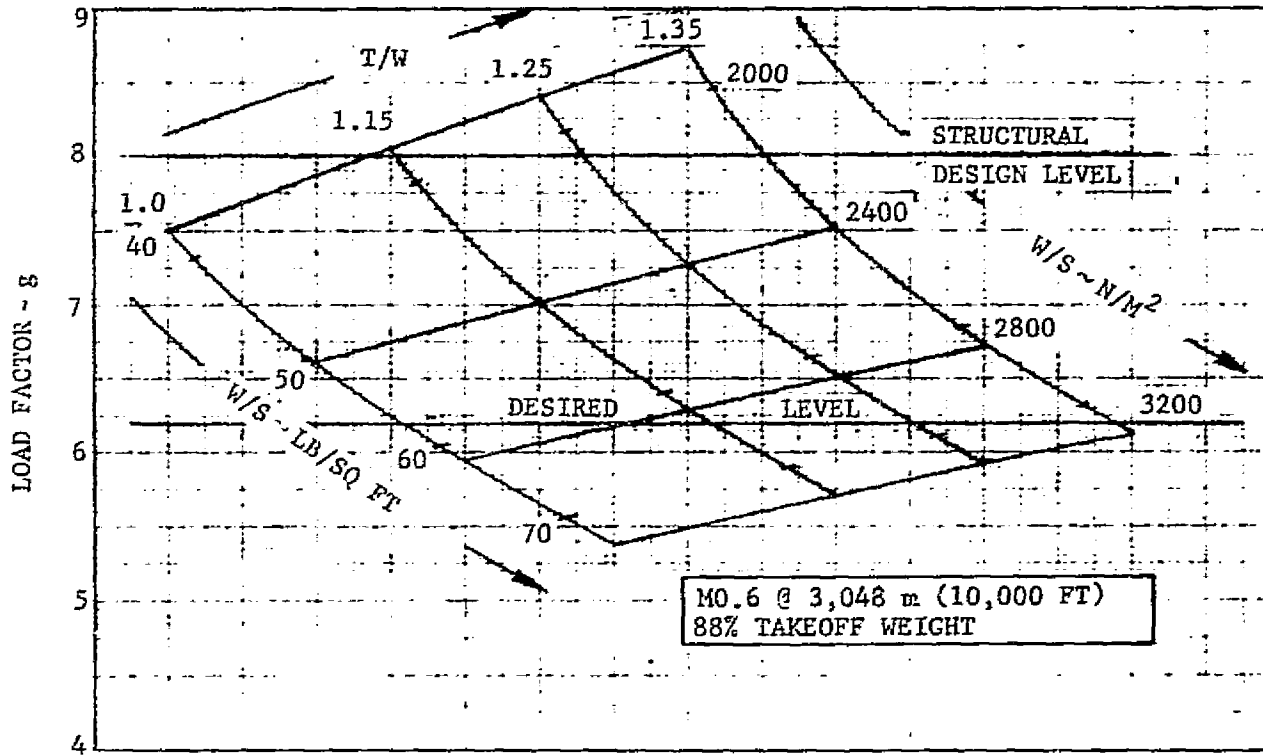


FIGURE 6-7. VARIATION OF SPECIFIC EXCESS POWER WITH T/W AND W/S FOR AIRCRAFT SIZING MATRIX

ORIGINAL PAGE 1  
OF POOR QUALITY



ORIGINAL PAGE IS  
OF POOR QUALITY

FIGURE 6-8. VARIATION OF SUSTAINED LOAD FACTOR WITH T/W AND W/S FOR AIRCRAFT SIZING MATRIX

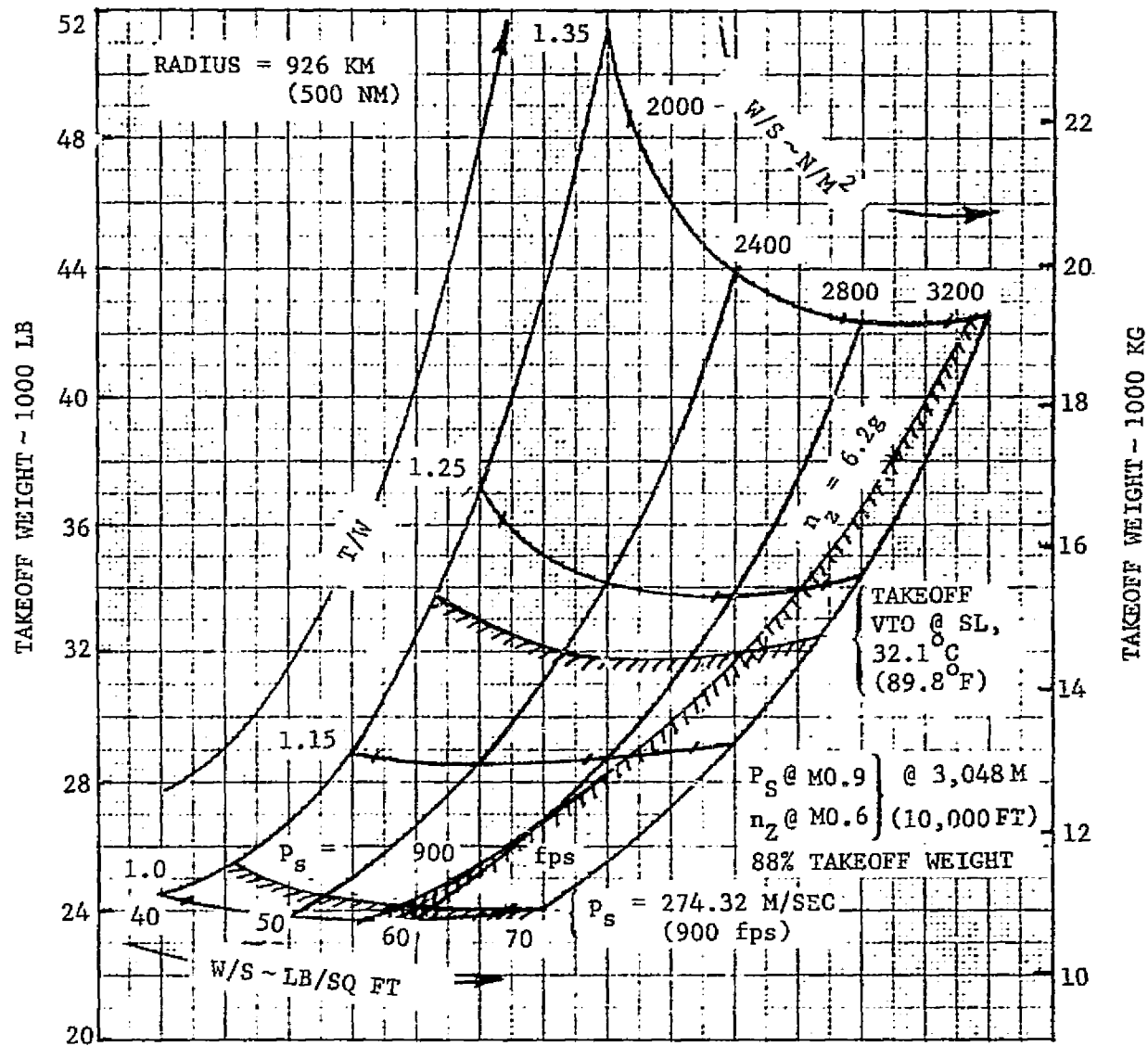


FIGURE 6-9. PERFORMANCE GOALS RELATIONSHIP TO AIRCRAFT SIZING MATRIX

ORIGINAL PAGE IS  
OF POOR QUALITY

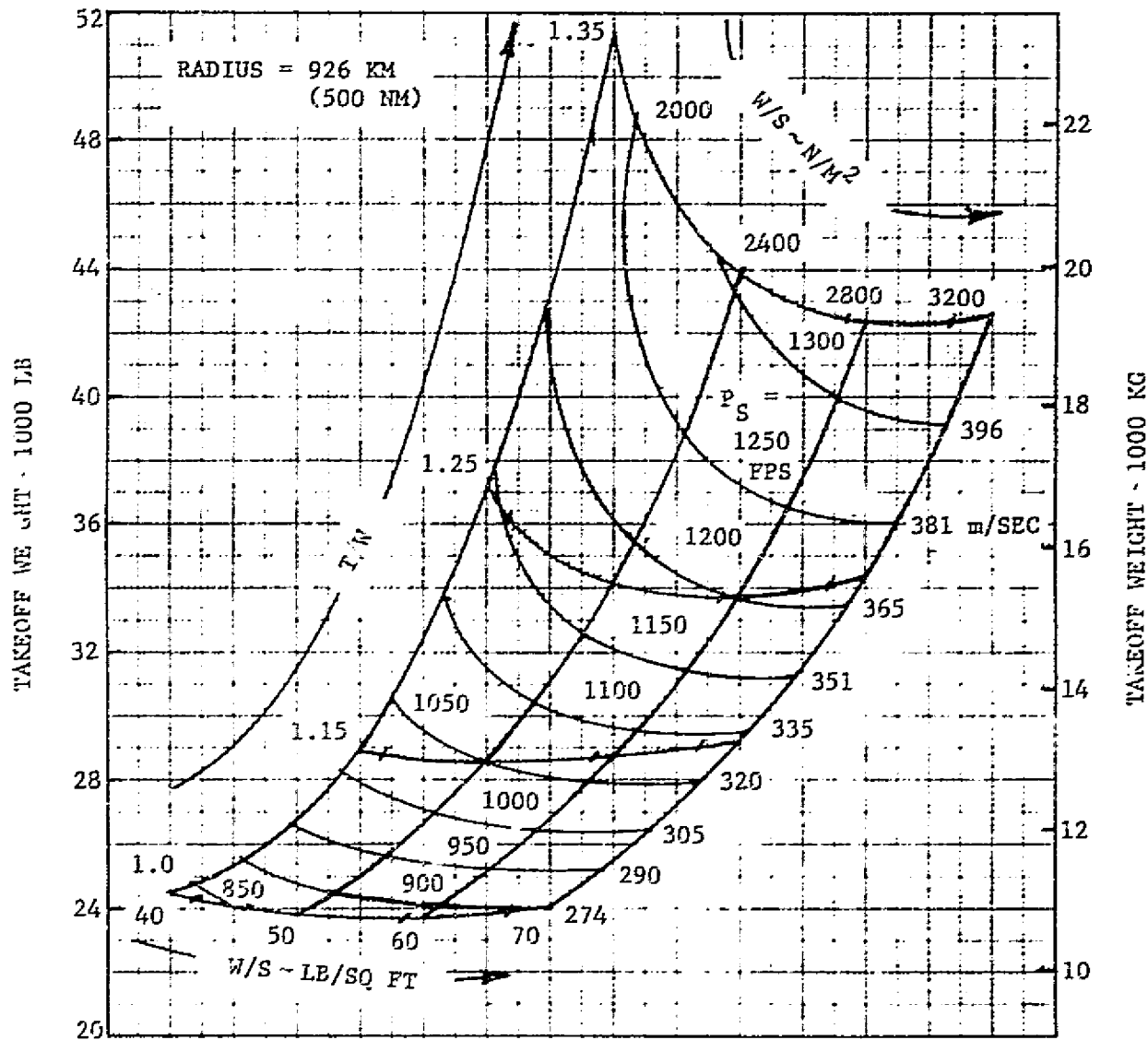


FIGURE 6-10. SPECIFIC EXCESS POWER LEVELS ON AIRCRAFT SIZING MATRIX

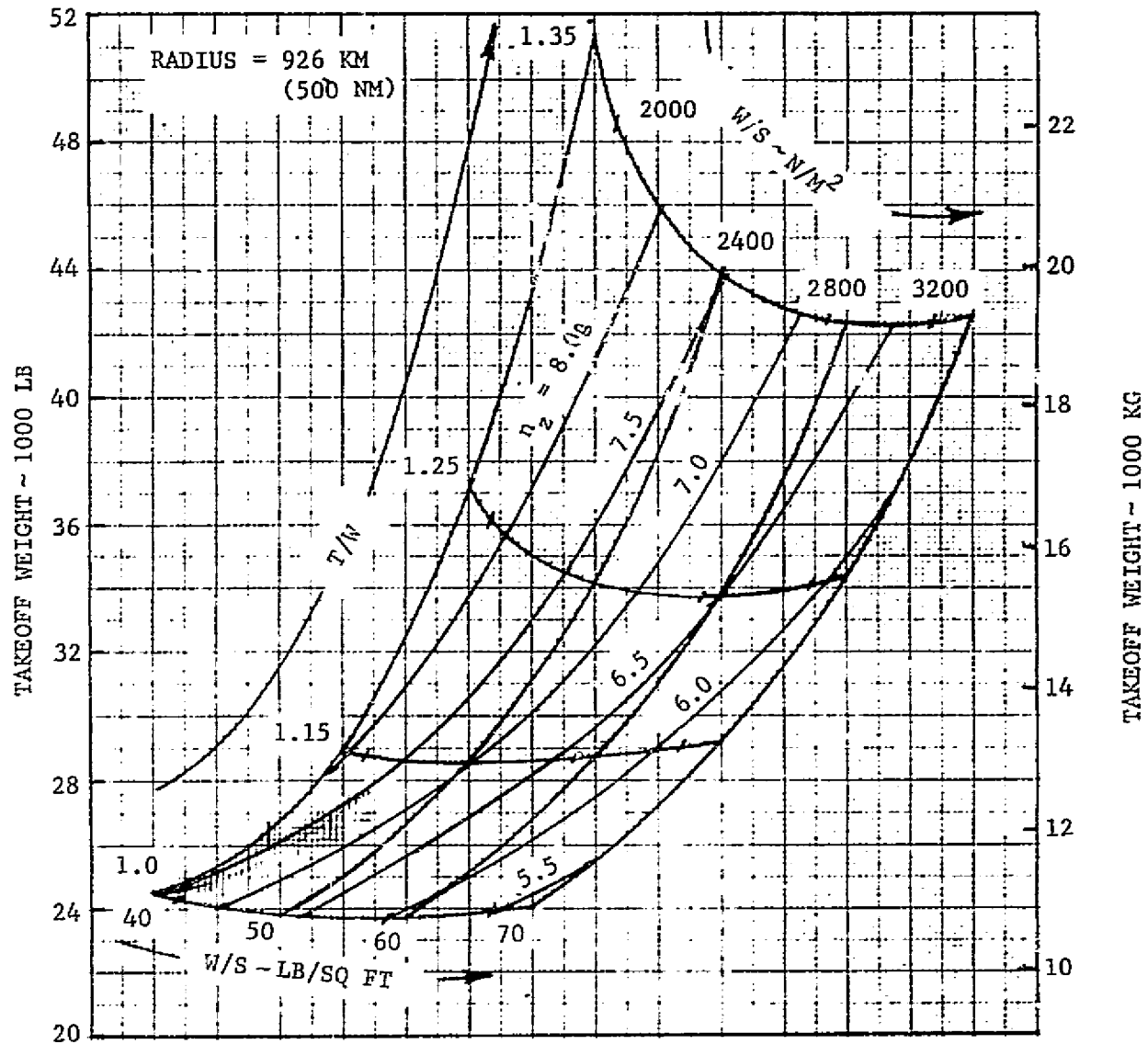
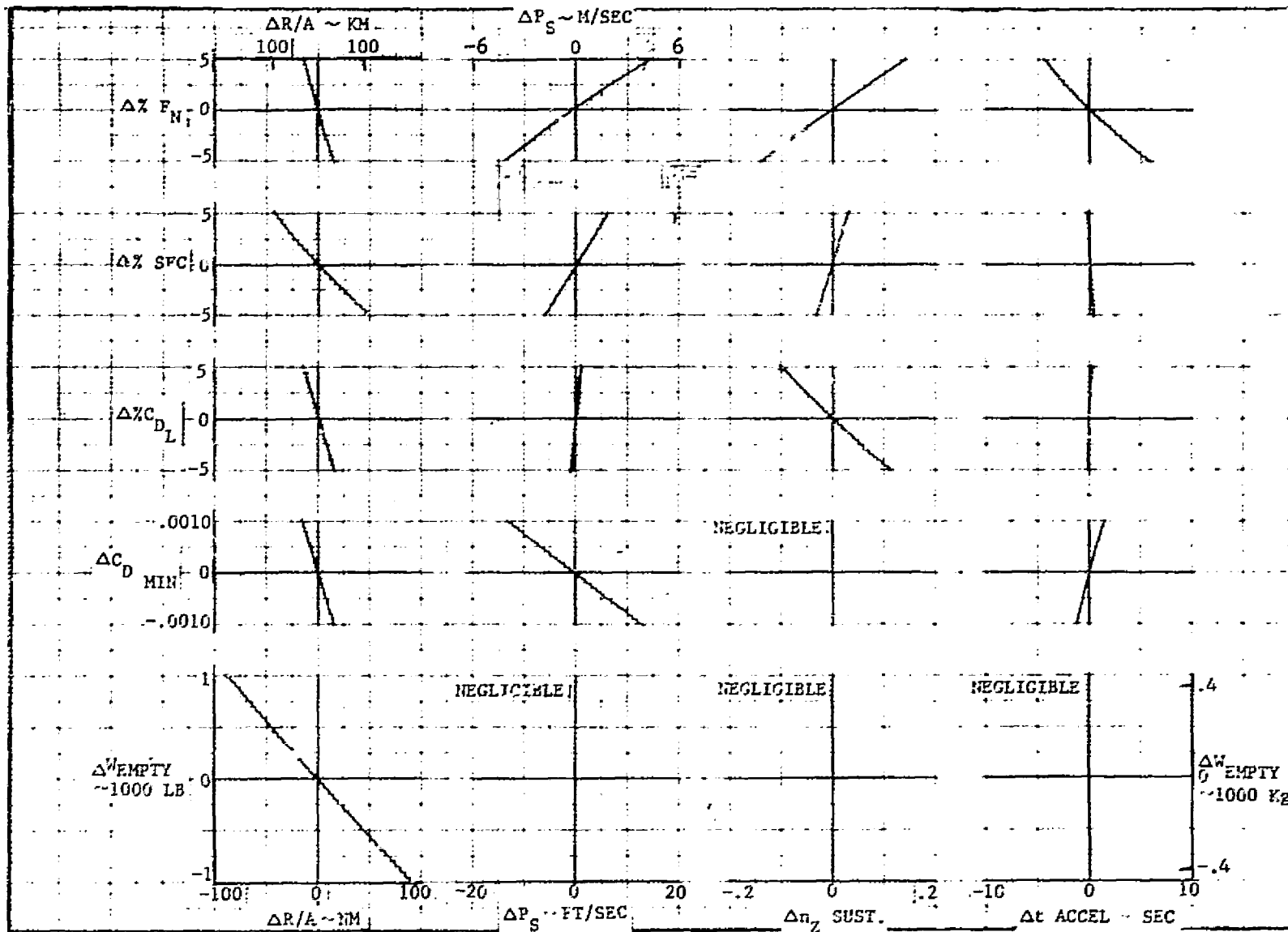


FIGURE 6-11. SUSTAINED LOAD FACTOR LEVELS ON AIRCRAFT SIZING MATRIX

ORIGINAL PAGE IS  
OF POOR QUALITY



ORIGINAL PAGE IS  
OF POOR QUALITY

FIGURE 6-12. EFFECT OF THRUST SPECIFIC FUEL CONSUMPTION, DRAG AND EMPTY WEIGHT ON RADIUS OF ACTION, SPECIFIC EXCESS POWER, SUSTAINED LOAD FACTORS AND ACCELERATION TIME FOR THE SIZED AIRCRAFT

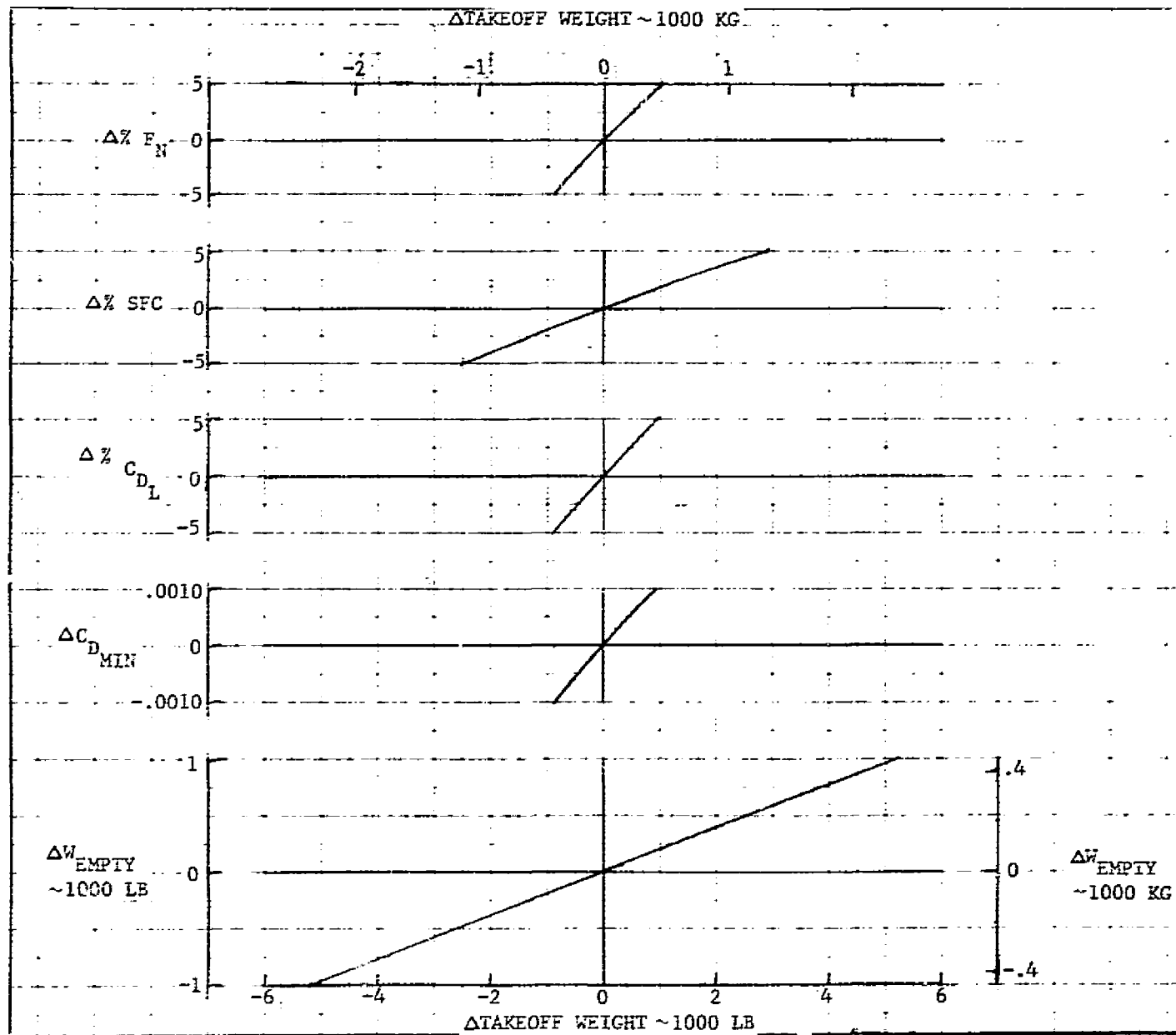


FIGURE 6-13. EFFECT OF THRUST, SPECIFIC FUEL CONSUMPTION, DRAG AND EMPTY WEIGHT ON TAKEOFF WEIGHT FOR 926 KM (500 NM) RADIUS

6-13

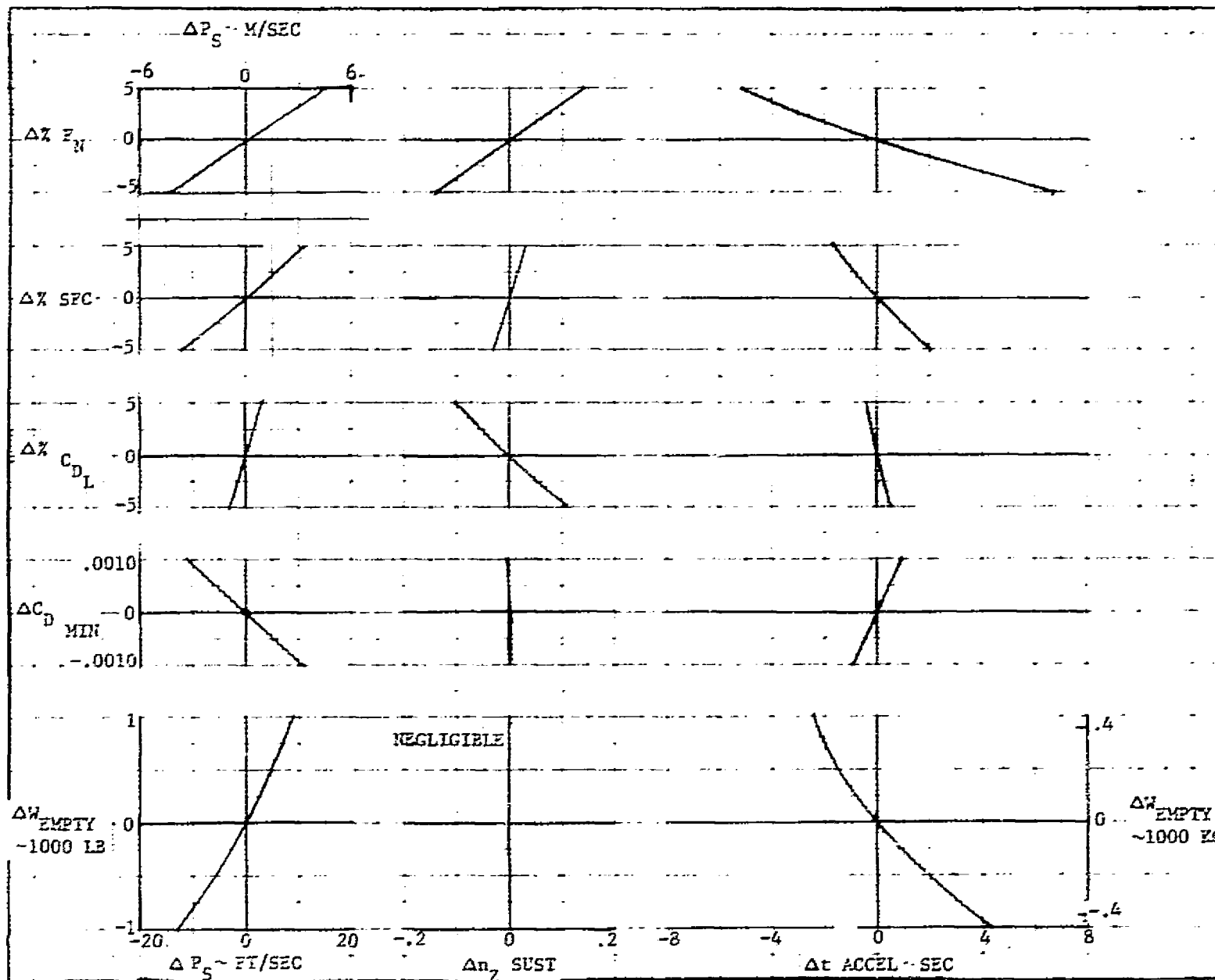


FIGURE 6-13. CONCLUDED

CONTINUED PAGE 18  
OF POOR QUALITY

## 6.2 TAKEOFF AND LANDING PERFORMANCE

### 6.2.1 Vertical Takeoff

The configuration reflects consideration of propulsive lift interference in that the main nozzles are located at the trailing edge of the wing. This location is favorable in minimizing suckdown acting on the lower wing surface and fuselage in both ground proximity and transition flight. Therefore, potential propulsive lift interactions will mainly derive from the forward jet. These interactions will be reduced primarily by a unique operating concept rather than configuration shaping. A stepped or staged liftoff concept has been studied which features initial rotation to a high attitude prior to application of full liftoff thrust. Forward nozzle suckdown and mid-body fountain are expected to be reduced or eliminated both by raising the forward jet away from the ground and by fore and aft splaying of forward and aft nozzles. Horizontal thrust balance is assumed to preclude the airplane from moving forward or aft during this maneuver. Although wheel chocks could be used to prevent horizontal motion during takeoff, reversal of the procedure is not envisioned for landing, and horizontal hold must be achieved through balancing the fore and aft components of the thrust.

The procedure (without the horizontal hold condition) is also directly applicable to STO operations by allowing full use of wing/canard lift at high angles of attack in addition to the propulsive lift. In the following, calculations are presented which encompass conditions for stationary rotation and vertical liftoff from the staged attitude. Thrust forces and nozzle deflections required to initiate the rotation maneuver are shown in Figure 6-14. Consideration of excess thrust needed at the forward nozzle include moment balance about the main gear axle plus a force for pitch acceleration. In general, this means a forward thrust augmentation leading to nozzle exit temperatures in excess of the nominal value of 1100°C (2000°F). Thrust spoiling at the aft nozzles would aid the rotation but was not included as no satisfactory mechanical solution has been developed.

Thrusts and deflections required to stabilize the airplane at a 20-degree pitch attitude are shown in Figure 6-15. For this case, the thrust split forward to aft is maintained at the nominal value of 0.67. In holding at this attitude (which may be desirable for engine function check), some load on the main gear is desirable to preclude undue motion on an unsteady deck. Liftoff is achieved by simultaneously applying full thrust and directing both nozzles perpendicular to the ground.

### 6.2.2 Takeoff Transition

Accelerating transitions have been calculated in which pitch attitude was held approximately constant at 20 degrees and thrust vectoring was used to control the flight path. In the initial phase, forward and aft jets are rotated aft in unison until the forward jet reaches its stop at 30 degrees aft from the airplane normal axis. At that point (after a rotation of only 10 degrees considering the 20-degree attitude), forward thrust is reduced to maintain pitch balance. This is accomplished first through throttling fuel flow to the forward nozzle then toward the end of transition, through throttling airflow to the forward nozzle. Full throttle is maintained throughout the transition. The forward jet is rather limited in producing a horizontal thrust component because of the deflection limit and through throttling and the primary nozzles do not deliver maximum capable thrust until near the end of the transition when all RALS bypass airflow is diverted aft. Consequently, the horizontal acceleration capability is somewhat compromised.

Figure 6-16 shows a typical accelerating transition trajectory. Figure 6-17 shows the associated commanded primary thrust vector angle relative to the aircraft fuselage reference line. At the end of 10 seconds approximately 90 percent of the aircraft weight (assuming it remains constant at 13608 Kg) is supported aerodynamically. While some altitude is lost in this trajectory during acceleration to flight speed, changes in commanded thrust angle or pitch attitude may minimize the loss. Additional study is required.

### 6.2.3 Landing

Landing approach, as considered here, is that portion of the landing during which the aircraft is approaching the landing area or apparatus with the engines operating in vertical landing mode. The primary purpose of this phase is to descend and reduce speed simultaneously until hover is reached.

Switching from aerodynamic flight to vertical landing configuration necessarily involves rotating the primary nozzles down and lighting the RALS burner. Idling thrust on the engines puts a limit on the airspeed at which this switch can be made smoothly. Even so, the engine operation must be accompanied by a reduction in angle of attack in order to reduce aerodynamic lift and create a sufficient requirement for lift due to vectored thrust so that the flight path is, at least nominally undisturbed.

From this point onward, a significant angle of attack is required to provide deceleration. In the early stages, deceleration depends heavily on aerodynamic drag

as too low an angle of attack results in acceleration on a descending path. For a 3 degree flight path, the upper limit of switchover speed at 10 degree angle of attack was m/sec (160 ft/sec) at 8618 kg (19,000 lb). As the speed reduces, aerodynamic lift reduces and more vectored thrust is required. At 41 m/sec (135 fps) the angle of attack may be increased to 20 degrees with reduction in thrust to idle to maintain the flight path, but increasing deceleration. From here on, thrust must be increased as speed reduces and at lower speeds steeper descent paths are feasible.

An outgrowth of the calculations performed indicated that the flight path is controlled by engine throttling (the RALS thrust is virtually proportional to engine thrust) while control of burning on the RALS is devoted essentially to maintaining the pitch trim. Deceleration is controlled by angle of attack and forward thrust vectoring with the RALS unit, which is reasonably powerful and has a fast response. At high speeds, aerodynamic drag is very important. At low speeds, the pilot may choose to operate at lower angles of attack for reasons of improved visibility in the neighborhood of the landing area. As angle of attack (pitch) is reduced, the main jet becomes less effective as a brake and the deceleration is more dependent on RALS forward vectoring.

A transition based on entering hover configuration at 160 fps with aircraft weight 8618 kg (19,000 lb) at 10 degree angle of attack on a 3 degree glide slope, holding the slope constant and the angle of attack at 10 degrees down to 41 m/s (135 fps), then going to 20 degree angle of attack for the rest of the deceleration to zero speed indicated about 23-36 seconds total deceleration time, depending on the maximum value of RALS thrust employed.

#### 6.2.4 Short Takeoff and Landing

Short takeoff performance as a function of takeoff weight and wind over deck is shown in Figure 6-18. A set of ground rules was established as a basis for a reasonable and conservative representation of the takeoff procedure. This approach was chosen because a large number of variables, especially with the RALS engine system,

would have to be considered in determining optimum takeoff procedures. The following assumptions were made:

1. Flat deck
2. Zero sink after leaving deck
3. Horizontal acceleration of 0.1 g required immediately after leaving deck
4. Airplane rotates to 20-degree angle of attack at the end of the deck
5. RALS is operating and thrusting aft 30 degrees during deck run. Main engines are thrusting full aft.

The last assumption makes the calculations conservative as more acceleration would be available, if in the initial stages of the deck run, all the engine airflow were exhausted (undeflected) out of the primary nozzles. The thrust vector angles, after leaving the deck, are determined by the conditions of maintaining sustained flight with an 0.1 g longitudinal acceleration and aerodynamic lift plus propulsive lift equal to weight.

Landings will normally be accomplished using essentially vertical touchdown. The unique capability of the concept studied also permits exceptional short landing performance even with one engine in the inoperative. As shown in Figure 6-19 approach speeds at normal landing weight will be in the order of 112 m/sec (60 knots) with only one engine operating.

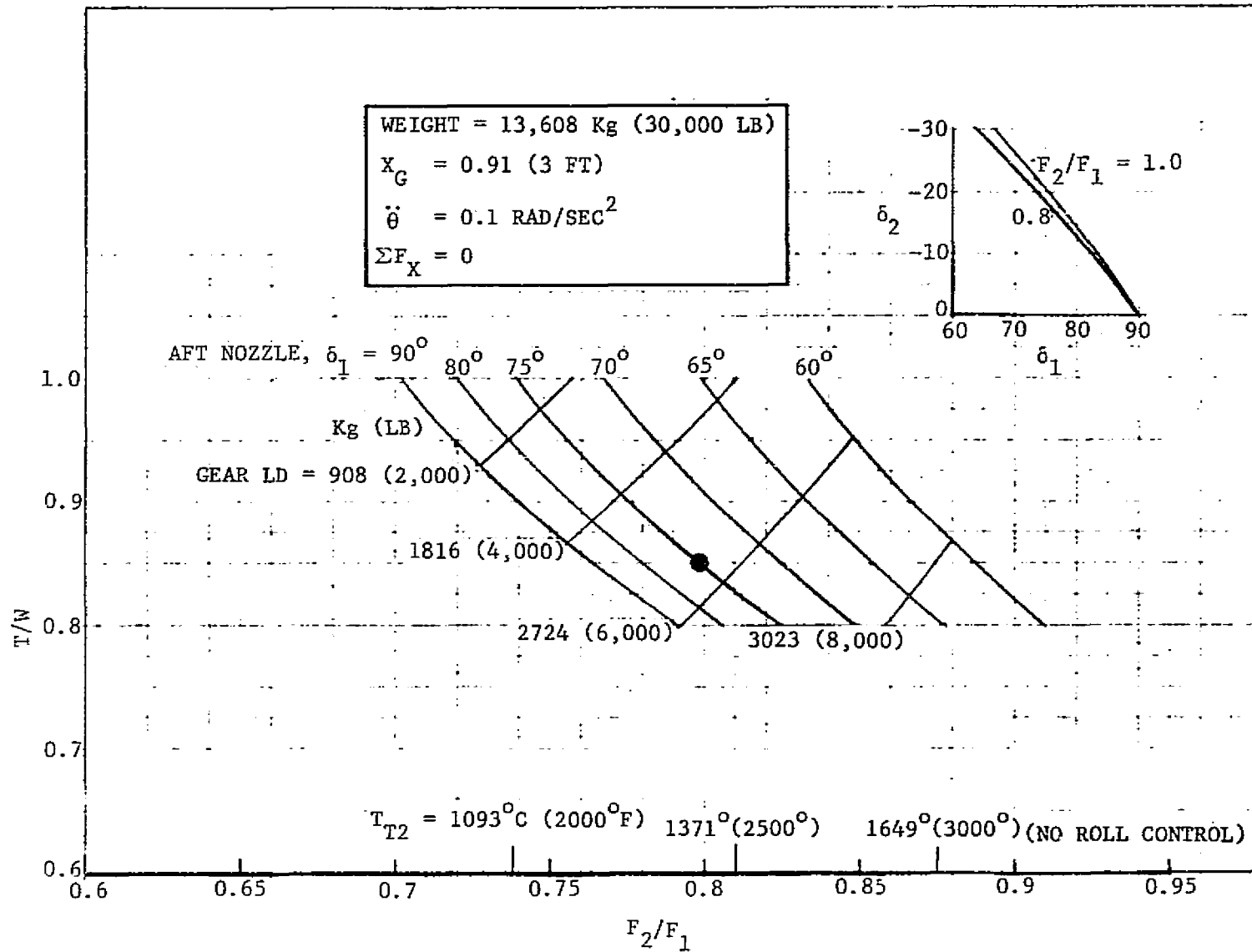


FIGURE 6-14. THRUST VECTORS FOR ROTATION

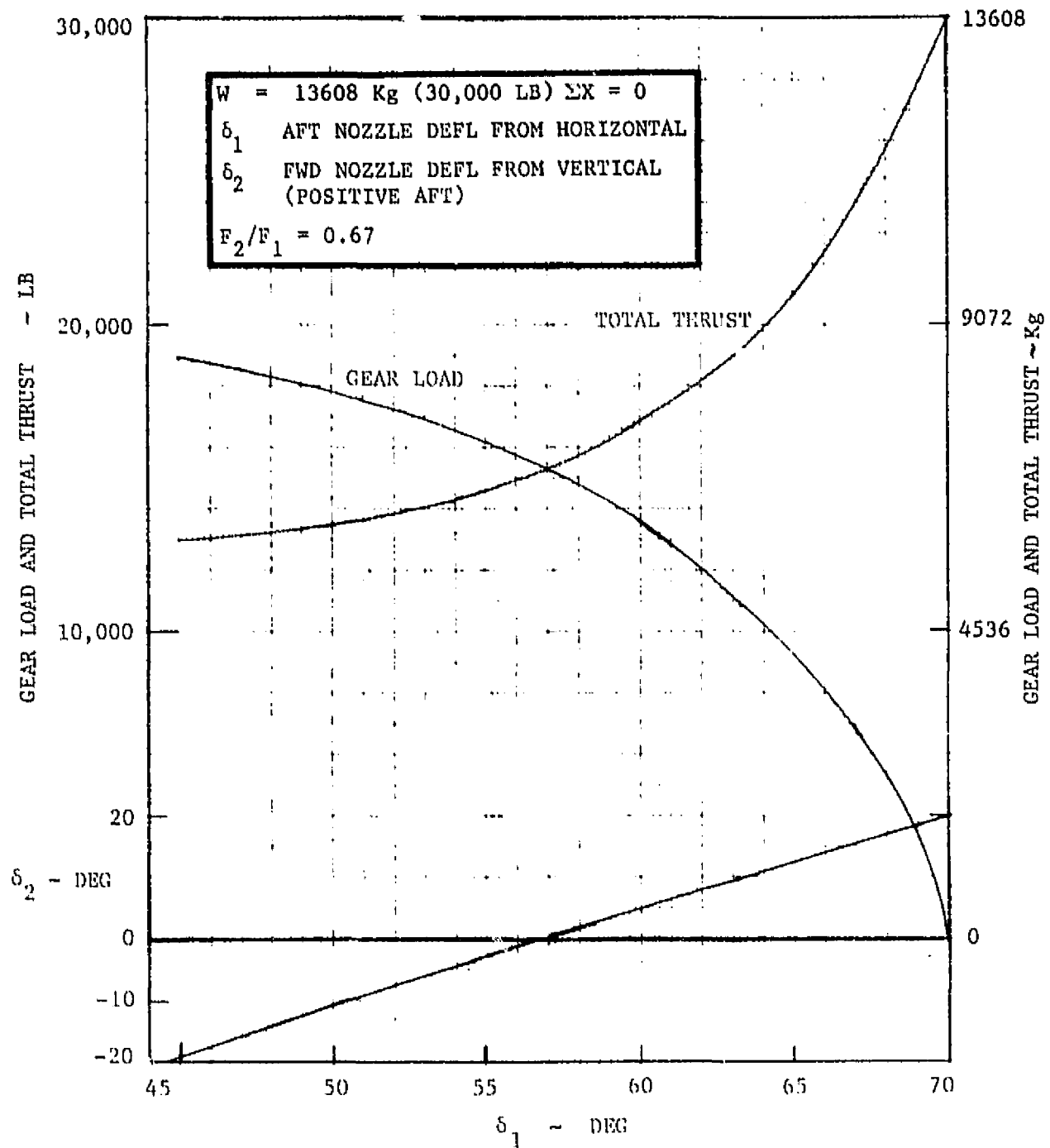


FIGURE 6-15. THRUST VECTORS TO HOLD 20° PITCH ON DECK

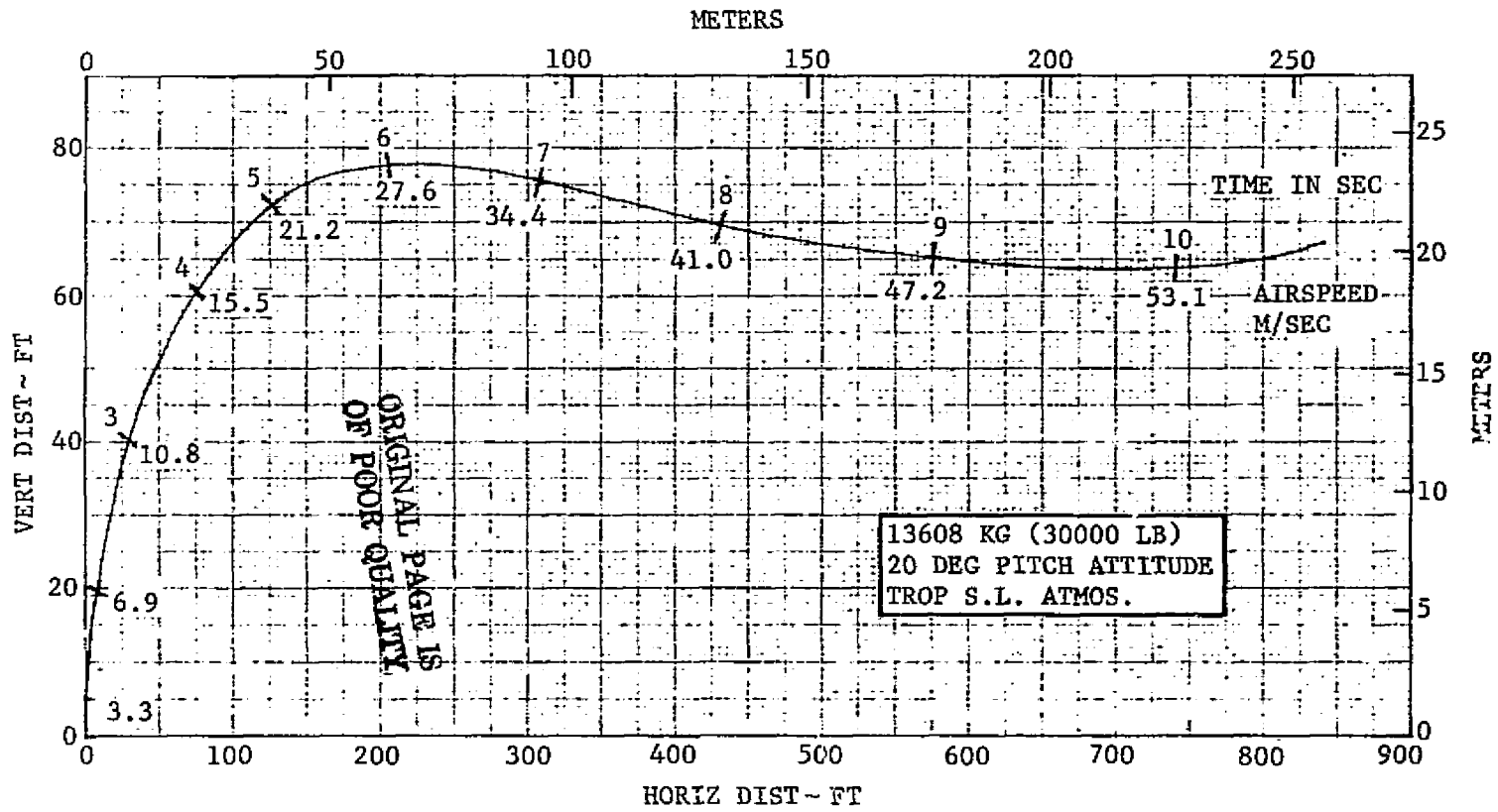


FIGURE 6-16. TAKEOFF TRANSITION TRAJECTORY

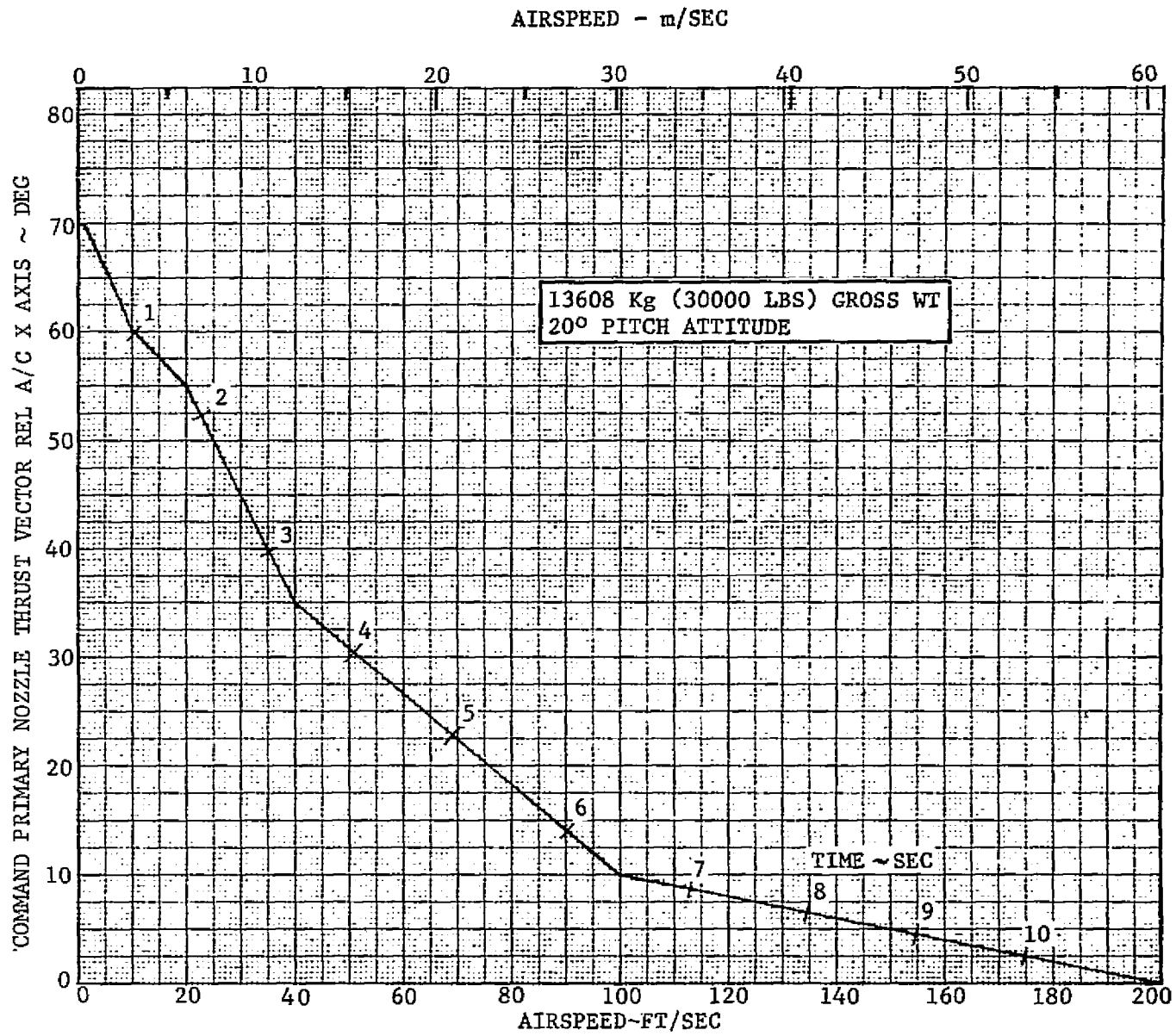


FIGURE 6-17. PRIMARY NOZZLE THRUST VECTOR COMMAND

ORIGINAL PAGE IS  
OF POOR QUALITY

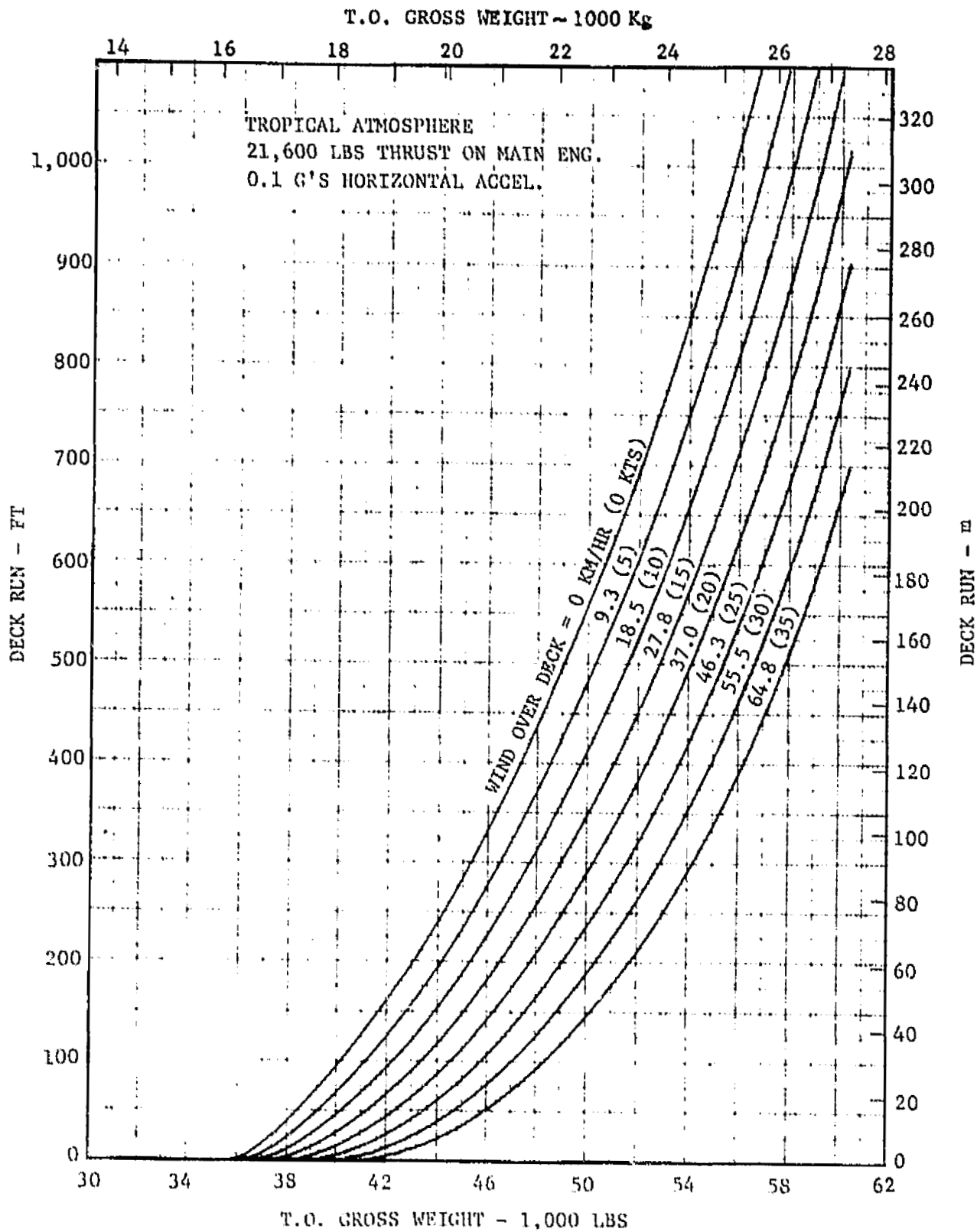


FIGURE 6-18. SHORT TAKEOFF PERFORMANCE

ORIGINAL PAGE IS  
OF POOR QUALITY

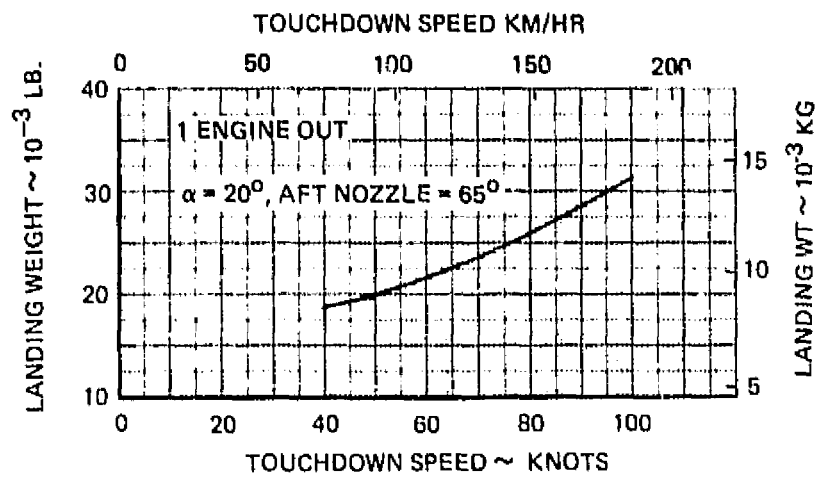


FIGURE 6-19. SINGLE ENGINE LANDING PERFORMANCE

PRECEDING PAGE BLANK NOT FILLED

## SECTION 7

### AERODYNAMIC UNCERTAINTIES

As the aerodynamic data were developed various aerodynamic uncertainties became apparent and are presented in this section.

#### 7.1 WAVE DRAG AT HIGH MACH NUMBER

Estimates show a rise in wave drag at M 0.85 which eases somewhat at M 1.1 but continues to about M 1.8 (Figure 3-2) which experimental data for similar wings and others indicate a leveling at about M 1.1. Tests should be made to resolve wave drag characteristics of the complete model.

#### 7.2 CANARD CONTRIBUTION TO STABILITY

Experimental data and estimates of the canard contribution to stability and the canard configuration aerodynamic center shift from subsonic to supersonic speeds do not match. Canard-off and canard-on tests should be made, including the effects of optimum maneuvering flap settings.

#### 7.3 OPTIMUM CANARD-FLAP DEFLECTIONS AT SUBSONIC SPEEDS

Because of the difficulty in estimating the canard contribution to longitudinal stability, the optimum canard-flap combination for minimum subsonic drag-due-to-lift as estimated needs to be verified. The estimates of optimum control deflections show small trailing-edge flap deflections and negative canard deflections about equal to the aircraft angle of attack. The drag is greater than for a tailless configuration regardless of static stability margin between 25 percent unstable and 10 percent stable. Also, the highly negative canard deflection may not produce a sufficiently strong vortex over the wing to delay stall. Test data are required for large negative canard deflections. These data will also be useful to more accurately determine safe angle-of-attack limits for the unstable aircraft where the canard can aid the trailing edge flaps in producing nose-down moment for recovery.

#### 7.4 CANARD EFFECTS ON DIRECTIONAL CHARACTERISTICS

Precise estimation of canard effects on directional stability and fin effectiveness is difficult, especially at high angles of attack. Experimental data taken on a YF-17 model with a single, all-movable fin indicates that directional control effectiveness is retained while stability is not. However, with a high-authority active control system, the directional characteristics should be good. Sideslip tests should be conducted at various angles of attack and Mach number. Combinations of canard off and at various deflections should be run with fin-off and fin-on with deflections.

#### 7.5 TWIN AFTERFAIRING DRAG

The afterfairings have been shaped to minimize interference from the inboard sides on the aft fuselage and from the exhaust plume. Outboard shaping is aimed at obtaining favorable interference on the lower outboard wing surface giving positive pressures. The aft slopes of the area plot are reduced by the afterfairings. The drag increment from the afterfairings should be checked by test.

#### 7.6 VECTORED THRUST FOR MANEUVER ENHANCEMENT

Vectoring of thrust could enhance the sustained maneuvering capability of the aircraft through supercirculation if the trim penalty is not too great. The direct effect cannot be obtained on a flow-through model. However, determination of canard deflections in the positive range to trim aft thrust vectoring would be very useful. These data, together with the estimated direct and induced propulsion effects would give a good assessment of the value of in-flight thrust vectoring.

With the availability of a wind tunnel model incorporating propulsion simulators, all direct and induced effects can be measured. An investigation of this type would provide the required data base for determination of the effectiveness of thrust vectoring for maneuvering.

#### 7.7 PROPULSION INDUCED EFFECTS IN HOVER AND TRANSITION

Simulation of thrust and inlet flow for the VTOL, nose-high operational concept could be provided using a wind tunnel model incorporating propulsion simulators. Inlet ingestion and suckdown characteristics would be investigated. The RALS would also need to be simulated. After tests in ground effect, tests out of ground effect and simulating transition would be accomplished. Pitching and rolling moments during transition would be of prime interest.

PRECEDING PAGE BLANK NOT FILLED

## SECTION 8

### PROPOSED RESEARCH PROGRAM

The proposed research program defines the objectives of the research, presents a recommended wind-tunnel test program to resolve the aerodynamic uncertainties described previously, and describes the wind-tunnel models to be used during the test program.

#### 8.1 RESEARCH OBJECTIVES

The following are the key objectives of the research program:

1. Verification of estimates
2. Assessment of estimation methods
3. Extension of limited test data through a more extensive Mach number range
4. Investigation of areas of aerodynamic uncertainty where analytical procedures are unavailable or inadequate.

#### 8.2 WIND TUNNEL TEST PLAN

The proposed wind-tunnel test plan addresses only those research tests that can be accomplished with an aerodynamic, flow-through-duct model. Thus, the uncertainties requiring propulsion simulation are not included. Also no tests are presently planned for the 12-foot Wind Tunnel where the models would be tested at angles of attack greater than the 30 degrees (estimated full scale stall angle of attack) planned for 11 x 11 foot Wind Tunnel. Tests beyond the stall with an aircraft which is 15-percent unstable are less important with a horizontal attitude VSTOL. There is no requirement to operate near the stall angle of attack for takeoff and landing and the aircraft will be limited to safe recovery angles of attack during other flight conditions. During subaerodynamic flight for takeoff and landing reaction control is available to augment the aerodynamic controls.

The test Reynold's number of over  $10 \times 10^6$  based on the wing  $\bar{c}$  precludes the necessity of conducting a series of runs to determine the effect of Reynold's number

on the aerodynamic characteristics. However, it may be desirable to conduct one series of tests at the highest possible Reynold's numbers, repeat it at a lower Reynold's number and conduct the rest of the program at the lower Reynold's number (also lower dynamic pressure) in the interest of conserving energy.

Tests with varying inlet mass flow ratio are not planned at present, but may be the subject of future tests with propulsion simulation. With full throttle, the spill drag is zero at M 0.3 and M 0.6, 1 drag count at M 0.9, 12 counts at M 1.2 and 1 count again at M 1.6. At cruise power settings and altitudes spill drag is of the order 12 drag counts and not significant enough for separate tests at the present time.

The proposed wind-tunnel test program is presented in tabular form in Table 8-1, grouped as described below.

Group 1 is a Mach number series in pitch to moderate angles of attack in order to assess the variation of wave drag with Mach number for the complete configuration. The canard is fixed at zero deflection.

Group 2 is for the primary purpose of obtaining the aerodynamic center variation with Mach number canard on and off and for finding the canard stability contribution. With canard on, data are also obtained at subsonic speeds with the leading and trailing edge flaps set for estimated approximate optimum from a trimmed drag standpoint. These tests will be used, together with Group 3, which has other canard deflections to obtain canard effectiveness.

Group 3 is for the purpose of determining canard effectiveness with the estimated optimum flap deflections at subsonic speeds and zero flaps at supersonic speeds. The aircraft is marginally stable and large (20 degrees) positive canard deflections are of interest when used in conjunction with thrust vectoring to enhance maneuvering. Ten degrees of positive canard deflection is also run with more positive trailing edge flap than estimated to be optimum (or the optimum flap angle untrimmed) to check on the validity of the estimates. The estimates presently show very small trailing edge flap together with very large negative canard deflections at subsonic speeds. Test with these flap-canard deflections are also included in this group. The high angle-of-attack range at subsonic speeds for large negative canard deflections will be used to find the effect of the canard on maximum lift.

Group 4 data are for the purpose of determining the basic lateral-directional characteristics of the complete configuration. Tests are conducted over a full Mach number range with flaps zero and at estimated optimum flap deflections and with

various canard settings at subsonic speeds. The canard setting of 0 degrees is for direct comparison, at angles of attack of 10 degrees and 20 degrees, with the data run previously at 0-degree angle of attack. The -10 degree deflection at 10 degrees angle of attack and -20 degrees at 20 degrees angle of attack are the estimated approximate optimum for trim. The effect of the canard-induced vortex on the lateral-directional characteristics will be determined with these tests and those with the +10 degree deflection, as might be used in conjunction with thrust vectoring.

Group 5 is for the purpose of extending Group 4 data to the case of no-vortex-strength by testing with canard off.

Group 6 is a repeat of Groups 4 and 5 without the vertical tails in order to measure the vertical tail contribution to lateral-directional stability without a canard and with various canard deflections.

Group 7 includes a vertical tail deflection and obtains the same data as Group 6 for determining fin effectiveness as opposed to stability.

Group 8 has the objective of obtaining the drag contribution of the twin after-fairings throughout the Mach number range in conjunction with Group 1.

TABLE 8-1. TEST PLAN

W = WING, B = BODY-CANOPY A = TWIN AFTERFAIRINGS, D = DUCTS  
 C = CANARD, V = VERTICAL TAILS,  $\delta_n/\delta_F$  = NOSE FLAP DEFLECTION/TRAILING EDGE  
 FLAP DEFLECTION ~ DEG,  $\delta_C$  = CANARD DEFLECTION ~ DEG  
 $\alpha$  RANGE A = - 4° TO 25° THROUGH M 1.4 AND - 4° TO 15° AT M 1.6 AND M 1.8  
 $\alpha$  RANGE B = 0 TO 30°,  $\beta$  RANGE A = - 3° TO 15°

GROUP	CONFIGURATION	$\alpha$	$\beta$	$\delta_C$	$\delta_n/\delta_F$	MACH NUMBER						
						0.6	0.8	0.9	1.2	1.4	1.6	1.8
1	WBADCV	A	0°	0	0/0	X	X	X	X	X	X	X
2	WBADV	A	0°	-	0/0	X	X	X	X	X	X	X
				-	15/0	X	X	X				
				-	15/5	X	X	X				
				-	30/0	X	X	X				
				-	30/10	X	X	X				
2	WBADCV	A	0°	0	15/0	X	X	X	X			
				0	15/5	X	X	X				
				0	30/0	X	X	X				
				0	30/10	X	X	X				
				0	30/10	X	X	X				
3	WBADCV	A	0°	+10	0/0	X	X	X	X	X	X	X
				+20	0/0	X	X	X	X	X		
				0	0/0	X	X	X				
				+10	0/0	X	X	X				
					15/0	X	X	X				
					15/5	X	X	X				
					30/0	X	X	X				
					30/10	X	X	X				
				-10	0/0	X	X	X	X	X	X	X
					15/0	X	X	X	X	X		
					15/5	X	X	X				
					30/0	X	X	X				
					30/10	X	X	X				
					0/0	X	X	X				
					15/0	X	X	X				
	15/5	X	X	X								
	30/0	X	X	X								
	30/10	X	X	X								
4	WBADCV	0°	A	0	0/0	X	X	X	X	X	X	X
				-10	15/0	X	X	X				
				0	15/0	X	X	X				
				+10	15/0	X	X	X				
				-20	30/0	X	X	X				
4	WBADCV	10°	A	0	0/0	X	X	X	X	X	X	X
				-10	15/0	X	X	X				
				0	15/0	X	X	X				
				+10	15/0	X	X	X				
				-20	30/0	X	X	X				
4	WBADCV	20°	A	0	0/0	X	X	X	X	X	X	X
				-10	15/0	X	X	X				
				0	15/0	X	X	X				
				+10	15/0	X	X	X				
				-20	30/0	X	X	X				
5	WBADV	0°	A	-	0/0	X	X	X	X	X	X	X
				-	15/0	X	X	X				
				-	30/0	X	X	X				
5	WBADV	10°	A	-	0/0	X	X	X	X	X	X	X
				-	15/0	X	X	X				
				-	30/0	X	X	X				
5	WBADV	20°	A	-	0/0	X	X	X	X	X	X	X
				-	15/0	X	X	X				
				-	30/0	X	X	X				
6	REPEAT GROUPS 4 & 5 WITHOUT VERTICAL TAILS											
7	REPEAT GROUPS 4 & 5 WITH VERTICAL TAILS DEFLECTED 10°											
8	WBDCV	A	0°	0	0/0	X	X	X	X	X	X	X

### 8.3 WIND TUNNEL MODEL DESIGN

In order to explore the aerodynamic uncertainties of the concept and to generate an aerodynamic data base, a wind-tunnel test model is required. As noted in the previous sections, the configuration features significant aerodynamic/propulsion interactions which can best be studied experimentally with simultaneous simulation of inlet and exhaust flow influences. This can be achieved by the use of a propulsion simulator. However, in order to obtain sideslip data and to reduce support system interference at transonic and supersonic speeds, an aft-sting mounted model with flow-through inlets is also desirable.

The initial model design work has been based on the approach of designing the model as a flow-through inlet model with consideration given to later modifications to include engine simulator testing and jet-effects model test. The impact on model size of including the compact propulsion simulator has been considered as well as the desirability of achieving full-scale mass flow ratios and minimizing aft-end geometry changes. Also, the model scale has been made common with that for the VATOL concept so that a number of parts would be common to both models.

The wind tunnel test model will be surface-defined by the NORLOFT computer program which represents conic shapes with parametric bi-cubic patches. This surface definition is now represented in a NORLOFT format, but the possibility exists that this data can be made suitable for the NASA/Ames analytical wind tunnel purposes. The wing, which has a 65A0004-series thickness distribution on a twisted and cambered planform, is shown in Figure 8-1 with section cuts at every ten percent semi-span. This wing represents the common wing that will be used on both wind tunnel test model configurations.

#### 8.3.1 General Considerations

The critical area of design which determines the size of the model is in the physical placement of the compact propulsion simulator in the model. The powered simulator to be used has a three-inch diameter compressor face with an additional 1.27 cm (0.5-inch) for exterior hardware. On this basis, an 8-percent scale model is required to physically contain the powered simulator without aborting the fuselage lines (see Figure 8-2). Maximum powered simulator performance is shown for three different model scales in Figure 8-3. The estimated full-scale intermediate power settings at 3,000 and 11,000 meters (10,000 and 36,000 feet) are superimposed on Figure 8-3 indicating the requirement of an 8.5 percent or less scale model to simulate full-scale airflow. However, the VATOL model must be no less than 9.5-percent

scale to permit simulation of full-scale airflow which dictates the same scale for the HAVSTOL model. At this scale, the mass flow simulation will be within 80 percent of full-scale requirements. Figure 8-4 will be used to determine drive and bleed manifold sizing to possibly reduce fuselage abortions. The degree of fuselage abortions has not been determined, but because the HAVSTOL fuselage is larger than the VATOL, no line deviations are expected.

Wind Tunnel Installation. The three wind tunnels being considered are the NASA-Ames 12-foot, 11-foot, and 9x7-foot. The sizing of the 9.5-percent model to fit in these tunnels has been analyzed and the results shown in Table 8-2. The test rhombus for M 1.5 and M 1.8 in the 9 x 7-foot tunnel is illustrated in Figure 8-5. Because models of this size and larger have been tested in these tunnels, it was concluded that the 9.5-percent model is well within tunnel operating limits.

Model Support. Two methods of support will be used. One is the conventional sting entering the aft end of the model. This method applies to the aerodynamic force model configuration incorporating flow-through ducts. A blade type strut will be used for the powered simulator and the jet-effects models. Figure 8-6 illustrates these mounting arrangements. The blade support will contain air delivery and return ducts. It will be shaped to minimize its effects on the flow over the model. This effect will be tailored either for the subsonic or transonic regime.

An analysis of the maximum dynamic pressure in the Ames tunnels versus model scale is shown in Figure 8-7. The limit criterion was the maximum load capability of the respective tunnel support system. As shown, for the 9.5-percent model, the maximum dynamic pressure is  $43000 \text{ N/m}^2$  (900 psf) in the 11-foot tunnel, giving a Reynolds number of 19 million per meter (6 million per foot). This maximum dynamic pressure results in a limit AOA of 28 degrees. There remains the capability of testing at higher dynamic pressures (higher Reynolds numbers) at lower AOA. For example, at AOA 10 degrees the maximum dynamic pressure, limited by the tunnel support system, is  $55000 \text{ N/m}^2$  (1150 psf). This would give a Reynolds number approaching 25 million per meter (8 million per foot). There may be a restriction on the test Reynolds number due to energy conservation. A few runs at higher Reynolds numbers, to check Reynolds number effect, would be possible.

Model Balance. A two-inch diameter Task MK XXIV balance, owned by Northrop, is being considered for the subject model. This balance has a normal force limit of 2900 kg (6400 pounds) and an axial force limit of 160 kg (350 pounds) corresponding to a maximum dynamic pressure of 29000 N/m<sup>2</sup> (600 psf). Figure 8-8 shows the balance envelope. The maximum normal force shown occurs at an angle of attack of approximately 28 degrees with trailing edge flaps deflected to 25 degrees and leading edge flaps deflected to 24 degrees. If the dynamic pressure is held to 29000 N/m<sup>2</sup> (600 psf), the maximum axial force that will be experienced by the balance will be approximately 75 percent of the gage limit. Thus, the balance is the limiting component in the system. The balance will be oriented in a reverse position when used with the blade support.

### 8.3.2 Aerodynamic Force Model

The aerodynamic force model will be a conventional flow-through-duct model mounted on a balance sting arrangement. A sketch of the model is shown in Figure 8-9. The six-component balance will measure all the forces and moments encountered. In addition, instrumentation will be included to measure duct airflow momentum and pressure losses through the duct. The aft end will be aborted to accommodate the sting and, if necessary, to obtain mass flow ratios approaching 1.0. The model will be capable of obtaining model build-up data. Off blocks will be provided for wing off, vertical off, etc., configurations. Control surfaces, such as leading and trailing edge flaps, rudder, and movable canard, will be provided.

### 8.3.3 Jet Effects Model

A jet-effects model can be designed using the basic parts of the aerodynamic force and powered simulator models. The blade sting will be used to support the model with the aft portion of the model metric. High pressure air will be provided to the internal nonmetric nozzles. Numerous external surface static pressure measurements can be obtained during this phase of testing. The inlets of the model can be faired over. The aft end abortions required to fit the powered simulator into the model and to sting mount the force model can also be duplicated and tested on and off for their effects.

TABLE 8-2. COMPARISON MODEL SIZE TO TUNNEL SIZE

(9.5% HAVSTOL MODEL)

PARAMETERS	AMES 11' TUNNEL	AMES 12' TUNNEL	AMES 9x7' TUNNEL
<u>WING REFERENCE AREA</u>			
FULL SCALE: M <sup>2</sup> (FT <sup>2</sup> )	46.45 (500)	46.45 (500)	46.45 (500)
MODEL SCALE: CM <sup>2</sup> (FT <sup>2</sup> )	4189.9 (4.51)	4189.9 (4.51)	4189.9 (4.51)
% TUNNEL CROSS-SECTION AREA:	3.7	4.5	7.2
<u>MAXIMUM FRONTAL AREA</u>			
FULL SCALE: M <sup>2</sup> (FT <sup>2</sup> )	2.71 (29.17)	2.71 (29.17)	2.71 (29.17)
MODEL SCALE: CM <sup>2</sup> (FT <sup>2</sup> )	244.3 (.263)	244.3 (.263)	244.3 (.263)
%TUNNEL CROSS-SECTION AREA:	0.21	0.26	0.41
<u>WING SPAN</u>			
FULL SCALE: M (FT)	9.94 (32.6)	9.94 (32.6)	9.94 (32.6)
MODEL SCALE: CM (FT)	94.49 (3.10)	94.49 (3.10)	94.49 (3.10)
% TUNNEL WIDTH:	28.2	27.4	44.2
<u>PLANFORM AREA</u>			
FULL SCALE: M <sup>2</sup> (FT <sup>2</sup> )	64.20 (691.0)	64.20 (691.0)	64.20 (691.0)
MODEL SCALE: CM <sup>2</sup> (FT <sup>2</sup> )	5797.1 (6.24)	5797.1 (6.24)	5797.1 (6.24)
% TUNNEL CROSS-SECTION AREA:	5.2	6.2	9.9

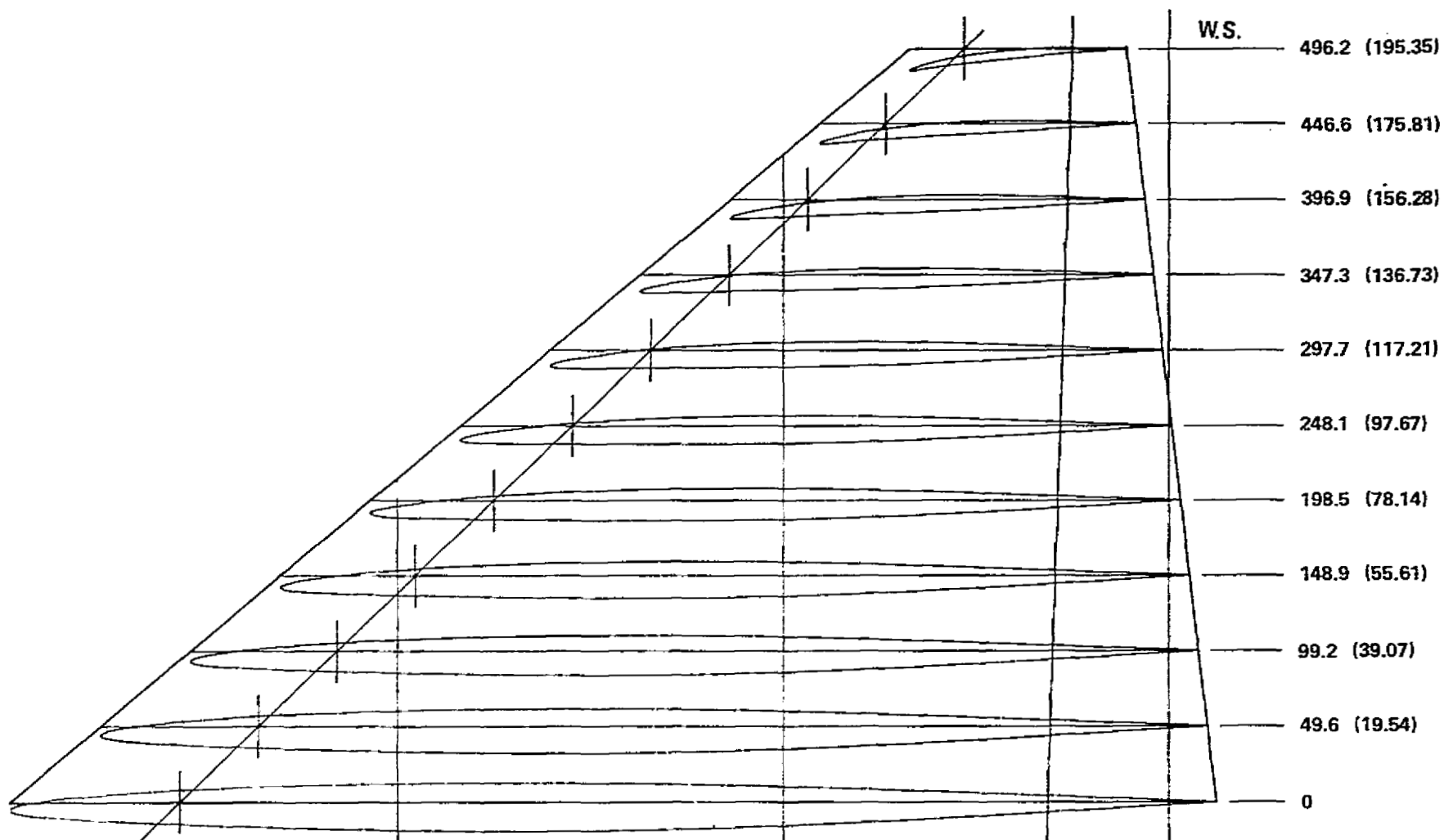


FIGURE 8-1. WIND TUNNEL MODEL WING

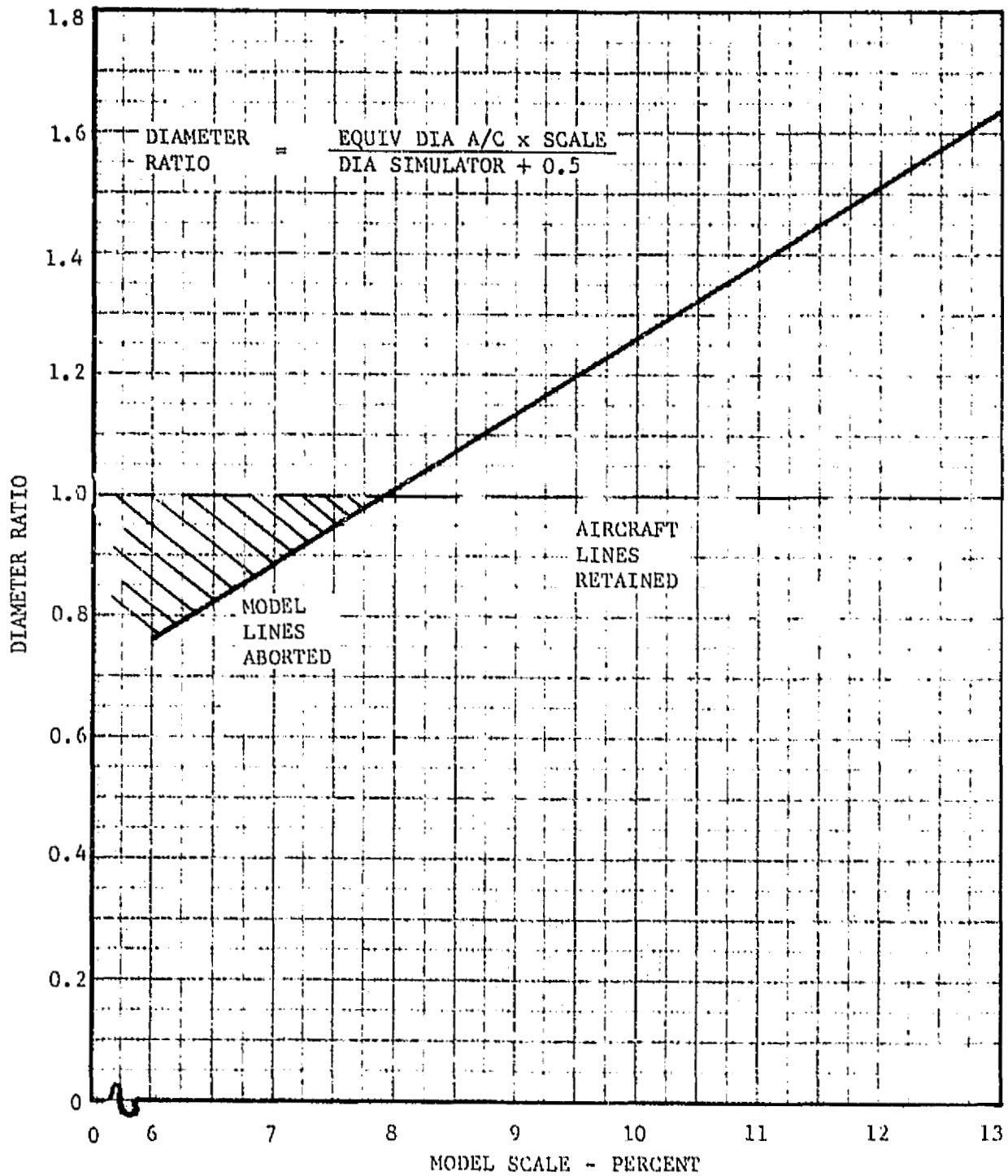


FIGURE 8-2. MODEL SCALE REQUIREMENTS FOR PROPULSION SIMULATOR SIZE

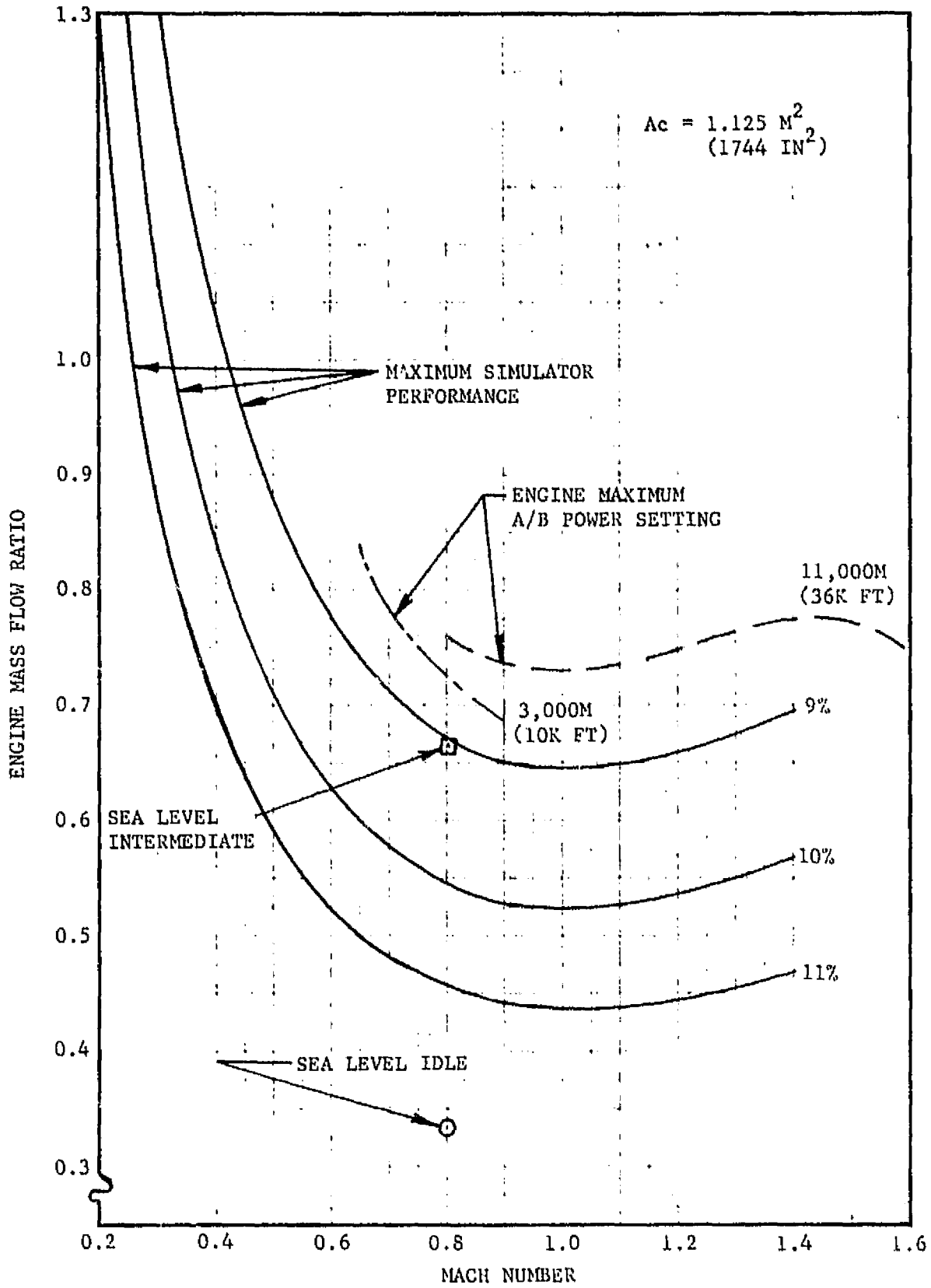


FIGURE 8-3. ENGINE SIMULATOR PERFORMANCE

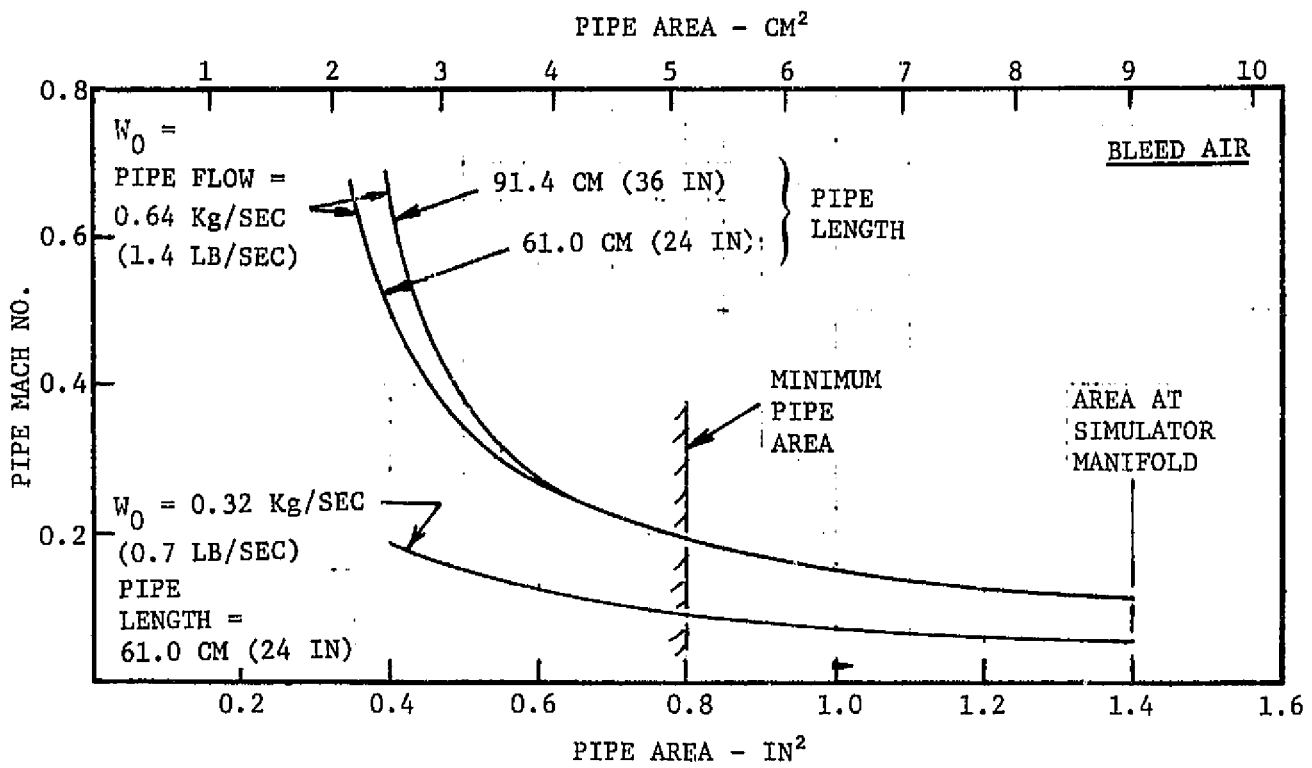


FIGURE 8-4. PIPE MACH NO. - SIMULATOR DRIVE AND BLEED LINES

ORIGINAL PAGE IS  
OF POOR QUALITY

ORIGINAL PAGE IS  
OF POOR QUALITY

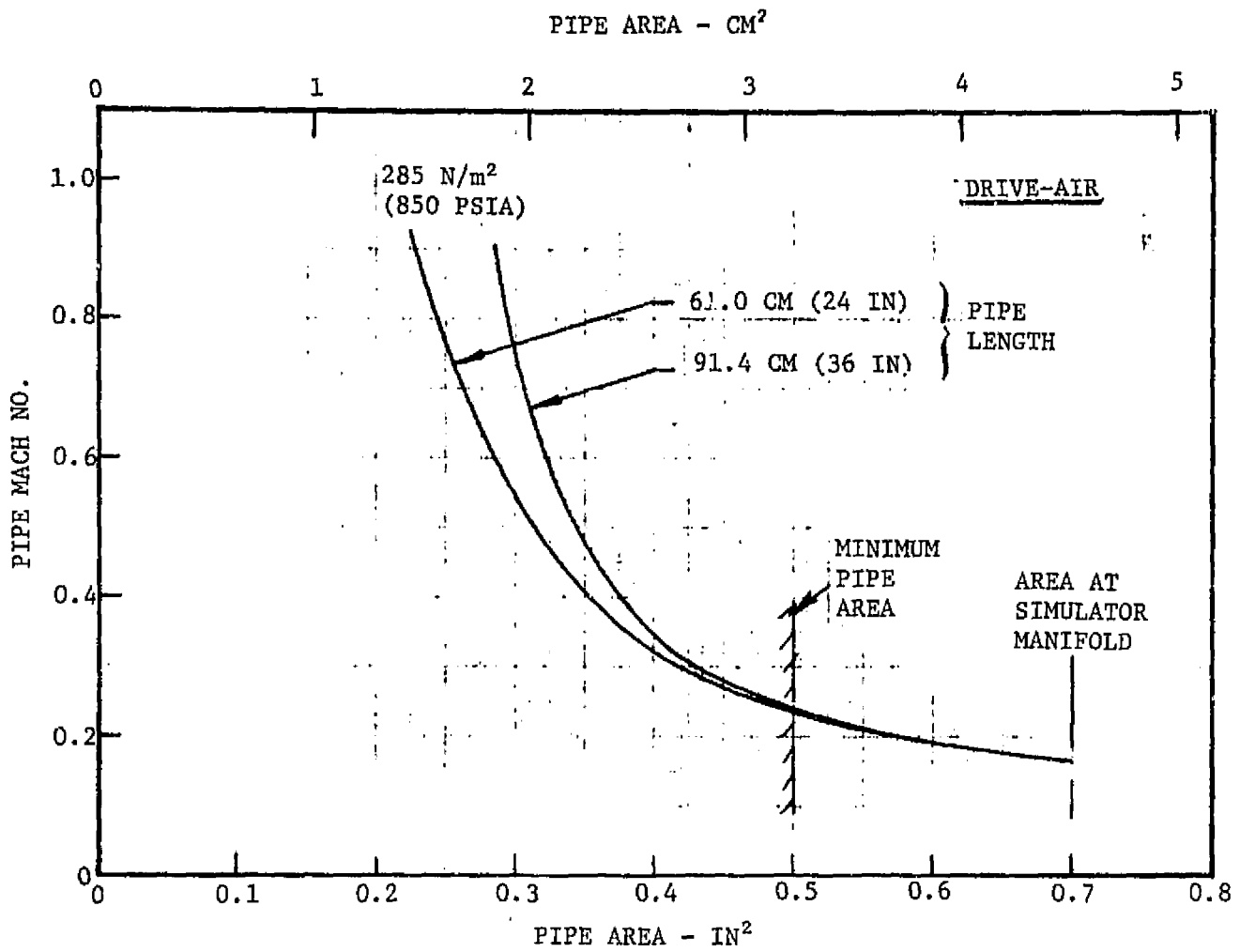


FIGURE 8-4. PIPE MACH NO. - SIMULATOR DRIVE AND BLEED LINE (CONCLUDED)

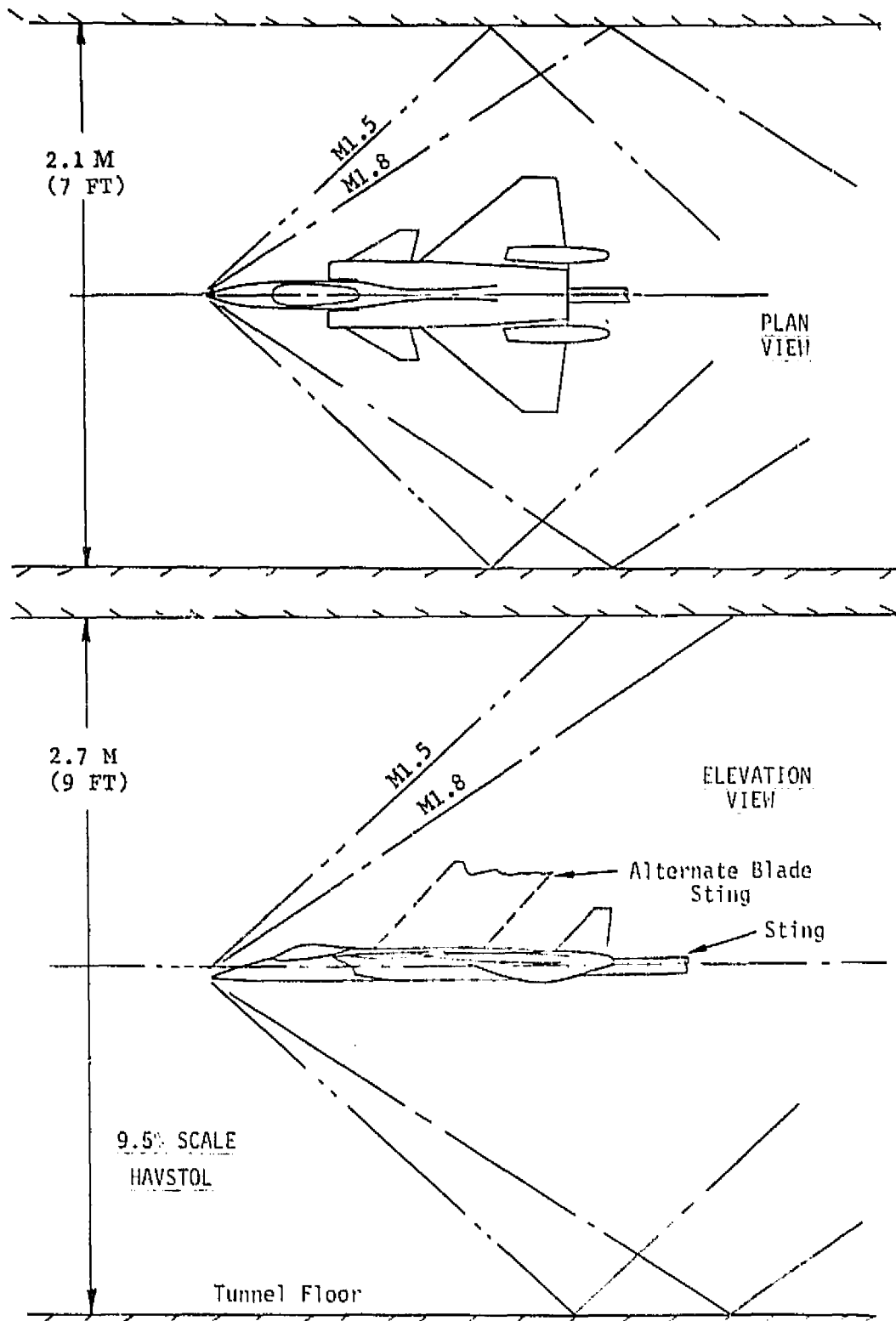


FIGURE 8-5. AMES 9x7 WIND TUNNEL ENVELOPE

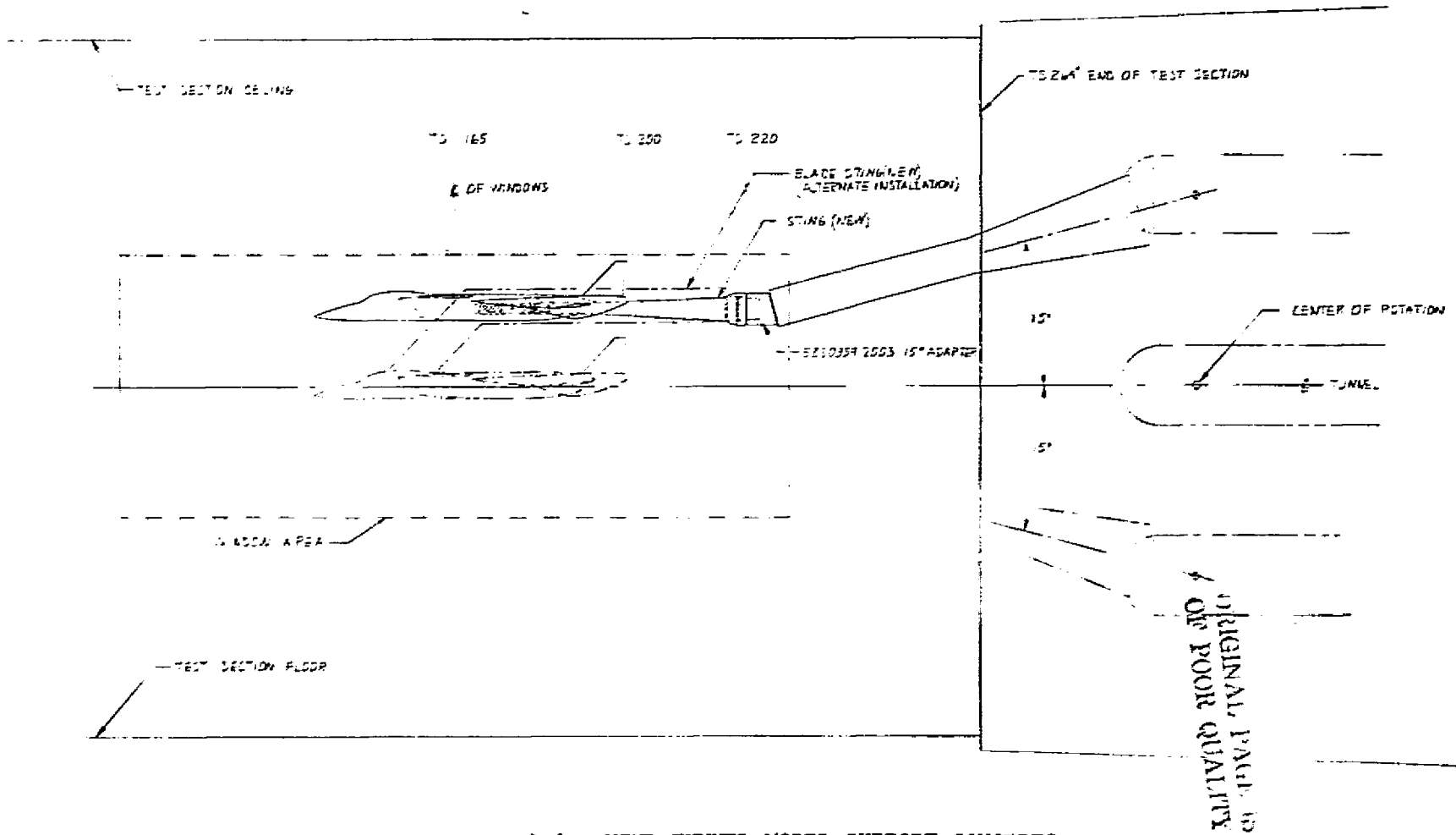


FIGURE 8-6. WIND TUNNEL MODEL SUPPORT CONCEPTS

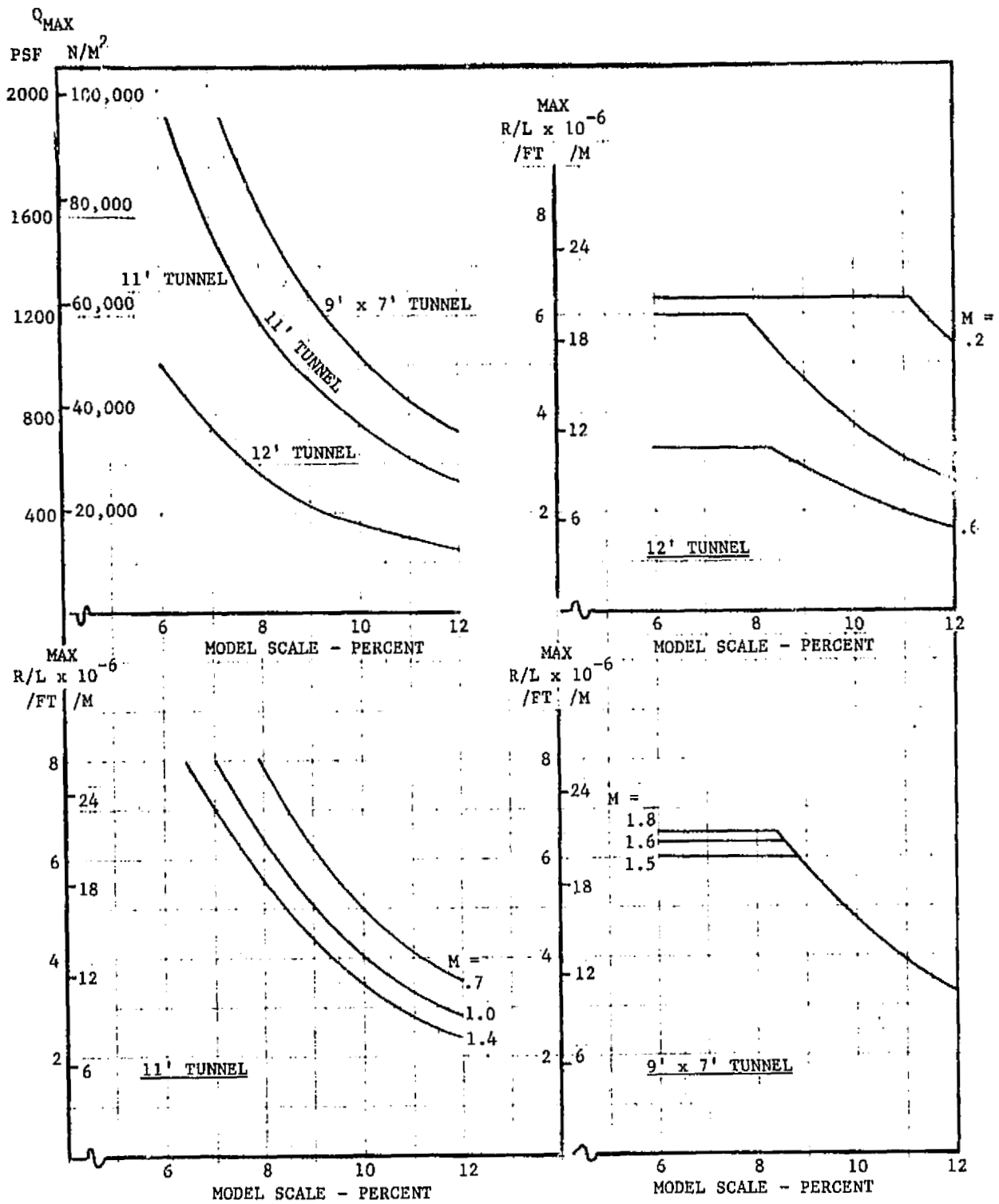


FIGURE 8-7. WIND TUNNEL DYNAMIC PRESSURE AND REYNOLDS NUMBER CHARACTERISTICS



ORIGINAL PAGE IS  
OF POOR QUALITY

8-18

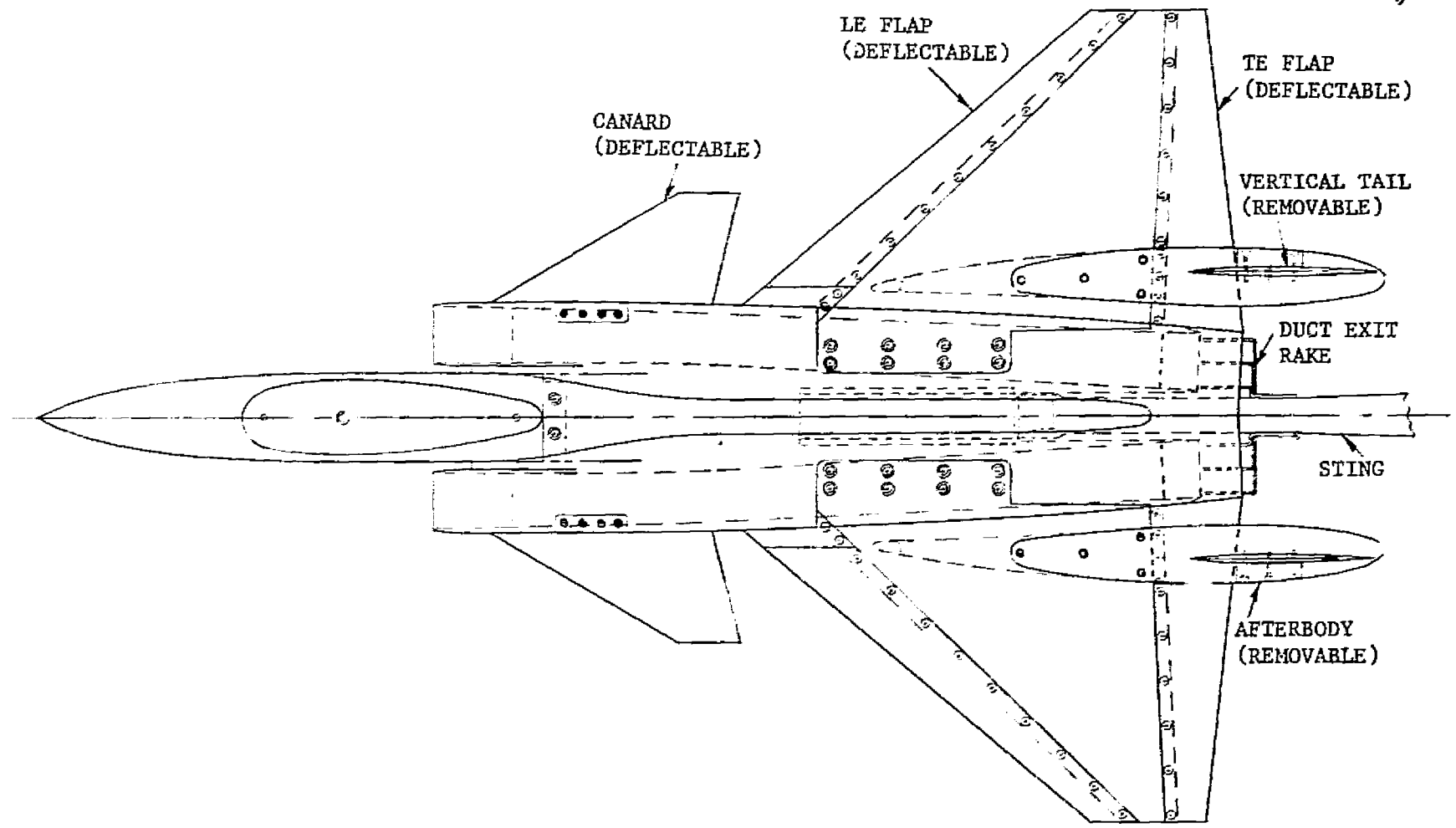


FIGURE 8-9. MODEL SKETCH

PRECEDING PAGE BLANK NOT REPRODUCED

SECTION 9  
CONCLUSIONS

The aerodynamic characteristics of a horizontal attitude VSTOL (HAVSTOL) fighter attack aircraft concept have been studied in some detail. The aircraft design relating to structures and subsystems was investigated in sufficient depth to ensure a credible design for the aerodynamic studies. The aerodynamic studies resulted in the following conclusions.

1. The HAVSTOL aircraft concept is a viable candidate for the shipboard VSTOL fighter/attack aircraft.
2. The VTOL requirements and resulting compromises to the propulsion-airframe configuration places most of the penalty of VTOL on the aircraft. However, the system should be more compatible to operations from many types of Navy ships than a vertical attitude VSTOL concept (VATOL).
3. The minimum drag estimated at supersonic speeds may be increasingly conservative as Mach number increases because of the corrections to the estimates that were applied. Test data is required to establish the correct drag levels.
4. Analytical procedures do not accurately predict the effect of canards on the aerodynamic characteristics of the aircraft. New methods should be developed and compared to past and future test results.
5. The longitudinal aerodynamics at high angle of attack, especially with large negative canard deflections should be investigated through wind tunnel test.
6. The NASA-Ames Wing-Body Aerodynamics Program is very useful for investigating the effects of fixed and variable camber. The effectiveness of variable camber at supersonic speeds should be determined from test.
7. The potential creation of a fountain between the fore and aft jets and possible alleviation of the effects with the high attitude VTOL concept requires further study and test.

8. Propulsion simulation would be very useful in determining a number of interactions between the propulsion system with vectored thrust and the aerodynamic characteristics of the airframe. Vectored thrust for maneuver enhancement could be analyzed. With simulation of the RALS in addition to the main propulsion nozzles with vectoring, the nose high VTOL operational concept could be studied and ingestion and suckdown characteristics determined. In addition, the propulsion interference on pitching and rolling moment during transition could be assessed.